Computational Estimation of Haemodynamics and Tissue Stresses in Abdominal Aortic Aneurysms

Katharine H. Fraser

A thesis submitted for the degree of Doctor of Philosophy.
The University of Edinburgh.
August 2007

Abstract

Abdominal aortic aneurysm is a vascular disease involving a focal dilation of the aorta. The exact cause is unknown but possibilities include infection and weakening of the connective tissue. Risk factors include a history of atherosclerosis, current smoking and a close relative with the disease. Although abdominal aortic aneurysm can affect anyone, it is most often seen in older men, and may be present in up to 5.9% of the population aged 80 years. Biomechanical factors such as tissue stresses and shear stresses have been shown to play a part in aneurysm progression, although the specific mechanisms are still to be determined. The growth rate of the abdominal aortic aneurysm has been found to correlate with the peak stress in the aneurysm wall and the blood flow is thought to influence disease development. In order to resolve the connections between biology and biomechanics, accurate estimations of the forces involved are required.

The first part of this thesis assesses the use of computational fluid dynamics for modelling haemodynamics in abdominal aortic aneurysms. Boundary conditions from the literature on healthy patients are used, along with patient specific aneurysm geometries, to obtain a first estimate of blood flow patterns and haemodynamic wall parameters within the aneurysms. The use of healthy patient boundary conditions is difficult to justify as the presence of the aneurysm is likely to alter the flow rate in the aorta. This is investigated with a Doppler ultrasound study of blood velocities in the normal and aneurysmal aorta. Archetypal waveforms reveal a significant difference in the diastolic maximum of young healthy volunteers and AAA patients. The archetypal aortic velocity wave for patients with abdominal aortic aneurysm is used to calculate the haemodynamics in a group of patients and these calculations are compared with those obtained using patient specific boundary conditions, and with phase-contrast magnetic resonance imaging measurements of blood velocity. With the correct z-velocity profile at the entrance to a short inlet section proximal to the aneurysm, the calculated velocities agreed qualitatively with the measured velocities. However, the velocities calculated using the correct inlet flow rate, but a simple velocity profile, are quite different from the measurements. These results show that the correct velocity profile at the aneurysm entrance is required to predict velocities within the aneurysm cavity.

In reality the blood and the artery wall interact: the blood flow domain continually dilates and contracts, altering the flow patterns; the flow controls the pressure on the wall and therefore the stresses within it. The influence of this fluid-structure interaction on the blood flow and tissue stresses is investigated in axially symmetric models of abdominal aortic aneurysm. Modelling of the complete fluid-structure interaction reveals how the pressure and flow waves are distorted by the aneurysm geometry. This distortion, which is absent from both static pressure and one way coupled models, accounts for the small errors in tissue and wall shear stresses obtained when using these models with lower computational complexity. These errors vary with the type of modelling as well as the aneurysm diameter and elasticity. A one dimensional, lumped parameter model of the aneurysm is developed to elucidate the effect of aneurysm geometry on the propagation of pressure and flow waves. It reveals interesting consequences of the diameter of the aneurysm on its inductance and resistance, and its use in improving the outlet pressure boundary condition is investigated.

Declaration of originality

I hereby declare that the research recorded in this thesis, and the thesis itself, was composed and originated entirely by myself, except were explicitly stated otherwise in the text, in the Department of Medical Physics, and the Institute for Materials and Processes, at The University of Edinburgh, and has not been submitted for any other degree or professional qualification.

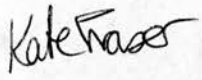

Katharine H. Fraser

Acknowledgements

Firstly, I would like to thank my supervisors, Pete and Bill, for accepting me into their group, and giving me all the help and support, and many invaluable discussions, I needed to complete this work, and as well, for giving me the freedom to explore my own ideas.

There are many other people I would like to thank for their help with different aspects of this thesis; without them the work would not have been possible: Tristan Lawton provided the anonymized CT scans used in chapter 2; Sarah Jane Carmichael, Margaret Glass and Dr. Paul Allan all scanned patients and normal subjects to acquire the Doppler spectra used in chapter 3; and Dr Ian Gillespie and Dr Graham McKillop helped with the MRI study in chapter 4 and Lesley Breen took the pressure tonometry measurements. Thanks also to David Stewart and his team at SEESUP for sorting out all my computer troubles.

I would like to thank all the members of my group, especially Mingxiu, for allowing me to use her FSI code and for help and advice on countless occasions, William, who really is very clever and gave me so much help with finding the source of my wobbles, Siobhan, for scanning volunteers for more Doppler spectra, and for broomcupboard giggles, James, for advice and debates on all things ultrasound and flow related and most importantly for being my cake comrade, Steven, for help with Magics, Dave, for proof reading parts of this thesis, Anis and Pavel, for happy conference memories, and to Tamie, Jason and Chaoquan for help in the early days on acoustic measurements, Fluent and segmentation respectively.

The EPSRC must be acknowledged for their generous financial support, without which none of this would have been possible.

All my friends in Medical Physics have been great and have made this a fantastic place to work for the last four years. Special thanks to Michael and Mairéad, for sausage stir-frys and Friday pints respectively, and to them both for proof reading thesis sections. Thanks to Norman for Burns Nights and wee drams, and to Irene who always made sure I was okay.

Thanks to Mum and Dad for their support and for finding random papers, and to Andy, whose jovial mocking reminds me there is a real world out there. Most of all I want to thank Chris, who has been encouraging all the way through, put up with all my moodiness, and has never once told me to hurry up; I dedicate my thesis to you.

Contents

Abbreviations and Symbols

Abbreviations

AAA	abdominal aortic aneurysm	PIV	particle image velocimetry
CFD	computational fluid dynamics	PWA	pulse wave analysis
CT	computed tomography	PWV	pulse wave velocity
ECG	electrocardiogram	RW	rigid wall calculation
GCI	grid convergence index	SP	homogeneous pressure analysis
FEM	finite element modelling	SV	sample volume
FSI	fluid-structure interaction	TDI	tissue Doppler imaging
IVUS	intravascular ultrasound	US	ultrasound
LDA	laser Doppler anemometry	vWf	von Willebrand factor
MMP	matrix metalloproteinase	WSS	wall shear stress
MRI	magnetic resonance imaging	WSSAD	wall shear stress angle deviation
OSI	oscillatory shear index	WSSG	wall shear stress gradient
PC	phase contrast		

Symbols

C	capacitance	$m^3\ Pa^{-1}$	V	voltage	V
E	ordered error estimate		V_{centre}	centreline velocity	m
E_p	pressure-strain elastic modulus	Pa	α	Womersley number	
E_Y	Young's modulus	Pa	γ	cross-correlation	
I	current	A	μ	dynamic viscosity	Pa s
L	inductance	$Pa\ s^2\ m^{-3}$	ν	kinematic viscosity	s^{-1}
R	resistance	$Pa\ s\ m^{-3}$	ρ	density	$kg\ m^{-3}$
Re	Reynolds number		τ_z	longitudinal stress	Pa
P	pressure	Pa	τ_{zr}	shear stress	Pa
Q	flow	$m^3\ s^{-1}$	τ_θ	circumferential (hoop) stress	Pa

Chapter 1
Introduction

The use of computational methods in the study of vascular biomechanics has shed new light on many medical problems and helped to reveal how physical forces are connected with biology. In this chapter the relationship between vascular biology and biomechanics, and between biomechanics and clinical practice, especially in abdominal aortic aneurysm, will be discussed. Methods for measuring the factors responsible for biomechanical forces, that is the blood flow and tissue motion, are also discussed and the limitations of measurement are evaluated. Calculations can be used to fill in some of the gaps left by measurements but there is still work to be done in improving and validating computational methods. Finally, some areas for improvement will be identified and a strategy for tackling these areas will be outlined.

1.1 Biological Effects of Stress on the Vascular System

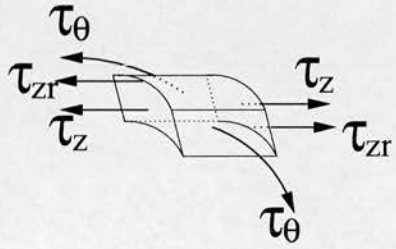

Figure 1.1: *Stresses on a small section of artery: τ_θ is the circumferential stress, τ_z is the longitudinal stress and τ_{zr} is the shear stress.*

Arteries are under constant pulsatile stresses, both tensile, in the circumferential (hoop) and longitudinal directions, and shear stress from the flowing blood (figure 1.1). The tensile stresses have magnitudes of the order of 10^4 - 10^5 Pa whereas the shear stresses are much smaller, of the order of 1 Pa. The wall shear stress (WSS) is the shear stress acting on the inner surface of the artery wall, which is in contact with the flowing blood. WSS is the most commonly studied flow related shear stress though there are a number of other shear stresses which will

be discussed later. These stresses have been shown to influence arteries both in their normal, healthy state and in disease.

1.1.1 Healthy Arteries

Normal arteries remodel to maintain a small range of wall shear stresses [1]. During blood vessel formation and growth the diameter is regulated by the flow rate. For example, in embryo development vessels with high flow enlarge while those with low flow get smaller. In adults, arterial diameters are moderated to maintain a shear stress of 1 - 2 Pa. However, in studies in which the endothelial cells have been removed arterial remodelling failed to occur showing that remodelling relies on an intact endothelium.

Healthy arteries must be capable of stopping the bleeding following injury, a process known as haemostasis. If an artery is ruptured a high velocity jet of blood is released. The high shear stress [2] within this jet is responsible for activating the platelets and causing platelet adhesion to exposed collagen, and aggregation through the blood glycoprotein von Willebrand factor (vWf) [3].

1.1.2 Diseased Arteries

When haemodynamic stresses are altered outside their normal ranges vascular diseases can occur. The following subsections describe the formation of atherosclerosis and thrombosis and the contribution of physical forces to these diseases. Aneurysm is another disease which is thought to be influenced by stresses and this will be discussed in detail later.

1.1.2.1 Atherosclerosis

Atherosclerosis is a disease of the larger arteries which are exposed to pulsatile deformations and stresses as well as time-varying shear stress [4]. Of the three layers constituting the artery (intima, media and adventitia) atherosclerosis affects the intimal and medial layers where an excessive inflammatory response is thought to result in atherosclerotic lesions. Mechanical stresses are important in both the early development and ultimate fate of the disease. Atherosclerotic lesions, or plaques, most often occur at bifurcations, branches and bends which typically have low shear and high tensile stress [4].

In regions of low shear the blood is moving slowly, thus prolonging the exposure of the endothelium to atherogenic particles such as lipids and activated white blood cells [4]. In the presence of flow, endothelial cells become aligned parallel to the flow, whereas in regions of low or oscillating flow endothelial cells are oriented randomly. The randomly aligned cells may have weaker attachments to each other which would increase the permeability allowing greater passage of leukocytes [4]. For leukocytes to be absorbed they must be adhered to the endothelium with specific molecules, the expression of which is inhibited by shear stress. Shear stress also upregulates certain genes which are likely to be vasoprotective.

In regions of high tensile stress the arterial wall tends to become thicker, a change helping to reduce tension, and its composition is altered. Early atherosclerotic lesions appear as localized areas of intimal thickening. Vessel thickness and density affect permeability and reduced permeability increases accumulation of cholesterol and leukocytes in the intima. With age, progressive accumulation of connective fibres tends to make the arteries denser and increasingly resistant to clearance across the wall. Arteries subjected to hypertension will become even denser [4].

Shear rate could be another important factor since regions with low shear stress also experience a low shear rate. A shear rate mediated mechanism implies that mass transport between the blood and the wall is a contributing factor [1].

1.1.2.2 Thrombosis

Blood clotting, or thrombosis, is strongly influenced by flow since flow determines the rate of platelet arrival at the surface and the level of shear stress experienced by the platelets influences their clotting [3]. As in haemostasis, if platelets are exposed to high shear they become activated through vWf, however there is another mechanism by which thrombosis occurs; stagnant blood is clotted by a cascade of coagulation proteins [2].

1.2 Abdominal Aortic Aneurysm

An aneurysm is a disease involving a dilation, stretching, or ballooning of a blood vessel. Aneurysms can occur in many of the major arteries but are most common in the aorta and the intracranial arteries. An aneurysm in the aorta is defined as an increase in the diameter of

the aorta of more than 50 %, as compared to the normal healthy section above or below the diseased section [5]. Aortic aneurysm may involve any of the aortic sections: ascending aorta, aortic arch, descending thoracic aorta or the abdominal aorta or may span several sections. Of these, the abdominal aorta is the most common location and abdominal aortic aneurysm (AAA) may be present in up to 5.9 % of the population aged 80 years [6]. Figure 1.2 shows a representation of an AAA.

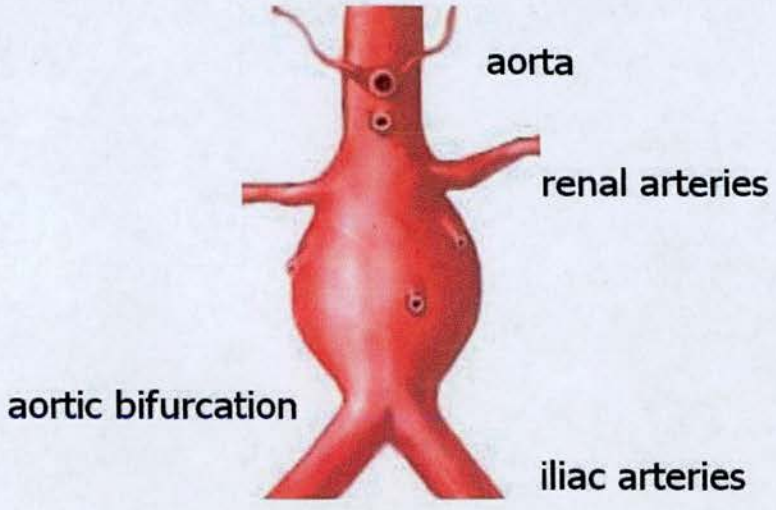

Figure 1.2: *Simplified diagram of an abdominal aortic aneurysm showing nearby arteries. Adapted from the U.S. National Library of Medicine's Medline Plus: http://www.nlm.nih.gov/medlineplus/ency/imagepages/18072.htm*

The mortality rate for AAA rupture is approximately 90%, when patients dying before they reach hospital are included. The mortality rate for emergency repair operations may be as high as 50% [7]. For these reasons it is preferable to repair the aneurysm before it ruptures and, in patients with low to normal surgical risk, conventional surgery (simple repair without use of a stent) is usually effective, with a mortality from 0 to 8% [6]. However, in patients with high surgical risk, for example those with lung problems, kidney problems, or angina, the risk is between 8 and 30% (but less with endovascular stent grafts). The decision to operate can be a tricky one for surgeons as they must balance the relative risks of rupture and surgery.

AAAs are usually fixed by a routine operation if their maximum anterior-posterior diameter is above 5.5 cm, or if they have symptoms, usually pain, they will be operated on immediately with an emergency operation. The 5.5 cm threshold is based on data from the United Kingdom Small Aneurysm Trial [8] and the United States Aneurysm Detection and Management study

[9]. The criterion is recognized to be imperfect since 60 % of aneurysms with diameters above 5.5 cm never rupture [10] and 10 % with diameters less than or equal to 5.5 cm do rupture [11].

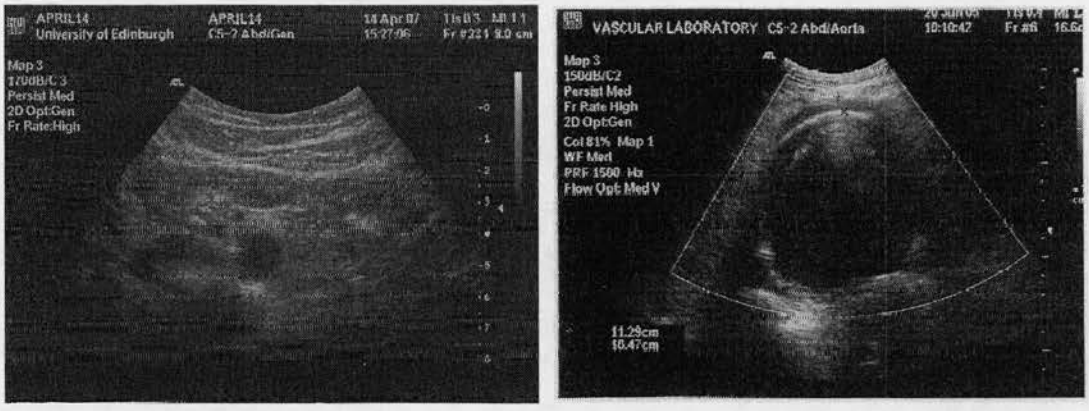

(a) normal aorta (b) large AAA

Figure 1.3: *Transverse B-mode US images of the normal aorta and a large (>10cm) AAA.*

Ultrasound (US) is the most accurate, least expensive and easiest method for diagnosis of abdominal aortic aneurysm [12] and patients with AAAs are usually monitored with serial US scans. Some regions of the UK have screening programs for AAAs [13]. B-mode scanning in the transverse plane is used to measure the anterior-posterior diameter: the most important measurement for prognosis (figure 1.3). B-mode scanning in the longitudinal plane is also useful as it shows the relative dilation of the aneurysmal section compared to the healthy section of the aorta (figure 1.4).

The exact cause of AAA is unknown. Risk factors for the disease include a history of atherosclerosis, current smoking and a close relative with AAA [14], but combinations of these factors increase the risk [15]. Although AAA can affect anyone it is most often seen in older men. A number of mechanisms are potential causes: atherosclerosis, wall stresses, vibratory forces (due to high frequency turbulent oscillations), enzyme imbalances, infection, congenital weakening of the connective tissue component of the artery wall, or rarely, trauma [16]. Once established, the risk of an ancurysm rupturing increases with its size.

The wall of the aorta, like other arteries, consists of three layers: tunica intima, tunica media and tunica adventitia [17]. The intima is the innermost layer, and in the aorta, consists of a mono layer of endothelial cells and a subendothelial layer comprising connective tissue and axially oriented smooth muscle cells. The internal elastic lamina is a thin, perforated sheet of

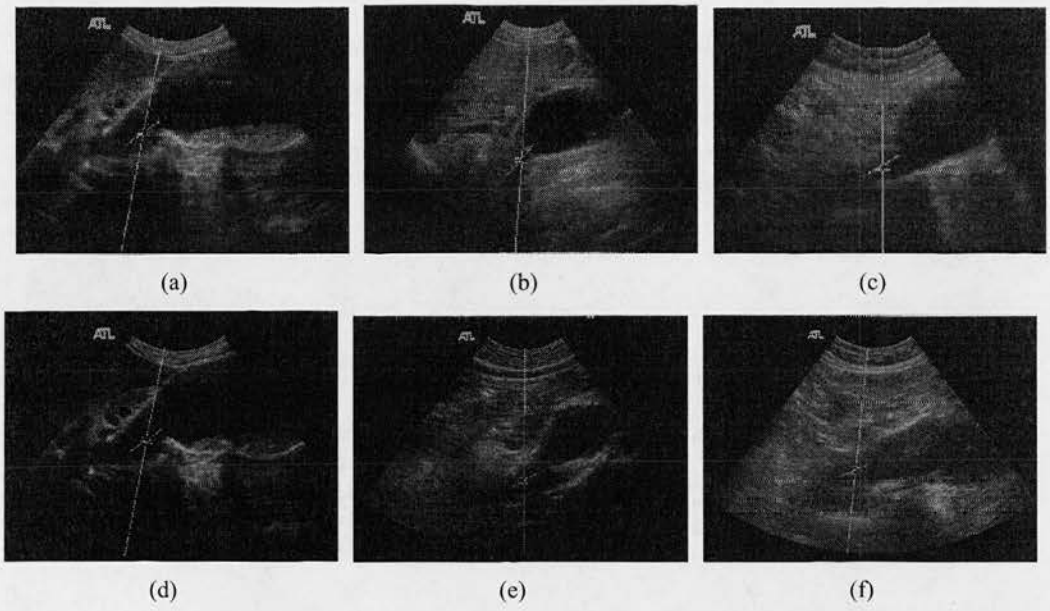

Figure 1.4: *Longitudinal B-mode US images of AAAs.*

elastin, which separates the intima and the media. The media contains smooth muscle cells arranged in concentric layers with elastin and collagen as well as ground substance, in what are termed lamellar units. Surrounding the media is the adventitia, a poorly defined, dense layer of collagen fibers, elastin, nerves, fibroblasts and the vasa vasorum (blood supply).

During the progression of aneurysmal disease the structure of the wall changes. The intima acquires mural thrombus, cholesterol and calcified lipid. Many of the smooth muscle cells in the media die [18] (volume fraction 2.2%, compared to 22.6% in healthy aorta [19]) and collagen and elastin fibres are broken. The structured lamellar units of the media in the aneurysmal wall are destroyed and there is a much lower elastin content (2.4 %) than in the healthy aortic wall (22.7 %). The collagen of the adventitia is replaced by a thicker layer of more structured and less pliable type I collagen.

So, the histology suggests that abdominal aortic aneurysms result, at least in part, from damage to the elastin, and the elastic lamallae [17]. Based on animal studies, showing that elastase induced degradation of elastin resulted in dilation of the normal wall, it has been suggested that an initial insult may spark infiltration of inflammatory cells, which go on to induce secondary degradation of the elastin [17]. Matrix metalloproteinases (MMPs) are a group of enzymes which break down matrix macromolecules, such as elastin, which would otherwise be long

lasting. Many MMPs have been found in higher quantities in human aortic aneurysm tissue than in the normal aorta [20]. MMPs are produced in an inactive form by macrophages, they are then activated by plasmin [21] and can be blocked by specific inhibitors. The role of MMPs in AAA is complicated [22] but there is evidence that a combination of MMPs is required to produce aneurysms, in particular MMP-2 and MMP-9 [23] which break down elastin, as well as gelatin and several types of collagen. A careful combination of MMPs, plasmin, and inhibitors appears to be responsible for the formation of abdominal aortic aneurysm [24].

There are several theories for the cause of the initial injury which prompts the inflammatory response:

Firstly, in the past, most wall degradation in abdominal aortic aneurysms has been attributed to atherosclerotic changes [25]. However, the relationship between aneurysm and atherosclerosis is unclear since aneurysms are often observed in patients without atherosclerotic disease [26] and aneurysms rarely form at sites of most severe plaque. Atherosclerosis is primarily a disease of the intimal layer while aneurysm is associated more with the media. Also, patients presenting with aneurysmal disease are usually older than those with atherosclerotic plaques (average ages 70 years and 55 years respectively) [16]. In favour of an atherosclerotic initiation is the fact that the abdominal aorta is a common site for atherosclerosis, as well as aneurysm. The constitution of the aorta changes along its length with lower concentrations of both elastin and collagen in the distal compared to the proximal aorta. In addition, the infrarenal aorta has a lower collagen content than the suprarenal aorta [27]. The thickening of the intima, which is an early sign of atherosclerotic disease, has been related to the complexity of the flow in distal aorta. An endothelial cell response to disturbed flow, which leads to plaque development in some patients, could perhaps result in aneurysm in others, due to other effects. For example patients with aneurysms may have enlarged arteries, both longer and wider (arteriomegaly), and have a tendency to be taller and thinner [16]. In addition, many AAAs do contain atherosclerotic plaques and it has been suggested that wall thickening due to atherosclerosis may help prevent aortic expansion due to aneurysm [28].

A second theory for aneurysm initiation is related to wave reflections [25]. Branches in the arterial tree cause the propagating pressure wave to be partially reflected. The amplitude of the wave reflected from the aortic bifurcation depends on the relative diameters of the aorta and iliac arteries, as well as on their relative elasticities. If the aorta is wider, perhaps due to arteriomegaly, or the iliacs get narrower, possibly due to atherosclerotic plaques, the reflected

amplitude is larger [29]. The increased pressure in the distal aorta [30], resulting from the reflection, may cause higher stresses in this region which could result in aneurysm. This wave reflection theory is usually associated with ageing [25]. The magnitude of the reflection coefficient of the aortic bifurcation increases with age above about 40 years [31] due to generalized stiffening of the aorta and increasing tortosity and narrowing of the iliacs. When combined with the increased wave speed in older arteries (also due to stiffening), which shifts the reflected pressure wave earlier in time relative to the forward wave, there may be an increase in the systolic pressure in the abdominal aorta. Assuming the increased pressure results in degeneration in the artery, and subsequent permanent dilation, the area ratio is increased further and disease progression is enhanced [25].

Thirdly, as arteries age they generally get longer [32], as well as stiffer. The abdominal aorta is relatively unconstrained in the abdominal cavity and as its length increases bends and kinks may form. This tortuosity would change the haemodynamics within the lumen leading to regions of flow separation, and the resulting oscillatory and low flow regions which have been shown to be susceptible to atherosclerosis [25]. Alternatively, kinks and bends result in an uneven distribution of tissue stresses and potentially stress hot spots in which the elastin is more damaged [25]. Either of these effects, if severe enough, could possibly trigger an inflammatory response of the sort thought to be required for aneurysm formation.

It is probable that aneurysm initiation is related to more than one of these theories and that these theories relate to the disease progression as well as initiation. All three theories consider the possible effects of changes in the forces on the aortic wall. In the following sections the effects of flow and tissue stresses on AAA are examined in more detail.

1.2.1 Effect of Flow on AAA

The effects of haemodynamics on abdominal aortic aneurysms can be grouped in to three main areas: effect of shear stress on the endothelial cells; effect of blood flow on delivery of cells to the wall; and effect of shear stress on platelets. The innermost layer of the aorta, the intima, is lined on the inside by a single layer of endothelial cells. These form a semi permeable barrier which protects the underlying artery but also allows substances to filter through [33]. Endothelial cells are usually flat and elongated in the direction of the blood flow and are linked to each other to enable communication. They can also communicate with the underlying smooth muscle cells [17]. The endothelial layer is anticoagulatory [33].

Endothelial cells, or possibly the glycocalyx [34], are sensitive to both shear stress and tensile stress. Alteration of stress levels signals the cells to modify their production of autacoids, the most important of which are nitric oxide and prostaglandins [34]. These act on the smooth muscle cells and can cause them to tense, relax or multiply. In this way arterial diameter is regulated by the shear stress on the endothelial cells: increased shear stress leads to increased arterial diameter and reduced shear stress leads to reduced diameter. Another effect of reduced shear stress is thickening of the intima-medial layer, which may be a precursor to atherosclerotic disease. Shear stress levels of 1.0-1.5 Pa have been found to have a protective effect on endothelial cells *in vitro* but levels of about 0.4 Pa stimulate atherosclerosis [34]. As previously discussed atherosclerosis is a possible initiation for abdominal aortic aneurysm.

Elevated WSS in the forward direction has been shown to increase endothelial cell and smooth muscle cell density in experimental AAA [35]. One mechanism by which increased forward WSS may reduce AAA progression may be through increased activity of endothelial nitric oxide synthases (eNOS) and nitric oxide (NO) production in response to temporal shear stress gradients. Nitric oxide in turn decreases production of MCP-1 which reduces intimal monocyte binding. In support of this possibility is increased eNOS expression in high flow experimental AAA [36].

An intact endothelium is important to inflammatory response since injured endothelial cells and smooth muscle cells make and secrete regulatory proteins that attract white blood cells to the arterial wall [37]. The proliferation and migration of endothelial cells is mediated by shear stress [38]. Shear stress also limits adhesion of white cells and migration of white cells through the arterial wall [4, 39].

Granulocyte macrophage colony stimulating factor (GM-CSF) is a protein produced by monocytes, fibroblasts, endothelial cells and smooth muscle cells which plays a vital role in stimulating blood stem cells to produce white cells and prolongs the life time of monocytes. Observations of experimental AAA suggest that flow conditions may influence GM-CSF expression and release [40].

The deoxyribnucleic acid (DNA) binding protein nuclear factor-kappa beta (NF-κB) has been found to play a role in AAA pathogenesis. NF-κB regulates production of many pro-inflammatories, including MCP-1, partly via influences in flow conditions and WSS. *In vitro* studies have demonstrated that MCP-1 and PDGF-A (MCP-1 helps monocytes move about and PDGF-A

helps SMCs reproduce and move about) expression in endothelial cells was enhanced by the application of impulse flow (a pulse of flow resulting in a stress of 0.16 Pa for 3 s), as compared to steady or ramped flow, suggesting that temporal shear stress gradients, in addition to shear stresses, could be an important factor in the disease process [41].

As previously discussed, inflammation is an important aspect of aneurysmal disease which involves macrophages and lymphocyctes permeating the aneurysm wall. These cells initiate the process of elastin degeneration by MMPs. The cells are in the blood stream; they must migrate to the artery wall and infiltrate in order to cause the inflammatory response. Fluid dynamics is responsible for this migration by convection and once at the wall the shear stress on the cells will determine whether they adhere.

Most aneurysms contain a layer of thrombus, or clotted blood, which lines the wall (figure 1.5). The role of the thrombus in aneurysm pathology is currently still under debate but it is thought to be an important aspect of the disease [42]. The thrombus consists of a fibrin structure incorporating blood cells, platelets, blood proteins and cellular debris. The thrombus is a laminated structure which can be divided into three main layers: luminal, medial and abluminal [43]. The luminal layer is in continuous contact with the flowing blood and is constantly being renewed [44] which gives it a reddish colour [43]. The medial layer is white and the abluminal layer is brown [43]. The abluminal layer is composed of a loose network of degraded fibrin in which the components of the luminal layer can no longer be identified but dying neutrophils are present [44].

The build up of the thrombus layer is partially determined by the platelet deposition rate which is affected by several factors: the rate of arrival of platelets at the wall; the shear stress on the platelets at the wall; and the level of activation of the platelets. Blood platelet deposition in an *in vitro* model aneurysm was found to be enhanced by the aneurysm cavity [45]. Platelet adhesion increased along the aneurysm length to a maximum at the distal edge, which can be attributed to the enhanced convection of particles along the locally curved streamlines. However, in a rat model of AAA, uptake of an activated platelet marker was most intense in the upper part of the aneurysm [44]. In the model aneurysm, during turbulent flow, platelet deposition was more uniform along the aneurysm because platelets are deposited on the wall by random fluctuations [45].

If the shear stress at the wall is too high, platelets will be convected distally. However, in areas

Figure 1.5: *Thrombus from aortic aneurysm. Note the layers on the exposed section. (Image obtained from The BioMed Image Archive, University of Bristol)*

of flow recirculation, such as in aneurysms, where there are areas of low wall shear stress, the stagnant blood beside the wall has time to clot [46, 47].

Platelet aggregation is thought to be responsible for thrombus renewal [42]. To aggregate, platelets must be activated, and platelets exposed to high shear stresses become activated [32]. In simple aneurysm models there are regions of high shear stress between the forward flowing core and the reverse flow near the wall. The bulge of an aneurysm has also been found to promote turbulence which has inherently high shear stresses [32]. In a rat model, inhibition of platelet aggregation was shown to limit aortic aneurysm expansion [42].

Shear stresses exist throughout the artery wall, resulting from continuity of the WSS across the wall, and from local bending due to geometric irregularity. The effects of this shear stress have not been studied in nearly as much detail as the effects of shear stress on the surface, and yet vascular smooth muscle cells must experience shear stresses of the same order as the endothelial cells [17]. This shear stress is much smaller than the normal component but examples of its effects on smooth muscle cells have still been shown, including numerous consequences on gene expression, increased rate of proliferation with shear stress and alignment of cultured smooth muscle cells perpendicular to the flow (their *in vivo* orientation) [17]. The effects of shear stress through the wall of an aneurysm have not been investigated.

In summary, both the initiation and development of abdominal aortic aneurysm are influenced

by haemodynamics. Aneurysm initiation might be related to shear stress on the endothelium. Once a small aneurysm exists the endothelial cells are likely to direct its growth through their production of chemicals in response to shear stresses. The haemodynamic conditions influence white blood cell concentrations in AAA which suggests that inflammation and therefore aneurysm progression are modulated by blood flow. The aggregation of platelets and growth of the thrombus is in part determined by shear stresses and flow streamlines. Hence, an understanding of the haemodynamics involved is essential if this life threatening disease is to be fully comprehended.

1.2.2 Effect of Tissue Stress on AAA

Tissue stress in abdominal aortic aneurysms has mostly been studied in relation to the final outcome of the disease, that is aneurysm rupture. It is clear that for rupture to occur the local tissue stress must exceed the strength. Less obviously, it has been shown *in vivo* that aneurysm expansion is also associated with peak tissue stress [48] and there have been attempts to model the growth of different aneurysms [49], including AAA [50], according to the tissue stress.

Much of the arterial wall consists of intricate networks of macromolecules which make up the extra-cellular matrix. The composition and structure of this matrix determine the artery's mechanical properties. Elastin and collagen bear most of the load. At small strains elastin takes the load and gives rise to the artery's isotropic behaviour and at large deformations collagen takes over [50]. Collagen is stiffer than elastin but is bunched up, or corrugated, at physiological, arterial strains. As the strain increases more of the collagen fibres straighten out and start to hold the load and it is this collagen recruitment which gives the artery its nonlinear behaviour [17].

If the elastin begins to be degraded, as in the case of aneurysm, the collagen starts to bear some of the load at physiological strains. This in itself will lead to a dilation of the artery as the collagen must be stretched above its initial level to bear any load. Whilst elastin is a stable macromolecule with a long half life, collagen is in continual production and decay [50]. At increased wall stress collagen synthesis is enhanced and the wall thickens to reverse the stress increase [17]. When new collagen is produced it is thought to be synthesized either in its zero stress state [49], to allow for further recruitment at higher strains, or in a prestrained state [50], such that the current load is primarily borne by the remaining elastin.

Leung *et al.* [48] performed a finite-element study of wall stress in four patients over four years. They found that maximum computed stress in the aneurysm wall was related to the growth rate: those aneurysms with higher peak stress (above 350 kPa) had higher growth rates (0.73-1.1 mm/year) than those with lower peak stresses (0-0.33 mm/year).

The effects of cyclic stretching on vascular smooth muscle cells and endothelial cells are numerous. For example cyclic stretch has been shown to enhance proliferation of both cell types as well as promotion of elastin and collagen production. Macrophages under cyclic stretch were found to produce higher levels of MMP-9 [51].

Vorp *et al.* [51] investigated the levels of various immune response chemicals and products of genes associated with remodelling in samples of AAA tissue from regions of aneurysms which had either high or low stress levels as assessed by computational modelling. They found that in regions of high stress there was a more activated immune component (high levels of C3 and P-Selectin) and impaired remodelling mechanisms (low levels of endothelin-1 and collagen IV) compared to the regions of low stress.

There have been many studies which have shown that peak stress in the aneurysm wall could predict rupture risk [52–56], probably better than the currently used maximum diameter [57, 58]. These have used finite element modelling of the arterial wall in patient specific models produced from patient scans. However, the failure strength of aneurysm tissue varies both between patients [59, 60] and within an individual patient [61, 62]. A better indicator of rupture potential would be achieved if the strength of the aneurysm wall could be estimated in addition to the stress [63, 64]. Vande Geest *et al.* [65] found that the strength of the wall could be estimated from four parameters: gender, family history, thickness of the intraluminal thrombus and normalized transverse diameter.

In summary, high stress in the aneurysm wall leads to remodelling of the collagen component but too much stress may accentuate the inflammatory response and inhibit this remodelling. Growth of aneurysms is increased with high peak stress and if the stress exceeds the failure strength the aneurysm will rupture. Hence, knowledge of the tissue stresses in the aneurysm wall is vital if the progression of this disease is to be limited and the fatal outcome prevented.

1.2.3 Summary

Abdominal aortic aneurysm is a potentially fatal disease about which there is still a lot to learn. The previous sections have shown the importance of, not only the tissue stresses within the aneurysm wall, but also the haemodynamics within the lumen, to the initiation, development and final outcome of this disease. This should have convinced the physical scientist reading this that they are a problem worthy of study by a physicist, but, in case the reader is still to be persuaded, it should be pointed out that Albert Einstein died of a ruptured abdominal aortic aneurysm in 1955 [66].

1.3 Measurement of Haemodynamics and Tissue Stress

In the previous sections what is known of the relationships between forces and biology in blood vessels, and in particular in abdominal aortic aneurysms, has been discussed. Knowledge of these relationships has only been possible because of detailed measurements of the forces involved. The following sections describe methods used for studying arterial flow and stress, both *in vitro* and *in vivo*, and what has been discovered about blood flow and tissue stress in AAAs.

1.3.1 Measurement of Haemodynamics

1.3.1.1 *In Vitro* Methods

Flow Visualization If a transparent model of a blood vessel is constructed then the flow patterns in a transparent fluid can be seen by adding a contrasting material which follows the flow. There are many experimental fluid dynamics techniques based on this principle which have been used to study qualitative flow fields at numerous locations in the cardiovascular system. For example: particle tracking velocimetry has been used to study the flow downstream of an artificial heart valve in a model of the aortic root [67]; hydrogen bubbles have been used to study vortices in stenosed and normal carotid arteries [68]; photochromic lines have been used to examine the correlation between stenosis length and post stenotic turbulence [69], as well as the shear stress in a coronary artery [70]; and dye washout has been used to measure the residence times of blood in the aorta and renal branches [71].

Laser Doppler Anemometry Laser Doppler Anemometry (LDA) uses the pattern of fringes produced by two interfering beams of laser light to measure the velocity of seed particles crossing the beams. Three components of the velocity can be measured simultaneously at a point. LDA has been used to study velocity profiles in models of many anatomical sites including a radiocephalic arteriovenous fistula [72], the aorta [73] and simple AAAs [74].

Particle Image Velocimetry Particle Image Velocimetry (PIV) uses a sheet of laser light to illuminate seed particles with two flashes of light and a camera to capture the two images. By looking at how far groups of particles have moved between the two images a vector map of the velocities in the plane can be produced. PIV has been used by several groups to study flow in AAA models [75–79].

Others The *in vivo* techniques of ultrasound and magnetic resonance imaging, discussed in section 1.3.1.3, have also been used *in vitro*. Generally this is to assess the accuracy of the technique in conditions where the flow is known. Ultrasound flow phantoms such as straight tubes (see for example [80]) and simple stenosis models (for example [81]) have been developed for studying the accuracy of velocity measurements. There are also occasions when details of flow fields have been revealed with *in vitro* US phantoms. The effects of flow in different shaped stenoses on Doppler US signals has been examined with the aim of improving specificity of clinical diagnosis [82, 83]. A feasibility study on the use of MRI for measuring the flow fields in intracranial aneurysms with an *in vitro* model revealed complex flow structures in the model which may be present *in vivo* [84].

1.3.1.2 *In vitro* studies on flow in the normal aorta

In vitro fluid dynamics studies on the abdominal aorta have revealed the complicated nature of the blood flow in this vessel. Whilst flow in the upper (proximal) section is relatively simple, that in the lower (distal) section experiences some very complicated conditions.

Flow in the section of the aorta proximal to the renal arteries, that is the suprarenal abdominal aorta, is generally forward throughout most of the cardiac cycle. The exceptions to this are: the formation of vortices at the level of the renal branches during systolic acceleration, which persist into systolic deceleration along with the formation of additional vortices on the posterior wall opposite the celiac and superior mesenteric branches [85]. Velocity profiles across the

suprarenal aorta are relatively flat and symmetrical in both the left - right and anterior - posterior directions [73]. The wall shear stress (WSS) is oriented in the same direction around the aorta in this region and the cycle averaged WSS is positive [86].

In contrast to the suprarenal section, flow in the infrarenal section of the aorta is more interesting. During systolic acceleration flow is almost all forwards with only the exception of small vortices below the renal arteries which spiral towards the centre of the vessel. During systolic deceleration a large flow separation zone forms at the posterior aortic wall. Three dimensional vortices formed in the iliac arteries are shed backwards, interfering with the separation zone to create complicated flow structures [85]. In the posterior section of the infrarenal aorta there is a slight skewing of the velocity profiles with the highest velocities located at the anterior wall. The skewing in the distal part of the infrarenal abdominal aorta is much more pronounced, especially during diastole, with the highest retrograde velocities near the posterior wall [73]. This corresponds with the flow separation zone which also results in a negative mean WSS on the posterior wall [86]. Radial velocities in both the suprarenal and proximal infrarenal sections of the aorta are small. In the distal section they are small during sytole but increase during diastole [73]. The greatest retrograde WSS in the distal section occurs on the lateral walls. The triphasic waveform, the reversed bifurcation during retrograde flow, and the different orthogonal planes of curvature all contribute to the complicated flow structures seen at rest in the infrarenal abdominal aorta [85].

At the aortic bifurcation there is flow separation at the lateral walls during systolic deceleration and reverse flow during diastole [85].

Under exercise conditions there is a smaller amount of reverse flow, explained by the larger steady component in the flow wave [85]. The velocity profiles are more highly skewed [73] and helical structures form below the renal arteries. These effects are explained by the higher Dean number ([87] and section 1.4.1.3) in the faster flow conditions [85]. The smaller amount of reverse flow has a corresponding reduction in shear stress reversal and the oscillatory shear index (OSI) ([86] and section 2.2.5) is much lower [86].

These fluid dynamical findings of more complicated flow conditions in the infrarenal aorta are reflected clinically in the greater incidence of atherosclerosis in the distal section. Intimal thickness correlates with OSI and the length of time in the cardiac cycle with reverse flow. There is also a negative correlation with the mean WSS [86].

1.3.1.3 *In Vivo Methods*

The *in vitro* methods rely largely on transparent models and transparent blood mimicking fluids. While there are some occasions when they can be used *in vivo*, see, for example, the work of Vennemann *et al.* [88] on blood flow in embryonic bird hearts, in general other methods are required.

Invasive Techniques The methods described in this section require either that a probe be inserted into a vessel or that a device is positioned around a vessel. Both of these involve surgical interventions and carry the associated risks and unpleasantness. In addition probes inside vessels disturb the blood flow.

Hot-Film Anemometry As blood flows past an electrical resistor it is cooled causing the resistance to change [32]. By measuring the voltage required to maintain a constant temperature the velocity of blood near the tip can be determined. The hot-film anemometer has a high frequency response and has been used to measure velocity fluctuations up to 1000 Hz; for this reason it has been used in the study of turbulent blood flow. It has also been used to measure velocity profiles across a vessel.

Electromagnetic Flow Meter Blood is a conductor, if it moves perpendicular to a magnetic field a voltage is generated across the blood vessel, and perpendicular to the magnetic field [32]. If the magnet is in a cuff outside the blood vessel the voltage across the whole vessel, perpendicular to the magnetic field, can be measured and used to determine the mean velocity within the blood vessel. The electromagnetic flow meter can also be built into a catheter tip [89] and inserted into the artery, which negates the need for exposing the blood vessel. This type of catheter tip electromagnetic flow meter has been used to measure the velocities in the aorta and its branches [90].

Ultrasonic Flow Meter Like electromagnetic flow meters, ultrasonic flow meters take the form of both cuffs and catheters [32]. There are two ways of using ultrasound to measure velocity: transit times and the Doppler effect. Transit time flow meters exploit the fact that the speed of sound is faster in the direction of the flow than against it. Transducers are placed on either side of the blood vessel, one downstream of the other. The difference between the

time taken to travel from transducer A to B and the time taken to travel from B to A is used to calculate the velocity. Doppler flow meters use the erythrocytes as scatterers and calculate their velocity from the frequency shift in the scattered ultrasound compared to the incident ultrasound.

X-ray Angiography An iodine-containing contrast agent is injected into the blood vessels and x-ray images are recorded as the the contrast bolus flows through the vessels and washes out. The images are digital and by subtracting a pre-contrast image from the subsequent post-contrast images the background can be removed [91]. The velocity of the contrast bolus through the vasculature, as determined from the timing of the images, can be used to calculate the blood velocity [92].

Non-Invasive Techniques These are techniques which can be used without putting devices inside the body. They do not affect the blood flow.

Doppler Ultrasound Transcutaneous Doppler ultrasound (US) uses the same principle as the Doppler US flow meter. The frequency shift in the US scattered by erythrocytes in the blood, as compared with the incident US, is used to calculate the blood velocity (figure 1.6):

$$v = \frac{c f_D}{2 f_e \cos\theta} \tag{1.1}$$

where the Doppler shift, f_D, is given by the difference in the incident and scattered frequencies, $f_D = f_s - f_e$, c is the speed of sound and θ is the angle between the beam and the direction of blood flow.

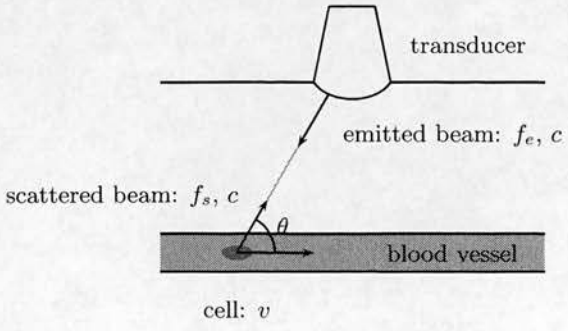

Figure 1.6: *Ultrasonic measurement of blood velocity.*

Modern clinical US uses pulses of sound rather than a continuous beam, in order to acquire depth information. Typically a pulse lasts for just 2 to 3 cycles which is not long enough to accurately measure its frequency. Instead the difference in the phases of successive returned pulses is used to calculate the frequency shift [93]. Motion of the blood perpendicular to the beam results in decorrelation of the signal over time.

The returned US signal actually consists of a range of frequencies, firstly, because the short pulse has a wide bandwidth and, secondly, because in reality there are many scatterers each with a slightly different velocity.

The two most popular methods of displaying the velocity data employed on current clinical scanners are spectral Doppler and colour flow. Spectral Doppler displays a graph of the changing frequency shift in the signal received from one sample volume with time. The whole frequency spectrum is displayed with the intensity of the signal at each frequency represented by the brightness (figure 1.7(a)). The colour flow image depicts the velocities in a whole section of the field of view. None of the spectral information is obtained, instead a fast estimate of the mean velocity and deviation in each sample volume is obtained using an auto or cross-correlation based method [94]. The mean velocity is then displayed in colour, overlayed on the grayscale B-mode image (figure 1.7(b)).

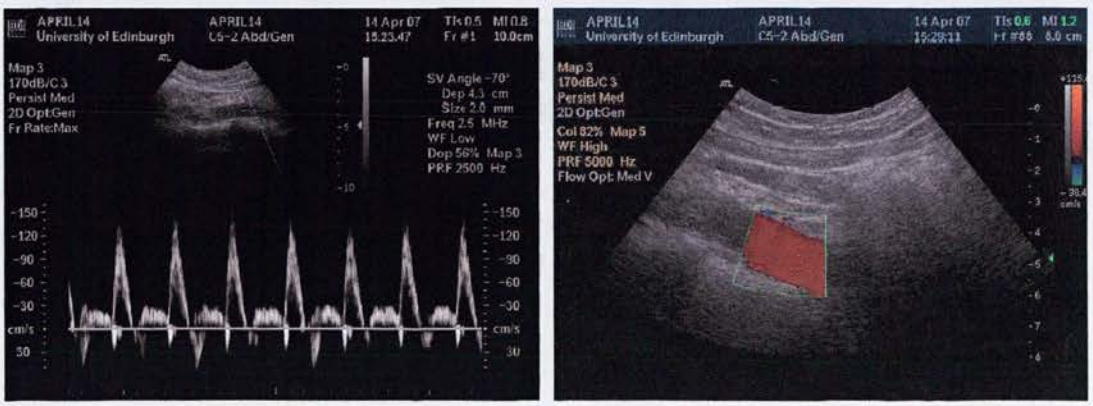

(a) Spectral Doppler

(b) Colour Flow

Figure 1.7: *Ultrasonic measurement of blood velocity in the normal aorta.*

A transducer converts the electrical signal to sound using a piezoelectric material. Different transducers are used for different applications: in abdominal US a curvilinear probe is most often used. This gives an increasing field of view with depth. The large depths needed for

examining the abdomen require low frequencies and around 2.5 MHz is typical.

Vieli *et al.* [95] used Doppler US to study anterior-posterior velocity profiles in the normal abdominal aorta. The profile was blunted and approximately symmetrical during the forward flow phase whereas during reverse flow the fastest velocities were found on the posterior side. This agrees with the *in vitro* results of authors such as Pedersen *et al.* [73], who found the highest retrograde velocities in their aortic model to be near the posterior wall due to a recirculation zone during diastole.

Phase-Contrast Magnetic Resonance Imaging Magnetic Resonance Imaging (MRI) can be used in a variety of ways to examine blood flow. When a pulse sequence which has a finite duration and a spatial variation is applied, the magnetic moments (spins) in the blood will experience the sequence differently to those spins in the surrounding tissue because those in the blood move as the sequence progresses. The two main groups of methods for flow measurement use either differences in the phase of the transverse magnetization of the spins (phase-contrast) or differences in the magnitude of their transverse magnetization (modulus-contrast) [96]. Both of these can be used for viewing blood vessels, as in angiography, as well as for quantitative flow imaging. Phase-contrast imaging is discussed here as it is the most widely used method and was used in this thesis.

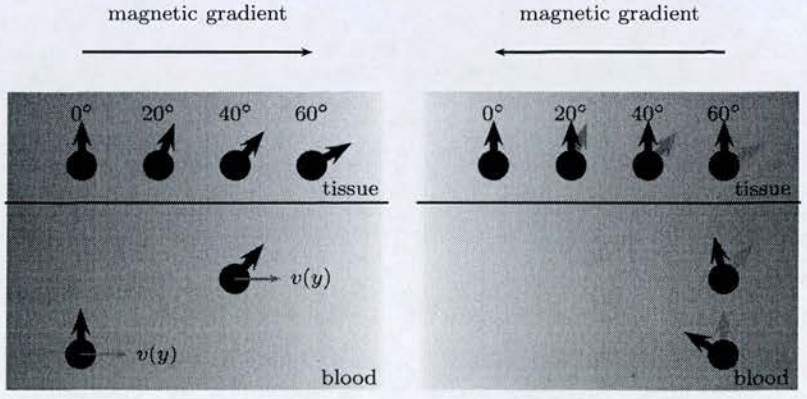

(a) $t = 0$ (b) $t = T$

Figure 1.8: *Velocity measurement using phase contrast MRI (adapted from similar figures in [97]).*

Spins moving along a magnetic field gradient acquire a phase shift in comparison to stationary tissue and this phase shift is proportional to their velocity (figure 1.8(a)). At time $t = T$ a second

gradient in the opposite direction is applied which cancels the phase shifts in the stationary tissue (figure 1.8(b)). The phase difference remaining is used for a voxelwise calculation of the velocity. By applying gradients in all three directions the three components of velocity can be determined. Since a phase shift can only be in the range -180 to $+180°$ the range of velocities that can be measured is limited. The velocity encoding, V_{enc}, of the pulse sequence must be tuned so that a phase shift of 180° corresponds to the maximum velocity present [97].

MRI data is collected in k-space (frequency domain) and the image is then obtained by a 2D inverse Fourier transform [91]. The signal, as a function of time, is given by tracing a trajectory in k-space, with the trajectory vector proportional to the position encoding magnetic field gradient [91]. Since it takes a finite time to move through k-space, about one line of k-space can be collected per cardiac cycle, and many cardiac cycles are required to sample the whole k-space. This requires that the pulse sequence be gated. Gating can be done either prospectively, in which case the data acquisition is started by a trigger signal, or retrospectively, meaning that the data is acquired continuously and during image reconstruction the trigger signals are used to split the data [97].

Figure 1.9 shows the measurement of velocity within the aorta using phase-contrast MRI. The magnitude image (figure 1.9(a)) shows the anatomy. The phase data from the area of the highlighted rectangle has been used to calculate the velocity perpendicular to the slice (z-direction) and this is shown in figure 1.9(b).

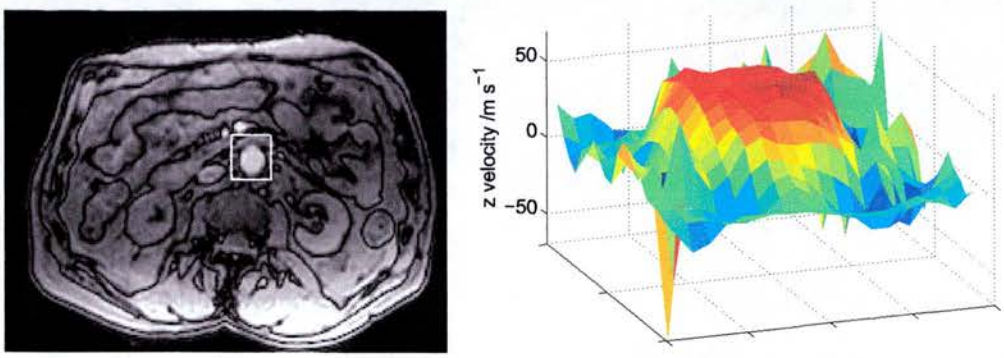

(a) magnitude image

(b) velocity obtained from phase data

Figure 1.9: *Phase contrast MRI measurement of z-component of velocity in the aorta.*

Oyre *et al.* [98] used phase-contrast MRI to look at WSS in the normal aorta. WSS was lower in the infrarenal aorta compared to that in the suprarenal aorta whereas OSI was higher in the

infrarenal aorta. WSS in the suprarenal aorta was similar at both the anterior and posterior. In the infrarenal aorta mean WSS was highest on the anterior, as was the maximum forward WSS, whereas the maximum retrograde WSS and the highest OSI were both found on the posterior, which is consistent with *in vitro* studies [73, 85] and *in vivo* Doppler US results [95]. However, in the suprarenal aorta they found a higher OSI on the anterior wall than the posterior which is in contradiction to the *in vitro* study of Pedersen *et al.* [73] who found the WSS in the suprarenal aorta was invariant with circumferential position. This difference is most likely due to the shape of the model which had no curvature in the suprarenal portion unlike the real aorta.

Phase contrast MRI was also used by Taylor *et al.* [99] and Cheng *et al.* [100] to study flow and WSS in the abdominal aorta during rest and exercise. The resting OSI in older subjects (aged 50 - 70 years) was more than double that of younger subjects (aged 20 -28) in both the supraceliac and infrarenal sections of the aorta. However, they found that exercise conditions reduced the OSI to zero in both younger and older subjects.

1.3.2 Measurement of Tissue Stresses

Stress is defined as a force acting over an oriented area and therefore in order to measure a stress, the applied force and the area are required. In measurements on excised tissues, for example in load cells, it is possible (though perhaps nontrivial) to measure the cross-sectional area of the the tissue sample, and to measure the force used to stretch the sample and in this way to measure the stress within. *In vivo* loads are applied in three dimensions and on whole organs. To measure the stress is then more complicated and a model of the organ, blood vessel, is required. The model may be as simple as a straight tube for an artery but still, a calculation is required to relate the applied load and the area to the stress within the tissue. The accuracy of the stress estimation is then dependent on the many factors involved in modelling the vessel.

Since it is difficult to measure stresses within tissues *in vivo* a common approach has been to measure strains instead using imaging techniques. Assuming a homogeneous tissue region, areas with high strain will also experience high stress and the strain field can be used to produce a qualitative stress field. The stress field can be made more quantitative with knowledge of the constitutive relationship, that it the relationship between strain and stress, for that tissue.

The following sections describe how imaging techniques have been used to measure strains, stresses and the elastic properties of tissues. Details of stress estimations using modelling or

calculation are described later.

1.3.2.1 Ultrasound

Estimation of strain fields with ultrasound has been accomplished via two methods: tissue Doppler imaging and elastography. Tissue Doppler Imaging (TDI) uses the Doppler signal from moving tissue to calculate its velocity [101]. In the heart a strain image can then be calculated from the velocity gradient between two points in a block of tissue [102] but strain imaging with TDI has not been used for arteries. Elastography works by cross-correlating regions within two images obtained at different times to give displacement vectors for each of the regions. From these the strain image, or elastogram, can be calculated. Arterial elastography is usually performed using intravascular US (IVUS) [103], which has a higher spatial resolution than transcutaneous US, and can identify atherosclerotic plaques.

As well as calculating strain fields in arterial cross-sections, which aim to give the strain at each location, US can be used to calculate properties averaged over the whole circumference. TDI can be used to measure arterial distension by integration of the instantaneous velocity measurements [104]. Arterial wall motion cannot provide strain information directly but knowledge of the distension can infer qualitative information about the strain and stress within the wall tissue. The pressure-strain elastic modulus, defined as $E_p = \delta p/(\delta d/d)$, where δp is the pulse pressure, δd the change in diameter and d the diameter, has often been used as a measure of wall elasticity because it does not require the wall thickness [105]. Therefore it can be measured quite precisely with B-mode imaging or the M-mode trace, or in principle with TDI. Progression from the E_p, the pressure-strain elastic modulus, to E_Y, Young's modulus, requires a measurement of arterial thickness, which increases the error, especially as the thickness of many arteries is only comparable with transcutaneous US resolution [105].

Pulse wave velocity (PWV) is an indirect measure of the elasticity of a whole artery, or long section of an artery, which can be derived by measuring the transit time of the flow wave, or distension wave, between two points in the artery. This can be accomplished using two synchronized US systems measuring either the velocity wave with spectral Doppler or the distension wave [105]. Then, $E_p = 2\rho c^2$ where ρ is the density of blood and c is the PWV [105].

1.3.2.2 MRI

Like US, MRI can be used to measure local, cross-sectional and regional properties. Strain fields have been measured using phase-contrast MRI. The wall velocity is measured, in the same way as blood velocities, and if a cross-sectional image of the wall is divided into a number of segments, the velocities of each of these segments can determined. Then the circumferential strain between the segments can be found [106].

The average compliance around an arterial cross-section has been found. An automatic method was used to find the wall at each time step and then the enclosed area was measured. By dividing the change in area by the change in pressure the compliance of that cross-section was determined [107].

PWV can also be measured with MRI and used to determine the regional elasticity of the vessel. This can be done by measuring the change in area of an artery throughout the cardiac cycle at two locations [108].

1.3.3 Measurements in Abdominal Aortic Aneurysms

1.3.3.1 Haemodynamics

In vitro studies on aneurysms, or bulged tubes, can be divided into different types: rigid or compliant models; cylindrically symmetric or asymmetric models; and steady or 'pulsatile' flow.

The earlier flow studies looked at steady flow in rigid, axisymmetric bulged tubes [109–111]. Flow through an axisymmetric aneurysm model comprises a jet passing directly through the centre and a slowly recirculating, toroidal vortex within the bulge (figure 1.10). The centre of the vortex is located in the distal half of the model; the precise position depends on the model shape and the flow rate.

Pressure is greatest at the midpoint of the bulge because, as the cross-sectional area increases, the velocity decreases to maintain the same flow rate, and kinetic energy is converted to potential energy (Bernoulli's principle). The maximum pressure increases with aneurysm diameter. Energy conversion from kinetic to potential in the expansion region is inefficient since it results in flow separation and the formation of vortices, and therefore viscous dissipation of energy. In the contraction region energy conversion from potential back to kinetic is more efficient, and

hence pressure is lower after the aneurysm than before.

With laminar flow the WSS in the bulge is in the opposite direction to that in the entrance and exit tubes and is an order of magnitude smaller. WSS peaks at the distal end near the reattachment point.

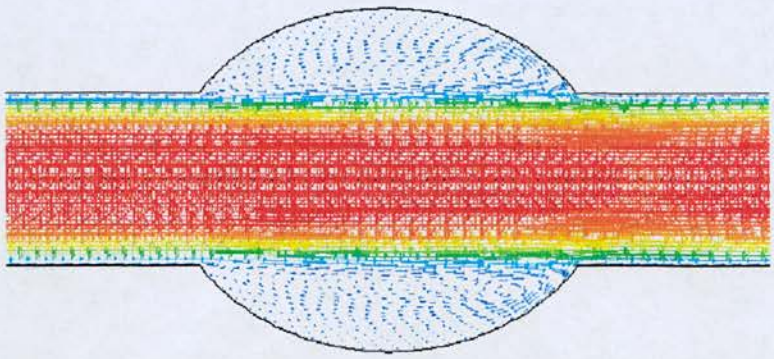

Figure 1.10: *Steady flow in an axisymmetric bulged tube.* $Re = 1000$

Peattie *et al.* [110] found that flow was intermittently turbulent for *Re* ([112] and section 1.4.1.3) between 1750 and 2250 and fully turbulent *Re* over 2250, while Budwig *et al.* [109] found *Re* between 2000 and 2500 gave intermittent turbulence. The geometry of the bulged tube was found to encourage turbulence to develop and flow in the larger aneurysm models was turbulent at lower *Re* than that in smaller aneurysm models. With turbulence the flow pattern changed: the recirculation vortex broke down and the fast core spread outwards as it moved towards the aneurysm exit, completely filling the distal half of the bulge. In the presence of turbulence the WSS in the bulge was comparable to that in the entrance tube [109].

Pulsatile flow through rigid axisymmetric models has been studied by a number of groups [74, 76, 113, 114]. In contrast to steady flow, during pulsatile flow the toroidal vortices are present only intermittently depending on the phase of the flow cycle (figure 1.11). The strength, position and even number of toroidal vortices depends on the flow waveform used.

Yu *et al.* [76] looked at sinusoidal flow with a steady offset. The vortex started to develop at the proximal end of the aneurysm bulge as the acceleration of the flow decreased before the velocity reached its maximum. After the flow rate peaked and the flow decelerated, the strength of the vortex increased and it moved downstream, towards the centre of the bulge. With further deceleration the vortex moved to the distal end of the bulge. As the flow began to accelerate again the vortex decayed rapidly. Increasing α, the Womersley number ([32]

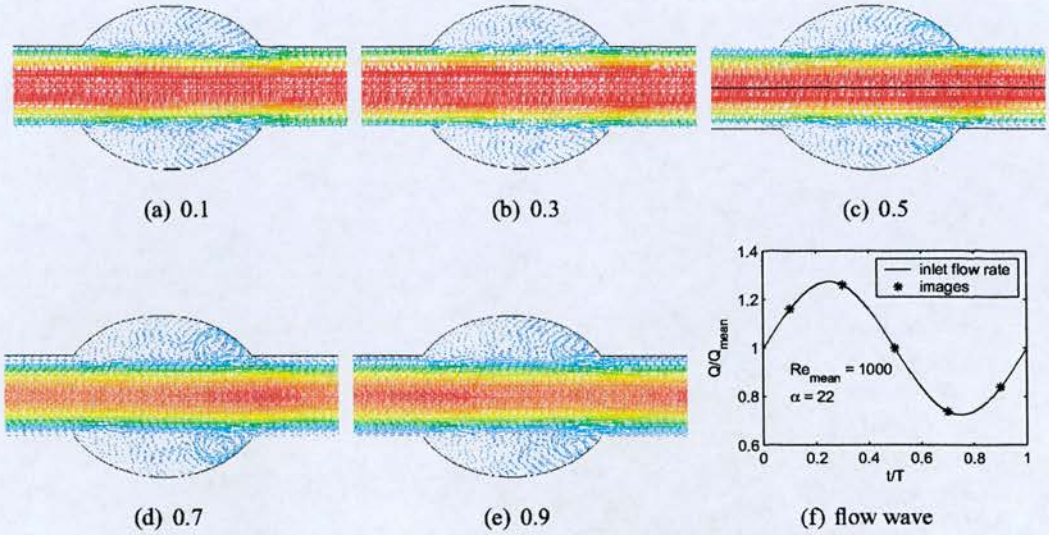

Figure 1.11: *Pulsatile flow in an axisymmetric bulged tube.*

and section 1.4.1.3), resulted in stronger vortices. They found the peak WSS to be larger with pulsatile flow than with steady flow. When Yu *et al.* [113] used a physiological flow wave an additional vortex formed near the entrance to the bulge and on increasing the flow wave to give exercise conditions, three vortices were present during diastole. Salsac *et al.* [79] performed a comprehensive study on the variation of WSS with aneurysm size. They found that flow separation occurred even in their model with the smallest ratio of bulge diameter to tube diameter, $D/d = 1.3$. The mean WSS magnitude decreased with dilation ratio. The proximal half of the aneurysms experienced oscillatory WSS with very low and negative mean WSS. Very large WSS gradients were found at the location and time of flow separation. The region of flow reattachment was characterized by large negative WSS and sustained WSS gradients.

In asymmetric aneurysms the vortices are weaker than those in symmetric aneurysms and do not form complete tori [74].

Flow in compliant aneurysms has been studied by Deplano *et al.* [75]. They found that the main effect of having compliant walls was that the walls absorbed kinetic energy during systole which was emitted during diastole. This meant that larger vortices were formed and these vortices lasted throughout the cardiac cycle, unlike the ones in their rigid walled model, and impacted on the distal wall of the aneurysm at the start of the subsequent cardiac cycle. During exercise conditions the vortices were larger, and moved down the aneurysm faster, to impact on

the distal wall within the same cardiac cycle.

In clinical practice velocity measurement contributes little to the the assessment of AAAs [12] and so there have been few *in vivo* studies of flow in AAAs. Bluth *et al.* [115] used colour flow imaging to study 15 aneurysms. They found two distinct patterns of blood flow: the first was smooth and laminar and in the second the blood circulated within the aneurysm. There was no difference in either aneurysm or lumen diameter between these two groups, however, they note that those with the circuitous pattern had a higher ratio of thrombus to sack volume. Colour Doppler US images of flow in AAA phantoms have been compared with LDA measurements and it was found that recirculating flow in the aneurysm bulge was too slow to be imaged with the colour Doppler [116].

1.3.3.2 Tissue Stresses

Local, cross-sectional and regional techniques have all been used to look at the material characteristics of abdominal aortic aneurysms. Brekken *et al.*[117] measured the strain in the aneurysm wall using B-mode US. They manually placed a contour around the wall of the aorta and then automatically tracked its motion through the cardiac cycle by cross-correlation of the intensity pattern. The intensity information along the circumferential line was then extracted to form an M-mode image and the circumferential strains were then obtained by cross-correlating sections in successive times. They report that the local strain can be significantly greater than the circumferentially averaged strain.

Distensibility [118, 119], pressure-strain elastic modulus [118], Young's modulus [118] and compliance [120, 121], for cross-sections of the aneurysm, have all been measured in patients with aortic aneurysm using different US modalities. Koullias *et al.* [119] found that aortic distensibility decreased with aneurysm size while Wilson *et al.* found that although large aneurysm are generally stiffer [122], AAAs which ruptured or required operation were more compliant than those, of the same maximum diameter, that remained stable [123].

PWV has also been measured in one patient with AAA using MRI to look at vessel area, showing that this technique can still be applied when there is localized aortic dilation [108].

1.3.4 Summary

There are a wide variety of techniques for measuring fluid velocities experimentally but in general these are unsuitable for measuring blood flow in arteries. The techniques of Doppler US and phase-contrast MRI are the most useful for looking at blood flow *in vivo*. Much has been learnt about blood flow in the normal and aneurysmal aortas from measurements in models and *in vivo*. Blood flow in the infrarenal section of the aorta, where most AAAs occur, is complicated by its curvature, by vortices and helical flow induced by the renal branches, by reflections from the aortic bifurcation and by the considerable amount of reverse flow. Flow in model aneurysms consists of toroidal vortices which are formed at the proximal end of the aneurysm and move distally over the course of cardiac cycle. There have been very few measurements of haemodynamics in AAAs *in vivo*.

Tissue stress cannot be measured *in vivo* but measurement of tissue strain can provide clinically useful results. For example local circumferential strains can greatly exceed average strains in AAAs. Measurements of tissue motion when combined with pressure measurements can be used to obtain parameters representative of tissue properties such as compliance and pressure-strain elastic modulus. Large aneurysms are generally less distensible than smaller ones and compliance in larger aneurysms may be an indicator of high rupture risk.

1.4 Calculations of Haemodynamics and Tissue Stress

The previous section discussed the current knowledge on haemodynamics and tissue stresses in the normal aorta and in abdominal aortic aneurysm as obtained from measurements both *in vivo* and *in vitro*. Aneurysm phantoms have provided great insight into the general characteristics of pulsatile flow in bulged tubes with a range of shapes and have revealed the flow fields within in detail. However, real aneurysms have much more complicated shapes than the models and are different in every patient. By measuring the flow *in vivo* with either Doppler US or MRI it is possible to find the correct flow in the patient's aneurysm. Of these two techniques however, only MRI is capable of providing the full 3D velocity field, but its limited spatial resolution leads to underestimates of the wall shear rate [34].

Measurements of tissue motion have provided some information about the strains in vascular tissues and in aneurysms in particular. However, stress cannot be measured directly *in vivo* and at least a simple model of the artery is required in order to calculate the stress within.

When making measurements *in vivo* the situation is known to be correct. The arterial geometry, flow and pressure are all as they should be and 'complications' such as wave reflections, spiral flow and tissue motion are all, by necessity, included. However, by making models it is possible to remove some of these elements and simplify the situation. In this way the importance of different features can be explored and their interactions determined. Phantoms, or *in vitro* models, are useful in this respect but computational models are even better. Their parameters are fully under control and can be adjusted independently.

This section describes how haemodynamics and tissue stresses can be calculated in simplified arteries and in patient specific geometries.

1.4.1 Calculation of Blood Flow

Depending on the parameters which are required different types of models can be used for calculating blood flow. 0D and 1D models relate pressure and flow waves in simple models of the arterial tree or specific sections. For some simple tubes the flow field can be solved analytically, while in order to obtain the detailed flow field in a 3D artery, numerical simulation is required.

1.4.1.1 0D Models

Lumped parameter models take the properties of the whole vascular system, or the interesting section of the system, and 'lump' them together into a few parameters. The complex vascular structure is ignored and the network is replaced by a single tube having the properties of the whole system [124]. Viscous dissipation is treated as resistance, compliance of the vessels is accounted for by capacitors and fluid inertia is handled as inductance. There is then an analogy between the mechanical system of fluid filled tubes and a system of electrical components [125]. The simplest lumped parameter model is the Windkessel: a resistor and a capacitor in parallel. In the 1950s studies of haemodynamics were based on treating the whole arterial system as a Windkessel chamber into which blood from the heart was pumped [32]. This model was used for calculating the stroke volume of the heart.

Lumped parameter models have been used effectively in, for example: investigating the interaction of the heart and the arteries, including assessing the relationship between stroke volume and pulse pressure, and showing that the effective arterial stiffness is determined by peripheral

resistance and heart rate, rather than by the actual stiffness of the arteries [126]; and in modelling the coronary circulation including the effect of myocardial contraction which has been shown to produce a back pressure which causes reverse flow during systole and forward flow in diastole [124]. Wolters *et al.* [127] investigated endoleaks in endovascularly repaired abdominal aortic aneurysms using a lumped parameter model. They also made an *in vitro* aneurysm with endoleak and results from that and the lumped parameter model agreed well.

One intrinsic disadvantage of lumped parameter models is that they provide no information about the spatial variation in pressure or flow waves. Distributed models, such as the one by Avolio [128], consider each arterial segment as a transmission line, with resistance, capacitance and inductance, and all the segments connected to form the arterial tree. Distributed models can be used to study wave propagation, reflections and damping [129]. A similar model was used by Stroev *et al.* [130] and predicted that wall shear rate varied throughout the arterial tree.

1.4.1.2 1D Models

The alternatives to models based on electrical analogies involve solving the Navier-Stokes equations in one dimension. A straight section of artery is approximated as a cylindrical compliant tube in which [131]: all quantities are axially symmetric; the wall only displaces radially; the axis of the tube cannot move; the pressure on a cross-section is a constant; there are no external forces; and the axial velocity is much bigger than any orthogonal components so these can be ignored. The Navier-Stokes equations can then be solved in a number of different ways to create a 1D model [131]. Olufsen *et al.* [132] created a 1D Navier-Stokes model of the whole arterial system. The larger arteries were modelled physiologically with parameters based on measurements of length and diameter obtained from one subject where possible and the rest obtained from the literature and adjusted to match the flow measured using MRI. The smaller arteries were modelled as an asymmetric fractal tree based on geometrical relationships. Flow results from their model agreed well with the MRI measurements.

1.4.1.3 Tubes

Poiseuille studied the flow of water in glass capillary tubes and published his results in 1846. He found that the flow in the tube was proportional to the pressure gradient and the fourth power of the tube's diameter. This result was later derived independently by Wiedemann in

1856, and by Hagenbach in 1860, who produced the result that is now commonly referred to as Poiseuille's equation [32]:

$$Q = \frac{\pi R^4 (P_1 - P_2)}{8\mu L} \tag{1.2}$$

where Q is the flow rate, R the radius, $(P_1 - P_2)$ the pressure difference, μ the viscosity and L the length. The velocity profile is found to be a parabola [32]:

$$v = \frac{P_1 - P_2}{4\mu L} R^2 \left(1 - r^2\right) \tag{1.3}$$

where v is the velocity and r is the radial location as a fraction of the tube radius R. The characteristics of steady flow are described by the Reynolds number ($Re = 2\rho VR/\mu$, where ρ is the density and V is the velocity) which is the ratio of inertial to viscous forces. In a tube the transition from laminar to turbulent flow typically occurs at about $Re = 2300$.

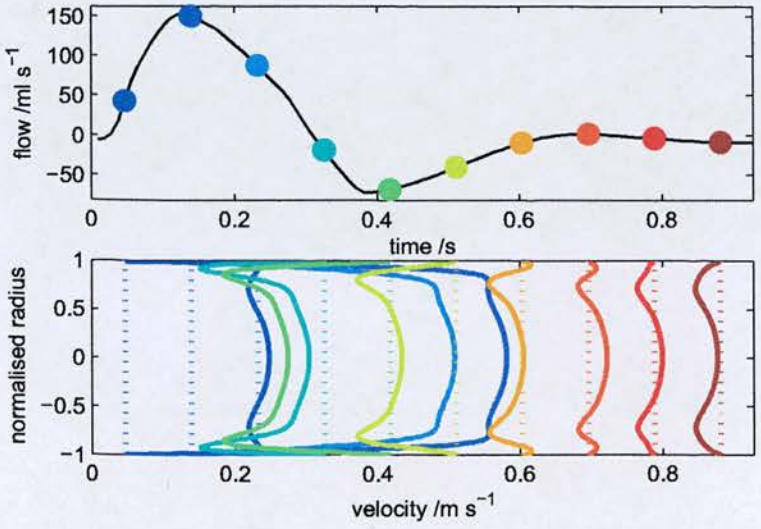

Figure 1.12: *Flow and velocity profiles for blood flowing in a tube with radius typical of that of the aorta (1.11 cm) and a flow wave typical of patients with AAA*

Although Poiseuille's equation may be applicable in some veins, blood flow in the arteries is pulsatile so it cannot be applied there. Womersley solved the equation of motion for a viscous fluid with an oscillatory pressure gradient ($\frac{\partial p}{\partial z} = A_k e^{i\omega t}$) and found the velocity profile [32]:

$$v_k = \frac{A_k R^2}{i\mu\alpha^2}\left(1 - \frac{J_0\left(\alpha r i^{3/2}\right)}{J_0\left(\alpha i^{3/2}\right)}\right) e^{i\omega t} \tag{1.4}$$

where $\alpha = R(\omega/\nu)^{1/2}$ is the Womersley number, a non-dimensional parameter characterizing

the ratio of oscillatory to viscous components and J_0 is a zeroth order Bessel function of the first kind.

The individual components can be calculated from the pressure gradient using a Fourier transform:

$$A_k = \sum_{j=1}^{N} a(j) e^{(j-1)(k-1)(-2\pi i)/N} \tag{1.5}$$

where $a(j)$ is the measured pressure gradient discretized with N samples and A_k is the kth frequency component of the pressure gradient. The Womersley equation can then be used to calculate a velocity profile for each component of the pressure wave and these can be summed to give the complete velocity profile for flow in the long, straight, cylindrical tube:

$$v = \sum_{k=1}^{N} v_k \tag{1.6}$$

An example of velocity profiles calculated using Womersley's solution is shown in figure 1.12.

Flow in curved tubes is significantly more complicated than the flow in straight tubes [87]. In the entrance region, before the boundary layer has formed, the profile develops such that the velocity is highest on the inner wall and lowest on the outer wall and depends only on r (figure 1.13). Further downstream the boundary layer expands due to the viscous forces and the velocity profile is dependent on the azimuthal position with the fastest flow making a 'C' shape at the outer wall. The secondary flow consists of two counter rotating vortices. In curved tubes there are two important non-dimensional parameters: $\delta = R/R_0$ (where R_0 is the radius of curvature) describes the curvature of the tube and the Dean number $\kappa = \delta^{1/2} Re$ which is the ratio of the square root of the product of the inertial and centrifugal forces to the viscous force. For small curvature ($\delta << 1$) only the Dean number needs to be considered.

Figure 1.13: *Velocity profiles in the entry and fully developed regions of a curved tube. (Axial velocity - blue, secondary flow - red.)*

1.4.1.4 3D Arteries

Conservation of mass, momentum and energy governs fluid flow. By accounting for surface and body forces on a fluid element, and assuming the viscous forces are proportional to the rate of deformation the Navier-Stokes equations for a Newtonian fluid can be derived [133]. These are:

x momentum:

$$\rho\frac{Du}{Dt} = -\frac{\partial p}{\partial x} + \nabla\cdot(\mu\nabla u) + S_{Mx} \tag{1.7}$$

y momentum:

$$\rho\frac{Dv}{Dt} = -\frac{\partial p}{\partial y} + \nabla\cdot(\mu\nabla v) + S_{My} \tag{1.8}$$

z momentum:

$$\rho\frac{Dw}{Dt} = -\frac{\partial p}{\partial w} + \nabla\cdot(\mu\nabla w) + S_{Mz} \tag{1.9}$$

u, v and w are the x, y and z components of the velocity vector $\vec{v}$, and S_M are the source terms. Along with the continuity equation,

continuity:

$$\frac{\partial\rho}{\partial t} + \nabla\cdot(\rho\vec{v}) = 0 \tag{1.10}$$

the Navier-Stokes equations are the fundamental equations governing fluid flow, but their non-linearity prevents them from being solved directly in all but the simplest of tubes. Computational fluid dynamics (CFD) techniques solve the full Navier-Stokes equations by discretizing them. The finite volume method is a type of finite difference discretization which involves dividing the domain into many control volumes, integration of the equations over all of the volumes, conversion of the resulting integral equations into algebraic equations and solving the algebraic equations iteratively [133].

There are many arteries for which the flow has been calculated using CFD [134]. A popular site is the carotid bifurcation where the application of CFD has provided a wealth of information on velocity and wall shear stress which has aided research into atherosclerosis and bypass grafts [135–137]. The aorta has also been investigated quite extensively. Studies of the effect of the aortic arch on skewing of the velocity profiles throughout the cardiac cycle showed that in the ascending aorta the velocity profile is skewed towards the inner bend, whilst by the apex the skew has shifted to the outer wall and the effects of the arch on the descending thoracic aorta

are minimal [138, 139]. The wall shear stress distribution in the aortic bifurcation has been examined [140]. The geometry of the abdominal aorta induces flow reversal and oscillatory shear stress on the posterior side [141] which are greatly reduced during exercise [99]. CFD has also been used for predicting additional parameters of interest biologically such as residence times [142], particle deposition [143] and mass transfer (exchange of substances between blood and artery) [144].

Compared with experimental studies, numerical investigations have many advantages, for example parameters are easily varied to consider their individual effects and less specialist equipment (for example pumps, phantoms and lasers) is required. However, computational studies cannot stand alone. Patient specific investigations require velocity and pressure data as boundary conditions, and most importantly, computational results need to be validated. Validation could be against the analytical solution for the problem, for example the Poiseuille [145] or Womersley [134] equations, which have already been described, or alternatively against empirical results. Many of the *in vitro* measurement methods described earlier have been used in anatomical models for comparison with numerical simulation. Good qualitative and quantitative agreement between numerical and LDA results was found in a model of an anastomosis [146]. In models of AAA Yu *et al.* [113] found good agreement between simulation and PIV results except at the upstream end of the bulge near the beginning of the cycle. They attribute this to the sensitivity of the circulating flow to the impingement of the vortices downstream. Comparison of CFD and MRI has particular interest from a physiological perspective since MRI can also be used *in vivo*. In a study of flow through a U bend Glor *et al.* [145] found excellent agreement between their numerical results and MRI measurements. They found that having the correct flow rate at the inlet improved the CFD-MRI match and achieved this by scaling the inlet velocity profile by the flow rate measured using a flow meter. Validation of numerical results against *in vivo* measurements is more challenging since experiments are more difficult to control and precise measurements are difficult to acquire [134]. Long *et al.* [147] compared *in vivo* MRI measurements with simulation of flow in an aortic bifurcation. They compared the results on a plane through the aorta since MRI is subject to uncertainties in complex flow regions such as the vicinity of the bifurcation which creates recirculation and secondary flow. On this plane the velocities agreed qualitatively and differed by 3-52 % in magnitude. Jin *et al.* [148] looked at the effects of wall motion in the aortic arch on the velocity profiles obtained computationally and found that there was good quantitative agreement with MRI measurements when the wall motion was included. In general compuational studies appear to be able to pre-

dict the velocities *in vivo* but experimental validation is still in the early stages and more work is required to confirm this.

1.4.2 Calculation of Tissue Stresses

1.4.2.1 Straight Tubes

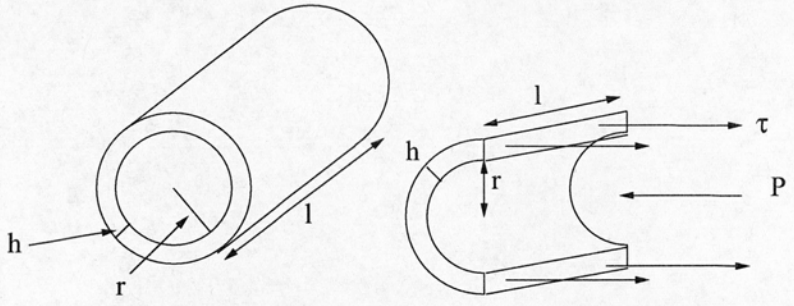

Figure 1.14: *Circumferential tension in an elastic tube under pressure*

The circumferential stress in an elastic cylinder can be calculated by slicing it in half and equating the force due to the pressure and the tension (figure 1.14):

$$2\tau hl = 2Prl \tag{1.11}$$

$$\tau = \frac{Pr}{h} \tag{1.12}$$

where τ is the stress, h is the thickness, l the length, P the pressure and r the radius. This result is known as Lamé's equation [32]. It is the basis of the pressure-strain elastic modulus which is used a lot in ultrasonic studies of blood vessels and can be used to derive a value for Young's modulus for the artery. Multiplying by the thickness, h, gives an equation for the total tension in the wall which is known as the law of Laplace. This is the basis of the clinically used maximum aneurysm diameter as a measure of the rupture risk.

1.4.2.2 Arteries

Arterial tissue is a bit like rubber: it has a nonlinear stress-strain curve which is initially linear, then softens and with further loading stiffens rapidly; it is viscoelastic but nearly elastic if preconditioned; and, since it is mostly ($\approx$ 70 %) water, it is nearly incompressible [17]. How-

ever, arteries, which are constructed from cells and fibres aligned in preferred directions, are anisotropic, and since they consist of three distinct layers they are also heterogeneous [17]. The artery wall is also known to exhibit residual stresses so that even in its unloaded, or zero pressure, state the layers are stressed. If the wall is sliced longitudinally it uncurls itself showing that the intima was under compression and the adventitia was under tension [17].

Under physiological conditions arteries behave basically elastically and a useful way to describe their behaviour is hyperelasticity [17]. This means the strain energy, W, is a function of the strain state, independent of the path between the states. The stress can be computed by differentiating the strain energy. Different forms of W have been used for the aorta including polynomial, exponential and combined polynomial - exponential [17]. Vande Geest *et al.* [149] compared normal and aneurysmal abdominal aorta with biaxial mechanical tests and used the following strain energy function:

$$W = b_0 \left(e^{b_1 E_{\theta\theta}^2/2} + e^{b_2 E_{LL}^2/2} + e^{b_3 E_{\theta\theta} E_{LL}} - 3 \right) \tag{1.13}$$

where $E_{\theta\theta}$ and E_{LL} are the Green strain tensor components in the circumferential and longitudinal directions and b_0 - b_3 are the fitted parameters. They found that AAA tissue was significantly stiffer than AA tissue but there was no significant difference in the stiffness in the two directions.

In general arteries are not just straight tubes, they taper, bend and branch and contain inhomogeneities such as plaques. Finite element modelling (FEM) provides a way of calculating the stresses and strains in these nonuniform shapes. The tissue is divided up into elements and the balance of linear momentum is solved for each element iteratively [150]. FEM has now been used extensively for looking at blood vessels in health and disease. One particular application has been atherosclerotic plaques where models, based on idealized cross-sectional geometries or more recently distributions obtained from histology or from IVUS images [151], have revealed the relationships between plaque location, stress and stability [144, 152]. Angioplasty is another area where FEM has been applied, again both idealized and geometrically accurate models have been used to show the locations of stresses and stress gradients in the tissue [152]. FEM has shown that damage during stenting is highly dependent on inflation pressure and geometry of the stent struts [144] and that mismatching of host tissue and graft tissue compliance is a cause of graft failure because the disparity causes chronic stretching at the junction [144].

1.4.3 Calculation of Blood Flow in AAA

Numerical studies of flow in axially symmetric aneurysms confirm the main results of *in vitro* studies [74, 113]. That is, during steady flow there is a forward flowing core surrounded by a toroidal vortex, with location of the vortex centre dependent on *Re*. During pulsatile flow, vortex formation occurs at the proximal end of the aneurysm during flow deceleration and the vortex moves distally over the cardiac cycle [74, 113]. The vortices in asymmetric aneurysms are crescent shaped, only occupying the bulged side of the vessel [74, 153]. In a study of two axisymmetric aneurysms in series it was shown that the presence of the second aneurysm downstream of the first affects the flow in the first and *vice versa*. This is relevant to real AAAs since their lumen are often convoluted and may contain a series of dilations.

In comparison with intracranial aneurysms, or the healthy aorta, there have been few numerical studies on flow in patient-specific abdominal aortic aneurysms. Yeung *et al.* [154] performed numerical simulations on flow in the abdominal aortas of patients with spinal cord injury and control subjects. Spinal cord injury patients are at increased susceptibility to developing aneurysms and although the patients in the study were specifically chosen to have aortic diameters <3.0 cm (that is, nonaneurysmal) their aortas all still had irregular ectatic segments at the distal end and their iliacs were narrow. Average WSS in the spinal cord injury patients was 0.301 Pa compared to 0.723 Pa in normal subjects. No information on flow patterns is given. From *in vitro* and numerical studies in simplified AAA geometries, flow *in vivo* is almost certain to be complicated, with recirculation zones and oscillatory WSS. Also, since real AAAs have far more complicated shapes, with lumpy and tortuous lumen, the haemodynamics will probably also contain helical flow with large secondary velocities. However, more work in this area is required to confirm this and since the flow is likely to be so complicated the numerical results should be validated against *in vivo* measurements.

1.4.4 Calculation of Tissue Stress in AAA

Since rupture is the eventual fate of all nonoperated aneurysms, provided the patient survives long enough, much work has been devoted to patient specific analysis of rupture risk. Although both stress and strength are required in order to assess rupture it has been shown that just knowing the stress gives a better indicator of risk than the current clinically used measure of diameter [55, 57].

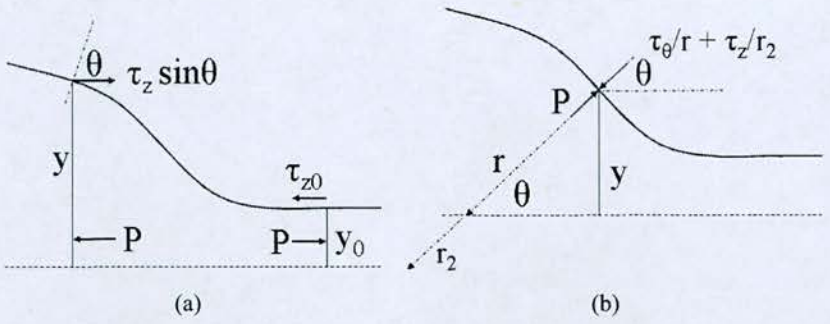

Figure 1.15: *Tension in an aneurysm wall assuming membrane theory.*

Elger *et al.* [155] showed analytically that maximum wall stress did not correlate with maximum diameter, for different aneurysm shapes, but instead correlated with wall curvature. They found that the maximum stress typically occurred near the inflection point of a curve drawn along the wall length, and that the circumferential stress was much greater than the longitudinal stress. The reason for this apparent contradiction with Laplace's law can be explained as follows. The longitudinal tension must balance the difference in the force due to the pressure acting over a larger area in the aneurysm bulge (figure 1.15a). Hence the longitudinal tension peaks where the bulge has its maximum area. Then, considering components normal to the aneurysm wall (figure 1.15b), as in the derivation of Lamé's equation (section 1.4.2.1), the sum of the longitudinal and circumferential tensions is equal to the pressure, P, a constant. Hence when the longitudinal radius of curvature (r_2) is a maximum, that is at the point of inflection (infinite radius), the longitudinal tension plays no role in balancing the pressure and circumferential tension peaks.

One of the first groups to use FEM to look at aneurysm stresses were Mower *et al.* [156] who studied an axially symmetric geometry. They found that peak stress occurred on the inner wall in two bands either side of the peak diameter. Other studies have also shown that peak stress occurs on the inner wall [52, 157], but none have included the residual stress which may act to even out the radial stress distribution. *In vivo* aneurysms bulge out more anteriorly than posteriorly because the posterior is supported by the spine. In asymmetric aneurysms which bulged more anteriorly peak wall stress was located at the inflection points of the more highly curved wall on the anterior [158].

Patient specific stress analyses require: 3D geometry of the artery, which is obtained from segmenting medical images, usually from x-ray contrast enhanced computed tomography [52,

53, 58], but alternatively MRI [56], a constitutive model for the wall, and the patient's systolic blood pressure. From the segmented geometry a mesh of the aneurysm wall is created and then FEM is used to inflate the aneurysm to systolic pressure. The 3D stress distribution is then readily obtained. To be useful clinically this technology must be fast and easy to use and to this end progress is underway to automize the processes of segmentation, mesh generation and stress analysis [159].

The geometry of the aneurysm influences the position and value of the peak stress. The peak stress in all aneurysms in the study by Raghavan and Vorp [53] was on the posterior surface and in the study by Fillinger *et al.* [58] the peak was located either in the posterior or lateral areas. Da Silva *et al.* [160] found that 62 % of aneurysms ruptured in the posteroinferior wall, 20 % ruptured at the maximum diameter and 18 % in the inferior portion. So, although the position of the peak stress is dependent on the geometry there is a correlation between the site where the most aneurysms have their peak stress and the site where the most aneurysms rupture, which is also the posterior [58]. In ruptured aneurysms where the site of the rupture was known, either by inspection, CT scan or operation report, it correlated with the position of the peak stress [58]. However, in this study the ruptured AAAs were scanned post rupture and the process of rupturing would influence the stress distribution.

Peak wall stress in a group of AAAs ranged from 0.29 to 0.45 MPa compared to the peak stress in a control normal aorta of 0.12 MPa [53]. Ruptured aneurysms were found to have significantly different peak stresses to unruptured aneurysms (1.02 compared to 0.62 MPa [54], and 0.477 compared to 0.369 MPa [58]). This difference persisted in diameter matched AAAs (0.517 compared to 0.397 MPa) [55]. There was no difference between peak stress in symptomatic but unruptured aneurysms and ruptured aneurysms (0.475 compared to 0.477 MPa [58]). In all of these studies ruptured AAAs were scanned post rupture. Fillinger *et al.* [57] performed a prospective study in which 103 patients with asymptomatic aneurysms were scanned and followed up. They found that wall stress (sensitivity 94 %, specificity 81 %, accuracy 85 %) was a better predictor of rupture than diameter (sensitivity 81 %, specificity 70 %, accuracy 73 %).

The relative importance of geometry and pressure has been investigated but the results are inconclusive. After standardizing blood pressure some authors have found that ruptured aneurysms still have a significantly higher peak stress that nonruptured aneurysms [54] while other authors have found it is important to use the correct patient blood pressure as without the correct pres-

sure the differences between ruptured and nonruptured groups are not significant [55].

The intraluminal thrombus has been shown to have an important role biologically, and it is also thought to be important from a mechanical perspective. FEM studies of simplified aneurysms [161] and patient specific aneurysms [162] have shown that a thrombus layer, modelled as an elastic solid with much lower stiffness than the aneurysm wall, reduces the stress on the wall and that increasing the thrombus thickness reduces the stress [163]. In a study on the effect of changing the stiffness of the thrombus over the range found by Wang *et al.* [43] it was shown that there is insufficient variation in the population to cause significant variation in the wall stress [164]. A study on whole thrombi, both *in vivo* and excised, showed that although the thrombus only reduces pressure transmission to the wall by about 10 %, aneurysms dilated more after the thrombus was removed than before when inflated to the same pressure. This backs up the idea found by the numerical studies that the thrombus reduces wall stress and they go on to suggest this is because the thrombus is a fibrous network adherent to the aneurysm wall [165].

One of the main problems in calculating the tissue stress is knowing the thickness of the artery wall. It is clear from Lamé's equation that the stress in a cylindrical tube is inversely proportional to the the wall thickness and this has been shown to be almost the same in patient specific aneurysms [54]. Raghavan *et al.*[53] showed that varying wall thickness over the 99 % confidence interval for wall thicknesses found in 132 *ex vivo* samples (1.79-2.10 mm), produced a range of wall stresses in the models of ± 5 to $\pm 12\%$ of the wall stress using the mean wall thickness (1.9 mm). This implies that having the exact wall thickness is perhaps nonessential, that is, if the wall thickness is uniform. However, arterial tissue in general is heterogeneous in thickness [166] and as a diseased state aneurysm tissue is even more so [61]. The effect of nonuniform thickness on wall stress is much greater than simply changing the thickness of the whole wall [156].

Although changing the elasticity of the wall over the 95 % confidence interval found in a study of *ex vivo* samples produced only a 4 % error in the peak wall stress, like wall thickness [59], material properties are heterogeneous [61]. One type of tissue inhomogeneity which can be seen relatively easily on a CT scan is the calcifications. Stress in finite element models of small tissue segments containing calcifications, modelled as locally stiffer regions, was shown to be dependent on the shape and stiffness of the calcifications [167]. Including calcifications in AAA models resulted in alteration of the stress distribution with a maximum increase in peak

stress of 22 % [168].

Another problem with basing FEM on patient scans is that the geometry obtained is not the zero pressure geometry but rather the geometry under blood pressure: an average blood pressure if CT is used or, if gated MRI is used the geometry throughout the cardiac cycle can be obtained. Finding the zero stress state is non-trivial since the aneurysm is both materially and geometrically nonlinear. However, estimates of the zero pressure geometry have been found using either inverse analysis based on CT scans [169, 170] or MRI scans [171], and the wall stresses based on zero pressure geometries were 25 - 50 % higher than those based on diastolic pressure geometries.

So far, only static pressure analysis of the wall tissue stress has been considered. In reality the pressure on the wall is a result of the fluid flow and, since aneurysm geometries are, at their simplest, bulges, and more often also tortuous and convoluted, the fluid flow is complicated with recirculating regions and secondary flow. This causes local variations in the pressure which may alter the stress distribution in the aneurysm wall. In order to calculate the effects of these regional pressure variations the fluid-structure interaction must be modelled. Scotti *et al.* [172] looked at fluid structure interaction in idealized models of AAAs and concluded that 'solid stress techniques underestimate wall stress calculations when compared to the fluid-structure interaction predictions'. In contrast Leung *et al.* [173] looked at fluid-structure interaction in patient-specific geometries and found that the difference in peak stress between that and static stress analysis was less than 1 %.

In summary, there is a large body of work on tissue stresses in abdominal aortic aneurysms and many factors, such as geometry and finding the correct geometry, blood pressure, wall thickness, wall properties and inhomogeneities, presence of intraluminal thrombus have been found to influence the wall tissue stress to different degrees. However, there are still improvements to be made, most importantly, determination of local wall thickness, which will require improvements in image resolution, and also, resolution of the controversy over the effects of local variation in pressure caused by fluid flow.

1.4.5 Summary

Calculations can provide additional information to that which can be obtained from measurements. Calculations can be performed in regions, or under circumstances, that are difficult to

measure and calculations can provide insight and understanding. Blood flow has been calculated for the normal aorta and for simple aneurysm models, however numerical studies on real aneurysmal aortas are very limited. The complex geometries are likely to produce complicated flow fields which will alter properties such as the wall shear stress and delivery of cells to the wall which influence the biology. There is already extensive literature on numerical estimation of tissue stresses in AAA. However, two areas have been identified as needing more investigation and these are measurement of wall thickness and the importance of the interaction with the blood.

1.5 Thesis Outline

Having reviewed the literature on arterial, and specifically abdominal aortic aneurysm, biomechanics, it is clear that while much progress has been made and useful relationships have been found, there is still work to be done. Most of the biomechanical work on AAA has focused on tissue stresses, which is logical as knowledge of these can help avoid rupture and save lives. However, as shown here the blood flow is also important to the biology of aneurysms and studies in this area could provide useful information on the disease process which may help prevent or manage aneurysms in the future.

1.5.1 Aims and Objectives

The aim of this thesis is to investigate blood flow and tissue stresses in abdominal aortic aneurysms.

This aim will be accomplished through the following objectives:

- Develop methods for modelling haemodynamics in patient specific AAAs;
- Validate numerical results against *in vivo* measurements;
- Determine the effect of wall motion on blood flow;
- Determine the effect of blood flow on tissue stress.

1.5.2 Thesis Structure

Chapter 1 has introduced the subject of arterial biomechanics and its relevance to a particular disease.

The first part of this thesis is concerned with haemodynamics in real patient AAAs:

Chapter 2 describes methods for obtaining patient AAA geometries and calculating the haemodynamics based on velocity and pressure boundary conditions from the literature on healthy subjects. CT scans are segmented using a semi-automated threshold based technique and the resulting contours are assembled into a model of the artery. Commercial software is used to calculate the blood flow and the complexity of the flow structures are revealed.

Chapter 3 is focused on obtaining a typical abdominal aortic velocity wave in patients with AAA for use as an inlet boundary condition for calculations. This is accomplished by averaging spectral Doppler US waveforms using a method based on characteristic feature points.

Chapter 4 compares AAA haemodynamics as calculated using 3 different inlet conditions with MRI measurements of velocity with a view to validation.

The second part of this thesis uses simplified models to examine the effects of incorporating a fluid-structure interaction model:

Chapter 5 describes different ways of accounting for the pressure variation due to fluid flow on deformation of the aneurysm wall, and compares the results of these in terms of differences in blood flow and tissue stress in axially symmetric aneurysm models. Models of varying diameter and material properties and with different amounts of thrombus are used.

Chapter 6 investigates how a 3D aneurysm can be modelled using an electrical circuit, and what this can reveal about bulk flow characteristics, and examines whether this model can improve the pressure outlet boundary condition.

Chapter 2
Haemodynamics in Patient Specific Aneurysms

The importance of understanding the complete biomechanics of abdominal aortic aneurysm, with a view to fuller comprehension of the disease process, and to potentially improving clinical practice has been stressed. However, in the past, the haemodynamics of real AAAs has been subject to less attention than the solid mechanics. In this chapter a method for estimating the haemodynamics *in vivo* will be developed.

2.1 Introduction

The first computational fluid dynamics studies of haemodynamics used idealized or averaged geometries, or casts of postmortem specimens. With improvements in imaging techniques, developments in image processing and high performance processors it is now possible to simulate pulsatile flow in individual patient geometries [144, 174]. Such image guided CFD has been used for studying disease in a range of arteries. For example: the relationship between haemodynamics and atherosclerosis progression in the coronary arteries has been investigated using cine angiography and angiography combined with intra-vascular ultrasound (IVUS) [174]; the relationship between stent restenosis and wall shear stress (WSS) has been studied with CFD based on IVUS images [175]; and a comparison of haemodynamics in the carotid bulbs of a normal volunteer and an atherosclerotic patient showed increased wall thickness in regions with low and oscillating shear [176]. No studies could be found on investigating possible correlations between haemodynamics and disease progression in abdominal aortic aneurysm, although Leung *et al.* [177] studied the flow patterns and WSS in a single aneurysm patient.

Image guided CFD for elucidating biomechanical relationships in disease consists of four main sections: an imaging technique, which should ideally be high resolution, nonionizing and non-invasive; image segmentation for delineating the arterial geometry, which may be 2D, in which

case the slice data must be reconstructed to form the 3D geometry, or fully 3D; mesh generation and solution of the discretized Navier-Stokes equations with post-processing to extract the biologically relevant parameters; and finally the whole process must be repeated in several follow up studies in order to draw any conclusions on the influence of the haemodynamics in the disease.

The work here concentrates on the middle two of these sections, image segmentation and geometry reconstruction, and calculation of the blood flow. However, the method should have the potential to be used for investigating haemodynamic parameters across the AAA population.

AAA patients undergo regular monitoring in the form of US scans. If the aneurysm exceeds the 5.5 cm threshold, is symptomatic or is expanding fast, the patient will be considered for surgery. At this point a CT scan of the AAA is performed to examine the shape of the AAA more closely and decide how best to operate. MRI scans are not performed in general. Therefore a large scale clinical study to investigate haemodynamic parameters across the AAA population would be easiest to implement if the data required came from CT and US. That is not to say that if better methods were available these should not be used, but CT and US data are an appropriate first choice.

The aim of this work was to develop a method for estimating the flow field within AAA using CT scans of the geometry and the velocity in the aorta proximal to the aneurysm, which could be measured using Doppler US, and to use this method to study blood flow in several patients.

2.2 Methods

2.2.1 Segmentation

Contrast enhanced x-ray computed tomography (CT) data were used to obtain three patient geometries. Individual CT slices were segmented using a semi-automated threshold based method implemented in Matlab v. 6.5 r.13 (The Mathworks Inc., Natick, MA) (see figure 2.1). The interactive part of the method required a user to mark a small rectangle in the centre of the lumen on roughly every 10th data slice. These rectangles were linearly interpolated to give a rectangular region on each slice. Thus, if the geometry changed rapidly more user defined rectangles were required to ensure the interpolated rectangles fell within the lumen.

The automatic part of the method consisted of thresholding and converting the thresholded

image to a contour surrounding the lumen. The images were thresholded based on pixel values within the rectangular regions. The thresholded lumen region was converted to a contour by defining lines radiating from the centre of the lumen, as found from the centre of the rectangle, and then locating the points on the lines at which the pixel value dropped. In this way, points at equal angles around the edge of the lumen were found, and these formed a contour. The x-y coordinates around each contour were filtered firstly using a median filter to remove any outliers and then using a mean filter to ensure they were smooth.

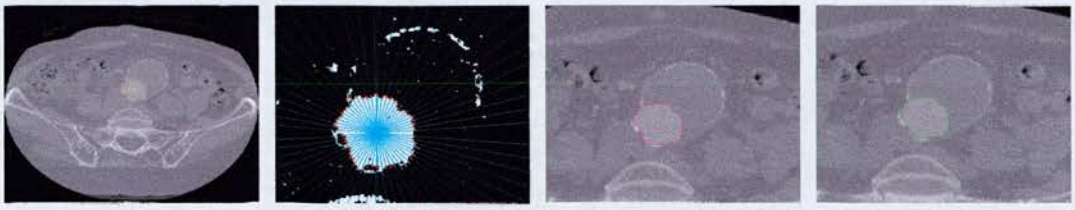

(a) slice data showing manually placed rectangle (b) thresholded image and construction of contour points (c) median filtered contour (d) mean filtered contour

Figure 2.1: *Segmentation: from manually placed rectangles to contour points.*

2.2.2 Geometry Reconstruction

The contours were stacked vertically and the x-y coordinates were smoothed using a moving average. To deal with the iliac bifurcation the last 3 slices of the aorta were attached to each of the iliac arteries before smoothing and then removed. An example of the resulting contours is shown in figure 2.2.

The contours were converted to a surface representation of the lumen, from just below the renal arteries, up to and including a portion of the iliac arteries, in the form of a Standard Tessellation Language (STL) file, using the software Nuages (Bernhard Geiger, INRIA Sophia-Antipolis, France [178]). Nuages uses Delauney triangulation to convert the contour data into a surface of triangles [178]. Since the triangulation results in a linear interpolation of the slice data some parts of the resulting surface had sharp corners. These were removed by manual correction using Magics X SP1 (Materialise, Leuven, Belgium).

Magics was also used to add inlets and outlets to the geometries. Each end of the geometry was cut off as close to the end as possible and perpendicular to the walls of the artery. A cylin-

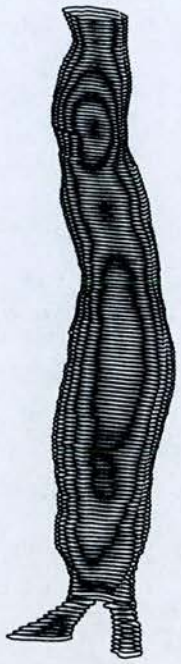

Figure 2.2: *Individual contours reconstructed to form AAA geometry.*

drical inlet (length = 5 x diameter) was attached smoothly to the aortic end. The outlets were extrapolated to give straight lengths perpendicular to the cut section (length = 10 x diameter) to ensure a computational boundary was not placed inappropriately [136]. Manual smoothing and extension of geometry are shown in figure 2.3.

2.2.3 Boundary Conditions

The boundary conditions used were velocity at the inlet and pressure at the outlet. Mills *et al.* [90] used a catheter tip electromagnetic velocity probe to measure the blood velocity in the aorta and some of the branch arteries of patients undergoing routine diagnostic cardiac catheterization. Their measurement from the abdominal section of the aorta was used here. The measurement was assumed to have been taken on the axis of the blood vessel and from this centreline velocity measurement a time dependent flow wave was calculated for each patient geometry using the radius of the inlet section and assuming fully developed, Womersley flow [179]. From this flow wave the same theory could then be used to calculate the time dependent velocity profile across the inlet boundary. The velocity at each inlet boundary face was calculated using a user defined function (UDF) in Fluent v. 6.216 (Fluent Inc., Lebanon, New

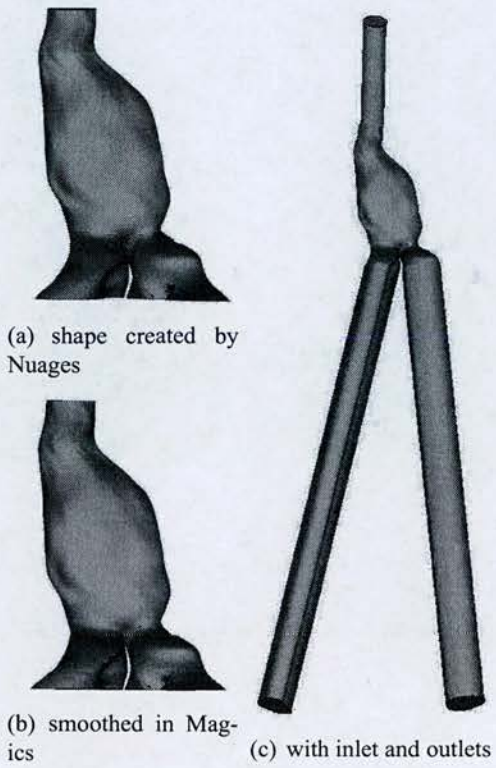

(a) shape created by Nuages

(b) smoothed in Magics

(c) with inlet and outlets

Figure 2.3: *Subsequent smoothing and extension of iliac arteries using Magics X SP1.*

Hampshire, USA) and then applied perpendicular to the face.

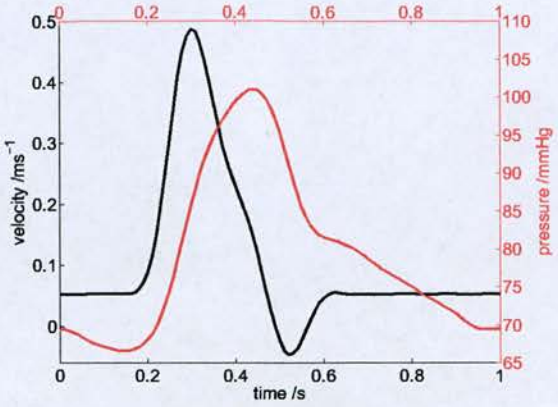

Figure 2.4: *Boundary conditions used were a Womersley velocity profile at the inlet and pressure at the outlet. Plotted here are the peak or centreline, velocity (black) in the inlet profile and the outlet pressure (red).*

Mills *et al.* [90] also measured the pressure in their patients and the pressure wave from the iliac artery was used here as the outlet boundary condition. At pressure outlets the flow is forced to be perpendicular to the boundary and so the boundary should be positioned where this flow is expected, that is, well down stream of any possible recirculation zones. In this work outlets with a length equal to 10 diameters were used, thus ensuring they were beyond any recirculation [136].

2.2.4 Computational Fluid Dynamics

Gambit v. 2.2.30 (Fluent Inc., Lebanon, New Hampshire, USA) was used to mesh the volumes of the arteries. An extremely coarse volume mesh of 3 mm tetrahedral elements was produced initially. A very fine surface mesh of 0.5 mm triangles was also produced. Fluent's mesh adaption capabilities were used to create a mesh that was fine in the necessary areas. Hanging node adaption was used [180]. Hanging node adaption is characterized by the existence of nodes which are not vertices of every cell sharing that vertex. For tetrahedral meshes, hanging node adaption requires trimming each corner of the tetrahedron and then splitting the enclosed octahedron along the shorted diagonal. First a steady flow solution was obtained for the extremely coarse grid with 50 cm/s flow across whole of the velocity inlet and a constant pressure of 100 mmHg (13328 Pa) at the outlet. Geometry based adaption [180] was activated using the very fine surface mesh. This ensures that as cells are refined the nodes are moved towards the shape

of the wall and so the surface becomes smoother rather than remaining the blocky shape of the original mesh. Boundary adaption with a surface mesh is illustrated in figure 2.5. Boundary adaption was then used to refine the near wall mesh of the lumen surface, and gradient adaption based on the gradient of the velocity magnitude was applied to the whole volume mesh to create the 'standard' mesh. After obtaining a converged solution with the standard mesh, gradient adaption, based on gradients of the velocity magnitude at peak flow, was used to produce a finer mesh. The resulting mesh should be fine in the areas with high velocity gradients but small enough that the calculation time was reasonable.

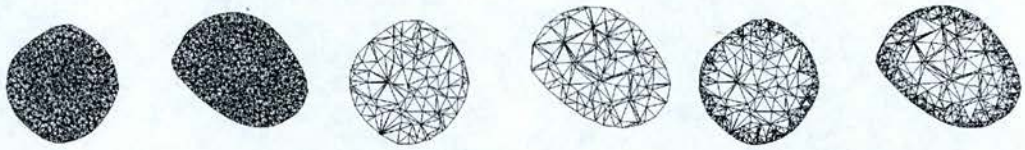

(a) fine mesh (b) coarse mesh (c) refined mesh

Figure 2.5: *Mesh refinement using hanging node, boundary adaption with a surface mesh. Note how the shape of the coarsely meshed iliac artery cross sections has grown towards that of the fine mesh in the refinement process. This is most obvious at the left corner of the right artery.*

Fluent v. 6.2.16 (Fluent Inc., Lebanon, New Hampshire, USA) was used to perform unsteady computational fluid dynamics (CFD). The flow was assumed to be laminar and the Navier Stokes equations were solved using Fluent's unsteady, segregated solver. Second-order upwind schemes were used to discretize time, and the continuity equations. The Pressure Implicit with Splitting of Operators (PISO) scheme [133, 180] was used for pressure-velocity coupling as this is the most appropriate for unsteady flow. Blood was assumed to be a Newtonian fluid with $\rho = 1040\ \mathrm{kg\ m^{-3}}$ and $\mu = 3.64 \times 10^{-3}\ \mathrm{kg\ m^{-1}\ s^{-1}}$ [32]. The calculations were performed on a Pentium-4 Linux workstation. There were 400 timesteps per cardiac cycle.

2.2.5 Haemodynamic Wall Properties

The local WSS and its variations can be used as indicators of disturbed flow which identify arterial regions where disease is likely to continue developing. Regions of high WSS may be sites of endothelial cell dysfunction and platelet activation [32]. Regions of very low WSS are susceptible to platelet aggregation and surface attachment [46].

Endothelial cells located in regions of oscillating shear stress are stimulated differently to those in steady shear stress. The variation in the WSS direction can be expressed in terms of the oscillatory shear index (OSI),

$$\mathrm{OSI} = \frac{1}{2}\left(1 - \frac{\left|\int_0^T \vec{\tau}_w dt\right|}{\int_0^T |\vec{\tau}_w dt|}\right) \tag{2.1}$$

where $\vec{\tau}_w$ is the WSS and T is the period time [135]. If the numerator and denominator are the same, that is if the WSS is always in the same direction, the OSI is zero. However, if the WSS integrates to zero the OSI is 0.5. Regions of high OSI have been found to correlate with elevated intima-media thickness, an early sign of atherosclerosis [86, 141].

It has been suggested that WSS gradients (WSSG) may influence AAA disease development since temporal shear gradients affect enzyme expression differently to steady shear stresses [41, 181]. Spatial WSSG magnitude was calculated as,

$$\overline{|\mathrm{WSSG_s}|} = \frac{1}{T}\int_0^T |\mathrm{WSSG_s}|\, dt \tag{2.2}$$

where,

$$|\mathrm{WSSG_s}| = \left(\left(\frac{\partial \tau_{w,m}}{\partial m}\right)^2 + \left(\frac{\partial \tau_{w,n}}{\partial n}\right)^2\right)^{1/2} \tag{2.3}$$

where m is the mean flow or $\tau_{w,mean}$ direction and n is the normal to m on the surface [143]. The temporal WSSG magnitude was calculated as,

$$\overline{|\mathrm{WSSG_t}|} = \frac{1}{T}\int_0^T \left|\frac{\partial \tau_w}{\partial t}\right| dt \tag{2.4}$$

The wall shear stress angle deviation (WSSAD) is a measure of the motion of fluid elements towards the wall and it has been suggested that it may correlate with disease since monocytes will be carried towards areas of high WSSAD [143]. In aneurysms the WSSAD will also represent regions where platelets are moving towards the wall. The WSSAD, which is an expression for the mean angle between the shear stress τ_i and the surrounding shear stresses τ_j, was calculated as [143],

$$\mathrm{WSSAD} = C\arccos\left(\frac{\overline{\tau_i}\cdot\overline{\tau_j}}{|\overline{\tau_i}|\cdot|\overline{\tau_j}|}\right) \tag{2.5}$$

where,

$$C = \begin{cases} 1; & \overline{v_{n,i}} \cdot \overline{n_i} \geq 0, \\ 0; & \overline{v_{n,i}} \cdot \overline{n_i} < 0. \end{cases} \tag{2.6}$$

and,

$$\overline{\tau_i} = \frac{1}{t}\int_0^T \tau_i dt, \qquad \overline{v_i} = \frac{1}{t}\int_0^T v_i dt \tag{2.7}$$

where τ_i is the wall shear stress at point i, $v_{n,i}$ is the near wall velocity component normal to the surface at point i and C is zero if the blood is moving away from the wall.

The static pressure on the lumen surface is an indication of the normal force experienced locally. The blood flow creates pressure variations which mean locally measured static pressure will differ from the systolic blood pressure.

Flow patterns, shear stress parameters, and pressure were calculated and compared in the three aneurysm geometries.

2.3 Results

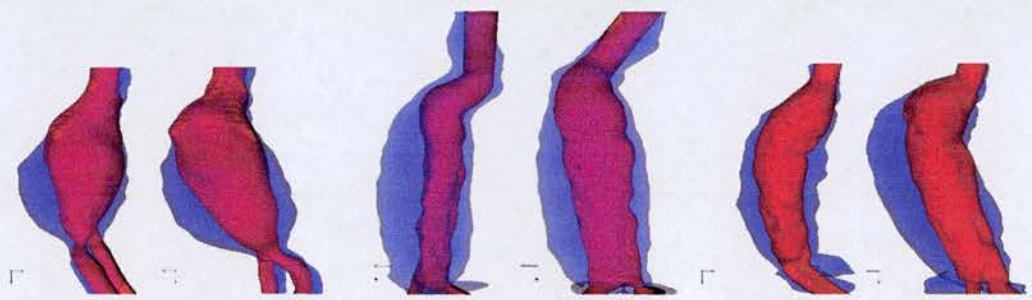

(a) AAA02 (b) AAA04 (c) AAA10

Figure 2.6: *Shape of lumen, thrombus and wall in the three patient aneurysms. The lumen is shown in red and the region between the lumen and the wall, that is the thrombus, is shown in purple. Views are of the patients left side (left) and posterior (right).*

2.3.1 Geometry

The shapes of the three AAAs are shown in figure 2.6 and the maximum anterior-posterior diameter of the aneurysm and the lumen are given in table 2.1. The lumen of both AAA04 and AAA10 were both fairly tubular, with gradually increasing and decreasing diameters whereas

Patient	maximum A-P diameters /cm		diameter of healthy section /cm
	lumen	wall	
AAA02	4.40	6.69	1.86
AAA04	3.60	7.24	2.50
AAA10	6.13	8.22	2.44

Table 2.1: *Measurements of AAAs (A-P is anterior-posterior.)*

AAA02 had a higher ratio of lumen diameter to length. All the aneurysms were curved so that they bulged out more on the anterior side.

2.3.2 Convergence

Mesh independence was assessed by comparing the velocity magnitude, on several planes, between the coarse and fine meshes. The mean percentage difference on each plane in AAA02 throughout the cardiac cycle is shown in figure 2.7. The largest difference occurred on plane 6 during the diastolic phase of the cardiac cycle when there was low flow. Plane 6 is located in the iliac arteries (figure 2.7a) which are beyond the main region of interest so some error here is less concerning. The largest difference on planes 3 or 4, which lie in the bulge of the aneurysm, was 25 %. The effect of this 25 % difference is shown in figure 2.7c and 2.7d which shows the V_{mag} profiles in the coarse and fine meshes for plane 3 at 0.2 s. The mean difference in velocity magnitude between the coarse and fine meshes, in each patient geometry, along with the time taken to compute one cardiac cycle is shown in table 2.2.

Solution time should vary linearly with mesh size, for a given mesh geometry. However, these computers are in a shared computer cluster so there may have been other processes running simultaneously and computational times have been included only as a guide.

Patient	mesh size			time taken		difference
	3 mm	standard	fine	standard	fine	in V_{mag} /%
AAA02	4.7×10^4	2.2×10^5	2.5×10^5	11 hr 15	13 hr 49	10
AAA04	6.3×10^4	2.6×10^5	2.8×10^5	25 hr 53 *	15 hr 15	8
AAA10	9.7×10^4	4.1×10^5	4.5×10^5	29 hr 28	37 hr 52	20

Table 2.2: *Number of elements used and time taken. *Other processes running at the same time.*

Cyclic independence was assessed by comparing the velocity magnitude at a number of points

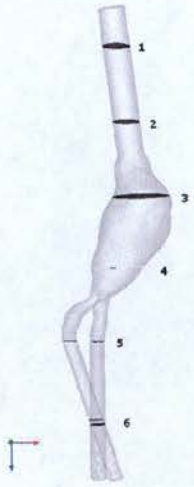

(a) plane positions

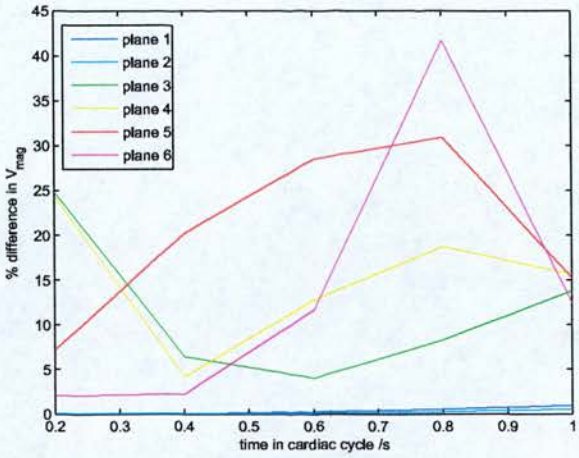

(b) mean % difference between V_{mag} in coarse and fine meshes

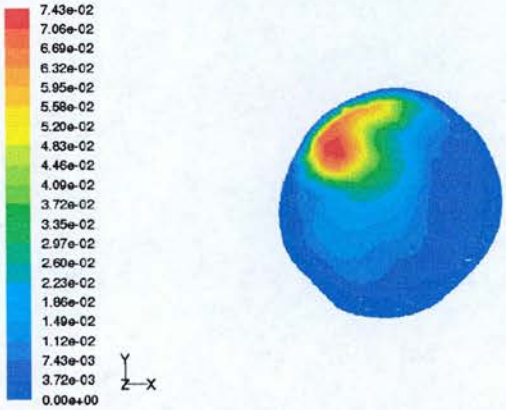

(c) Coarse mesh: V_{mag} on plane 3 at 0.2 s

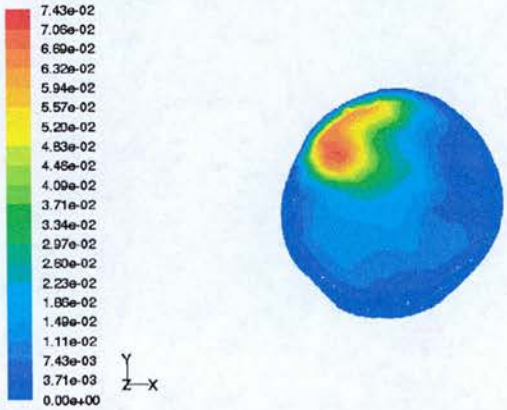

(d) Fine mesh: V_{mag} on plane 3 at 0.2 s

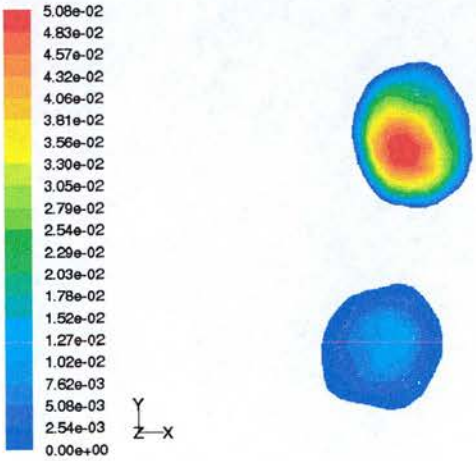

(e) Coarse mesh: V_{mag} on plane 6 at 0.6 s

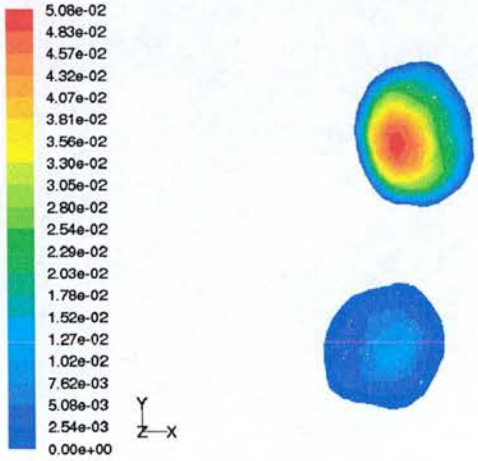

(f) Fine mesh: V_{mag} on plane 6 at 0.6 s

Figure 2.7: *Difference in V_{mag} between coarse and fine meshes.*

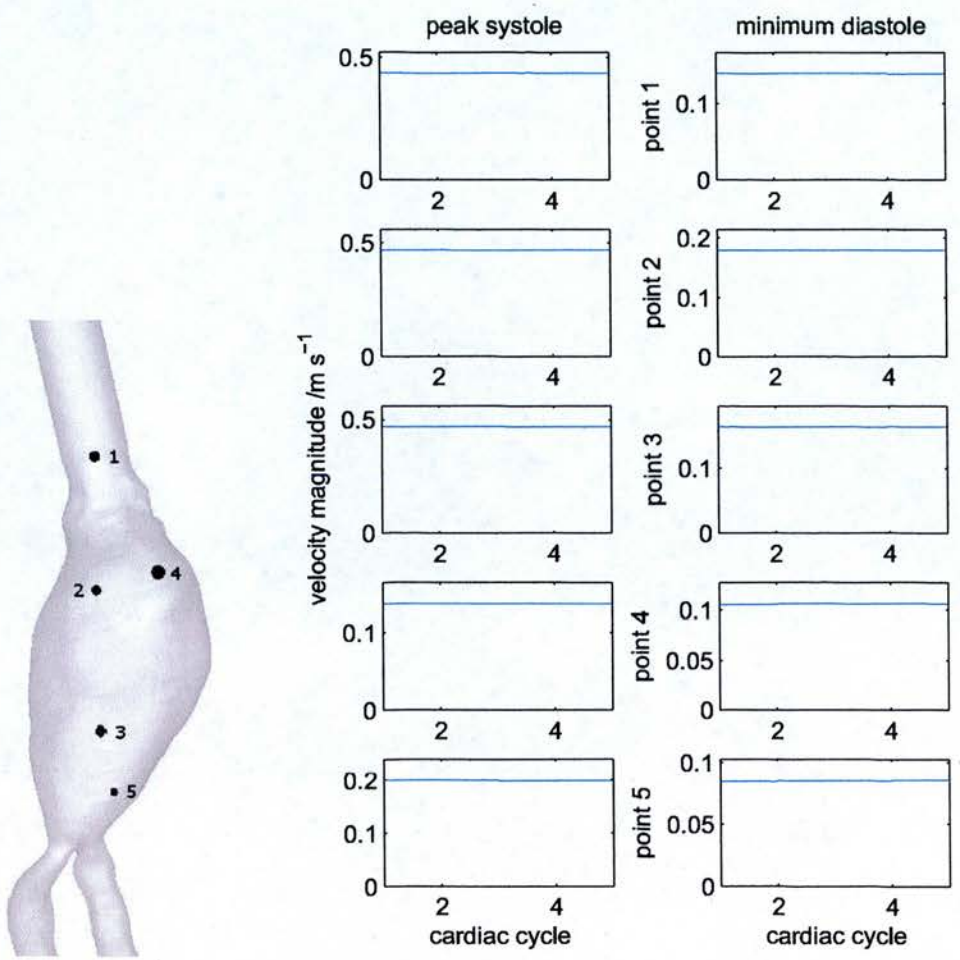

(a) location of points

(b) convergence of velocity magnitude

Figure 2.8: *Cyclic convergence of velocity magnitude at select points. Velocity magnitude at peak systole and minimum diastole has been plotted for each cardiac cycle.*

throughout time. Plots of the variation in velocity magnitude at peak systolic velocity and minimum diastolic velocity at 5 points are shown in figure 2.8 for the first aneurysm geometry. The solutions were considered cyclically converged after the 4th cardiac cycle. Although the velocity at one of the points shown suggests the solution might not be completely converged by this time, 5 cycles were used as a balance between precision and limiting the computational resources required. The mean percentage difference in the velocity magnitude, at all cells and at 20 time points, between the 4th and 5th cardiac cycles was 1.9%, 0.7% and 8.2% for the three aneurysms respectively.

2.3.3 Velocity

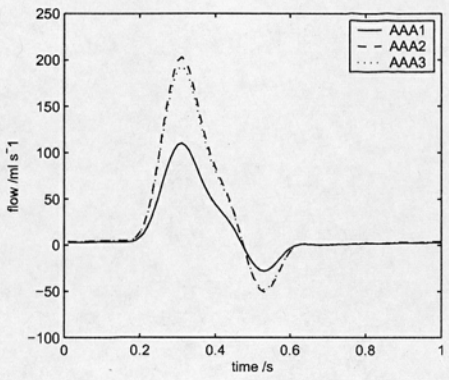

Figure 2.9: *Flow waves for the three aneurysms.*

The flow waves for the three aneurysms have different magnitudes since they were calculated to each give the same centreline velocity but each had a different inlet diameter (1.86 cm, 2.5 cm, and 2.44 cm). The flow waves are shown in figure 2.9. Velocity profiles on selected planes within the three aneurysms are shown in figures 2.10 to 2.12. In all three geometries the velocity profiles in the inlet length were very similar, with a blunt profile and peak velocity just less than 0.5 m/s. This is expected since the inlet boundary condition was set up such that the velocity profile produced a time varying flow waveform with a specific centreline velocity. In fact the peak velocities in the inlet tubes were 0.471, 0.484 and 0.483 m/s. The peak velocity should have been 0.488 m/s and the differences (3 %, 0.8 % and 1 %) can be attributed to discretization errors. The blunt profile is typical of that in all the larger arteries and occured because the Womersley parameter, α, was high. When the inertial forces are large compared with the viscous forces, the fluid moves like a solid mass. Near the wall, where the viscous

forces dominate, there is a high shear region [32].

At 0.3 s (peak systolic velocity) flow throughout all the aneurysms was in the forward direction (towards the legs). At 0.5 s (peak negative velocity) most of the flow was backwards, however just distal to the aneurysm neck in all three geometries the core flow was still in the forward direction. By the end of the cardiac cycle (1.0 s) the blood in the sac was almost stationary. The directional vectors clearly show the flow recirculated and there was no predominant direction. In the inlet section the bulk flow was small but directed forwards.

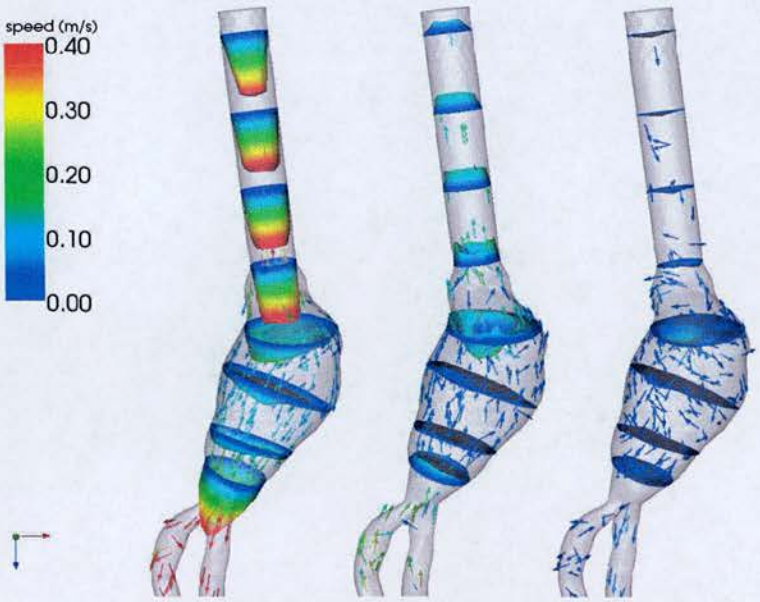

Figure 2.10: *Velocity profiles in AAA02, from left to right: 0.30, 0.50 and 1.00 s.*

Examining the flow patterns in detail revealed their intricacies. At 0.30 s, peak systolic flow, the streamlines in AAA02 all went straight through the aneurysm cavity (see figure 2.13). A vortex began to develop at 0.35 s on the anterior of the aneurysm neck as the flow decelerated. As the flow continued to decelerate the vortex got stronger and became a complete, but lopsided, torus by 0.45 s. This toroidal vortex occupied the majority of the aneurysm cavity but there was a region at the posterior of the distal half where the flow passed straight through. By 0.50 s, the flow in the inlet and exit sections was completely in the reverse direction and the vortex filled the whole of the aneurysm cavity. At 0.55 s the vortex was no longer a complete torus but was crescent shaped, the flow on the posterior side being forward. At 0.60 s blood within the aneurysm cavity was trapped there, continually circulating. Since the development of the vortex at 0.35 s its centre had moved downstream and was located in the proximal half. This

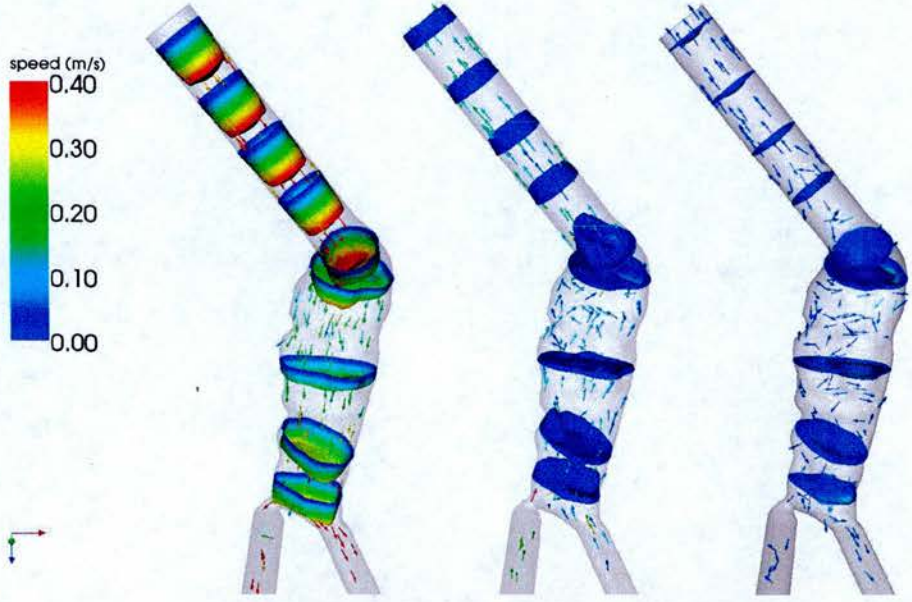

Figure 2.11: *Velocity profiles in AAA04, from left to right: 0.30, 0.50 and 1.00 s.*

Figure 2.12: *Velocity profiles in AAA10, from left to right: 0.30, 0.50 and 1.00 s.*

pattern lasted until the end of the cardiac cycle and beyond, into the next cycle, with little change. Indeed, remnants of the vortex could still be seen at 0.15 s although there was also a lot of other flow recirculation. As the flow began to accelerate again at 0.2 s the recirculation disappeared and by 0.25 s the streamlines were all straight.

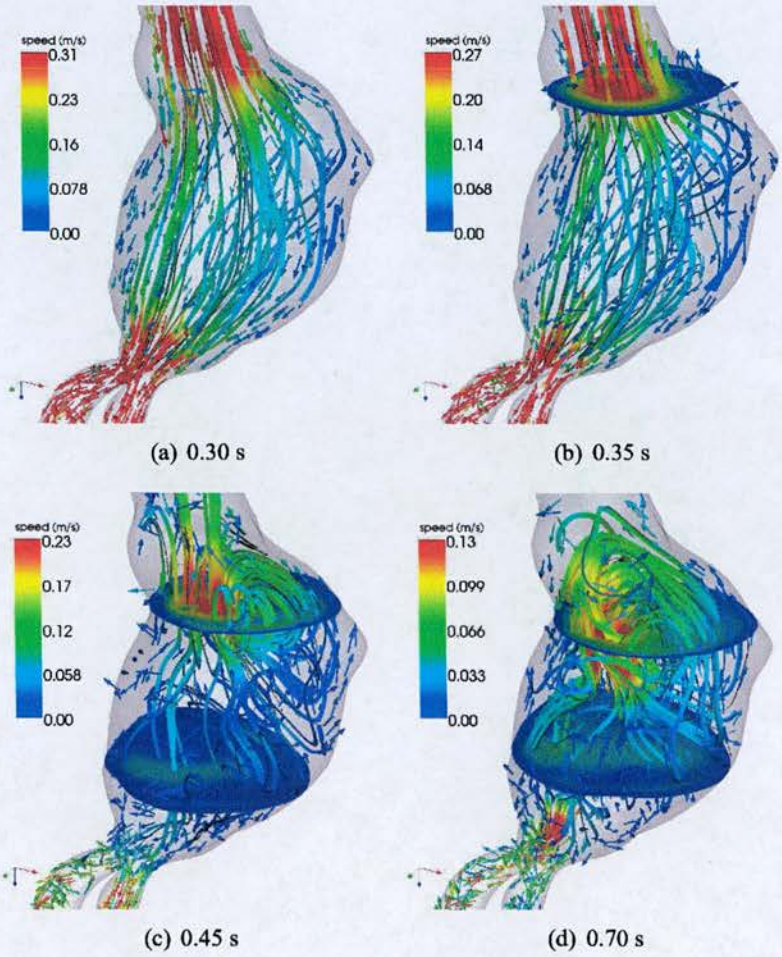

(a) 0.30 s (b) 0.35 s

(c) 0.45 s (d) 0.70 s

Figure 2.13: *Formation and evolution of vortices in AAA02.*

The flow patterns in AAA04 were quite different from those in AAA02 (figure 2.14). The healthy section of the aorta entered the aneurysm section at one angle and directly posterior to that the aorta bent at another angle. The two bends caused helical flow through the artery. At peak systolic flow (0.3 s) the pitch of the helix was long so there was only a small twist to the flow. However, as the flow started to decelerate (0.35 s) the helix was tighter and the blood swirled more. At 0.40 s, although there was almost a vortex present in the aneurysm neck, the flow was still helical. As the flow decelerated the blood spent longer spiralling through the

aneurysm. The helical flow lasted throughout the cardiac cycle and into the next one with tight spiral flow still present at 0.2 s.

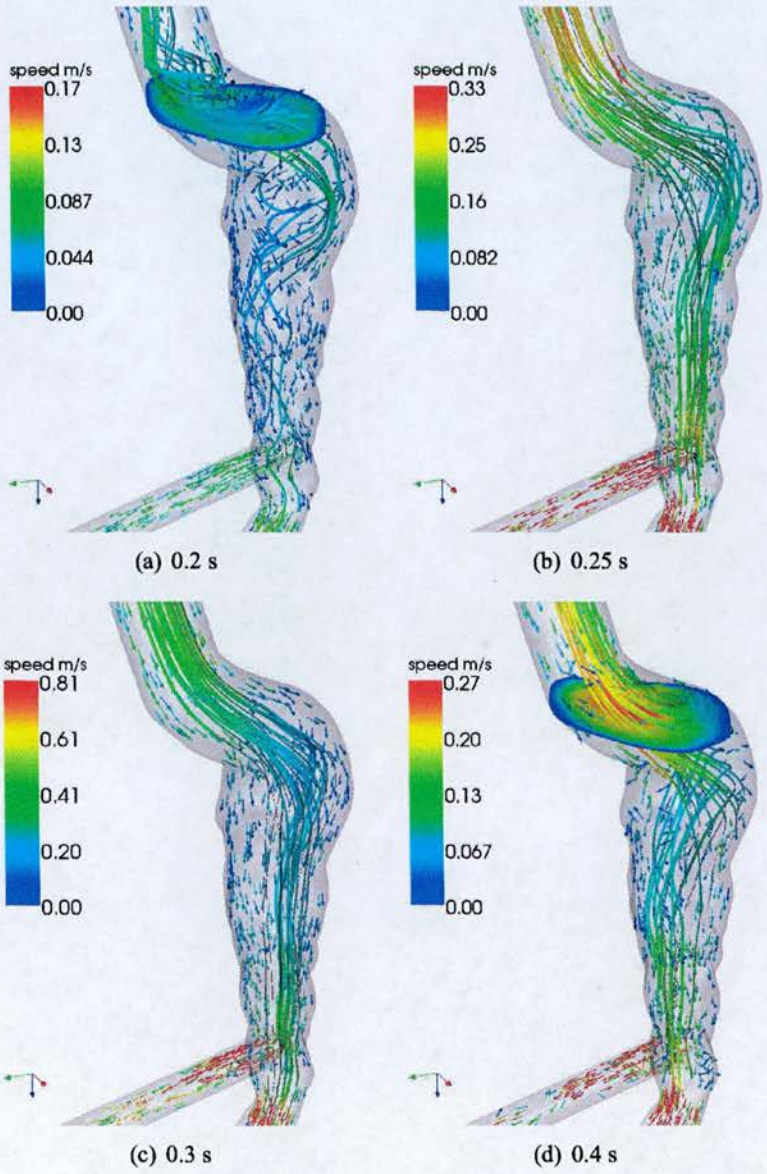

(a) 0.2 s (b) 0.25 s

(c) 0.3 s (d) 0.4 s

Figure 2.14: *Formation and evolution of vortices in AAA04.*

The flow patterns in AAA10 had similar elements to those of both AAA02 and AAA04 (see figure 2.15). Since the ratio of the bulge diameter to the neck diameter was smaller in AAA10 than AAA02 the vortices were correspondingly smaller. There was no toroidal vortex, however as the flow decelerated at 0.4 s a crescent shaped vortex formed in the aneurysm neck and there was a second vortex in the lower half of the aneurysm just after the bend. As the flow reversed

(0.5 s) the second vortex disappeared and the first one encompassed the whole of the top section of the aneurysm. This vortex remained in the aneurysm until the flow started to accelerate again in the next cardiac cycle.

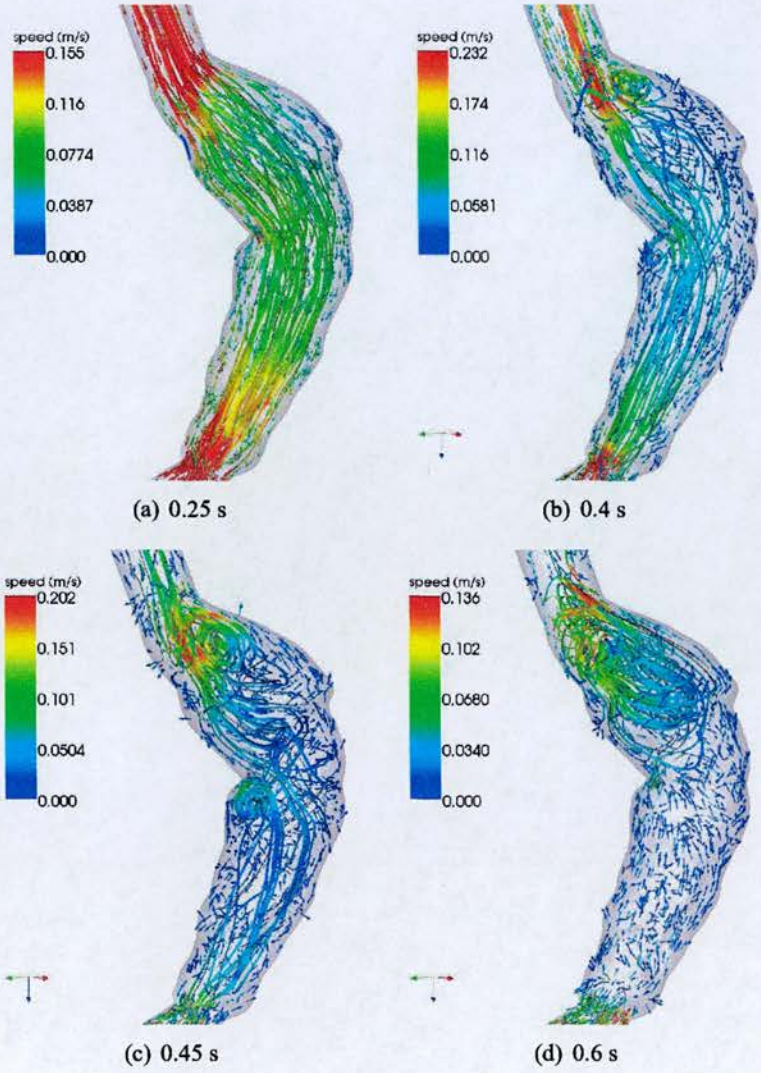

(a) 0.25 s (b) 0.4 s

(c) 0.45 s (d) 0.6 s

Figure 2.15: *Formation and evolution of vortices in AAA10.*

2.3.4 Wall Shear Stress

As an example of the variation in the WSS throughout the cardiac cycle figure 2.16 shows WSS magnitude and direction in AAA02 throughout time. Even at peak systolic flow there were regions where the WSS magnitude was less than 0.5 Pa and for most of the cardiac cycle the

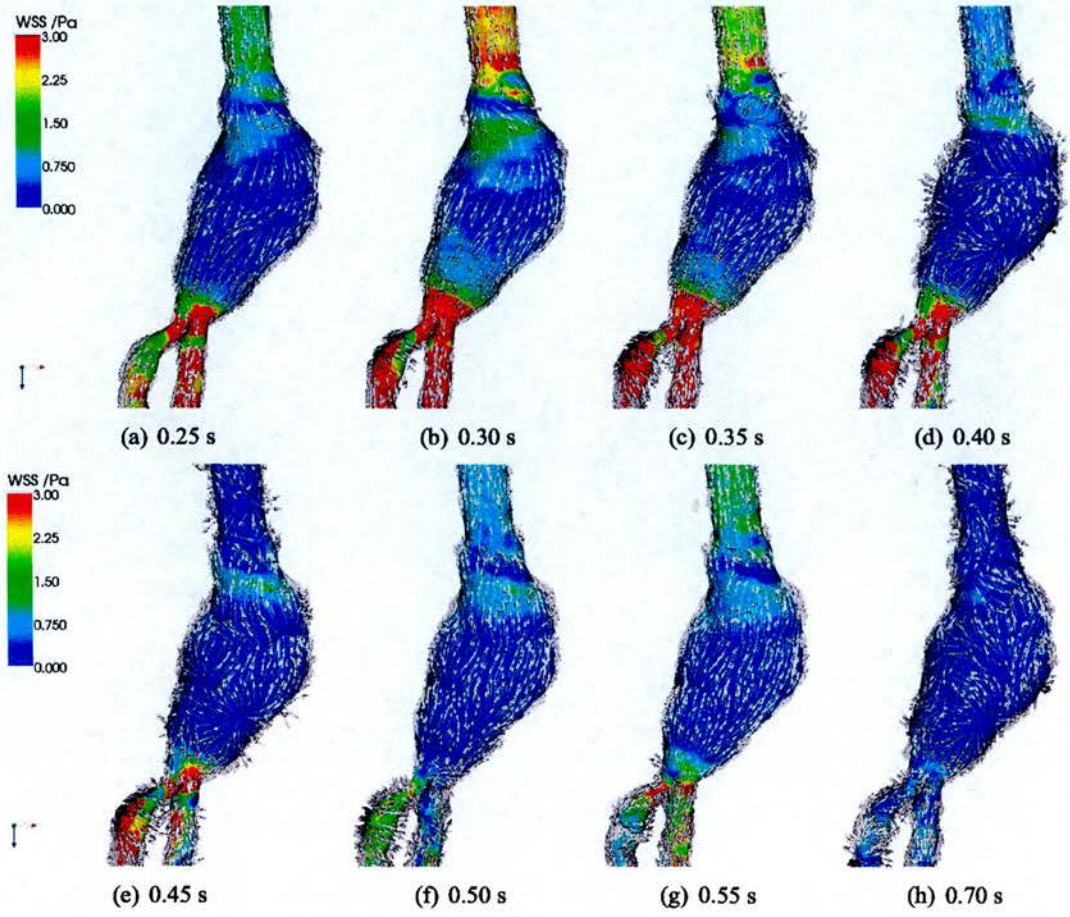

Figure 2.16: *WSS magnitude and direction in AAA02 at selected points through the cardiac cycle.*

majority of the bulge experienced far lower WSS. Although around the times of peak forward and peak negative flow the WSS direction was forward and reverse respectively, during the periods of flow deceleration and very low flow, the directions were more varied and there were regions where the arrows formed star shapes indicating points of flow separation.

The cycle averaged WSS properties for the three aneurysms are shown in figures 2.17, 2.18 and 2.19. In the inlet sections the mean WSS magnitude ($\overline{|\vec{\tau}_w|}$) was around 0.45 Pa for each AAA geometry while the mean WSSs ($\overline{\vec{\tau}_w}$) were around 0.18, 0.14 and 0.11 and were directed forwards in the inlet lengths of the aneurysms. For comparison, the value of $\overline{|\vec{\tau}_w|}$ calculated using the Womersley assumption were 0.439, 0.441 and 0.441 Pa and $\overline{\vec{\tau}_w}$ were 0.084, 0.063 and 0.064 Pa for AAA02, AAA04 and AAA10 respectively. Whilst the values of $\overline{|\vec{\tau}_w|}$ differ from the Womersley values by just 2 % the values of $\overline{\vec{\tau}_w}$ differ by between 71 and 122 %. This can be explained because although the inlet length is a straight tube it opens out onto the aneurysm which is obviously not a straight tube. The flow in the inlet length is affected by the downstream geometry and is therefore not exactly aligned with the direction of the cylinder. This means that, although at every time point the magnitude of the WSS in the inlet length is very close to that in a straight tube, the WSS vectors are not precisely parallel with the inlet tube axis. For the particular flow wave used here, the WSS in a straight tube has a similar positive and negative component thus, integrating the WSS in a true straight tube throughout the cardiac cycle results in a very small mean WSS. However, since in the inlet tube the flow is not directed precisely parallel with the tube, integrating over the cardiac cycle results in a significant resultant WSS as the vectors do not 'cancel out'.

$\overline{|\vec{\tau}_w|}$ in the bulge of AAA02 (figure 2.17) was between 0.02 and 0.2 Pa with the lowest values on the posterior side and the highest values on the anterior. This is about 4 - 40 % of that in the inlet length. $\overline{\vec{\tau}_w}$ was 0 - 0.15 Pa with the lowest values found laterally and the highest on the posterior which is 0 - 80 % of that in the inlet length.

In contrast, in AAA04 (figure 2.18) the $\overline{|\vec{\tau}_w|}$ in the bulge was much higher than that in AAA02, 0.1 - 0.7 Pa or 20 - 200 % of that in the inlet while $\overline{\vec{\tau}_w}$ was 0 - 0.5 Pa or 0 - 400 % of the inlet value. The much wider range of WSS values in the bulge of AAA04 is accounted for by the lumen geometry which is wider than that of the inlet but not as wide as that of AAA02. The highest of both $\overline{|\vec{\tau}_w|}$ and $\overline{\vec{\tau}_w}$ are found at the distal end where the anterior-posterior diameter is actually lower than the inlet diameter.

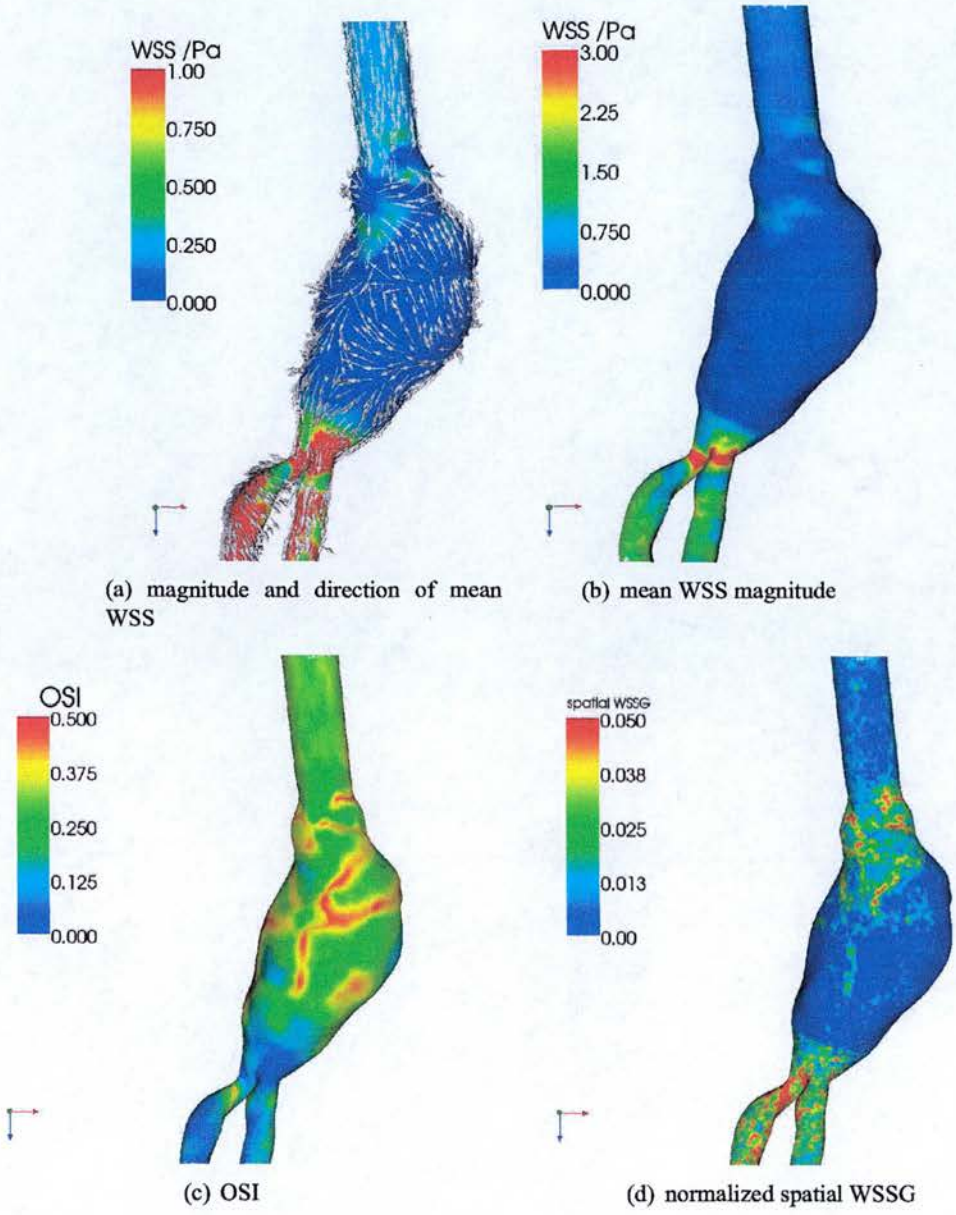

(a) magnitude and direction of mean WSS

(b) mean WSS magnitude

(c) OSI

(d) normalized spatial WSSG

Figure 2.17: *Haemodynamic wall parameters: AAA02.*

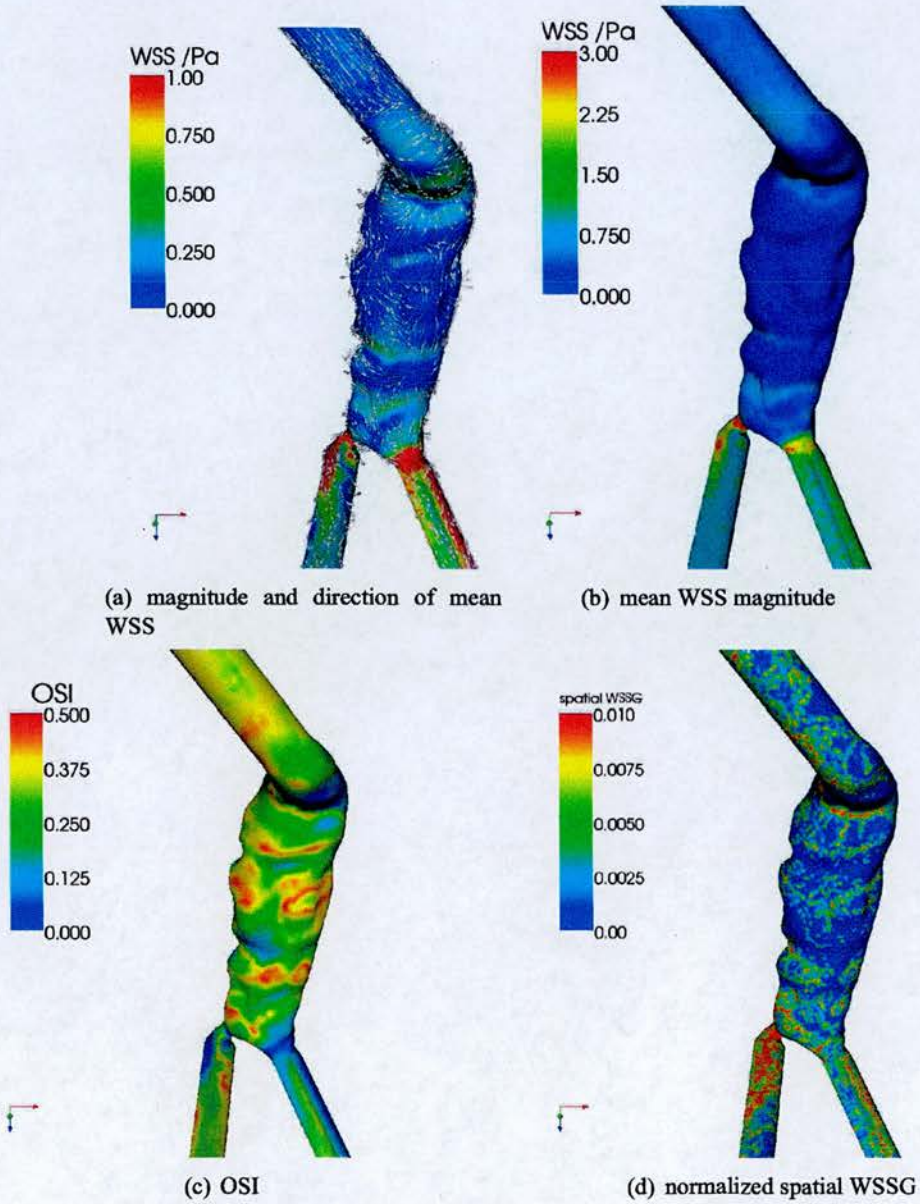

(a) magnitude and direction of mean WSS

(b) mean WSS magnitude

(c) OSI

(d) normalized spatial WSSG

Figure 2.18: *Haemodynamic wall parameters: AAA04.*

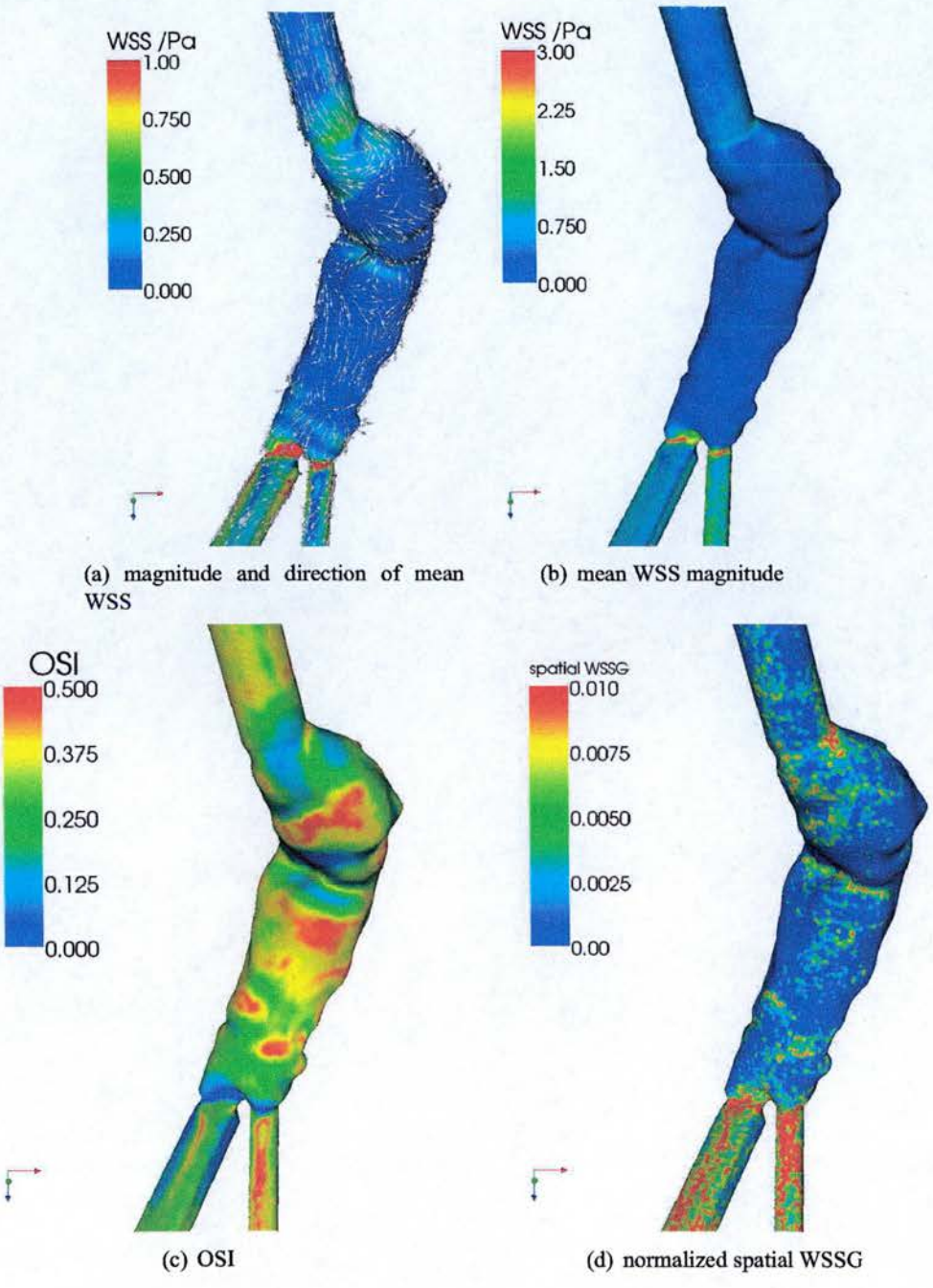

(a) magnitude and direction of mean WSS

(b) mean WSS magnitude

(c) OSI

(d) normalized spatial WSSG

Figure 2.19: *Haemodynamic wall parameters: AAA10.*

Mean WSS values in AAA10 (figure 2.19) were similar to those in AAA04. $|\overline{\vec{\tau}_w}|$ was 0.05 - 0.4 Pa (10 - 90 % of the inlet value) and $\overline{\vec{\tau}_w}$ was 0 - 0.3 Pa (0 - 300 % of the inlet value) with the highest values on the inner side of the curved bulge which corresponds to the posterior. The geometry of AAA10 is similar to that of AAA04 in that the bulge is fairly narrow, however, AAA10 is more curved accounting for the anterior-posterior difference.

In all three aneurysm geometries the OSI in the inlet length was between 0.3 and 0.4. Within the aneurysm sack there was more variation with regions in each of the aneurysms where the OSI was up to 0.5 and others where it was down to about 0.1. This reinforces the idea of aneurysms being regions of disturbed flow. Some, but not all, bands of high OSI appear to correlate with ridges in the aneurysm geometries.

High spatial WSS gradients were found in both the neck and most distal regions of the aneurysm bulges. The neck region is only surrounded by thrombus in AAA04, in the other two aneurysms this region is thrombus free (figure 2.6). Hence the shear stresses in this region are acting directly on the endothelial cells and shear stress gradients have been found to stimulate the expression of proinflammatories in endothelial cells. Temporal WSS gradient patterns followed those of the WSS itself and hence are not shown.

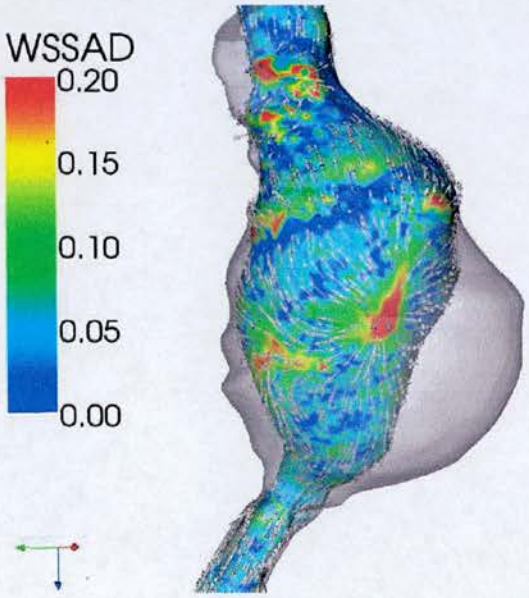

Figure 2.20: *WSSAD, direction of mean WSS and thrombus location in AAA02*

WSS angle distribution is a measure of how much the near wall flow is directed towards the wall. In the two AAAs with narrower lumen (AAA04 and AAA10) the WSSAD was found

to vary across the aneurysm bulge depending very much on the local curvature of the lumen surface. In AAA02 the largest region of high WSSAD was located on the distal anterior wall, near to where the thickest section of thrombus was located, see figure 2.20. WSSAD indicates the motion of blood, including platelets, towards the wall and platelets are required at the wall for the thrombus to grow. The shape of the lumen changes as the thrombus grows and as the aneurysm sack grows but the correlation in positions of highest WSSAD and thickest thrombus suggest the blood may have been flowing towards this spot for some time.

2.3.5 Pressure

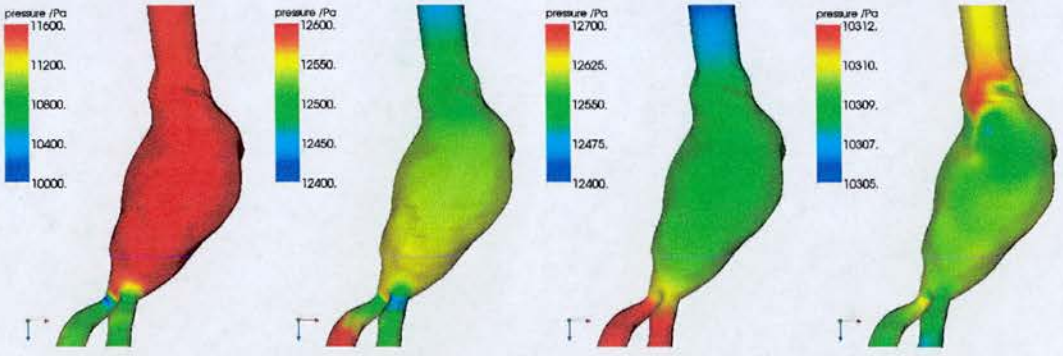

(a) 0.30 (b) 0.40 (c) 0.45 (d) 0.80

Figure 2.21: *Static pressure in AAA02*

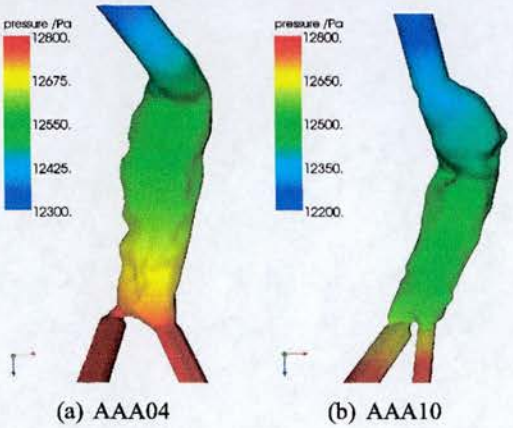

(a) AAA04 (b) AAA10

Figure 2.22: *Peak systolic static pressure in AAA04 and AAA10*

Spatial variation in static pressure at selected times in the cardiac cycle for AAA02 is shown in

figure 2.21. The pressure gradient is negative when the flow is forward but as the flow changes direction the pressure gradient becomes positive. The highest pressure gradient is at the distal end of the aneurysm where the artery narrows and branches into the iliacs. The largest pressure difference along the length of the aneurysm is 1600 Pa and occurs at peak systolic flow (0.30 s). The highest pressure gradient is found at the iliac bifurcation. At peak systolic pressure the difference is 300 Pa, 2 % of the systolic pressure. Spatial variation in pressure at peak systole in AAA04 and AAA10 is shown in figure 2.22. The total pressure differences along the aneurysms are 500 and 600 Pa or 4 % of systolic pressure.

2.4 Discussion

A method was developed to calculate haemodynamics in patient specific AAAs. The method used a CT scan of the patient's aorta to obtain the arterial geometry along with published velocity and pressure data for the boundary conditions [90]. The published velocity wave could be exchanged for a spectral Doppler US measurement to make this boundary condition patient specific. The data used are obtained routinely from AAA patients which makes the method suitable for extension to a larger study of AAA haemodynamics.

Flow patterns depended on the specific geometries of the arteries. Toroidal vortices formed during flow deceleration if there was a large enough ratio of bulge diameter to healthy aorta diameter and if the bulge extended fully circumferentially. Most of the time the vortices were crescent shaped rather than toroidal since the aneurysms tended to bulge more anteriorly than posteriorly. Helical flow was present if the inlet entered at an angle to the aneurysm bulge. In the presence of vortices regions of high and low velocity are located nearby creating regions of high shear. Platelets are activated by high shear stresses and may then clot in stagnant regions [2]. Both vortices and helical flow prolong the residence time of blood within the aneurysm, prolonging the exposure of the artery to inflammatory cells.

WSS was low and oscillating in the aneurysms. Although low and oscillating WSS is commonly associated with development of atherosclerotic lesions [4] the aneurysm bulges were surrounded by thrombus and hence, in the bulk of the aneurysm bulge, the endothelial cells were not in contact with the flow. However, low and oscillating shear stress is an indicator that the flow is slow, ideal conditions for clotting. The large region of high WSSAD in AAA02 suggests blood motion towards the wall, bringing platelets towards the already thick thrombus.

The mean WSS magnitude in the aneurysm necks, whilst being higher than that in the main bulge was still low compared with that usually quoted for healthy arteries (1-2 Pa). The neck also experienced regions of high OSI and had the largest areas of high spatial WSSG. Since the neck had little or no thrombus in the three aneurysms the flow in this region will be in contact with the endothelium. High shear stress gradients and oscillating flow may enhance the endothelial expression of proinflammatories such as MCP-1 and PDGF-A which may inhibit the disease development.

An aneurysm will rupture if the stress in the wall exceeds its strength. Static pressure in the aneurysm bulge is the cause of the wall stress, so, it has been suggested that fluid dynamic spatial variation in wall pressure is important in assessing rupture risk of aneurysms [182]. However, in this study the pressure variation was at most 4 % of the systolic pressure.

The results in these patients were in general agreement with those of Leung *et al.* [177], in that vortices developed just after peak systolic flow and there was low WSS in the aneurysm bulge. However, it has been shown here that the specific flow in individual patient aneurysms is highly dependent on their geometry.

2.4.1 Segmentation and Geometry Reconstruction

The contours were reconstructed to form arteries by stacking them and then smoothing the x-y coordinates of neighbouring points in the z-direction using a moving average. The bifurcation was reconstructed by smoothing the top few contours of each iliac artery onto the final few contours of the aorta. Morris *et al.* [138] cautioned that differences in reconstruction techniques can lead to differences in flow fields. They compared models created by: smoothing just the contours; smoothing the contours and smoothing in the axial direction; and treating each contour as a circle with axial smoothing. Maximum differences in the WSS were over 10 Pa since their geometry without axial smoothing created spikes due to sharp corners. The geometry reconstruction technique used here included smoothing in the axial direction to prevent these sharp spikes but the technique has not been compared with others and should be in future work.

2.4.2 Boundary Conditions

The boundary conditions used here were taken from a paper by Mills *et al.* [90]. Although the shape of the velocity wave is typical of velocity waves from the abdominal aorta, that is a large

forward pulse followed by significant reverse flow, it was taken from just one person and the quantitative variation in the wave shape across the population is unknown. The person did not have AAA and the effect of the disease on the velocity wave is unknown. The velocity wave was applied at the centreline velocity at the entrance to an inlet length attached to the top of the patient geometry. The rest of the velocity profile was calculated by assuming Womersley conditions. The assumption of fully developed flow in a model of the carotid bifurcation was investigated by Moyle *et al.* [137]. They found that the effects of secondary velocities in the inlet profile on the WSS and OSI died out within a few diameters of the inlet.

2.4.3 Rigid Geometry

The effect of wall motion on the flow field of arteries is controversial. Jin *et al.* [148] found that calculated flow fields in the aortic arch agreed best with MR measurements only when the wall motion was incorporated but WSS difference between rigid and compliant models was less than 0.5 Pa throughout the cardiac cycle. Scotti *et al.* [172] looked at fluid-structure interactions in simple bulged tube models of AAAs and found that during flow deceleration there were no vortices present, a pattern which is typical of flow acceleration in rigid walled models. Deplano *et al.* [75] found differences in flow patterns and vortex strength in compliant AAA models compared to rigid ones. Wall displacements in aneurysmal aortas are around 5 % of the diameter (see Chapter 4) which is a 10 % area or volume change, or 6.5 ml assuming a 5 cm diameter spherical aneurysm. Then changing the volume by 6.5 ml over half the cardiac cycle induces a flow rate of 13mls^{-1} which is small compared with the peak flow rate through an aneurysmal aorta (150mls^{-1}) found in Chapter 3 and hence compliance effects are unlikely to be important.

2.4.4 Newtonian Blood

A Newtonian constitutive model for viscosity is generally accepted as a reasonable approximation in large arteries [141]. Johnston *et al.* [183] compared a Generalized Power Law blood model with a Newtonian model when calculating the flow through coronary arteries. Regions of high and low WSS were the same with both models and there were only significant quantitative differences during the low flow parts of the cycle which amounted to about 30 % of the time. They concluded that a Newtonian model was a reasonable first approximation in coronary arteries which are much smaller (3-5 mm) than the aorta.

2.5 Conclusions

A method to calculate haemodynamics in patient specific aneurysms based on CT scans has been developed. Blood flow has been estimated in three patient specific aneurysms using the same boundary conditions. Flow patterns were found to be strongly influenced by the specific geometry of the aneurysmal aorta. Unlike in simple axially symmetric aneurysm models, the vortices were usually crescent shaped rather than toroidal. Some helical flow was usually present but this was enhanced if the healthy section of the aorta entered the diseased section at an angle. Mean WSS magnitude in the aneurysm bulges was usually lower than that in the inlet section but there were also regions where it was higher. OSI in the aneurysm bulge varied from 0.1 to 0.5 whereas in the inlet section it was between 0.3 and 0.4 and high WSS spatial gradients were found in the aneurysm necks and at the distal ends. Pressure differences along the aneurysms at peak systole were around 4 % of systolic pressure. The blood flow patterns and haemodynamic wall parameters presented here are interesting but there is no way to know if they are accurate. Validation is an essential step in developing an image guided CFD method and this will be attempted in a later chapter.

Chapter 3
Characterization of an Abdominal Aortic Velocity Wave from Patients with Abdominal Aortic Aneurysm

Blood flow in axially symmetric aneurysms consists of toroidal vortices which form at the proximal end during flow deceleration and move distally throughout the cardiac cycle. In Chapter 2 it was shown that flow patterns in patient specific geometries are significantly more complicated: the vortices are more likely to be crescent shaped than toroidal and are accompanied by helical flow. Haemodynamic wall parameters such as wall shear stress, oscillatory shear index and wall shear stress gradients were shown to be dependent on these flow characteristics. However, the calculations in Chapter 2 were performed using boundary conditions obtained from measurements made on normal subjects. In this chapter Doppler ultrasound will be used to measure the blood velocity in patients with abdominal aortic aneurysm and the measurements will be used to produce an archetypal velocity wave which could then form the inlet boundary condition for numerical calculations of flow in aneurysms.

3.1 Introduction

The use of *in vitro*, see for example [77, 114], and *in silico* [184] simulations in studying AAA haemodynamics and the interaction of blood with the arterial wall [172] has become popular. The results of both *in vitro* and *in silico* haemodynamics simulations are highly dependent on the flow conditions imposed [74] and yet there is only limited data in the literature on flow in aneurysmatic aortas. Whilst some patient specific studies use flow waves measured in the patient [182, 185], the majority of studies are based on abdominal aortic flows taken from one of two papers: Mills *et al.* [90] measured blood velocity in the major arteries using a catheter tip velocity probe, which is an invasive method, and Olufsen *et al.* [132] used magnetic resonance imaging (MRI) to measure the flow at points along the aorta of a single healthy subject. Early work on arterial velocity and pressure relationships examined change in velocity and pressure

wave along the aorta in numerous species [32], including humans, but there are only very limited studies examining the variation in the velocity wave within the human population. In addition, the presence of the aneurysm was expected to affect the waveform.

There are two noninvasive methods for measuring blood flow: Doppler ultrasound (US) and MRI. Of these only spectral Doppler US can be used routinely and has high enough temporal resolution to characterize the waveform. In this work Doppler spectra were recorded in the aortas of 31 patients with AAA. From these a population average velocity waveform was calculated based on feature points and the variation in velocity parameters within the population was determined. Flow information is also of interest in cardiovascular haemodynamics studies. Womersley's solution for pulsatile flow in a rigid walled tube was used to calculate the flow wave in the normal section of the aorta, and a numerical study of the errors due to the differences in geometry from a straight tube was performed.

3.2 Methods

3.2.1 Patient Protocol

31 patients gave informed consent to participate in the study. The study was given ethical approval by Lothian NHS Ethics Committee. All patients were attending for a routine diagnostic scan of their AAA. The maximum diameter of the AAA was recorded and sizes of the aneurysms varied with a range of 3.6-6.4 cm (mean 5.0 cm). Each patient was supine for at least 15 minutes while their diagnostic scan was performed and then the Doppler US spectrum was recorded. Scanning was performed by Sarah Jane Carmichael and Margaret Glass at the Vascular Lab, Edinburgh Royal Infirmary. The Doppler spectrum was recorded for as long as possible but patient motion or breathing meant this was only a few cardiac cycles (mean 7, range 3 - 12). Although it was sometimes possible to ask patients to hold their breath, often they could not do that. Of the 31 patients in the study, 10 Doppler spectra had to be excluded. There were 18 males and 3 females remaining and the age was (mean $\pm$ s.d.) 75 ± 8 years. Waveforms were included in the analysis if they passed a quality assurance test which rejected waveforms of low quality. Waveforms were excluded if there was clutter breakthrough which obliterated the blood flow signal for a significant proportion of the recording, and if it was clear from the waveform outline that the data had been acquired with an angle greater than 70°.

3.2.2 Doppler Ultrasound

A Philips HDI 5000 (Philips Medical Systems, Bothell, USA) with a C5-2 (2.5 MHz) curvilinear probe was used to detect the blood velocities. The pulse repetition frequency (range 1.5 - 8.3 kHz) was chosen such that there was no velocity aliasing. To minimize the blood velocity distribution the sample volume (SV) length was kept to a minimum that still ensured adequate signal quality. The SV length, as displayed on the scanner console, was recorded (mean 2.9 mm, range 2-5 mm). The dimensions of the Doppler beam, at its focus and with clinical settings applied, were measured later (elevation plane: mean 3.6 mm, range 2.4 - 7.7 mm; scan plane: mean 2.1 mm, range 1.1 mm - 2.8 mm).

The SV was positioned in the aorta, distal to the renal arteries and proximal to the bulge of the aneurysm. By moving the volume across the diameter of the aorta, the position with the maximum systolic velocity was found, thus ensuring that the quantity measured included the peak velocity within that section of the aorta. In a straight, cylindrical tube the position of the peak systolic velocity would lie on the centreline of the tube. Although this is not necessarily the case in a real artery the quantity measured was called the centreline velocity, and assumed to be the centreline velocity for the purpose of calculating the flow wave. The limitations of this assumption are discussed later. Figure 3.1 shows an example of one of the spectra beneath the small B-mode image showing its position.

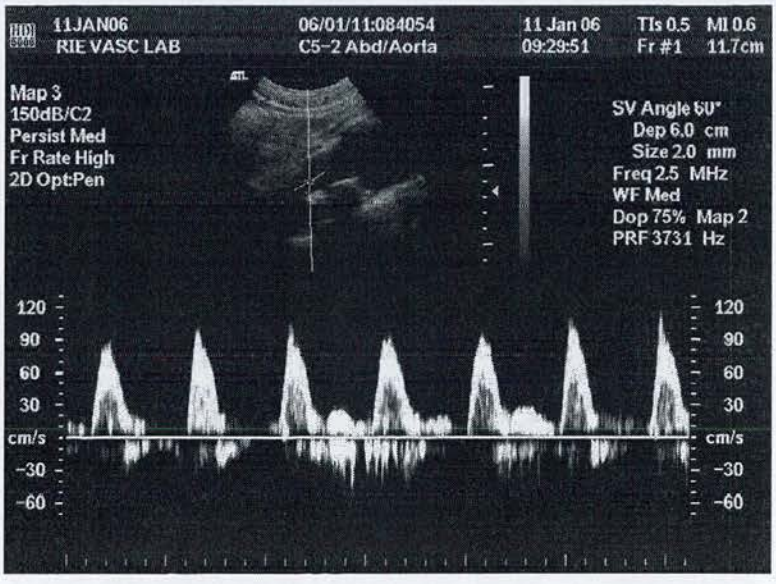

Figure 3.1: *Example of a Doppler Spectrum with B-mode image for positioning.*

The Doppler frequency spectrum, from the position in the abdominal aorta with the maximum velocity, was analysed using HDILab (Philips Medical Systems, Bothell, USA) to extract the peak frequency within the sample volume. The peak frequency was converted to peak velocity using the Doppler equation.

3.2.3 Geometric Spectral Broadening

Intrinsic spectral broadening results in a measured peak speed which is greater than the actual peak speed in the sample volume [186–188], so it was necessary to correct the patient data. The largest contribution to the intrinsic spectral broadening arises from geometric spectral broadening [189, 190]. A string phantom was used to investigate the degree of broadening by comparing the Doppler measured string speed with the known, actual, speed of the string. The ratio of measured to actual speed was found to vary as a function of the tangent of the Doppler angle, increasing from 1.13 at 25° to 1.54 at 70°. The correction was performed by dividing each patient's velocity wave by the correct ratio for the Doppler angle used to measure their spectrum.

3.2.4 Data analysis

The velocity waveforms were analysed using code developed in MATLAB 6.5 r.13 (MathWorks Inc., Natick, MA, USA). For each patient the velocity waveform was gated into individual cardiac cycles based on thresholding the velocity. The individual cycles were aligned using cross-correlation. The variability in the heart rate affects the resting phase (diastole) so it is the length of the 'tail' that changes. The mean heart beat for each patient was found. A value for the mean patient velocity, at each time point, was found by averaging the data from all the cardiac cycles at that time point. Since the cycles were different lengths the mean patient velocity wave used data from fewer cycles at the 'tail' end. The mean patient velocity wave was then trimmed to the length of the mean heart beat. The resulting, mean patient velocity wave was then called the V_{centre} wave.

Simply averaging the V_{centre} waveforms acts as a low pass filter and blurs the features. Eight individual patient V_{centre} waves, normalized by maximum velocity, are shown in figure 3.2 along with their mean. The low pass filtering effect is most apparent on the maximum velocity, the mean of which is reduced to 0.9, and the minimum velocity. To avoid this low-pass filter-

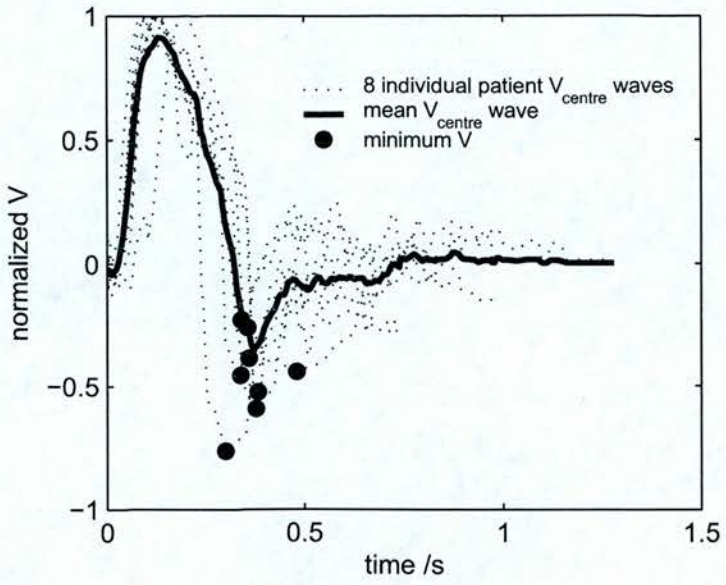

Figure 3.2: *Individual patient velocity (V_{centre}) waves from 8 patients normalized to their maximum peak velocity and the mean of these patient velocity waves. Spots show positions of minimum velocity. Note the low pass filtering effect on the positive and negative peaks which acts to reduce the size of these.*

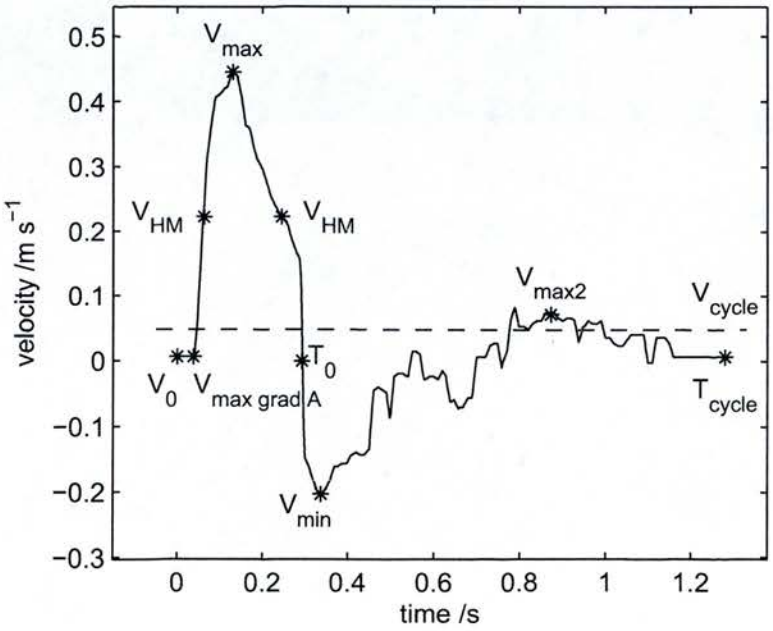

Figure 3.3: *Automatic location of the characteristic points on an example patient waveform.*

Parameter	Definition
V_0	Velocity at T = 0
$V_{\text{max grad A}}$	Velocity at time of maximum gradient of acceleration
$T_{\text{max grad A}}$	Time of maximum gradient of acceleration
V_{HM}	Velocity at half maximum
T_{HM}	Times of velocity at half maximum
V_{max}	Maximum velocity during systole
T_{max}	Time of maximum velocity during systole
T_0	Time of zero crossing
V_{min}	Minimum velocity
T_{min}	Time of minimum velocity
V_{max2}	Maximum velocity during diastole
T_{max2}	Time of maximum velocity during diastole
T_{cycle}	Length of cycle
V_{cycle}	Average velocity over the cycle length

Table 3.1: *Characteristic points found for each V_{centre} waveform.*

ing effect the method used to define the population average waveform was based on that of Holdsworth *et al.* [191]. Characteristic points were used to define the V_{centre} waveform for each patient. An automated routine was used to find the time and velocity at the characteristic points and these were then verified by graphical observation. A list of these characteristic parameters is given in table 3.1 along with an explanation of each one. Figure 3.3 shows an example of a V_{centre} waveform and the automatically determined characteristic points. The population mean and standard deviation for each parameter were calculated.

3.2.5 Normal Subjects

In addition to the 31 AAA patients the same measurement procedure was also performed on normal subjects without AAA. There were 9 older subjects (6 male, 3 female, age range 48 - 72) without AAA as well as 8 younger subjects (6 male, 2 female, age range 24 - 31). The older subjects were attending hospital for abdominal scans unrelated to their aorta and are called normal subjects here as they did not have AAA. Scanning was performed by Dr. Paul Allan. The younger subjects were volunteers who were assumed to be healthy as they had no diagnosed arterial disease. Scanning of the younger subjects was performed by Siobhan Meagher. In all the normal subjects the measurement site was just below the renal arteries.

3.2.6 Flow Wave

The volumetric flow waveform is of interest in haemodynamic studies of the arterial system. As an example of how the archetypal velocity wave can be used, the flow wave associated with the V_{centre} wave was calculated.

Holdsworth *et al.* [191] used Womersley's solution for the velocity profile [179] of an oscillating fully developed, laminar flow in a long, straight, cylindrical, rigid tube, along with the Fourier-decomposed centreline velocity waveform:

$$V_{\text{centre}}(t) = \sum_{k=0}^{\infty} \text{Re}\left[V_{\text{centre},k} e^{i(k\omega t - \phi_k)}\right] \tag{3.1}$$

and Fourier decomposed mean velocity waveform:

$$V_{\text{mean}}(t) = \sum_{k=0}^{\infty} \text{Re}\left[V_{\text{mean},k} e^{i(k\omega t - \psi_k)}\right] \tag{3.2}$$

to calculate the relationship between the Fourier coefficients for the centreline velocity V_{centre} and the mean velocity V_{mean}. From [191], Womersley's solution for the velocity profile, as a function of the mean velocity:

$$v(y,t) = \text{Re}\left\{V_{\text{mean},k}\left(\frac{J_0(\tau_k) - J_0(\tau_k y)}{J_0(\tau_k) - 2J_1(\tau_k)/\tau_k}\right) \text{e}^{\text{i}(k\omega t - \psi_k)}\right\} \tag{3.3}$$

where J_0 and J_1 are the zeroth and first order Bessel functions of the first kind, $\text{Re}\{\cdot\}$ denotes the real part, y is the radial position normalized to the vessel radius, R, and $\tau_k = \alpha_k \text{i}^{3/2}$, where α_k is the Womersley number of the kth harmonic, $\alpha = R\sqrt{\frac{k\omega}{\nu}}$ and ν is the kinematic viscosity of blood.

Holdsworth *et al.* [191] then considered this equation at the centre of the tube, when $y = 0$:

$$v(0,t) = \text{Re}\left\{V_{\text{mean},k}\left(\frac{J_0(\tau_k) - 1}{J_0(\tau_k) - 2J_1(\tau_k)/\tau_k}\right) \text{e}^{\text{i}(k\omega t - \psi_k)}\right\} \tag{3.4}$$

Then recognizing that $v(0,t)$ is simply the kth term of V_{centre} they equated the real parts to get an equation for the relationship between the Fourier coefficients of $V_{\text{centre}}(t)$ and $V_{\text{mean}}(t)$:

$$V_{\text{mean},k} \text{e}^{-\text{i}\psi_k} = V_{\text{centre},k} \text{e}^{-\text{i}\phi_k}\left(\frac{J_0(\tau_k) - 2J_1(\tau_k)/\tau_k}{J_0(\tau_k) - 1}\right) \tag{3.5}$$

The Womersley solution for velocity depends on both spatial and temporal position. At the time of peak systolic flow the position of the maximum velocity is located on the centreline of the tube. So, by finding the radial position in the tube with the highest velocity, in both space and time, the centreline has been located. Then, by measuring the velocity in this position the centreline velocity has been recorded and the above equation can be used to calculate the mean velocity from it.

In order to calculate the flow rate from the centreline velocity the diameter of the artery is required as well as an assumption of the velocity profile across the artery. The diameter of the abdominal aorta in AAA patients was found by measuring the aorta on 3D reconstructions of contrast enhanced computed tomography (CT) scans of a group of 8 AAA patients. CT scans were used for measuring the diameter, rather than B-mode US on the same patients as the spectral measurements, as the lumen is much more clearly defined. The mean of these measures was used as a typical abdominal aortic diameter in AAA patients.

The flow wave was then calculated as the product of the mean velocity and cross sectional area, based on the mean abdominal aortic diameter and assuming a circular lumen. This resulted in a flow wave which gave velocity profiles with V_{centre} on the axis. The limitations of the assumption of fully developed (Womersley) flow are discussed later.

3.2.7 Error in Womersley Prediction Due to Geometry

The flow wave, in the section of the aorta distal to the renal branches and proximal to the aneurysm, was calculated by assuming fully developed flow in a long, straight, rigid tube with circular cross section. In this case the velocity profile across the artery is given by Womersley's solution [179] and the mean velocity in the cross section was calculated from the archetypal centreline velocity. In reality, however, at the measurement site the aorta is curved and about to open out into an aneurysm, the flow is not fully developed, the walls are flexible and the flow is likely to be turbulent [192].

The effects of three geometric deviations from a long, straight tube, on the relationship between V_{centre} and mean velocity, were examined using CFD. Flow was calculated in three tubes: a straight tube, a curved tube (radius of curvature = 50 cm) and a tube with a bulge (radius = 4.2 cm). The tubes were all circular in cross section and had an inlet radius of 1.4 cm. The inlet boundary condition for the straight tube was a flat velocity profile, to mimic the velocity profile

from the heart, while the bulged and curved tubes had fully developed profiles. All gave the archetypal flow rate found in this study. Models of three different types of tube were created in Gambit v. 2.2.30 (Fluent Inc., Lebanon, New Hampshire, USA), as described below, and Fluent v. 6.2.16 (Fluent Inc., Lebanon, New Hampshire, USA) was used to solve the Navier Stokes equations.

3.2.7.1 Straight Tube

The geometry for the straight tube is shown in figure 3.4. The tube length was 30 cm which was chosen to be of the same order of magnitude as the aorta. The calculation was performed in 2D since the geometry has cylindrical symmetry about the x axis. After a mesh independence study (with meshes of 1800, 6200 and 24000) the model contained 24000 quadrilateral elements. In a straight tube the maximum temporal velocity occurs on the centreline. So the velocity at 4 points on the centreline was calculated along with the mean velocity across the tube. The mean velocity, assuming a Womersley profile, was then calculated from the peak velocity and this was compared with the CFD result for the mean velocity.

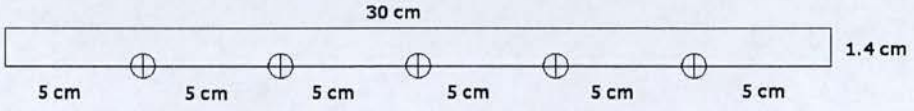

Figure 3.4: *Straight tube geometry*

3.2.7.2 Curved Tube

A curved tube model was created (figure 3.5) with radius of curvature of 50 cm. The calculations were performed in 3D and the symmetry plane was used to model just half the flow domain. After a mesh independence study (with meshes of 12075 and 84150 elements) the curved tube had 84150 hexahedral elements.

In a curved tube the peak velocity occurs off the centreline, some way towards the outer wall of the bend. The spatial position of the peak was found by projecting the velocity vectors on specific planes onto the normals of those planes and then finding the largest. This analysis was carried out in Matlab v. 6.5 r.13 (The Mathworks Inc., Natick, MA). The velocity, in the direction normal to the analysis planes, at these points was calculated throughout the cycle. The

mean axial velocity on each of the planes was also calculated. This 'peak' velocity waveform was then used to calculate a 'mean' velocity waveform assuming a Womersley profile, and this was compared with the CFD result for the mean velocity.

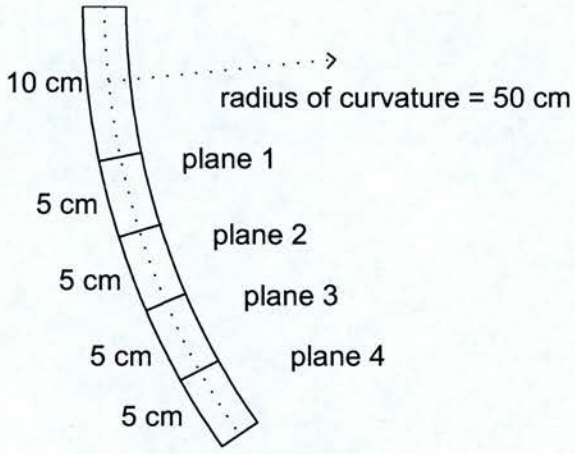

Figure 3.5: *Geometry of curved tube*

3.2.7.3 Aneurysm

An aneurysm was made from a parabola-exponential shaped bulge in a straight tube and was modelled in 2D. The geometry is shown in figure 3.6 and more details of the geometry are given in Chapter 5. After a mesh independence study (with meshes of 7894, 28455 and 105565) the model contained 105565 quadrilateral elements. The aneurysm had a diameter of 8.4 cm and there was a 20 cm straight tube before the bulge. The region of interest is that proximal to the aneurysm. The peak velocity lies on the centreline, so the centreline velocity and mean velocity across the tube was calculated at points along the straight section before the aneurysm.

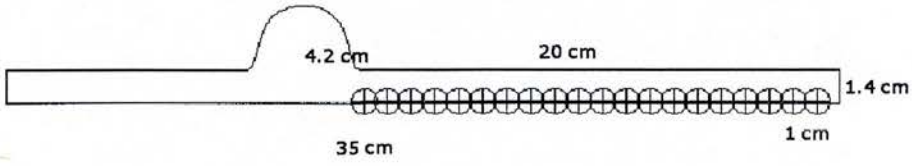

Figure 3.6: *Geometry of tube with a bulge*

3.3 Results

3.3.1 AAA patient Velocity Wave

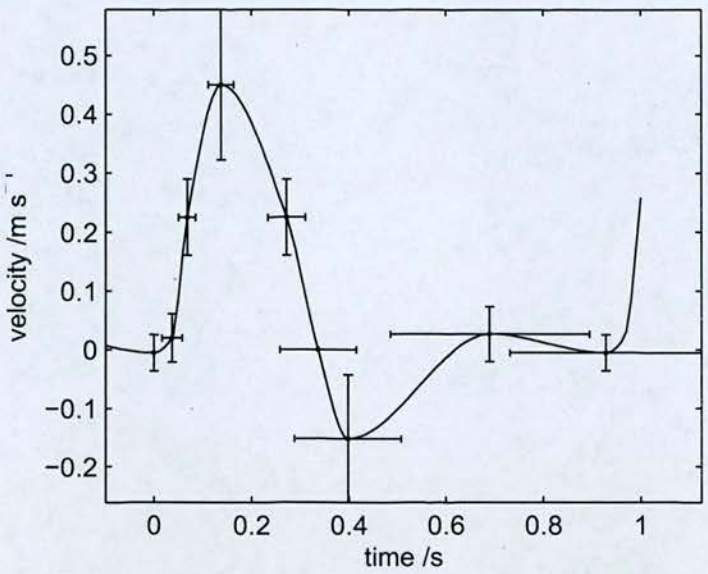

Figure 3.7: *The population averaged V_{centre} waveform showing characteristic points with error bars showing the inter subject standard deviation in the parameters.*

The population averaged V_{centre} waveform is shown in figure 3.7 with the characteristic points and their standard deviations. Detailed information about the characteristic points is given in table 3.2. The velocity wave is typical of that from the abdominal aorta in that it is triphasic; a large systolic maximum ($V = 45$ cm s^{-1}) is followed by a negative peak ($V = -15$ cm s^{-1}) and a second, much smaller, maximum ($V = 2.7$ cm s^{-1}) during diastole. The shape of the abdominal aortic velocity, or flow, wave can be explained as a distortion of the ascending aortic flow wave. As explained by Nichols and O'Rourke [32], the ascending aortic flow wave is driven by the pressure gradient between the left ventricle and the aortic root: as the ventricles contract there is a rapid rise in pressure until the aortic valve opens releasing a rapidly accelerating jet of blood. As the ventricular pressure then decreases the blood decelerates until the aortic valve closes. The result is a flow wave consisting of a large forward pulse followed by a small amount of negative flow as the aortic valve closes. As the flow wave travels down the aorta the flow oscillation diminishes due to both damped resonant reflection from the peripheral vessels and damped propagation. Backflow is more apparent in the abdominal section of the aorta below the renal arteries since flow in these branches is always forward.

parameter	units	mean	std	min	max
V_0	cm s^{-1}	-0.54	3.09	-5.74	7.05
$V_{\text{max grad A}}$	cm s^{-1}	2.01	4.08	-2.90	16.52
$T_{\text{max grad A}}$	s	0.04	0.02	0.01	0.11
V_{HM}	cm s^{-1}	22.52	6.40	10.52	35.59
T_{HM}	s	0.27	0.07	0.04	0.02
T_{HM}	s	0.19	0.04	0.34	0.13
V_{max}	cm s^{-1}	45.04	12.80	21.04	71.19
T_{max}	s	0.14	0.03	0.09	0.21
T_0	s	0.34	0.08	0.24	0.61
V_{min}	cm s^{-1}	-15.20	10.94	-37.26	3.72
T_{min}	s	0.40	0.11	0.28	0.76
V_{max2}	cm s^{-1}	2.67	4.69	-4.73	14.23
T_{max2}	s	0.69	0.20	0.36	1.10
T_{cycle}	s	0.93	0.20	0.57	1.28
V_{cycle}	cm s^{-1}	7.42	6.44	-0.59	22.36

Table 3.2: *Characteristic point parameters for AAA patients*

There was no correlation between any of the characteristic point parameters and the diameter of the aneurysm.

3.3.2 Normal Subject Velocity Waves

3.3.2.1 Older Normals

The older subject averaged waveform with characteristic points and their standard deviations is shown in figure 3.8. The characteristic point parameters are given in table 3.3. The older subject waveform oscillates more than the AAA patient waveform with a peak velocity of 57 cm s^{-1}, a minimum velocity of -19 cm s^{-1} and a second maximum of 8 cm s^{-1}.

For fair comparison between healthy normals and AAA patients it was necessary to use only the age matched members of the groups. V_{centre} waves for 6 of the older normal subjects (age (mean $\pm$ s.d.) $= 64 \pm 6$ years) and 6 age matched AAA patients (66 ± 4 years) were compared. No significant differences in any of the characteristic point parameters were found between the two groups. However, the group sizes used were very small and further investigation with larger groups would be required to confirm this.

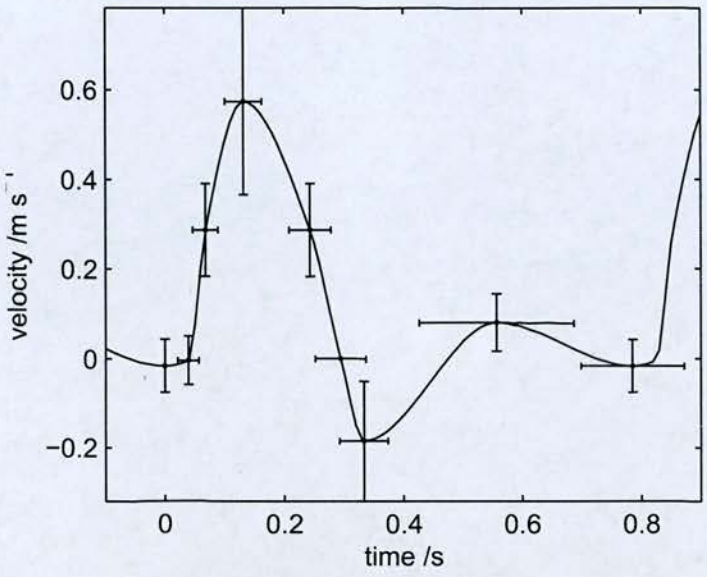

Figure 3.8: *The averaged V_{centre} waveform for older normal subjects showing characteristic points with error bars showing the inter subject standard deviation in the parameters.*

parameter	units	mean	std	min	max
V_0	cm s^{-1}	-1.58	5.99	-13.93	5.87
$V_{\text{max grad A}}$	cm s^{-1}	-0.36	5.42	-10.86	5.51
$T_{\text{max grad A}}$	s	0.04	0.02	0.02	0.07
V_{HM}	cm s^{-1}	28.70	10.38	11.40	49.52
T_{HM}	s	0.24	0.07	0.04	0.02
T_{HM}	s	0.16	0.04	0.28	0.10
V_{max}	cm s^{-1}	57.40	20.75	22.80	99.03
T_{max}	s	0.13	0.03	0.07	0.19
T_0	s	0.29	0.04	0.22	0.36
V_{min}	cm s^{-1}	-18.50	13.49	-45.45	2.35
T_{min}	s	0.33	0.04	0.26	0.41
V_{max2}	cm s^{-1}	8.04	6.42	-2.54	15.27
T_{max2}	s	0.56	0.13	0.40	0.81
T_{cycle}	s	0.79	0.09	0.72	1.00
V_{cycle}	cm s^{-1}	10.90	2.76	6.88	15.44

Table 3.3: *Characteristic point parameters for older normal subjects*

3.3.2.2 Younger Normals

The volunteer averaged waveform with characteristic points and their standard deviations is shown in figure 3.8. The characteristic point parameters are given in table 3.4. The volunteer waveform oscillates more than both the AAA patient waveform and the older normal subject waveform with a peak velocity of 68 cm s^{-1}, a minimum velocity of -20 cm s^{-1} and a second maximum of 18 cm s^{-1}.

T-tests on the characteristic points of the older and younger normal subject velocity waves showed a significant difference in the second (diastolic) maximum velocity ($P < 0.013$). The increase in the size of this second peak in the younger subjects volunteers, as compared with the older subjects, can be explained as a consequence of the higher pulse wave velocity (PWV) in older people [193]. The higher PWV is due to arterial stiffening which is a general symptom of old age regardless of specific localized atherosclerosis. The higher PWV means that the pulse wave from the aortic root is reflected sooner. As a result, the second peak occurs earlier altering the waveform [32].

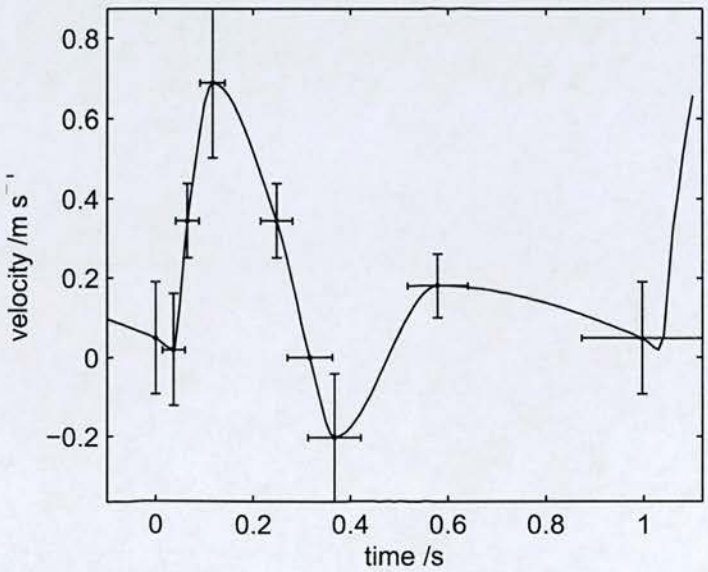

Figure 3.9: *The averaged V_{centre} waveform for younger normal subjects showing characteristic points with error bars showing the inter subject standard deviation in the parameters.*

parameter	units	mean	std	min	max
V_0	cm s^{-1}	4.93	14.21	-21.92	25.06
$V_{max\ grad\ A}$	cm s^{-1}	1.94	14.22	-26.47	15.92
$T_{max\ grad\ A}$	s	0.04	0.02	0.00	0.06
V_{HM}	cm s^{-1}	34.42	9.32	19.07	49.71
T_{HM}	s	0.25	0.07	0.03	0.02
T_{HM}	s	0.19	0.03	0.29	0.09
V_{max}	cm s^{-1}	68.84	18.63	38.14	99.42
T_{max}	s	0.12	0.03	0.07	0.14
T_0	s	0.32	0.05	0.24	0.37
V_{min}	cm s^{-1}	-20.33	16.19	-51.94	-2.11
T_{min}	s	0.37	0.05	0.31	0.47
V_{max2}	cm s^{-1}	17.98	7.97	4.27	27.99
T_{max2}	s	0.58	0.06	0.48	0.65
T_{cycle}	s	1.00	0.12	0.83	1.13
V_{cycle}	cm s^{-1}	15.34	10.51	-1.99	29.56

Table 3.4: *Characteristic point parameters for younger normal subjects*

3.3.3 AAA Patient Flow Wave

The mean aortic diameter in 8 AAA patients was 2.22 ± 0.29 cm. To obtain an archetypal flow waveform for AAA patients this diameter was used with the centreline velocity waveform to calculate the flow rate assuming a Womersley profile. This is shown in figure 3.10. The mean flow throughout the cardiac cycle was calculated as 13.3 ml s^{-1}.

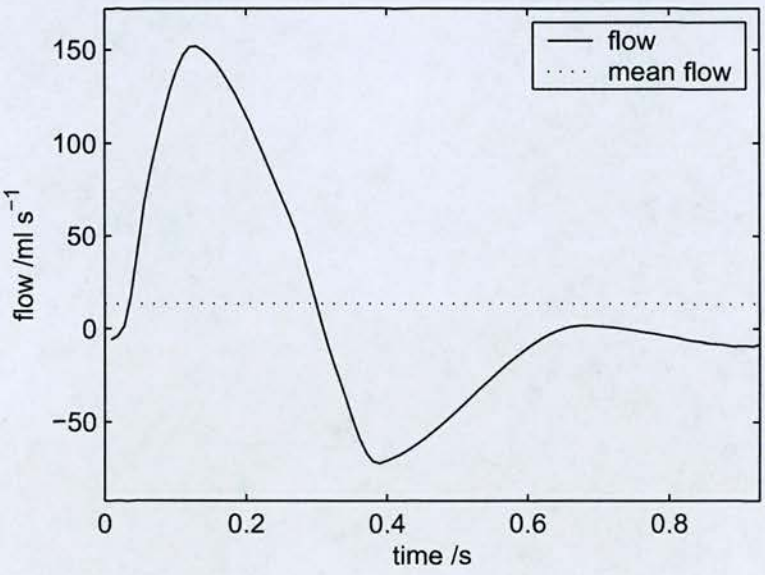

Figure 3.10: *The flow wave for AAA patients and mean flow throughout the cardiac cycle.*

3.3.4 Error in Womersley Prediction of Flow Rate Due to Geometry

Womersley's solution is only valid for fully developed flow in straight rigid tubes. To estimate the error involved in applying the solution when the geometry deviates from a long straight tube mean velocities in three different tubes were compared with the Womersley prediction.

3.3.4.1 Straight Tube

The mesh convergence study [194] (Chapter 5 contains more details of mesh convergence) gave an average value of 1.0 for the order of convergence showing that the calculation is, on average accurate to first order. The ordered error estimate was 2.5 % and the GCI (grid convergence index) was 7.5 %. The calculations used in the mesh study were in the asymptotic range since $GCI_{23}/r^p GCI_{12} = 0.95$.

Centreline and mean velocity waves for points at 5, 10, 15 and 20 cm from the inlet are shown in figure 3.11. The mean velocity, as calculated from the centreline velocity by assuming Womersley flow, is also shown and the absolute error is plotted on a different axis. The largest errors occur during the deceleration phase. The mean error throughout the cardiac cycle decreased with distance in to the tube from 1.9 cm s^{-1} at 5 cm to 1.1 cm s^{-1} at 20 cm and was similar at 25 cm. If the tube was longer the error would eventually reach 0 cm s^{-1} but the aim of this experiment was to determine the approximate errors in a tube the length of the aorta. At the level of the abdominal section, say 15 cm from the heart, the maximum error is 3.0 cm s^{-1} and mean error is 1.3 cm s^{-1}.

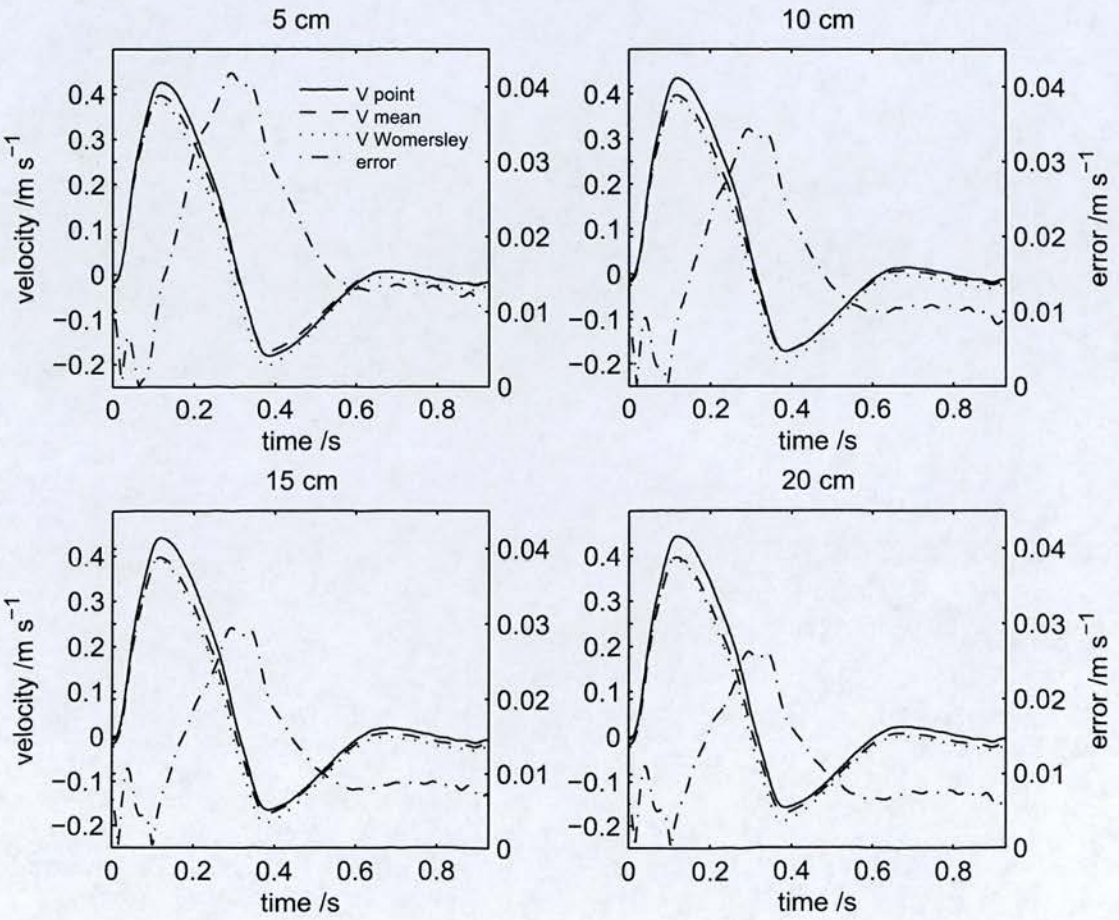

Figure 3.11: *Straight tube: Comparison of the mean velocity (V_{mean}) and the estimated mean velocity ($V_{Womersley}$) with the error (absolute difference between V_{mean} and $V_{Womersley}$) shown on the right hand axis.*

3.3.4.2 Curved Tube

The calculations were performed using second order equations so they were assumed to be accurate to second order. This gave an ordered error estimate of 4.9 % and a GCI of 15 %.

Velocity waveforms and the error in the estimated mean velocity for the curved tube are shown in figure 3.12. The largest errors occur at the times of peak speed. The mean error throughout the cardiac cycle does not decrease with distance along the tube. The maximum error was 5.1 cm s^{-1} and mean 1.7 cm s^{-1} at 20 cm.

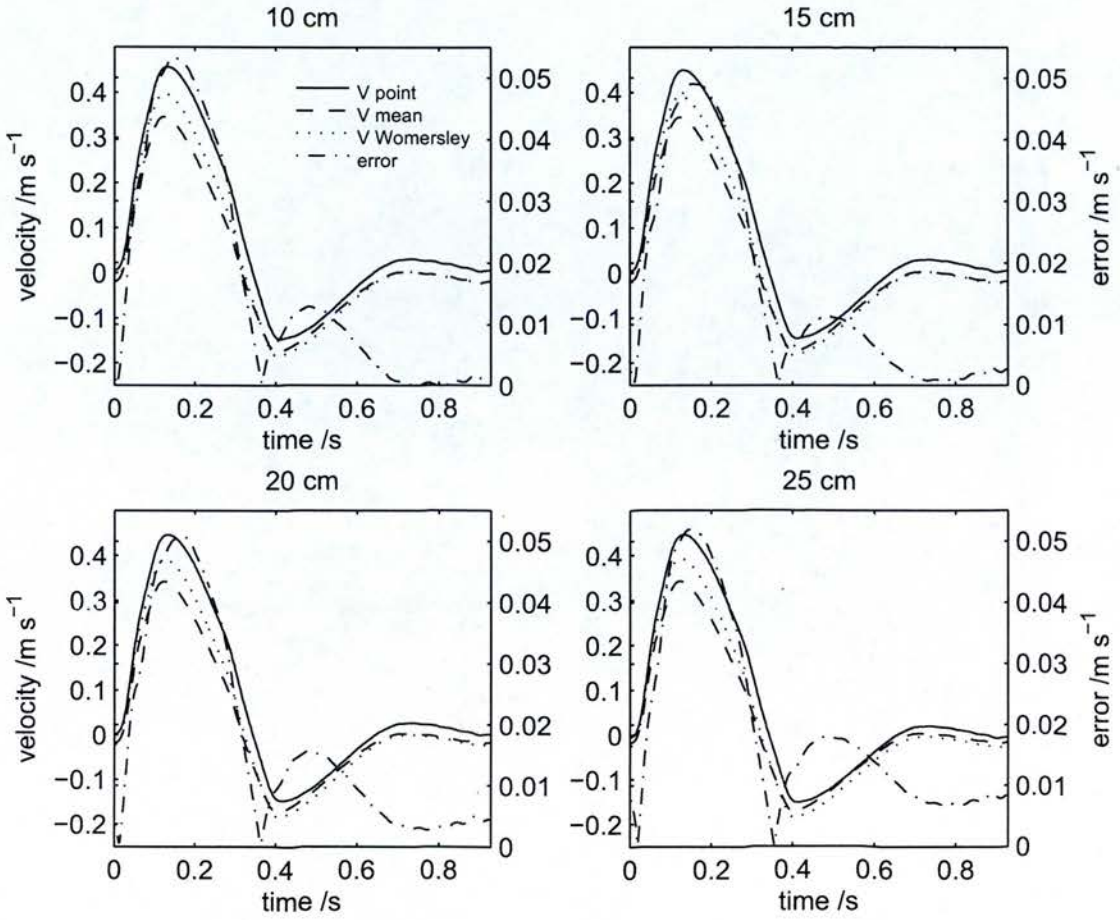

Figure 3.12: *Curved tube: Comparison of the mean velocity (V_{mean}) and the estimated mean velocity ($V_{Womersley}$) with the error (absolute difference between V_{mean} and $V_{Womersley}$) shown on the right hand axis.*

3.3.4.3 Aneurysm

The mesh convergence study gave an average value of 6.2 for the order of convergence showing that the calculation is accurate to at least second order. The ordered error estimate was 1.5 % and the GCI (grid convergence index) was 4.3 %. The calculations used in the mesh study were in the asymptotic range since $GCI_{23}/r^p GCI_{12} = 1.06$.

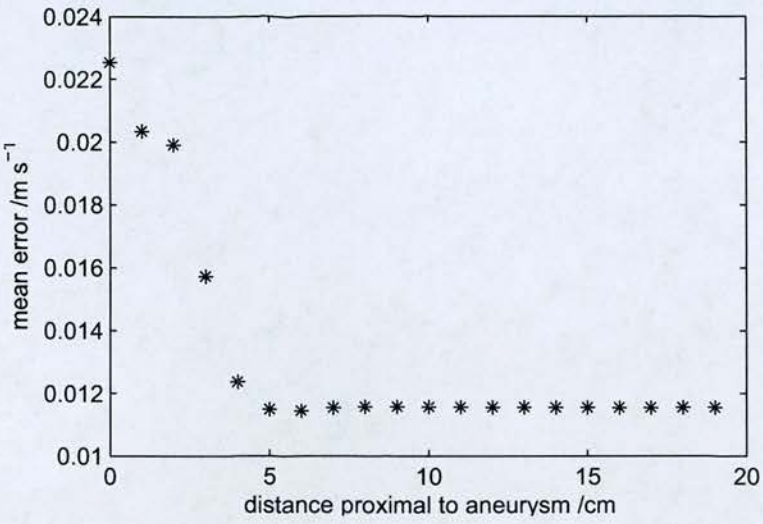

Figure 3.13: *Variation in mean error (absolute difference between V_{mean} and $V_{\text{Womersley}}$) with distance proximal to aneurysm.*

The variation in mean error with distance from the aneurysm is shown in figure 3.13. Velocity waveforms and the error in the estimated mean velocity for the bulged tube are shown in figure 3.14. Plots are shown for positions from just before the aneurysm up to 8 cm proximal to the aneurysm. Errors decrease rapidly with distance from the aneurysm: at 0 cm the maximum error is 5.9 cm s^{-1} and mean is 2.3 cm s^{-1} while at 4 cm the maximum is 2.5 cm s^{-1} and mean is 1.2 cm s^{-1}.

3.4 Discussion

In this study the centreline velocity (V_{centre}) waveform has been measured rather than the mean velocity waveform or the flow rate. The choice of V_{centre} was made as it is known that velocity within a given blood vessel is similar across the population, with haemodynamic scaling laws predicting that the blood velocity in a vessel is independent of body weight [195]. This scaling

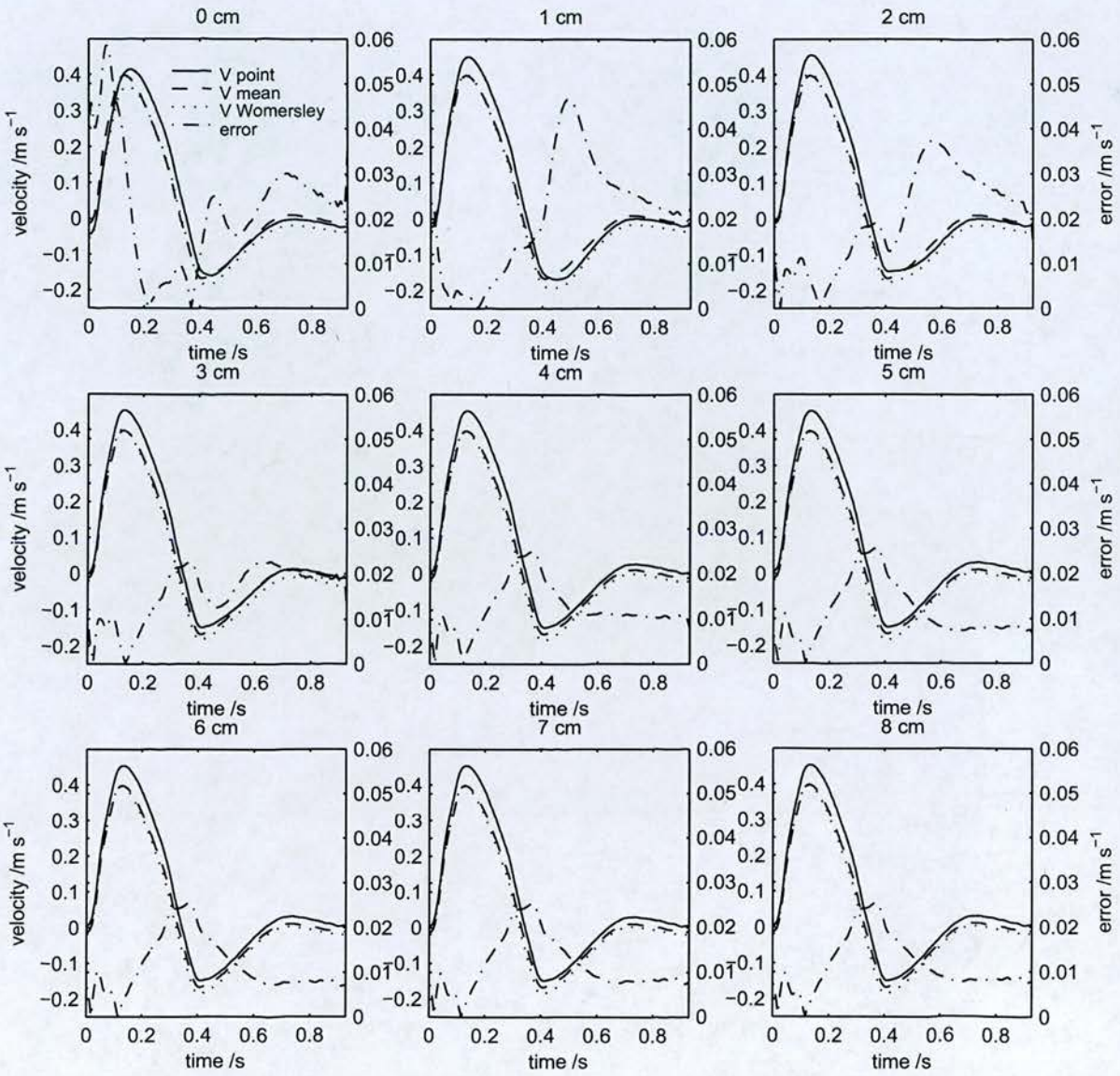

Figure 3.14: *Bulged tube: Comparison of the mean velocity (V_{mean}) and the estimated mean velocity ($V_{Womersley}$) with the error (absolute difference between V_{mean} and $V_{Womersley}$) shown on the right hand axis.*

law actually underpins much of Doppler clinical practice where diagnostic criteria are based on velocity and not volume flow.

The archetypal V_{centre} velocity wave for AAA patients was not found to be significantly different to that of age matched normal subjects which suggests that the presence of the aneurysm does not significantly alter the velocity wave. This is perhaps unexpected. The main reason for differences in velocity waves is the pulse wave velocity (PWV) of the arteries [32]. The PWV is determined by the arterial stiffness and AAA tissue has been shown to be stiffer than age matched abdominal aortic tissue [149] which may be expected to produce a different velocity wave in AAA patients compared to normal subjects. It may be possible to attribute the similarity between the velocity waves to the localization of the aneurysmal disease. The velocity wave is determined by pulse wave propagation, and reflections, from the whole arterial tree and not just a single artery. However, the group sizes used were very small and more studies would need to be performed to clarify this.

The older and younger normal subject velocity waves were found to have significantly different diastolic maxima which can be attributed to the increase in PWV in older subjects [32]. This suggests that *in vitro* and *in silico* modelling of blood flow in AAAs should be performed using an inlet velocity, or flow, boundary condition obtained from an older subject, if not an AAA patient.

The velocity wave found here may be used to calculate the input velocity profile for numerical studies of AAA haemodynamics in non specific geometries, or the flow wave may be used as input to similar *in vitro* studies. Patient specific computational fluid dynamics (CFD) studies require 3D vascular geometry entry and exit boundary condition data. While the 3D data is readily available as aneurysm patients routinely undergo CT, velocity data are not so routinely available. In these cases, where patient specific velocity data are not available, the population averaged V_{centre} waveform from this study could be used to provide the appropriate input boundary condition.

3.4.1 Characteristic Feature Point Method

The task of finding a typical velocity wave, from the aorta of patients with AAA, could have been approached by averaging appropriately scaled individual velocity waves. However, phase shifts between the individual waves would then act as a low pass filter to blur the features.

The effect is most obvious in regions of rapid change, such as at the maximum and minimum velocities, as shown earlier (in figure 3.2). The method used instead was to define recognizable points on the individual waves and use the means of these to create a representative wave.

The disadvantage of the feature point method is that the characteristic points might not be able to define the velocity wave well in all areas, especially if the wave has a non standard shape. To assess how well the characteristic points defined the individual patient waves, the error in the synthesized wave was calculated as the absolute difference between the velocity wave and the wave synthesized from the characteristic points. The mean error in all the patients was 2.6 ± 0.9 cm s^{-1} (range $1.1 - 4.4$ cm s^{-1}).

3.4.2 The Waveforms

The quality of abdominal US is lower than that of peripheral vascular US. Since attenuation increases with frequency, the extra distance travelled by the US beam requires a lower frequency. This reduces spatial resolution as well as reducing the Doppler frequency, leading to inferior image quality and Doppler trace. The scattering of US by blood is proportional to the fourth power of frequency [196] so the lower frequency beam gives a smaller back scattered signal power. Use of a curvilinear probe means it is not possible to take advantage of beam steering [197] which is used to improve the Doppler angle in peripheral vessels. In addition, the quality of the patient spectra may be reduced by turbulence, which broadens the Doppler spectrum, and breathing artefacts which occur if the sample volume moves. In this study only spectra which passed a quality assurance test, as described in the methods section, were used to create the archetypal waveform.

Table 3.5 shows a list of velocity and flow measurements from other studies in the literature which can be compared with the velocity and flow waves found here. V_{max} found by Vieli *et al.* [95] using Doppler US was 18 cm s^{-1} higher than for the young normal subjects in this study ($P = 0.029$) and V_{min} was 12 cm s^{-1} lower than in this study ($P = 0.076$). Vieli *et al.* [95] did not correct for geometric spectral broadening, which reduced V_{max} by $28 \pm 5\%$ in this study. V_{max} and V_{min} in the AAA patients and older normal suubjects in this study were both significantly different to the healthy subjects in the study by Vieli *et al.* [95] although V_{max} was in the range given by Stein *et al.* [198].

The calculated maximum flow, Q_{max}, for AAA patients is 20 % higher than the maximum flow

method	mean	std	units	N	age	reference
V_{max}						
Hot-film catheter	19-52		cm s^{-1}	7		Stein *et al.* [198]
Doppler US	87	13	cm s^{-1}	10	24-32	Vieli *et al.* [95]
MRI	77	18	cm s^{-1}	10	24-32	Vieli *et al.* [95]
V_{min}						
Doppler US	-32	9.9	cm s^{-1}	10	24-32	Vieli *et al.* [95]
MRI	-33	8.1	cm s^{-1}	10	24-32	Vieli *et al.* [95]
Q_{max}						
MRI	120		ml s^{-1}	1	35	Long *et al.* [147]
MRI	118	8	ml s^{-1}	4	21-31	Wedding *et al.* [106]
Q_{min}						
MRI	-30		ml s^{-1}	1	35	Long *et al.* [147]
MRI	-23	13	ml s^{-1}	4	21-31	Wedding *et al.* [106]
Q_{cycle}						
MRI	15	7	ml s^{-1}	11	20-28	Taylor *et al.* [99]
MRI	15	5	ml s^{-1}	8	50-70	Cheng *et al.* [100]

Table 3.5: *Velocity and flow data from the literature*

in the studies on healthy subjects obtained from the literature. The mean flow, Q_{cycle}, is 10% smaller than the mean flows given and within the standard deviations. The larger Q_{max} with a slightly smaller Q_{cycle} is probably attributable to the much higher temporal resolution of US (100 Hz) compared with MRI (about 16 Hz) which allows the peak to be fully resolved.

The diameter used to calculate the flow rate, 2.22 ± 0.29 cm, was an average of 8 patients and is in line with that of [199], who measured aortic diameter proximal to AAA in 39 patients, and found it was 2.67 ± 0.61 cm.

3.4.3 Womersley assumption

The flow wave, in the section of the aorta distal to the renal branches and proximal to the aneurysm, was calculated by assuming Womersley's solution [179] for the velocity profile. In reality, however, the aorta is not a straight tube with fully developed flow, and in addition the walls are flexible and the flow is likely to be turbulent [192]. Velocity profiles in the normal aorta have been measured by Vieli *et al.* [95], for example, who found the velocity profiles were skewed, particularly during reverse flow, which is probably due to the curvature of the aorta.

The effects of three geometric deviations from a long, straight tube, on the relationship between V_{centre} and mean velocity, were examined using CFD. The velocity, at the spatial position containing the peak systolic velocity (called the 'centreline' velocity (V_{centre}) although it was not necessarily found on the centreline), and the mean velocity over the cross section were calculated. The mean velocity was also calculated from V_{centre}, by assuming a Womersley velocity profile, and this was compared with the actual mean velocity. The errors at peak systole were: straight tube, at 15 cm from the inlet, 1.0 cm s^{-1}, curved tube, 4.2 cm s^{-1}, bulged tube, 2 cm upstream of the bulge, 1.0 cm s^{-1}. Adding these errors in quadrature gave an absolute error of 4.4 cm s^{-1} which is 14% of the mean velocity at peak systole and amounts to a 21 ml s^{-1} error in the peak systolic flow rate.

In addition to this estimate of the error in the calculated flow rate due to tube curvature and bulge, there will be an error due to the turbulence. However, in a large artery such as the aorta, the resistive component is small compared to the inertial component. Hence laminar profiles are plug-like and turbulent deviations should only make a small difference to that predicted by the laminar theory [32].

There will also be errors due to the flexible walls and helical flow from the heart and aortic arch [200]. Helical flow results in symmetry breaks which may be important and should be investigated in future work. It is accepted that all these deviations from the conditions required for Womersley flow are a limitation of this method for estimating the volumetric flow waveform, and that *in vivo* the true flow waveform may be modified by these effects.

3.5 Conclusions

Velocity waves were measured in AAA patients just proximal to the neck of the aneurysm at the position with the highest peak systolic velocity. Characteristic feature points from 21 of these waves were used to create an archetypal velocity wave and measure interpatient variability. The waveform was triphasic with a maximum velocity of 45 ± 13 cm s^{-1}, a minimum of -15 ± 11 cm s^{-1} and a second maximum of 2.7 ± 4.7 cm s^{-1}.

The diastolic maximum velocity was significantly different in younger subjects compared to that in older subjects. Simulations of blood flow in abdominal aortic aneurysms should use inlet flow conditions based on measurements made in either AAA patients, or subjects of the same age as AAA patients.

The velocity, V_{centre}, wave was used to calculate a typical flow wave for the abdominal section of the aorta in AAA patients. The diameter was taken as the mean diameter of the aortas of 8 AAA patients and was 2.22 cm. The flow was assumed to be fully developed flow in a straight tube. A numerical study of the errors in this assumption due to geometrical differences of the aorta from a straight tube gave an error estimate of 14 % at peak systolic flow.

The velocity wave and characteristic point parameters found here can be used in CFD or *in vitro* AAA flow studies to investigate the effects of variation amongst the population on flow parameters such as vortices, wall shear stress and oscillatory shear index.

Chapter 4
Comparison of Computational Fluid Dynamics with Magnetic Resonance Measurements

Flow in abdominal aortic aneurysms influences disease progression in a number of ways, for example via: platelet activation, flow stagnation and platelet deposition leading to thrombosis; macrophage concentration gradients; and shear stresses and shear stress gradients on the endothelium. Detailed predictions of AAA haemodynamics can be made using computational fluid dynamics, as in Chapter 2, and these may help to elucidate the connections between the blood flow and pathology. However, the flow fields in physiologically correct aneurysms appear to be very complicated, with temporally varying vortices, and recirculation, as well as helical flow. There is a need for validation of results in all *in silico* studies of arterial blood flow, but with such complicated flow fields, aneurysms have, perhaps, one of the greatest needs. In this chapter the numerical flow will be validated by comparison with measurements made by magnetic resonance imaging.

4.1 Introduction

Before numerical results can be trusted to advise clinicians, or even in collaboration with biological data for determining biomechanical relationships, it is vital that confidence in their accuracy is gained, and their error margins are obtained. Errors in numerical simulations of blood flow *in vivo* arise from a whole range of sources, from numerical errors in the computational fluid dynamics (CFD) code, to uncertainty in the boundary conditions obtained by measurements made *in vivo*.

Excluding coding errors, or 'bugs' in the software, and incorrect use of the code by the user, errors in CFD arise for numerical reasons [133]. Roundoff errors result from the use of a finite number of significant digits to represent a real number. They are limited by performing calculations such that subtraction of nearly equal numbers, and addition of numbers with a large

difference in magnitude, are avoided. Iterative convergence errors arise from truncation of iterative sequences and are controlled by specifying tolerances on the residuals. Discretization errors are produced by approximating spatial and temporal derivatives in the governing equations. They are restricted by careful mesh design and analysed by mesh convergence studies.

Uncertainties in CFD models are associated with discrepancies between the real flow and the CFD model, either in the input data or in the physical models used [133]. Discrepancies in the input data are: uncertainty in the geometry of the domain because it is not possible to make an exact model and because the mesh is a discrete representation; uncertainty in the boundary conditions because it is not possible to measure them accurately; and uncertainty in the fluid properties, such as density and viscosity, which may arise from their dependence on the flow conditions or on uncertainty in measuring them. The application of physical submodels, such as turbulence, leads to uncertainty because these models have been developed for a limited range of flows: in using them to model other flows the data they are based on must be extrapolated [133].

Verification is the process of determining that a model implementation accurately represents the developer's conceptual description of the model and quantifies the error [133]. The commercial code Fluent has been verified [201] and here it is assumed that numerical errors, with the exception of discretization error which will be investigated, are small compared to uncertainties produced by differences between the model and the real flow.

Validation is the process of determining the degree to which a model is an accurate representation of the real world and quantifies the uncertainty [133]. A simulation is considered to be validated if the differences between its results and experimental data are small and if uncertainties in the experimental results are small [133]. CFD models can be validated against *in vitro* models and against the *in vivo* situation and there are advantages and disadvantages of both.

Validation against *in vitro* results requires a phantom of the correct artery. This may either be anatomically correct (for example [202]) or simplified to illuminate the general characteristics of the flow (for example [202, 203]). The input uncertainties in *in vitro* models are relatively small. The models can be constructed precisely from mathematical descriptions of the geometry [204], or imaged precisely, for example using high resolution photography [205] or high resolution x-ray computed tomography (CT) [206] which limits the uncertainty in the domain geometry. The inlet velocity profile can be made to be fully developed by adding an inlet length

to the upstream end of the model or, if the profile is more complicated it can be measured accurately with optical methods, or if less precise *in vivo* methods are used for measuring the velocities, the inlet profile can be scaled by the flow rate measured using a flow meter which significantly improves the results [145]. *In vitro* validation permits the use of precise optical measurement techniques such as particle image velocimetry (PIV) [113] or laser Doppler anemometry (LDA) [146], techniques which have a small experimental uncertainty and therefore can provide increased confidence in the CFD, that is if the CFD and experimental results agree.

Comparison of numerical studies and flow in phantoms have provided substantial evidence that CFD can model complex flow in realistic artery geometries [174]. Budwig *et al.* [109] compared numerical results for steady, laminar flow in a symmetrical aneurysm with experimental flow visualization using fluorescent beads, measurements of velocity with LDA and measurements of wall shear stress (WSS) made with a hot film anemometer probe. The flow visualization showed there was qualitative agreement between the numerical and experimental streamlines. The numerical velocities agreed with LDA measurements within the limits of uncertainty, but the authors note that uncertainties in the recirculation are relatively large as the velocities are small in this region. Egelhoff *et al.* [74] performed similar studies with pulsatile flow and found good general agreement between simulation and experiment but found some discrepancy in the position of the vortex centre which they attribute to the finite length of time over which the pathlines were produced (one sixth of the cycle). Yu *et al.* [113] compared PIV results with numerical simulations of flow in symmetrical aneurysms and found good general agreement except at the upstream end of the bulge at the beginning of the cycle and their suggested reasons for this are: errors in the measurements in that region due to stray light reflections there, or sensitivity of the flow in this region to the upstream boundary layer and vortex impingement downstream.

There are far fewer validation studies in more realistic AAA geometries. As part of their study on the impact of stent grafts on AAA flow, Frauenfelder *et al.* [207] compared gas bubble streamlines in a patient-specific silicon model of one of the patient aneurysms with numerical streamlines. The qualitative agreement in the path of the main jet and the positions of the vortices is good, but they did not attempt any quantitative comparisons.

Validation against *in vitro* results has shown that, in the arteries in which it has been attempted, CFD can reliably model the flow [174]. However, these studies cannot determine whether CFD

can predict the haemodynamics *in vivo*. *In vivo* validation studies are much more difficult as the input uncertainties are much larger than those for experiments, and the *in vivo* velocity measurements have much larger uncertainties. The accuracy of reconstructed geometries depends on the resolution of the imaging method used and also on the reconstruction technique. While different reconstructions of a carotid bifurcation model from MRI scans were all very similar, and had a geometry error of ≤ 0.15 mm, the geometry of an *in vivo* carotid bifurcation was significantly affected by the reconstruction technique used [204]. The *in vivo* velocity measurement techniques, Doppler US and PC-MRI, both suffer problems preventing them from providing reliable validation results. Colour Doppler cannot resolve the low reverse velocities found in the aneurysm bulge [116] and has difficulty capturing the whole 3D field. PC-MRI is more promising but suffers a number of artefacts which become more important during physiological flow conditions [174]. If a reliable measurement method was available there would be no need to calculate the flow.

Steinman *et al.* [176] found good agreement between PC-MRI measurements and CFD in the carotid bifurcations of two volunteers. In studies on the healthy aorta, Jin *et al.* [148] showed that when wall motion was incorporated they could predict velocities in the aortic arch, and Long *et al.* [147] found small differences of 3-52 % between PC-MRI and simulation results proximal to the aortic bifurcation. There is one study which compares PC-MRI and CFD results in abdominal aortic aneurysms. Kose *et al.* [208] used PC-MRI registered with CT scans for validation of numerical simulations using the CT scans for the geometry and the PC-MRI for the inlet boundary data and the experimental validation. Their results show good qualitative agreement and, although they do not agree quantitatively everywhere, the RMS error is only $2-5$ cm s^{-1}. However, aneurysms in only two patients were investigated in this study, and since AAA geometries are wide ranging, good agreement in some does not necessarily mean the same is true for others. Other issues with their study include first order accuracy in the CFD, the fairly limited number of mesh elements, and lack of an attempt to quantify the mesh error.

The aim of this chapter is to validate patient-specific simulations of AAA haemodynamics against PC-MRI measurements. The method described in Chapter 2 used a measurement of the centreline velocity in the healthy section of the aorta, and the derived fully developed velocity profile, as the inlet boundary condition. In this chapter simulations based on an equivalent method are compared with simulations which use patient specific flow rates, as well as simulations which use the full patient specific inlet velocity profile.

4.2 Methods

4.2.1 Patient Protocol

Three subjects (two male, ages 83 and 73 years, and one female, age 57 years) gave informed consent to participate in the study. The study was given ethical approval by Lothian NHS Ethics Committee. All subjects had previously been diagnosed with AAA and were scheduled for surgical repair. The subjects underwent an MRI scan to measure the geometry and flow within the aneurysm, and then had pressure tonometry on their radial artery, which along with the systolic and diastolic pressure, as measured with a brachial cuff, was used to estimate the pressure in the aorta.

Subjects did not consume alcohol, caffeine or tobacco for at least 4 hours prior to the study. The subjects had the MR scan first. A Philips (Koninklijke Philips Electronics N.V., Amsterdam, Netherlands) Gyroscan Intera 1.5 T MR scanner was used to obtain cardiac gated transverse images at intervals (9.4 - 10.0 mm) along the aneurysmal section of the aorta and at 16 points throughout the cardiac cycle. Cardiac gated images of the z component of the blood velocity (QFlow images) were obtained on three transverse planes: one just proximal to the aneurysm, one midway through the aneurysm and one at the start of the iliac arteries. The subject lay supine for the MR scan which took about 1 hour. MRI scanning was performed by Tristan Lawton and colleagues in the Radiology Department, Edinburgh Royal Infirmary.

After the MR scan the subject underwent pressure tonometry. Pressure tonometry is a technique which uses a small probe to measure the blood pressure wave non invasively at a pulse point. There are various transfer functions based on one-dimensional models of the arterial system, which can be used to calculate the pressure in other arteries based on the pressure wave obtained at the pulse point, a method known as pulse wave analysis. A SphygmoCor pressure tonometry system (AtCor Medical, West Ryde, NSW, Australia) was used to perform pulse wave analysis on the subjects radial artery and from this the system automatically calculates the aortic pressure wave. The radial pressure wave was calibrated using an electronic brachial sphygmomanometer (Omron 705IT, Omron, Kyoto, Japan). However, in PWA the SphygmoCor does not record an electrocardiogram (ECG) which was required in order to synchronize the pressure wave with the MR images. To obtain the ECG a pulse wave velocity recording (PWV) was obtained on the radial and carotid arteries as this records the ECG simultaneously. Pressure tonometry was performed by Lesley Breen in the Clinical Research Facility, Edinburgh Royal Infirmary. By

post processing the signals the radial pressure signal obtained using PWA was aligned with the radial pressure signal obtained using PWV, to obtain the central pressure synchronized with the ECG.

4.2.2 Lumen Boundary Motion

The MR geometry images were time resolved which allowed the motion to be assessed. An active contour was used to locate the lumen boundary for each time. Active contours or deformable models work by moving a line, or contour, in 2d, or surface in 3d, according to a potential energy surface, until the line falls into an energy minimum [209, 210]. The energy of the contour has two sources: external and internal. The external energy comes from the position of the contour in the external energy field, which is a function of the image. The internal energy comprises of elastic energy from stretching and bending of the line. Active contours have been used to segment the lumen [211], wall [211, 212] and thrombus [213] of AAAs from CT scans, as well as for determining the motion of both lumen and wall from MRI scans [214]. The method used here is a simple 2D active contour based on these more complicated methods.

The active contour was formulated in Matlab v. 6.5 r. 13 (MathWorks Inc., Natick, MA, USA). The energy field used was based on the magnitude of the gradient of the image, I, so the external energy was:

$$E_{ext} = k_{ext} |\nabla I| \tag{4.1}$$

where k_{ext} is a constant.

The anatomical images are influenced by the flow, with images obtained during the high flow phase having a significantly brighter lumen. To prevent these images having wide regions of high gradient, which would tend to draw the contour further in, all pixels above the level of the mean, within the lumen of the first frame, were set to this mean value. The gradients outside a region defined by the initial contour were set to zero in order to eliminate their effects. The energy field was then normalized.

The internal energy was calculated based on simple harmonic motion of the nodes. Each section between two nodes had an elastic energy:

$$E_{elast} = k_{elast} (l - l_0)^2 \tag{4.2}$$

where l_0 is the total length of the contour divided by the number of sections, l is the actual distance between the two nodes and k_{elast} is a constant. Each node had a bending energy:

$$E_{bend} = k_{bend}(\pi - \theta)^2 \tag{4.3}$$

where θ is the angle made by the node and the nodes either side and k_{bend} is a constant.

Then the total energy is:

$$E = \sum_n E_{ext} + \sum_n E_{elast} + \sum_n E_{bend} \tag{4.4}$$

where the external energy is evaluated for each node, and the sums are over the n nodes or sections making up the contour. The contour was moved according to the forces due to this energy:

$$F = -\nabla E \tag{4.5}$$

The contour was initialized manually (see below), with the same initial contour for each time frame, and allowed to minimize its energy. Between each iteration it was necessary to smooth the contour. The area within the final contour was then calculated and the change in area over time was used as a measure of how much the aorta dilated at the level of that slice.

4.2.3 Geometry Reconstruction

Since lumen boundary motion was found to be small (<9.5 % diameter change) the original manual segmentation, which was used to initialise the active contour, was used in the geometry reconstruction. Manual segmentation was performed as follows. The region of the flowing blood, or lumen, was defined by the brightly lit area which shows where the blood flows. The images from each time frame were averaged so that the segmented lumen was in the mean position. Averaging the scans also eliminated any variation throughout the cycle due to the flowing nature of the blood. The boundary between the lumen and the thrombus was manually marked on each slice by placing markers around it and these markers were interpolated with a spline to form a contour. Matlab (MathWorks Inc., Natick, MA, USA) was used to view the images and define the contour bounding the lumen.

The resolution of the MR data was very low in the z direction, just 10 mm. Hence it was necessary to interpolate this data smoothly to obtain a realistic arterial geometry. The contours were

interpolated using splines. The majority of these splines linked vertical data points and were simply interpolated to obtain data every millimetre. A major complication was the bifurcation region. In order to interpolate this region smoothly two additional splines were used. The first joined the closest points on the two iliac branches and the second linked the closest sides of the aorta. It was impossible to see the precise point at which the artery bifurcated, the saddle point. As a best guess the saddle point was positioned midway between the last slice containing one contour and the first slice with two contours. The x-y position was defined as the point half way between the closest points of the first two contours on the iliac arteries. The splines are shown in figure 4.1.

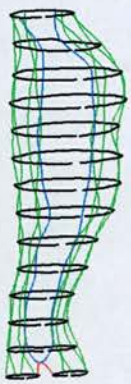

Figure 4.1: *Splines used to interpolate contours. Manually segmented contours are shown in black, in green are the vertical splines, and the splines through the saddle point are in blue and red.*

Spline interpolation smoothes the data and so alters the position of the contour. To check that the contours were not changed significantly from the original, manually segmented, ones the difference in their position before and after smoothing was examined.

The interpolated contours were assembled into a surface mesh, and stored in the form of an STL file, using Nuages (Bernhard Geiger, INRIA Sophia-Antipolis, France [178]). Nuages uses Delauney triangulation to convert the contour data into a surface of triangles [178]. Since the triangulation results in a linear interpolation of the slice data some parts of the resulting surface had small, sharp corners. These were removed by manual correction using Magics X SP1 (Materialise, Leuven, Belgium). Magics was also used to add inlets and outlets to the geometries. The iliac arteries were extended with outlet lengths (length = 10 × diameter) to ensure a computational boundary was not placed inappropriately [136]. This was achieved by cutting each iliac artery perpendicular to its walls and then extrapolating. Geometries with

straight cylindrical inlets were also produced. The MRI planning slices were used to measure the angle and diameter of the aorta just proximal to the first data slice. A cylinder with these specifications (and length = 5 $\times$ diameter) was created and attached smoothly to the rest of the aortic geometry. To assess the effect of manual smoothing of the sharp corners and of adding the outlet lengths to the iliac arteries, on the accuracy of the surface, contours on the same z planes as the original segmented contours were produced. These were compared with the original manually segmented contours and the differences were examined.

4.2.4 Meshes

Gambit (Fluent Inc., Lebanon, New Hampshire, USA) was used to mesh the volume with an unstructured grid of 3 mm tetrahedral elements. A surface mesh of 0.5 mm triangles was also produced. Fluent (Fluent Inc., Lebanon, New Hampshire, USA) was used to calculate the flow field in the 3 mm tetrahedral mesh assuming a steady inlet velocity of 50 cm s^{-1} and a constant outlet pressure of 100 mmHg. Fluent's 'geometry adaption' along with 'boundary adaption' was used to refine the mesh near the wall in keeping with the 0.5 mm surface mesh. 'Gradient adaption', based on gradients of velocity magnitude obtained from the steady flow simulation, was used to further refine the mesh such that regions with large velocity gradients contained more cells. Although the real flow field would not be the same as that with steady flow this was felt to be a good enough first approximation for producing the mesh. These meshes had between 2.7×10^5 and 7.7×10^5 elements. Further refined meshes were produced by refining based on the velocity magnitude gradients at the peak flow phase of the cardiac cycle. These meshes had between 3.1×10^5 and 9.0×10^5 elements. To get an idea of the mesh error the differences in velocity magnitude between the standard and fine meshes was calculated.

4.2.5 Boundary Conditions

Lumen boundary motion was assessed by examining the change in area using an active contour. The maximum change in diameter was 9.5 % over the cardiac cycle which occured for the healthiest sections proximal and distal to the aneurysm, while the most diseased regions had diameter changes of around 2.5 %. The lumen boundary was then fixed in position and a rigid wall calculation, with a no-slip boundary condition at the wall, was performed.

All calculations had the same pressure outlet boundary condition. This was the aortic pressure

wave obtained from pressure tonometry and was applied at the iliac artery outlets. Some post processing of the SphygmoCor signals was required in order to obtain the aortic pressure in phase with the ECG. First the average radial pressure wave was found by using the ECG to split the wave into individual cardiac cycles, scaling each cycle to the period of the heart beat during the MR scanning and then taking the mean of the cycles. There was some variation in the length of the heart beat during tonometry and MR (1.5, 0 and 16 % for the three patients) but the length of the heart beat during the MR scan was chosen so as to calculate flow with the same periodicity as the measured flow. Then the individual cardiac cycles from the radial PWA were aligned with the radial PWV signal by finding the peak in the cross-correlation. And finally, dividing the aortic pressure signal at the same time points as the radial pressure signal, resulted in the central pressure in phase with the ECG.

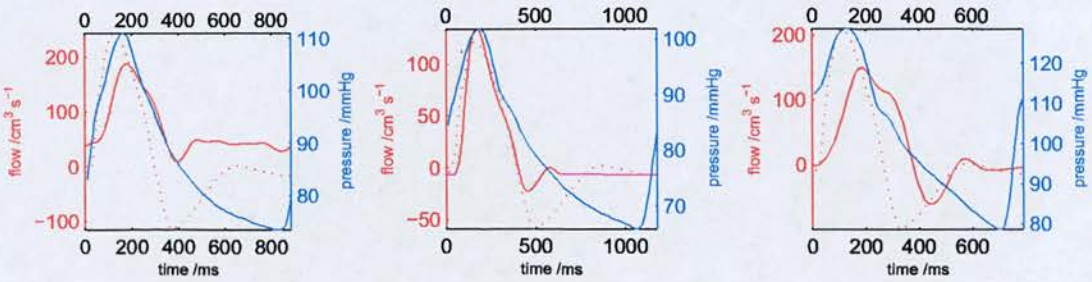

(a) Pat001 (b) Pat002 (c) Pat003

Figure 4.2: *Inlet flow and outlet pressure. Solid red line is the flow wave from the MRI data. Dashed red line is the flow wave from the archetypal velocity wave.*

A flow wave was used for the inlet boundary condition and the flow and pressure waves for each patient are shown in figure 4.2. Three different inlet velocity profiles were used in order to assess the effect of differences in the inlet velocity profile on the flow within the aneurysm, and also to assess the level of patient specificity required to give the correct velocities within the aneurysm. The velocity profile for each type of calculation is described in the sections below.

4.2.5.1 Velocity profile from MRI ('noinlet' calculation)

The z component of the velocity is given in the Q flow image. The Q flow image was positioned on a slice just proximal to the start of the aneurysm bulge. It was necessary to apply a median filter to velocity components outside a threshold to eliminate outliers. The data was also smoothed in the x, y, t directions by convolution with a top hat function. To obtain the ve-

locity component at each cell face on the inlet, and for each time step, the data was interpolated cubically.

4.2.5.2 Flow waveform from MRI ('inlet, specific' calculation)

The flow waveform was obtained by integrating the z velocity across the lumen at each time step. This meant the flow waveform was the same as that applied in the above case. However, the velocity profile used was a fully developed Womersley profile applied at the entrance to an inlet section.

4.2.5.3 Centreline velocity waveform from archetypal velocity wave ('inlet, archetypal' calculation)

As above, the velocity profile was a fully developed Womersley profile applied at the entrance to an inlet section. In this case the velocity profile was obtained using the centreline velocity from an archetypal velocity waveform for AAA patients as found in Chapter 3.

4.2.6 Calculations

Fluent v. 6.216 (Fluent Inc., Lebanon, New Hampshire, USA) was used to perform unsteady computational fluid dynamics (CFD). The flow was assumed to be laminar and the Navier Stokes equations were solved using Fluent's unsteady, segregated solver. Second-order upwind schemes were used to discretize time, and the continuity equations. The Pressure Implicit with Splitting of Operators (PISO) scheme was used for pressure-velocity coupling as this is the most appropriate for unsteady flow. Blood was assumed to be a Newtonian fluid ($\rho = 1040$ kg m^{-3}, $\mu = 3.64 \times 10^{-3}$ kg m^{-1} s^{-1} [32]). Each cardiac cycle contained 500 time steps which resulted in time steps of 1.76, 2.35 and 1.58 ms for the three patients.

4.3 Results

4.3.1 Lumen Boundary Motion

The area of the contour defining the lumen on the uppermost slice, considered to be the healthiest part of the aorta, is shown for each patient in figure 4.3. Although the shapes of the area

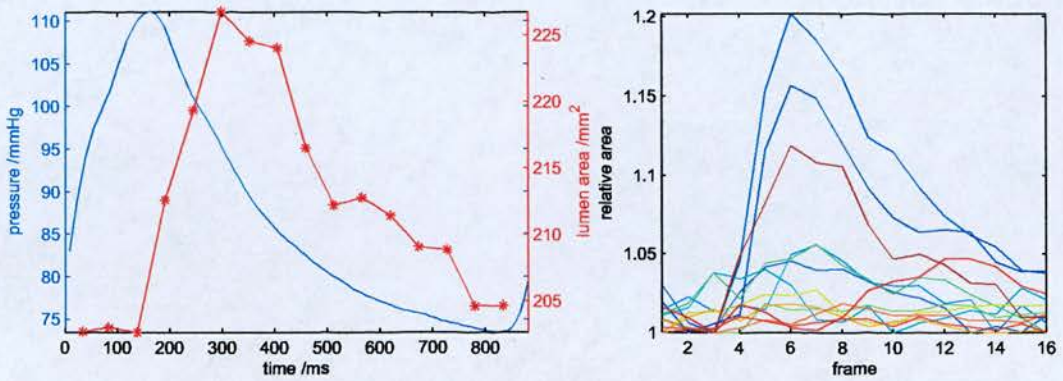

(a) Pat001

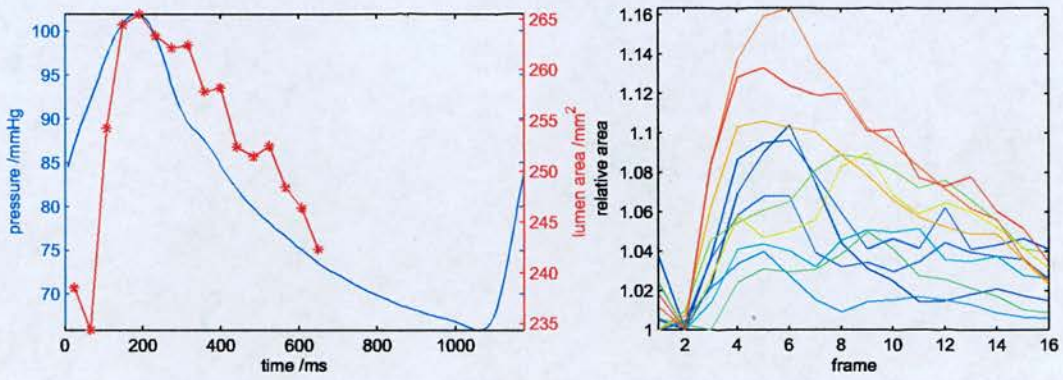

(b) Pat002

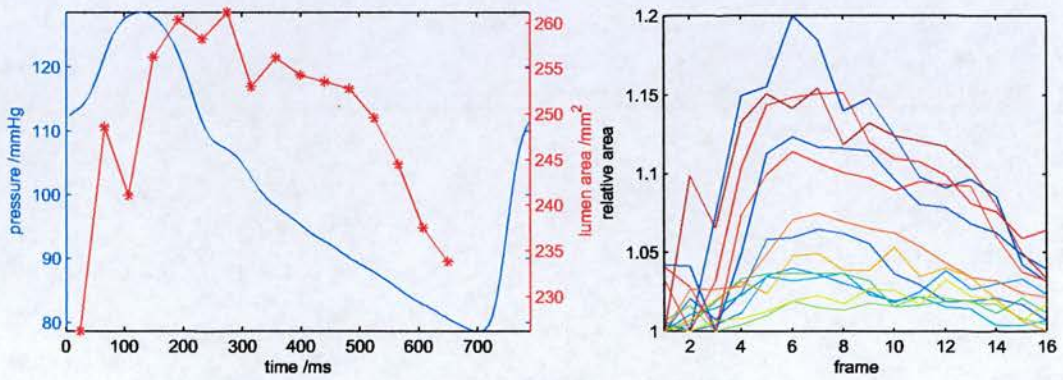

(c) Pat003

Figure 4.3: *Left: cross-sectional area of the lumen on the most proximal slice plotted with central pressure obtained from tonometry. Right: relative change in lumen area over cardiac cycle for each slice. Slices are rainbow coloured with reddish colours for the most proximal slices and blueish colours for the most distal.*

and pressure waves are not the same, there is a clear similarity which gives some confidence that the active contour is finding the correct boundary. The viscoelasticity of the artery results in a phase delay between pressure and area waves with area lagging behind pressure, which is consistent with these results. Gow and Taylor [215] found the phase lag for the 1st and 2nd harmonics in dog aortas to be around 0.15 radians, which is much smaller than the phase lag seen here (1.18, 0.24 and 1.45 radians for the three patients). Another factor is that the central pressure is estimated for the ascending aorta and as the pressure wave travels along the aorta a delay will be introduced and the wave will also be distorted. Estimating the time delay due to distance along the aorta assuming a pulse wave velocity of 10 m s^{-1} [32] for elderly patients and an aortic length of 30 cm gives a time delay of about 30 ms.

Figure 4.3 also shows the area change for each slice. The most proximal (reddish) and distal (blueish) contours can be seen to have the largest changes in area, up to 20 %, over the cardiac cycle while those contours located in the main part of the aneurysm have only a minimal change in area. This 20 % change in area means an average 9.5 % change in diameter is the maximum diameter change for the artery and in the diseased section the diameter change is on the order of 2.5 %.

4.3.2 Geometry Reconstruction

The interpolated contours for the three patients are shown in figure 4.4 and the reconstructed and smoothed geometries with inlet and outlet lengths are shown in figure 4.5.

The three sets of contours (original, after spline interpolation and final) for Pat001 have been plotted on top of the MR images in figure 4.6. They are clearly all very similar and the differences are difficult to see at this magnification.

In general, the contours are defined by a finite number of points equally spaced around the contour but starting at an unspecified location. Simply taking the difference in position of these points results in a greater value than the perpendicular difference between the two lines. To avoid this both the contours were resampled, at points on equally spaced lines radiating from the centre of the original contour, and the difference in positions of these points was examined. The RMS difference between the original and spline interpolated, and the original and final, contour positions is shown in figure 4.7. The RMS difference between original and final contours ranged from 0.05 to 0.63 mm in Pat001, from 0.03 to 4.6 mm in Pat002 and

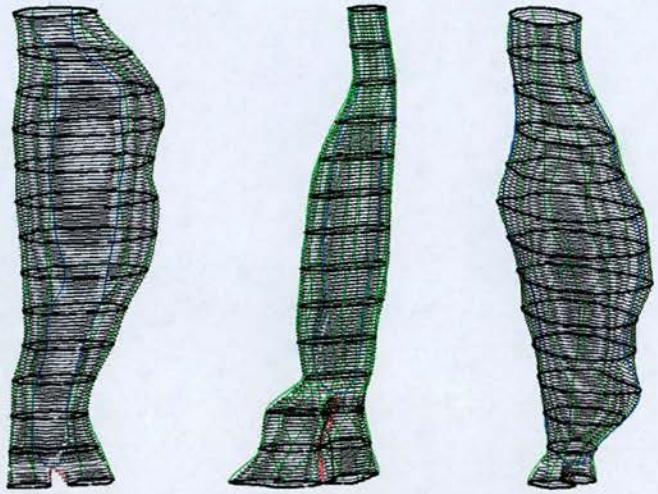

(a) pat001 (b) pat002 (c) pat003

Figure 4.4: *The patient contours. In bold are the manually segmented contours on the actual data slices. In green are the vertical splines and the splines through the saddle point are in blue and red. The interpolated contours are shown faintly. From left to right: pat001, pat002, pat003.*

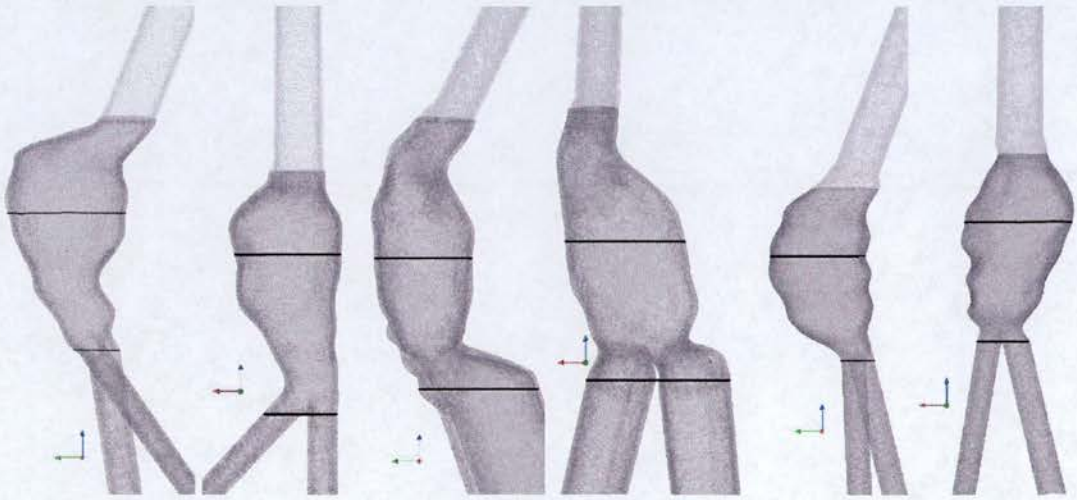

(a) pat001 (b) pat002 (c) pat003

Figure 4.5: *Reconstructed and smoothed aneurysm geometries with outlets. Geometry for 'noinlet' calculation is shown in darker grey with the extended geometry for 'inlet' calculations in lighter grey. Views are of the patients left side (left) and anterior (right). Positions of planes 2 (through aneurysm) and 3 (through iliac arteries) are also shown.*

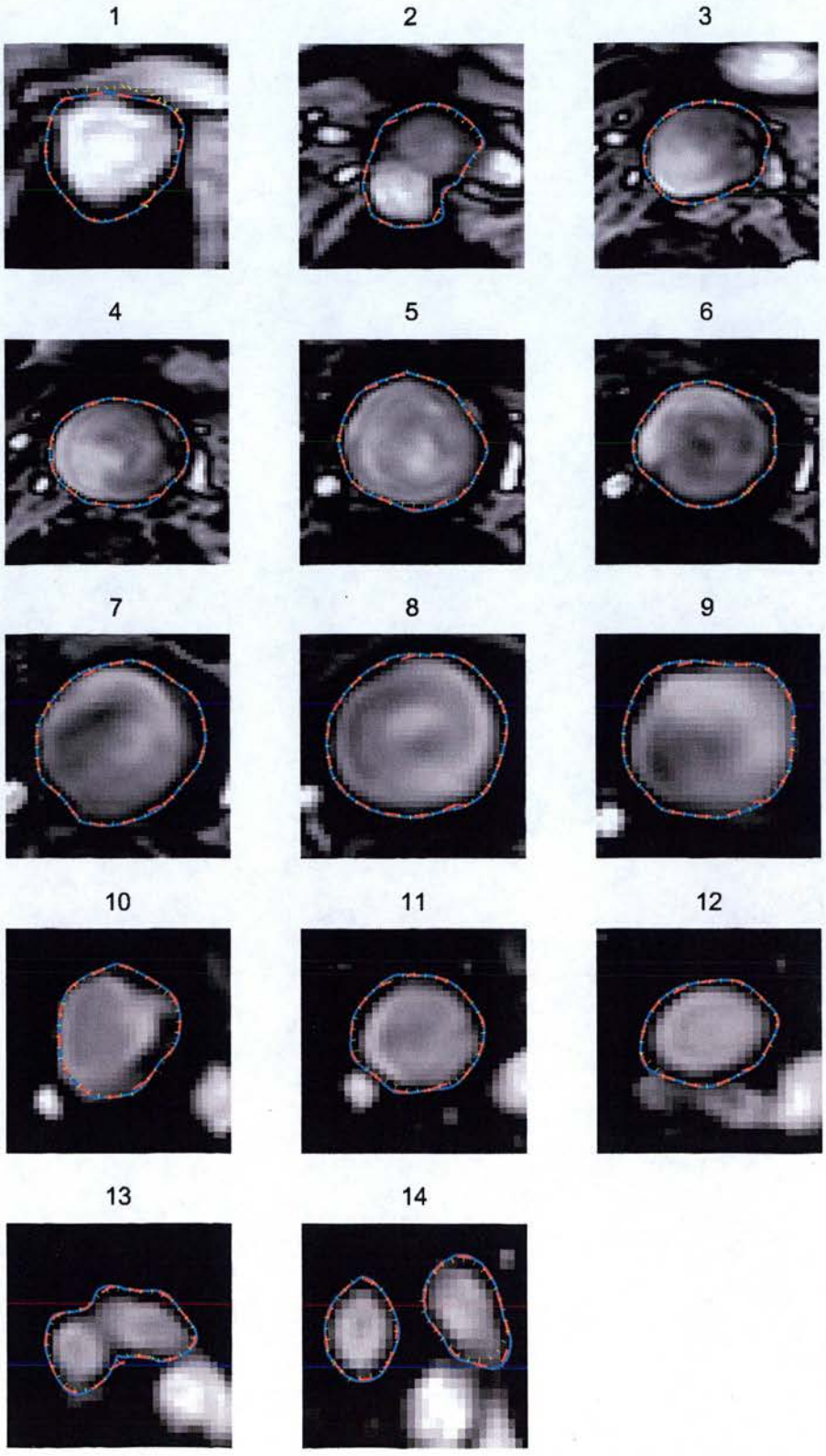

Figure 4.6: *MR slice data from pat001 with manually segmented contours (blue), contours after spline interpolation (red) and contours after manual smoothing and extensions (yellow).*

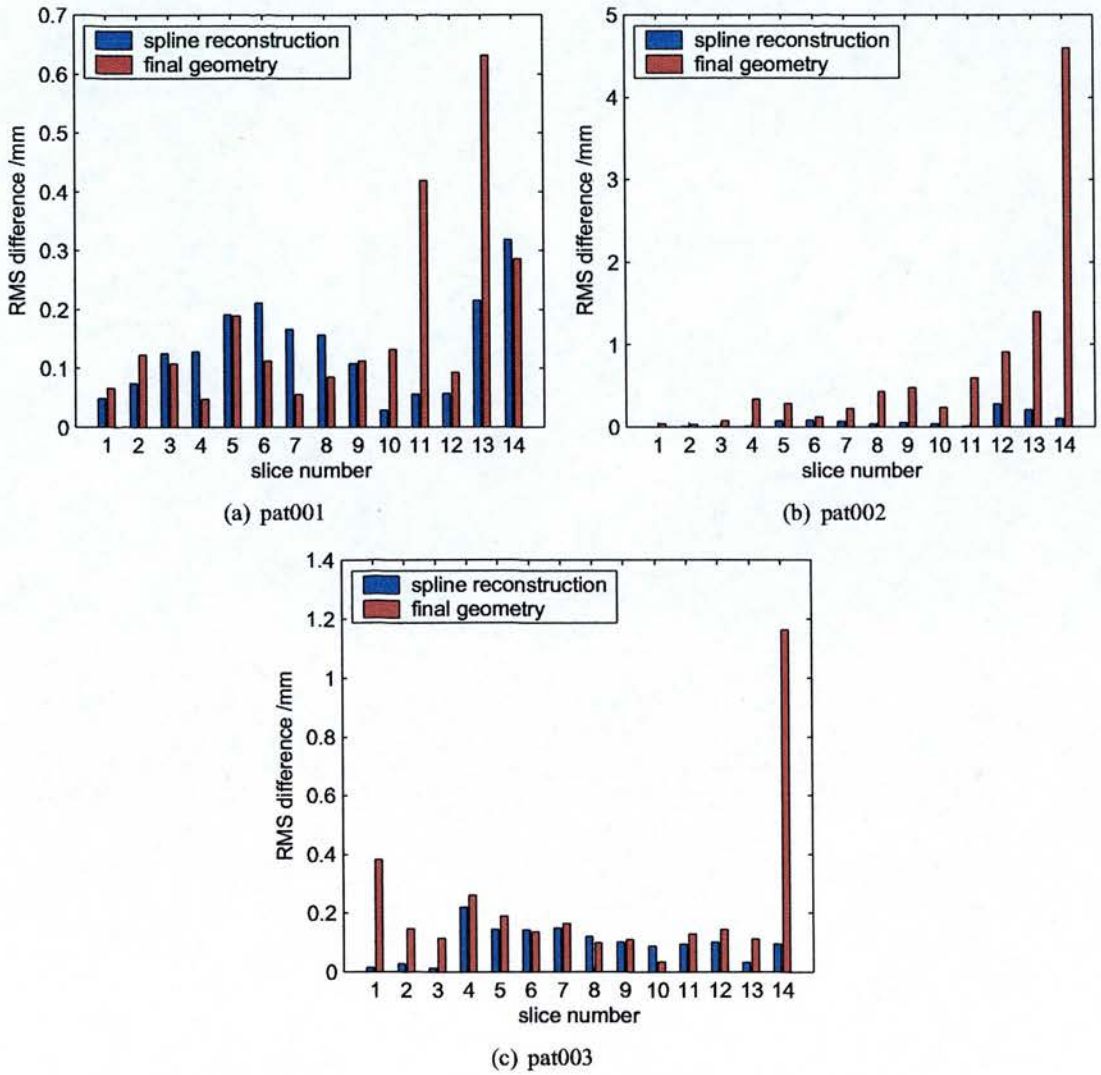

(a) pat001

(b) pat002

(c) pat003

Figure 4.7: *RMS difference in contour position after spline interpolation, and final meshing.*

Patient	simulation	mesh size /$\times 10^5$ elements		
		3 mm	standard	fine
Pat001	noinlet	0.79	2.7	3.1
	inlet specific	1.0	3.8	4.1
	inlet archetypal	1.0	3.8	4.0
Pat002	noinlet	2.2	6.5	7.7
	inlet specific	2.8	7.7	9.0
	inlet archetypal	2.8	7.7	8.9
Pat003	noinlet	0.56	3.9	5.5
	inlet specific	0.74	5.9	7.4
	inlet archetypal	0.74	5.9	7.7

Table 4.1: *Simulation sizes*

from 0.04 to 1.2 mm in Pat003. The rather large difference in the final contours of Pat002 and Pat003 is due to the difficulty in adding the outlet length on when the diameter of the iliac artery is nonuniform. Then there is no good way to slice the artery perpendicular to the edge all round its circumference, such that when the outlet length is added on the resulting contour remains in the same place. Since only the last part of the geometry is influenced in this way it should not have a large affect on the flow in the aneurysm bulge before the bifurcation.

The most distal contours of the iliac arteries of Pat002 were very large which has resulted in wide outlet lengths. The reason for the large contours is that the patient had iliac aneurysms, in addition to the aortic aneurysm. Ideally the imaged region would have been extended to the end of these aneurysms.

4.3.3 Mesh and Temporal Convergence

The standard mesh was produced by refining a tetrahedral mesh with 3 mm elements using gradients of velocity magnitude in a steady flow simulation. This produced a mesh which was finest in the necessary areas. To produce the fine mesh the standard mesh was refined again using the gradients of velocity magnitude at peak flow during the third cardiac cycle. The sizes of the meshes are shown in table 4.1. To compute one cardiac cycle took between 5 hr 42 and 16 hr 09 with standard sized meshes and between 7 hr 33 and 32 hr 25 with the fine meshes.

Mesh independence was investigated by studying the difference in the velocity magnitude on the plane midway through the aneurysm and the plane through the iliac arteries (planes 2 and

Patient	simulation	difference in V_{mag} standard cf. fine mesh /%	difference in V_{mag} 4th cf. 5th cycle /%
Pat001	noinlet	20	12
	inlet specific	18	8.0
	inlet archetypal	24	12
Pat002	noinlet	30	35
	inlet specific	20	8.0
	inlet archetypal	19	3.5
Pat003	noinlet	49	13
	inlet specific	33	5.0
	inlet archetypal	30	2.9

Table 4.2: *Mesh and temporal convergence*

3) at 16 time points with the standard and fine meshes. Mean percentage differences were between 18 and 49 %. Cyclic independence was assessed by comparing the velocity magnitude on planes 2 and 3 at 16 time points in cardiac cycles 4 and 5. Mean percentage differences were between 2.9 and 35 %. These are percentage errors relative to the point velocity magnitudes which means that when the velocity is very small, such as in recirculation regions, even a very small difference in the velocity results in a large percentage error. These were considered acceptable differences in order to limit the computational resources required.

4.3.4 Comparison of Z-Velocity Calculation Results and MRI Data

The z component of the velocity for the three different calculations on the three different patients was compared with the MRI measurements of the z-velocity. The results for Pat001, on the plane through the aneurysm and the plane through the iliac arteries, are shown in figures 4.8 and 4.9. Similarly the results for Pat002 and Pat003 are shown in figures 4.10 to 4.13.

It is clear that there are some similarities between the MRI and CFD results but also some differences. The cross-correlation of two signals, or images, is a measure their similarity. The cross-correlation, γ, for two images M and C is defined [216]:

$$\gamma(x,y) = \frac{\sum_n \sum_m \left(M(n,m) - \overline{M}\right)\left(C(x+n,y+m) - \overline{C}\right)}{\left(\sum_n \sum_m \left(M(n,m) - \overline{M}\right)^2 \sum_n \sum_m \left(C(x+n,y+m) - \overline{C}\right)^2\right)^{1/2}} \tag{4.6}$$

γ is a function of x and y which describes how well matched the two images are as they are moved across each other. The height of the maximum peak in the cross-correlation function,

Patient	plane	cross-correlation coefficient		
		noinlet, specific velocity	inlet length, specific flow	inlet length, archetypal V_{centre}
Pat001	aneurysm	0.307	0.347	0.262
	iliac	0.285	0.282	0.331
Pat002	aneurysm	0.396	0.311	0.339
	iliac	0.292	0.303	0.280
Pat003	aneurysm	0.403	0.402	0.424
	iliac	0.473	0.484	0.368

Table 4.3: *Mean γ_{max} for comparison of MRI and CFD results*

γ_{max}, was used as a measure of how well matched the MRI and CFD results were. The advantage of this measure over, say, taking the percentage difference, was that if the shapes of both MRI and CFD results were similar but misaligned, this similarity would contribute positively to the cross-correlation. If the percentage difference was used, such misalignment would create large percentage errors and the fact that there were similarities in shape would go unnoticed. The use of the maximum of the cross-correlation function, γ_{max}, as a measure of similarity between MRI and CFD results was found to be in line with the visually observed level of qualitative agreement.

The peak of the cross-correlation function between the MRI results and each of the numerical simulations, γ_{max}, is shown in 4.14. These results are for the plane through the aneurysm at each time step. The mean of γ_{max} for each calculation and on both the aneurysm and iliac planes is given in table 4.3.

For all patients the correlation is higher during systolic flow than during diastolic flow. This is due to the stability in the accelerating flow, which results in it all going forward and being much easier to predict than the diastolic flow, which is less well defined.

4.3.4.1 Pat001

For Pat001 it appears that during peak flow the calculation with archetypal V_{centre} has the highest correlation with the PC-MRI, while at early diastole it is the specific flow rate and at late diastole both specific flow rate and specific velocity are similar. Looking back at the actual z-velocity results (figure 4.8) it is difficult to tell which of the calculations match the MRI results best, but at peak systole (around 4th frame, 191 ms) there are patches of high velocity across the

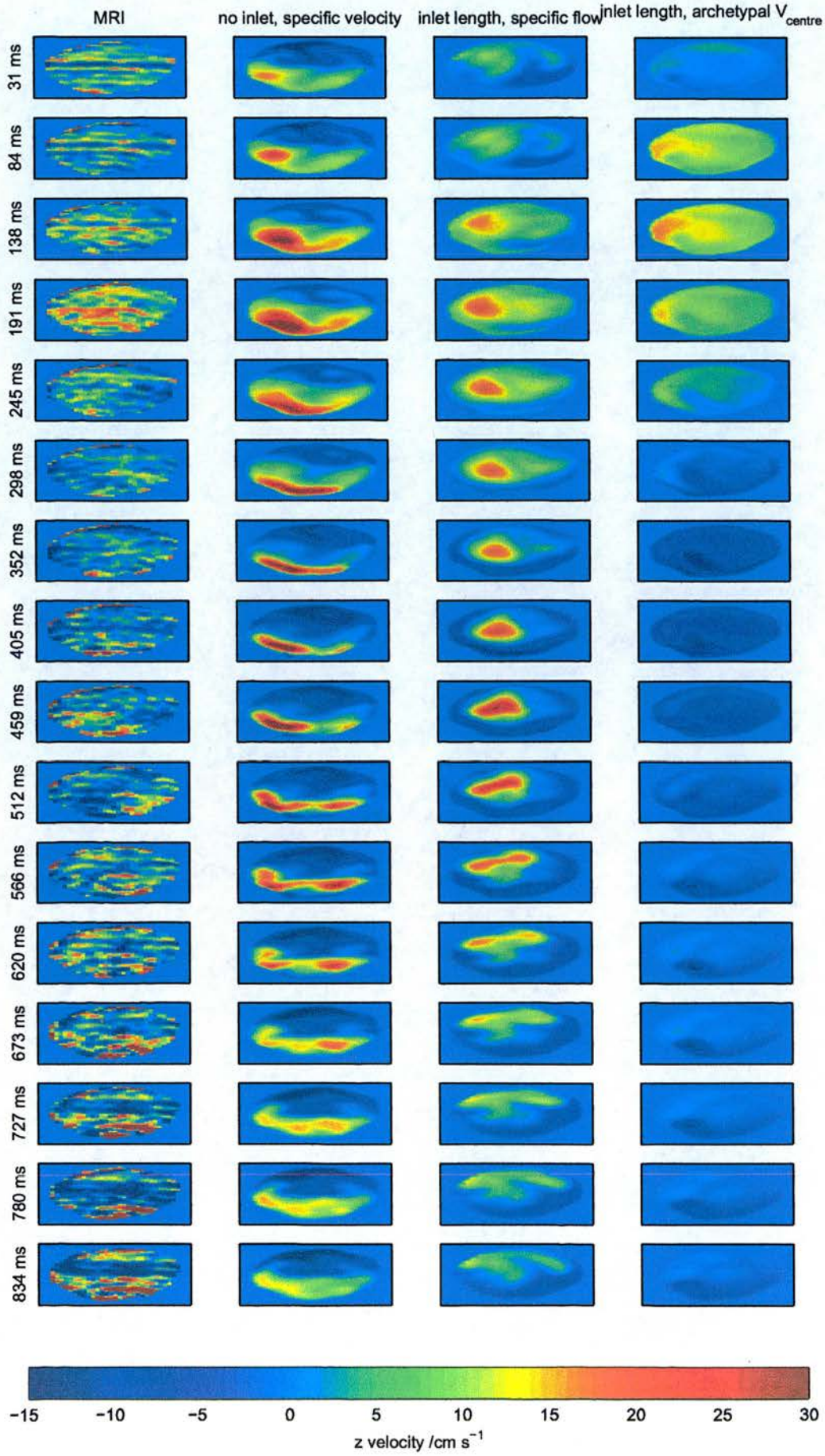

Figure 4.8: *z component of the velocity on a plane through the aneurysm, Pat001.*

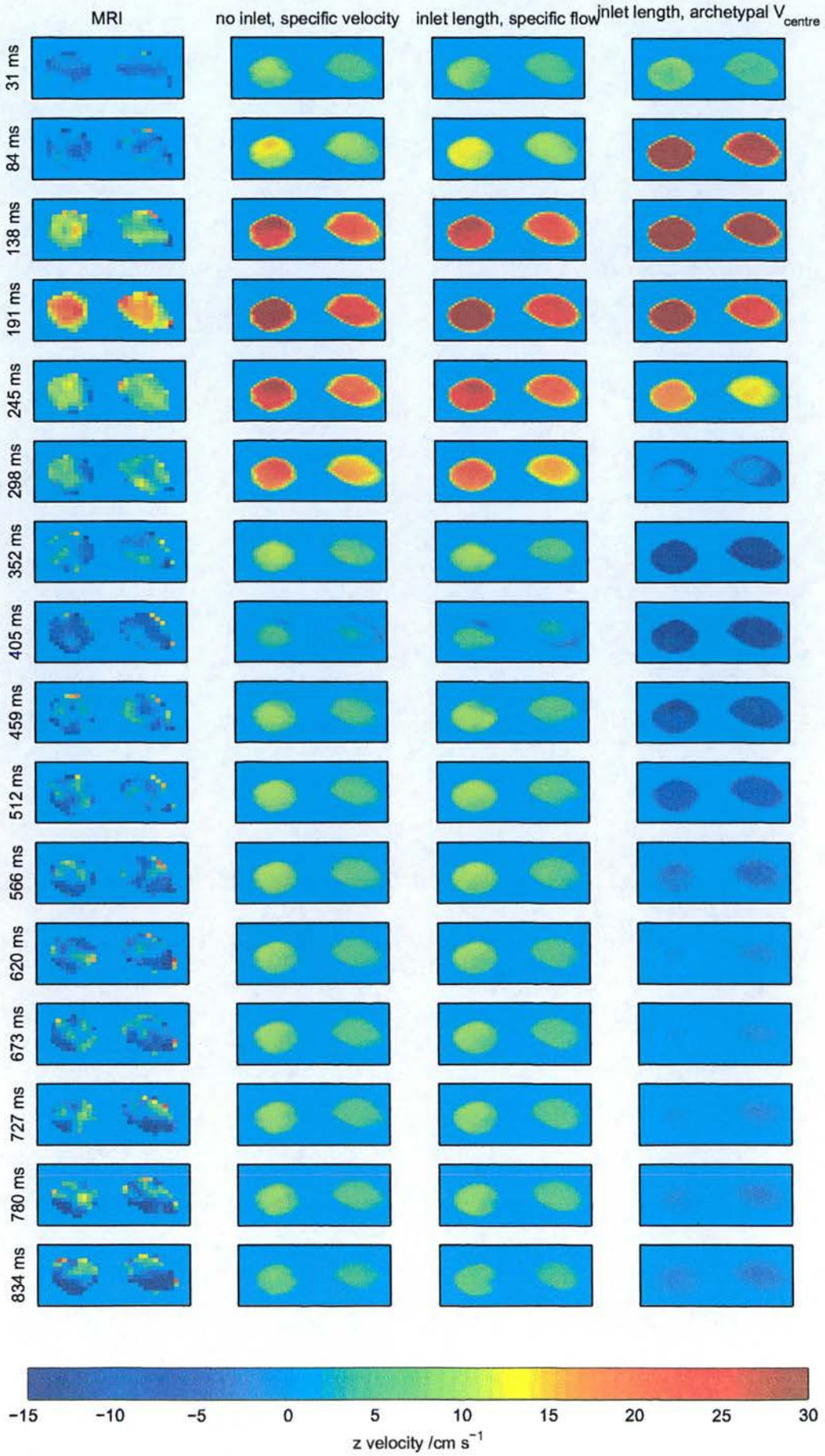

Figure 4.9: *z component of the velocity on a plane through the iliac arteries, Pat001.*

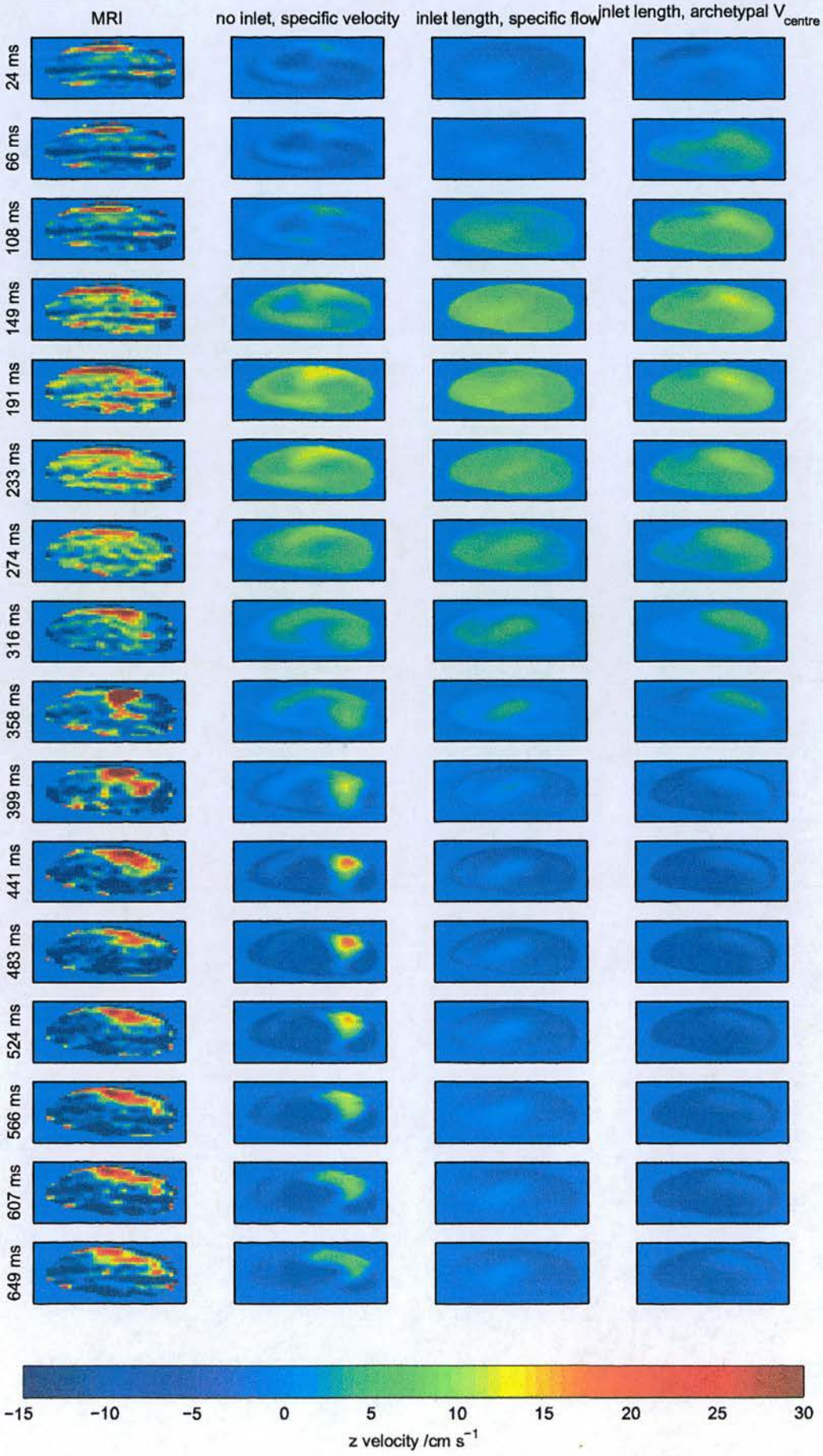

Figure 4.10: *z component of the velocity on a plane through the aneurysm, Pat002.*

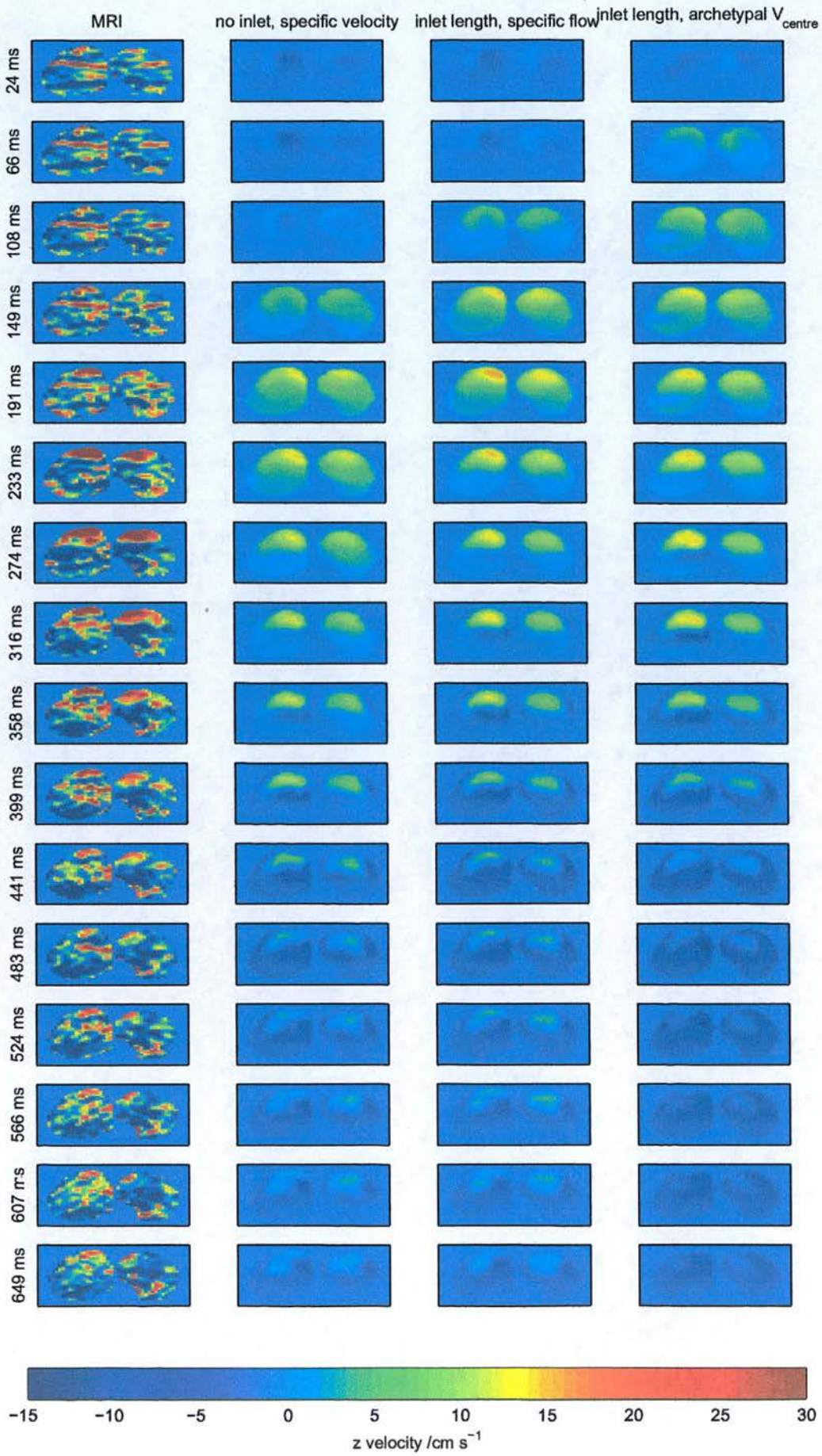

Figure 4.11: *z component of the velocity on a plane through the iliac arteries, Pat002.*

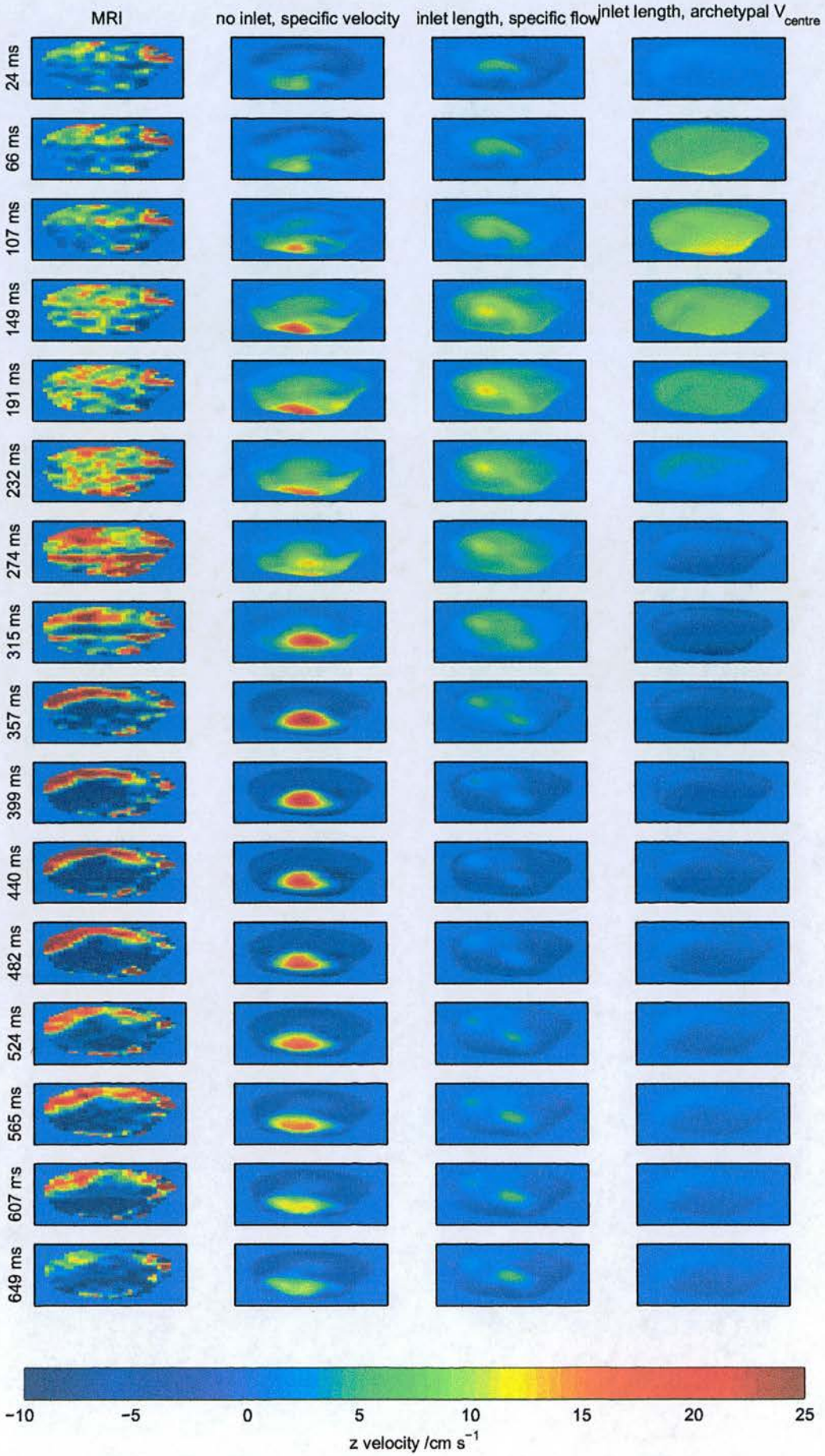

Figure 4.12: *z component of the velocity on a plane through the aneurysm, Pat003.*

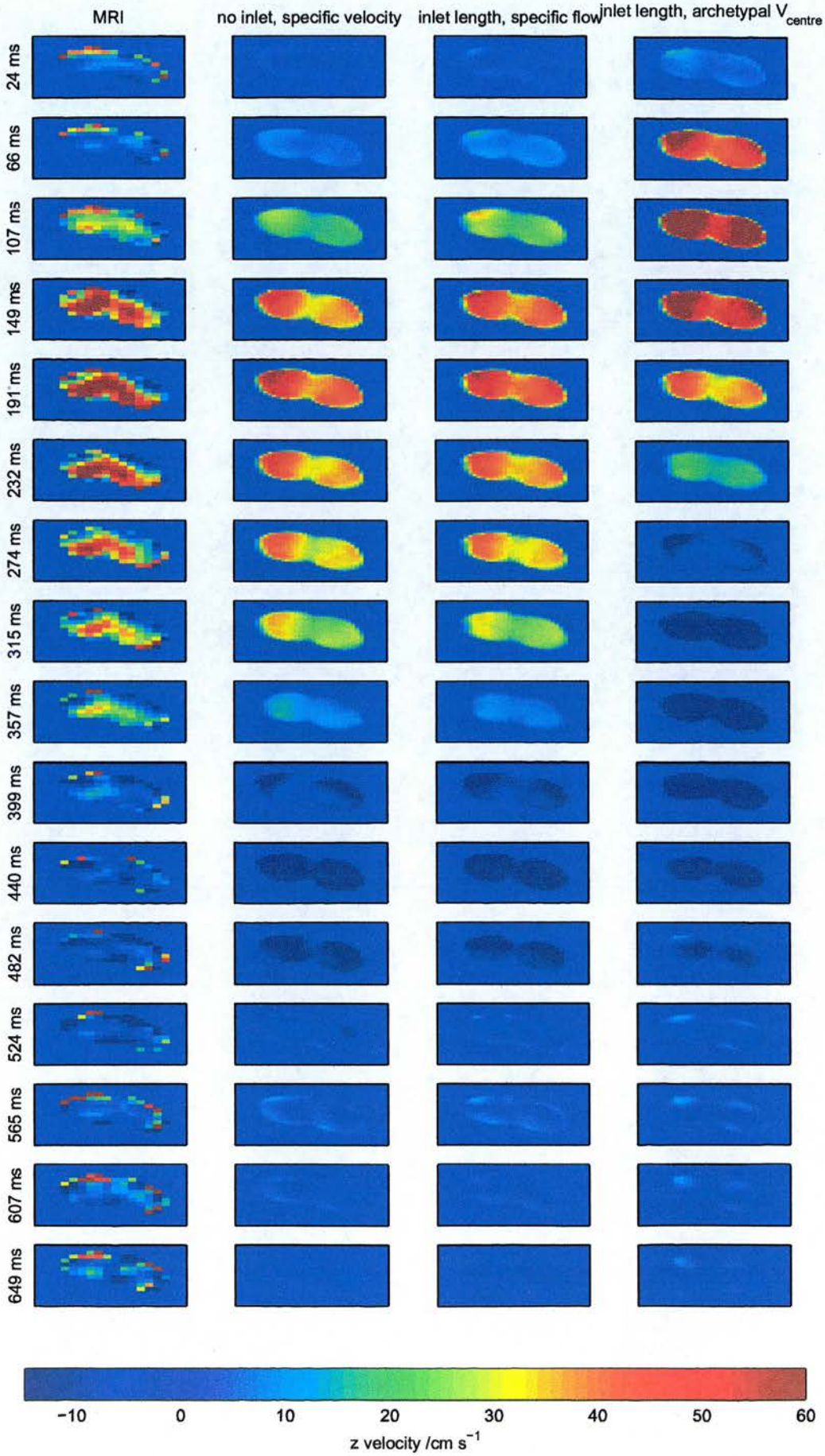

Figure 4.13: *z component of the velocity on a plane through the iliac arteries, Pat003.*

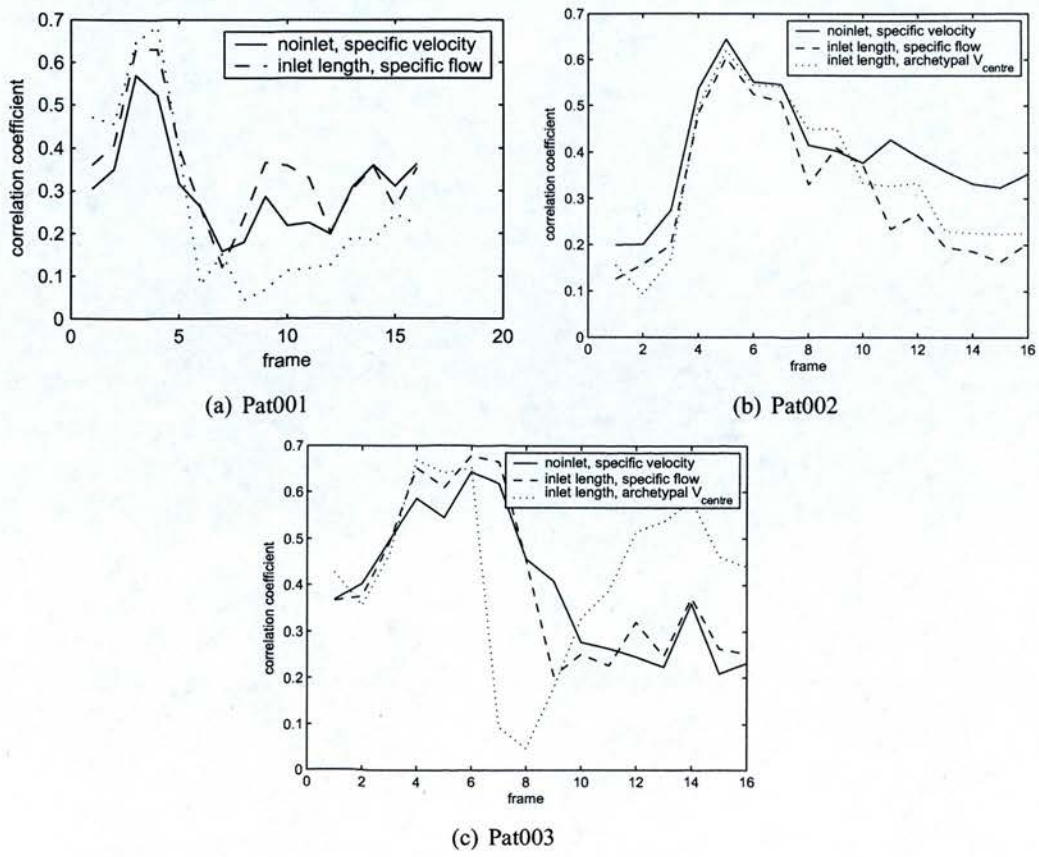

(a) Pat001

(b) Pat002

(c) Pat003

Figure 4.14: γ_{max} *on planes through aneurysms at each time step.*

whole aneurysm and although it appears that these are concentrated posteriorly (lower side of pictures) there are also some anteriorly and similarities with the inlet length calculations can be seen. During early diastole (around 9th frame, 459 ms) the region of faster flow still appears to be on the posterior side, agreeing with the noinlet calculation, however, the presence of other fast regions anteriorly probably accounts for the correlation with the inlet length, specific flow calculation where the z-velocity is distributed more evenly. During late diastole (around 16th frame, 834 ms) it is odd that both noinlet and inlet length, specific flow calculations correlate similarly with the MRI data as the two z-velocity profiles are completely different, almost the exact opposites with noinlet, specific velocity having the fastest velocities on the posterior side and inlet length, specific flow having the fastest velocities on the anterior side. In the MRI results there are two bands of fast velocities on the the anterior and posterior sides explaining why both simulations correlate well. However, the low velocity band across the centre of the aneurysm is probably an image artefact as it extends outside the artery and across the whole image. It can be seen in several of the images (31, 84, 673, 727, 780 and 834 ms). Although there are many similarities in the flow features of the noinlet calculation and PC-MRI results, the artefact, along with the level of noise in the images, makes comparison of CFD and MRI in this patient inconclusive.

4.3.4.2 Pat002

A similar stripe occurs across some of the z-velocity images for Pat002 (figure 4.10) most notably at the first three frames (24 - 108 ms). However, fewer images for this patient are affected and the images appear to be less noisy. The correlation coefficient for the aneurysm plane in Pat002 (figure 4.14) shows that over the whole systolic flow part of the cycle the results from the three calculations correlate similarly with the MRI results. The images confirm that there are only small differences in the z-velocity profile at this time (around 5th frame, 191 ms) as the flow is fast and uniform in direction across the whole aneurysm. However, in both the noinlet and inlet, archetypal results there are faster regions on the anterior side which accounts for why these calculations have a higher correlation. The largest differences in the peak correlation coefficient occur during the diastolic phase of the cycle where it is clear that the noinlet calculation matches the MRI results far better that the other two calculations. The MRI images reveal a fast region in the right anterior quadrant of the image which lasts throughout the diastolic phase but gradually slows. This is very well matched in the results for the noinlet calculation, which leads to the conclusion that the general *in vivo* flow features have

been reproduced in this patient, even if the details are difficult to assess.

The mean coefficient for the aneurysm plane confirms the result that the noinlet calculation out performs the other two. However, on the iliac plane the mean coefficient for the three calculations is much more similar. The z-velocity data shows that both noinlet and specific flow calculations have very similar z-velocity profiles and all three calculations show the fastest flow is at the anterior side throughout most of the cycle. The MRI data is noisier on this plane but still shows fast flow on the anterior side in many frames.

4.3.4.3 Pat003

From the correlation coefficients in the aneurysm plane (figure 4.14) the three calculations appear to predict the MRI results similarly well during peak systole (around 5th frame, 191 ms). The flow at this time is mainly forwards and although there are small fluctuations across the MRI velocity profiles they are fairly uniform. Small areas of faster flow in the inlet, specific velocity and noinlet calculations are not matched in the MRI data. During diastolic flow the correlation coefficients are surprising since it appears that the inlet, archetypal velocity calculation outperforms the other two. Looking at the z-velocity plots reveals that there is a region of forward flow along the edge of the anterior boundary, in the same location as the very fast flowing blood in the MRI data, albeit with completely different velocity.

4.3.5 Comparison of Flow Fields in Different Calculations

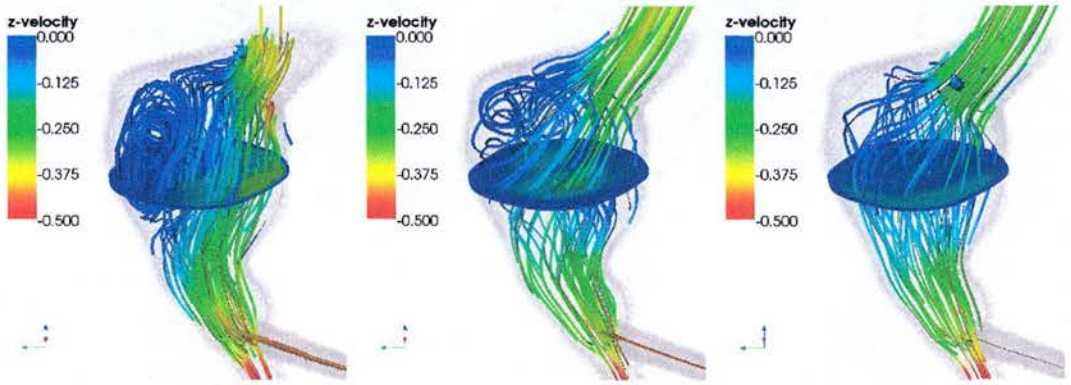

(a) noinlet, specific velocity (b) inlet, specific flow (c) inlet, archetypal V_{centre}

Figure 4.15: *Pat001: Blood flow in three different calculations at 191 ms*

The flow fields were examined using streamline plots. Flow fields are shown at several time

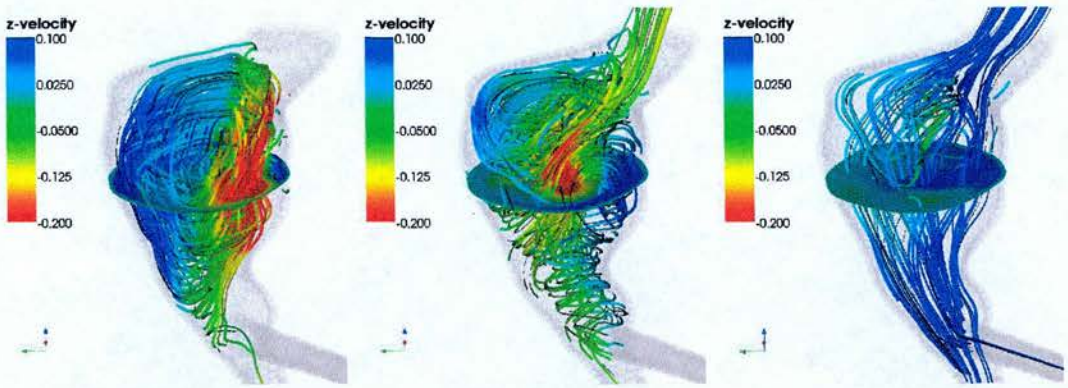

(a) noinlet, specific velocity (b) inlet, specific flow (c) inlet, archetypal V_{centre}

Figure 4.16: *Pat001: Blood flow in three different calculations at 405 ms*

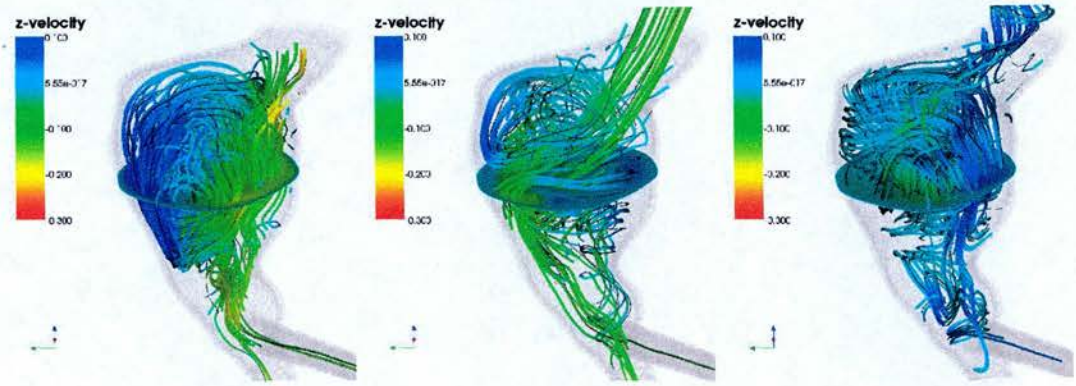

(a) noinlet, specific velocity (b) inlet, specific flow (c) inlet, archetypal V_{centre}

Figure 4.17: *Pat001: Blood flow in three different calculations at 727 ms*

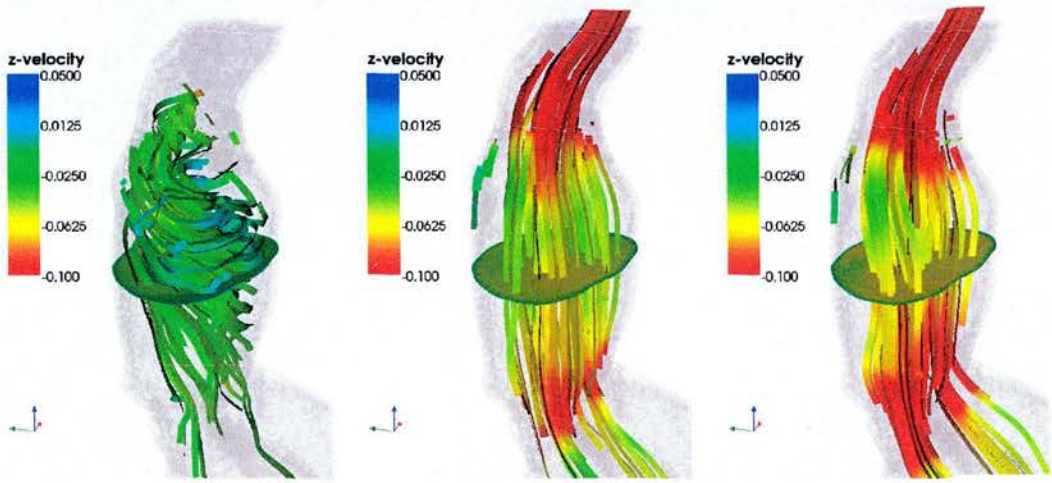

(a) noinlet, specific velocity (b) inlet, specific flow (c) inlet, archetypal V_{centre}

Figure 4.18: *Pat002: Blood flow in three different calculations at 108 ms*

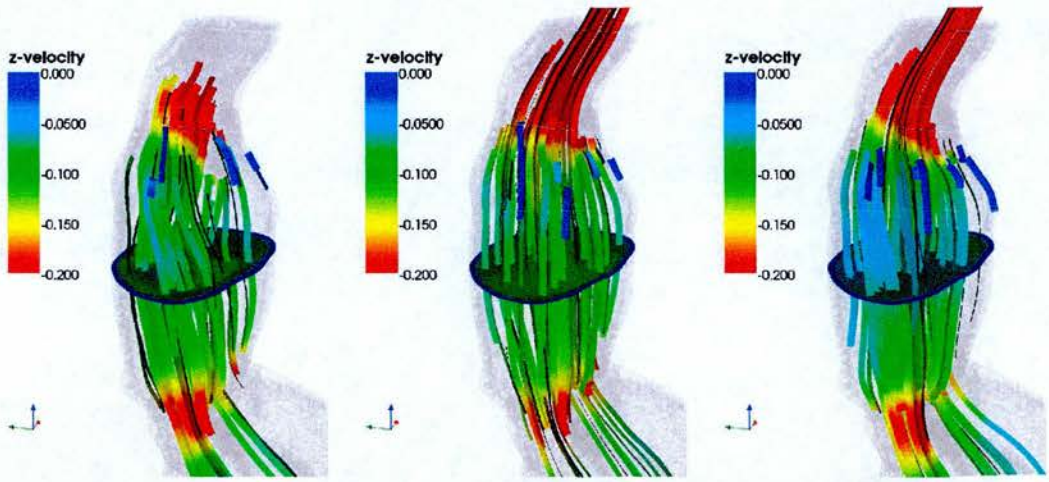

(a) noinlet, specific velocity (b) inlet, specific flow (c) inlet, archetypal V_{centre}

Figure 4.19: *Pat002: Blood flow in three different calculations at 191 ms*

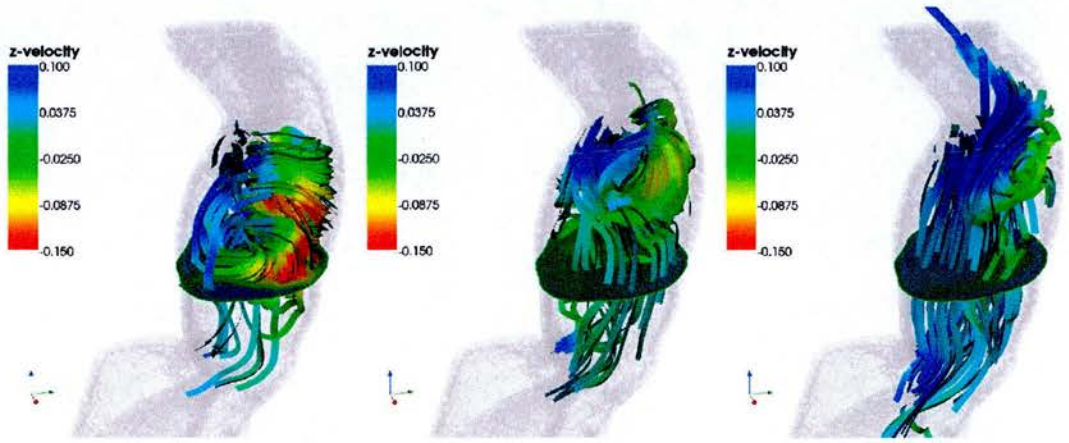

(a) noinlet, specific velocity (b) inlet, specific flow (c) inlet, archetypal V_{centre}

Figure 4.20: *Pat002: Blood flow in three different calculations at 483 ms*

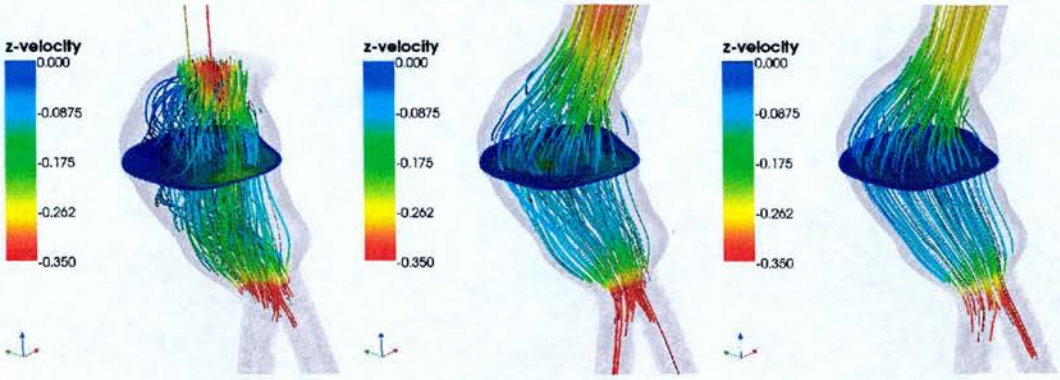

(a) noinlet, specific velocity (b) inlet, specific flow (c) inlet, archetypal V_{centre}

Figure 4.21: *Pat003: Blood flow in three different calculations at 191 ms*

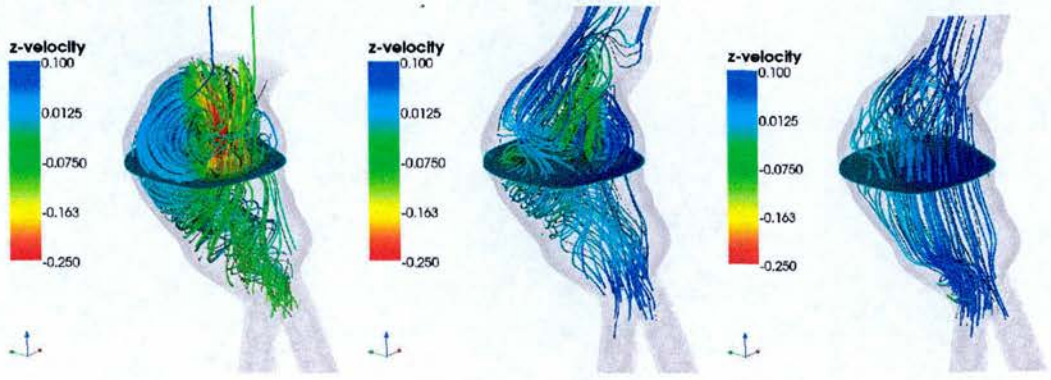

(a) noinlet, specific velocity (b) inlet, specific flow (c) inlet, archetypal V_{centre}

Figure 4.22: *Pat003: Blood flow in three different calculations at 399 ms*

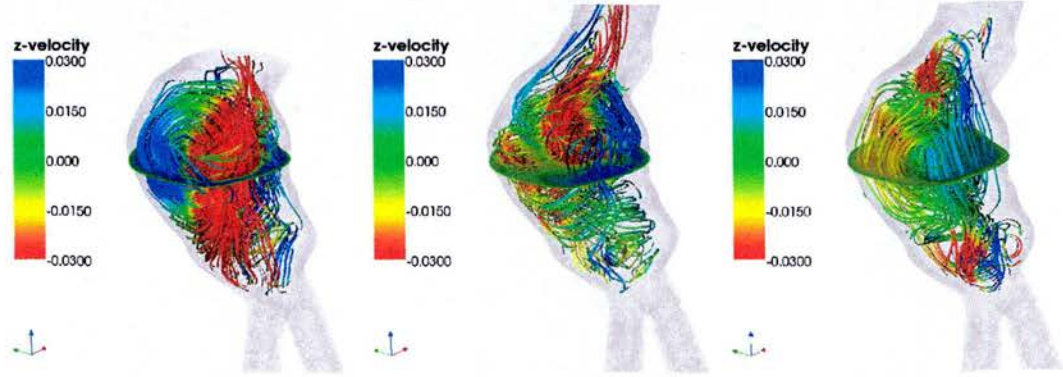

(a) noinlet, specific velocity (b) inlet, specific flow (c) inlet, archetypal V_{centre}

Figure 4.23: *Pat003: Blood flow in three different calculations at 607 ms*

steps in figures 4.15 to 4.17 for Pat001, in figures 4.18 to 4.20 for Pat002, and in figures 4.21 to 4.23 for Pat003.

The flow patterns for each of the three calculations show some similarities. For example during the systolic phases (Pat001: 191 ms, figure 4.15, Pat002: 191 ms, figure 4.19, Pat003: 191 ms, figure 4.21) most of the flow is forward. In Pat001 and Pat003 most of the flow is down the posterior side of the aneurysm, with a recirculation zone on the anterior in some of the calculations. In Pat002 the flow is laminar throughout the aneurysm.

However, there are also a number of clear differences in the numerical results. For example, the size of the vortex in Pat001: the noinlet calculation predicts a large, single vortex which lasts throughout the cardiac cycle, whereas the inlet-specific calculation predicts a smaller vortex which occupies just the proximal end of the bulge during systole and during diastole this vortex is accompanied by at least one other vortex on the posterior. The amount of helical flow is also clearly different with flow in the distal part of the aneurysm during the early diastolic phase (405 ms, figure 4.16) in the inlet, specific flow calculation being dominated by spiral flow, while in the noinlet calculation this section is filled with the vortex. During the diastolic phase in Pat002 (483 ms, figure 4.20) the noinlet calculation contains a vortex with reverse flow whereas the other two calculations predict mainly forward flow with less swirling. In Pat003 during the reverse flow phase (399 ms, 4.22) the vortex on the anterior wall of the noinlet calculation occupies much of the bulge whereas in the inlet, specific flow calculation there are several smaller vortices and in the inlet, archetypal velocity calculation the flow is slow but mostly laminar. The vortex in the noinlet calculation persists through the diastolic phase (607 ms, 4.23). There is also a slow moving vortex in the inlet, archetypal velocity calculation but this vortex rotates in the opposite direction to that in the noinlet calculation.

The geometry of the aneurysms Pat001 and Pat003 is similar, both have large asymmetric bulges, whereas the geometry of Pat002 is more symmetrical. In the noinlet calculations the z component of the velocity profile was applied at the inlet, on the correct plane. Since aneurysms Pat001 and Pat003 are highly asymmetric applying the z component of the velocity at the aneurysm entrance results in flow down one side of the aneurysm, the posterior side since the bulge is on the anterior. This explains why a large vortex, circulating down the posterior and up the anterior, persists throughout the cycle in these aneurysms. In the inlet, specific flow calculations the flow entered through a cylindrical tube which was positioned at the same angle as that section of the aorta, as found from the MRI planning scans, and so the jet entered into

the middle of the aneurysm, rather than down one side. This resulted in several smaller vortices and more helical flow, rather than just one large vortex.

The geometry of Pat002 was more symmetrical so applying the z component of the velocity resulted in flow entering the aneurysm in a similar direction to that with an inlet length (figure 4.19) although not the exactly the same direction which results in some flow differences (figure 4.20). In Pat002 the inlet velocity was measured on a plane slightly more proximal to the aneurysm bulge than that in Pat001 or Pat003 which gave a short inlet in the noinlet calculation which allows the direction to adjust accordingly.

4.3.6 Pressure

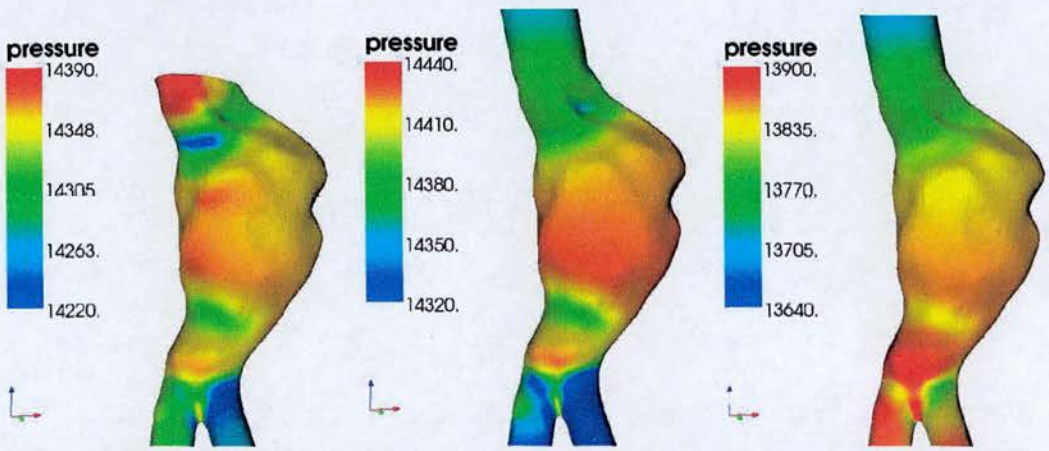

(a) Noinlet (b) Inlet, specific flow (c) Inlet, archetypal velocity

Figure 4.24: *Pressure at 191 ms in Pat001*

Pressure is shown for the the three patient aneurysms at peak systolic pressure in figures 4.24 to 4.26. Spatial variation in pressure across the aneurysm surface was very similar in all three calculations: between 120 and 170 for Pat001 (3 % of pulse pressure), between 130 and 160 Pa for Pat002 (3 % of pulse pressure) and between 230 and 310 Pa in Pat003 (4 % of pulse pressure).

Differences between the noinlet and inlet, specific flow calculations show the effect of differences in the haemodynamics, with the same flow rate, on the pressure exerted on the aneurysm wall. The differences in the peak pressure between noinlet and inlet, specific flow calculations were similar for all three patients at around 50 Pa or 1 % of the pulse pressure.

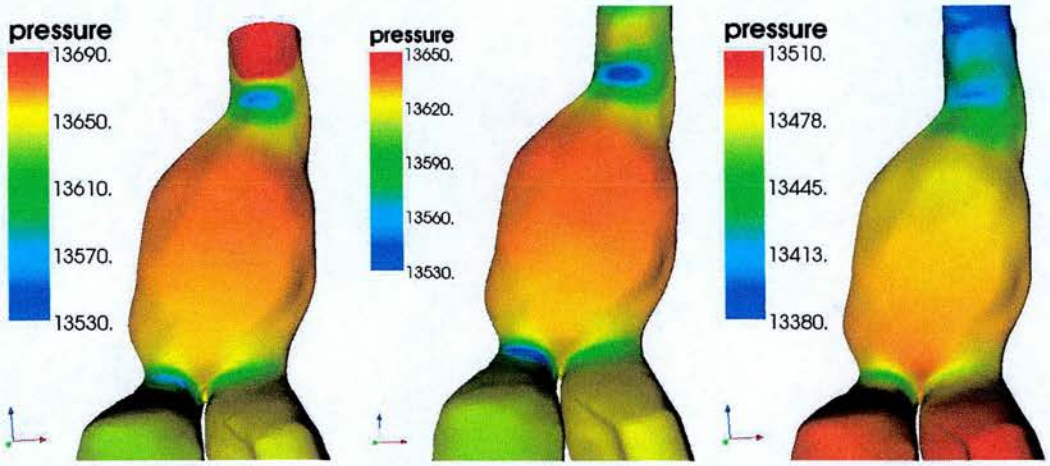

(a) Noinlet (b) Inlet, specific flow (c) Inlet, archetypal velocity

Figure 4.25: *Pressure at 191 ms in Pat002*

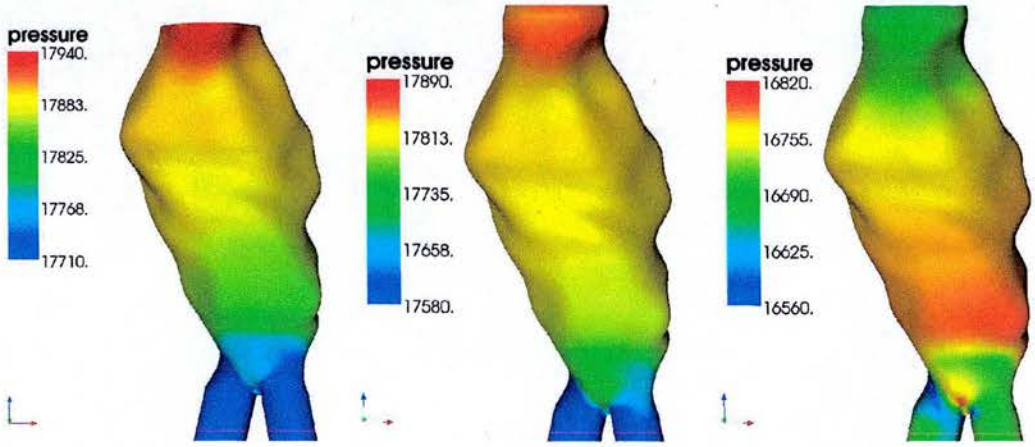

(a) Noinlet (b) Inlet, specific flow (c) Inlet, archetypal velocity

Figure 4.26: *Pressure at 149 ms in Pat003*

Pressure differences between inlet, specific flow and inlet, archetypal velocity calculations show the effect of a different flow wave on the wall pressure with the same geometry and outlet pressure wave. In Pat001 the phase difference between pressure and flow waves in the inlet, archetypal velocity calculation is slightly different to that in the inlet, specific calculation. At peak systolic pressure, the flow in the inlet, archetypal calculation has started to decelerate and hence the pressure at the inlet is below that at the outlet and the highest pressures in the aneurysm are at the distal end. This results in pressures which are lower than those in the inlet, specific flow calculation by around 540 Pa or 11 % of the pulse pressure. There is a much smaller difference in the two peak flow rates for Pat002 which means their peak pressure difference is smaller (around 140 Pa or 3 % of pulse pressure). Pat003 is similar to Pat001 with the archetypal velocity rate having started to decelerate leading to lower pressure throughout the aneurysm than at the distal end.

4.3.7 Flow Split

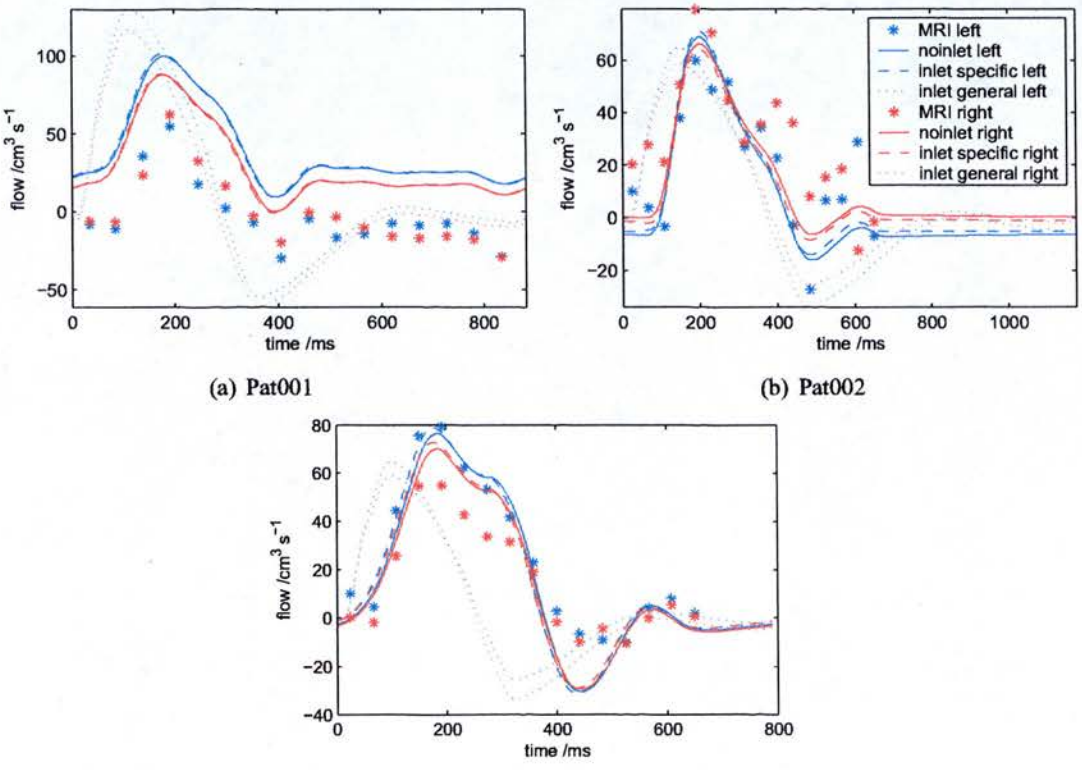

(a) Pat001

(b) Pat002

(c) Pat003

Figure 4.27: *Temporal variation in flow split at the bifurcation*

Patient	left iliac flow fraction			
	MRI	noinlet, specific velocity	inlet length, specific flow	inlet length, archetypal V_{centre}
Pat001	0.63	0.57	0.57	0.66
Pat002	0.43	0.32	0.42	0.39
Pat003	0.63	0.54	0.52	0.61

Table 4.4: *Cycle averaged flow split at aortic bifurcation*

The outlet boundary condition used for all calculations was patient specific pressure. No flow conditions were specified so the flow split was governed by the resistance caused by the geometry of the bifurcation and the diameters of the iliac arteries, and also by secondary flow components in the aneurysmal aorta [200]. *In vivo* the flow split is influenced by downstream resistance which may not be the same in both legs. The flow to each iliac artery, as measured by MRI and in the different calculations, is shown in figure 4.27. The cycle averaged flow split is shown in table 4.4.

The difference in the cycle averaged flow split of the numerical results from the MRI data was between 0.03 and 0.06 for Pat001, between 0.01 and 0.11 for Pat002 and between 0.02 and 0.11 for Pat003. These low differences suggest that in these patients it was acceptable not to apply any boundary condition on the flow split.

The difference between the total measured and calculated flow, in the iliac arteries of Pat001, is due to flow to other arteries which have not been modelled, probably the renal arteries.

There have been few studies comparing the effect of different outflow conditions on the daughter vessels of a bifurcation. Augst *et al.* [136] showed that while different flow split ratios at the carotid bifurcation significantly affected flow and WSS in to the internal and external carotid arteries, and at the bifurcation, they had very little effect on the flow or WSS in the common carotid artery. This suggests that as the aorta is the section of interest the flow split may make little difference. However, since flow in the aneurysmal aorta consists of large vortices, the flow may be more sensitive to downstream conditions than the flow in the common carotid.

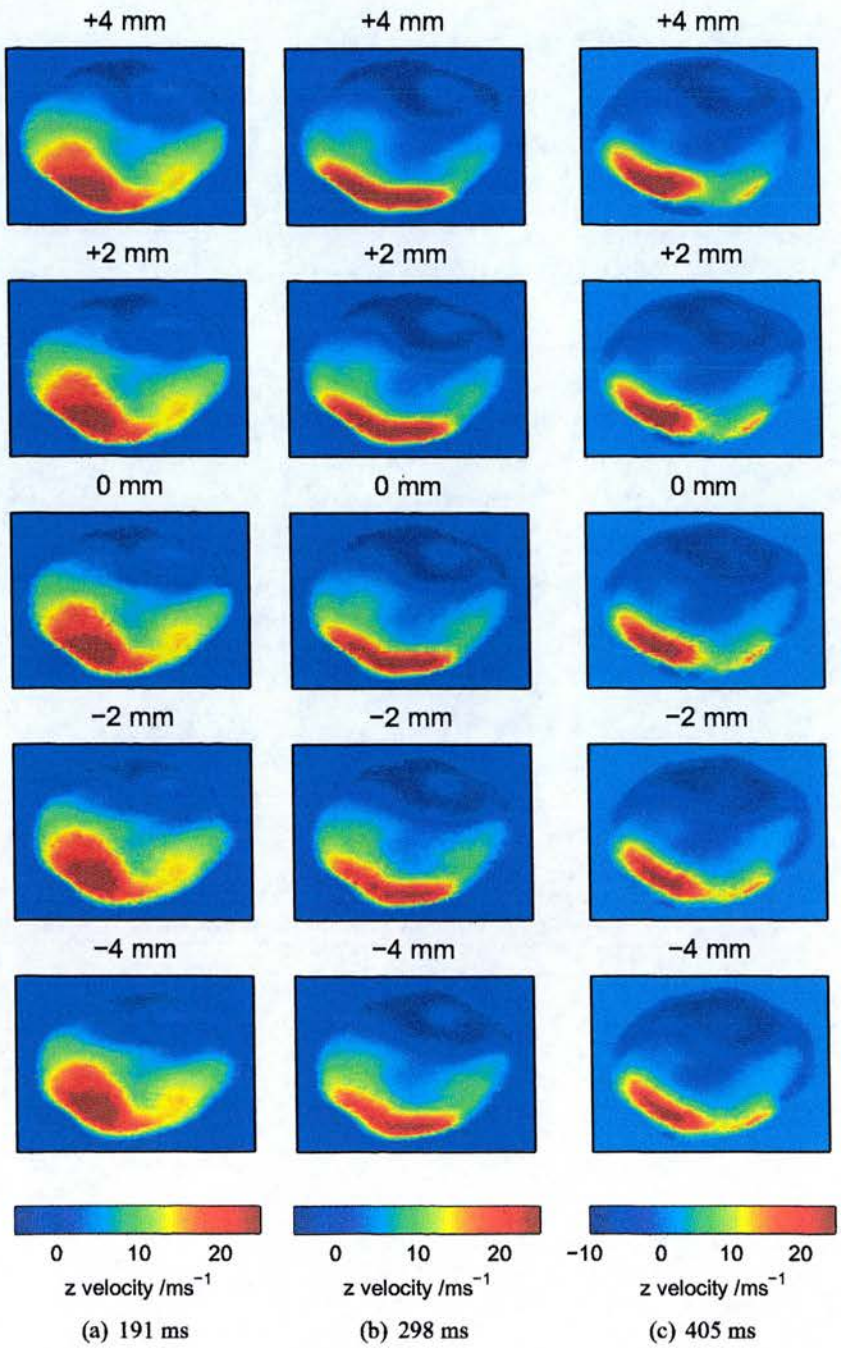

Figure 4.28: *Variation in z-velocity profiles through the thickness of the MRI slice. Profiles are for the noinlet calculation from Pat001.*

4.3.8 Spatial Averaging

The MRI flow images have a slice thickness of 8 mm. Figure 4.28 shows the variability in the CFD results for Pat001, over this slice thickness. Although the patterns are very similar there is some variability, for example, in the precise size of the forward flowing and reverse flowing regions. So, to fairly compare the CFD and MRI results it was suggested by Ku *et al.* [203] that some combination of the CFD results over the full MRI slice thickness should be used. Specifically they suggest averaging the CFD results.

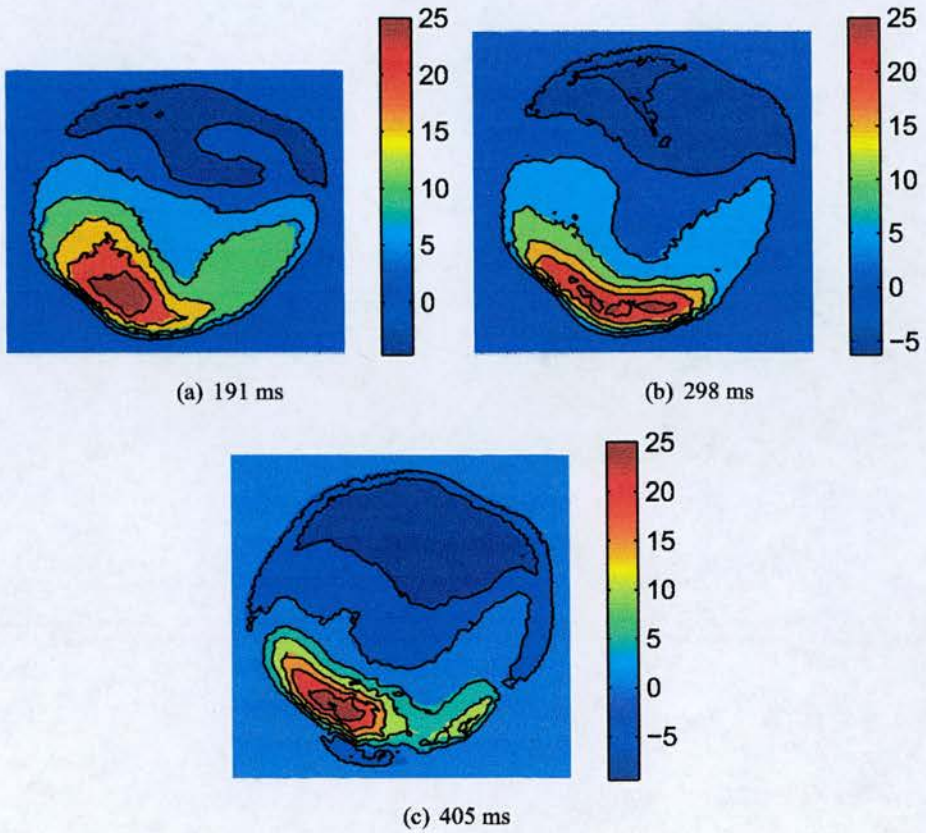

Figure 4.29: *0 mm (black lines) and mean z-velocity (colour) profiles compared. Profiles are for the noinlet calculation from Pat001.*

Figure 4.29 shows the effect of averaging the z-velocity profiles over the slice thickness, by showing isocontours for both the mean and the 0 mm z-velocity profiles. It is clear that although averaging makes some difference to the precise position of the isocontours, they are very still very nearly the same. This justifies the use of single plane profiles, rather than averaged profiles, elsewhere in this chapter.

4.4 Discussion

In this work, the results from rigid walled numerical simulations of blood flow in three aneurysmal aortas have been compared with phase contrast magnetic resonance imaging (PC-MRI) measurements of the velocity *in vivo*. Three different calculations were performed for each aneurysm with different inlet flow conditions. The first (noinlet) applied the z component of the velocity measured with PC-MRI at the inlet to the aneurysm. The second (inlet, specific flow) used the flow rate determined from the PC-MRI velocity profile at the aneurysm inlet but applied it at the entrance to a cylindrical tube inlet length. The third (inlet, archetypal velocity) calculation used the archetypal centreline velocity waveform found in Chapter 3 with the velocity profile calculated using a Womersley flow at the entrance to a cylindrical tube inlet length.

Blood flow patterns were dependent on the calculation. The application of just the z-velocity component at the inlet produced flow entering the aneurysm in that direction regardless of the aortic geometry in the entry region. In the two most asymmetric geometries this forced large vortices to be formed in the aneurysm, rotating down the posterior and up the anterior side. In one of the aneurysms this produced z-velocities, on a plane through the aneurysm, which were in agreement with the PC-MRI results. However in the other asymmetric aneurysm, the z-velocity results on the mid aneurysm plane were contradictory to the PC-MRI results, which had forward flow on the anterior side of the aneurysm. In the aneurysm which was more symmetrical, and which had a longer inlet section, z-velocities on the aneurysm plane showed good qualitative agreement, and some quantitative agreement with the PC-MRI results.

With the inlet, specific flow calculation, in which flow entered through an inlet length the jet entered the bulge more centrally. In general this produced several small vortices and helical flow. In two of the patients these results appeared to have lower correlation with the PC-MRI data but in the third the forward flow during diastole was closer to the anterior side and therefore in better agreement with the MRI results than the noinlet calculation.

The inlet, archetypal calculations produced quite different flow patterns to the inlet, specific calculations showing that flow patterns depend on the flow waveform and not simply the geometry.

One other group have compared CFD and PC-MRI results in real aneurysms. Kose *et al.* [208] imaged two patients using contrast enhanced computed tomography (CT), and measured

the z-velocity using QFlow images from PC-MRI which were then registered to the CT scans using anatomical MRI scans. The results they reported showed very good agreement for both patients. It is interesting that their results appear better than those in this work as their methods were very similar. The images of their geometries show a short inlet length before the aneurysm bulge which may be slightly longer than the inlets used in this work and could perhaps produce better results. In this work the quality of the agreement of the noinlet length results with the PC-MRI results was in the same order as the length from the inlet to the bulge (aneurysm geometries were shown in figure 4.5). That is, the aneurysm with the longest inlet (Pat002) had computational results which agreed most closely to the PC-MRI results, whereas the results from the aneurysm with the shortest inlet (Pat003) agreed least. Differences in inlet length were small, the length of the inlet in Pat002 was only about 21 mm, as compared to only 4 mm in Pat001, and in Pat003 a position distal to the neck of about 8 mm in Pat003, but this could still be important.

4.4.1 Diastolic flow

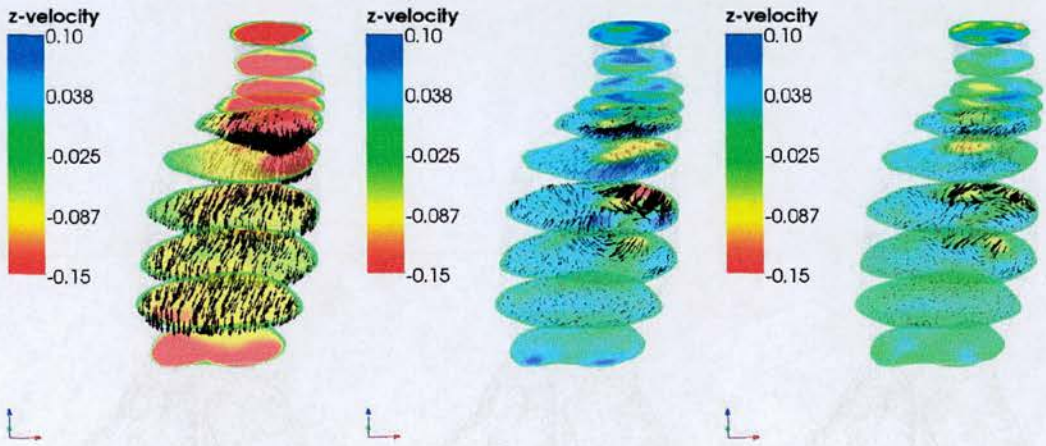

(a) 191 ms (b) 483 ms (c) 649 ms

Figure 4.30: *Formation of the diastolic jet in Pat002, viewed from the posterior. Systolic flow (a) is fast (up to 50cms^{-1}) throughout the inlet section and the iliac outlets but due to continuity is much slower in the bulge. Some of the fast flow remains at the start of diastole in the form of a jet down the right anterior side (b). As the diastolic phase progresses the flow slows as does the speed of the jet (c)*

The z-velocity results for the noinlet calculations of both Pat002 and Pat003 show spots of high velocity which appear to last throughout diastole. The maximum velocity in these spots is

higher, at some phases, than the maximum velocity anywhere on the same plane during systole.

In Pat002 this diastolic yet is down the right anterior (figure 4.30) while flow elsewhere with the aneurysm cavity is mostly slower and reversed. The flow is channelled into a jet at the top of the bulge which can be seen by the velocity vectors which point in towards the yellow spot marking the start of the jet. The volume with slow, reverse flow is much greater than the volume with fast forward flow and hence the flow rate is still negative. The maximum speed in the jet is around $20cms^{-1}$ and occurs just proximal to plane 2 at peak reverse flow. After that the flow slows down and for most of the remainder of the cycle the speed in the jet is slower than that on the same plane during systole, although a similar flow pattern persists. The length of the aneurysm is 9.2 cm and during diastole the speed of the jet decreases from the $20cms^{-1}$ to just above zero, being around $8cms^{-1}$ for the majority of the diastolic phase. The diastolic phase lasts around 700 ms so a blood element would be translated 5.6 cm along the jet.

4.4.2 Phase-Contrast MRI

Some of the MRI images, most noticeably in Pat001, but also in Pat002, showed bands which extended across the aneurysm and further. These appear to be due to ghosting, which occurs due to periodic motion [91]. The velocity scans were done with breath hold but it is possible that the patients could not hold their breath well.

Other artefacts occurring in PC-MRI images include intravoxel phase dispersion and displacement artefacts. Displacement artefacts occur because the spins move during the length of the pulse sequence. Lee and Doorly [217] investigated the causes of PC-MRI artefacts by simulating the MRI signal from a moving fluid in an arterial geometry. They showed that in regions where there were large in plane velocities the through plane velocity contours were shifted in the direction of the in plane velocities. Figure 4.31a and b, shows the PC-MRI and noinlet calculation results for Pat002 at 483 ms along with the in plane velocity vectors (figure 4.31c, d, and e) throughout the thickness of the PC-MRI slice. The region of fast flow in the PC-MRI data is shifted anticlockwise compared to the same feature in the calculation. There is significant motion in this direction predicted by the CFD and shown by the in plane vectors. This is a possible explanation for why these features do not appear in the same positions. Displacement artefacts in other images will have influenced these measurements too.

Intravoxel phase dispersion occurs when there there is a velocity gradient across the voxel,

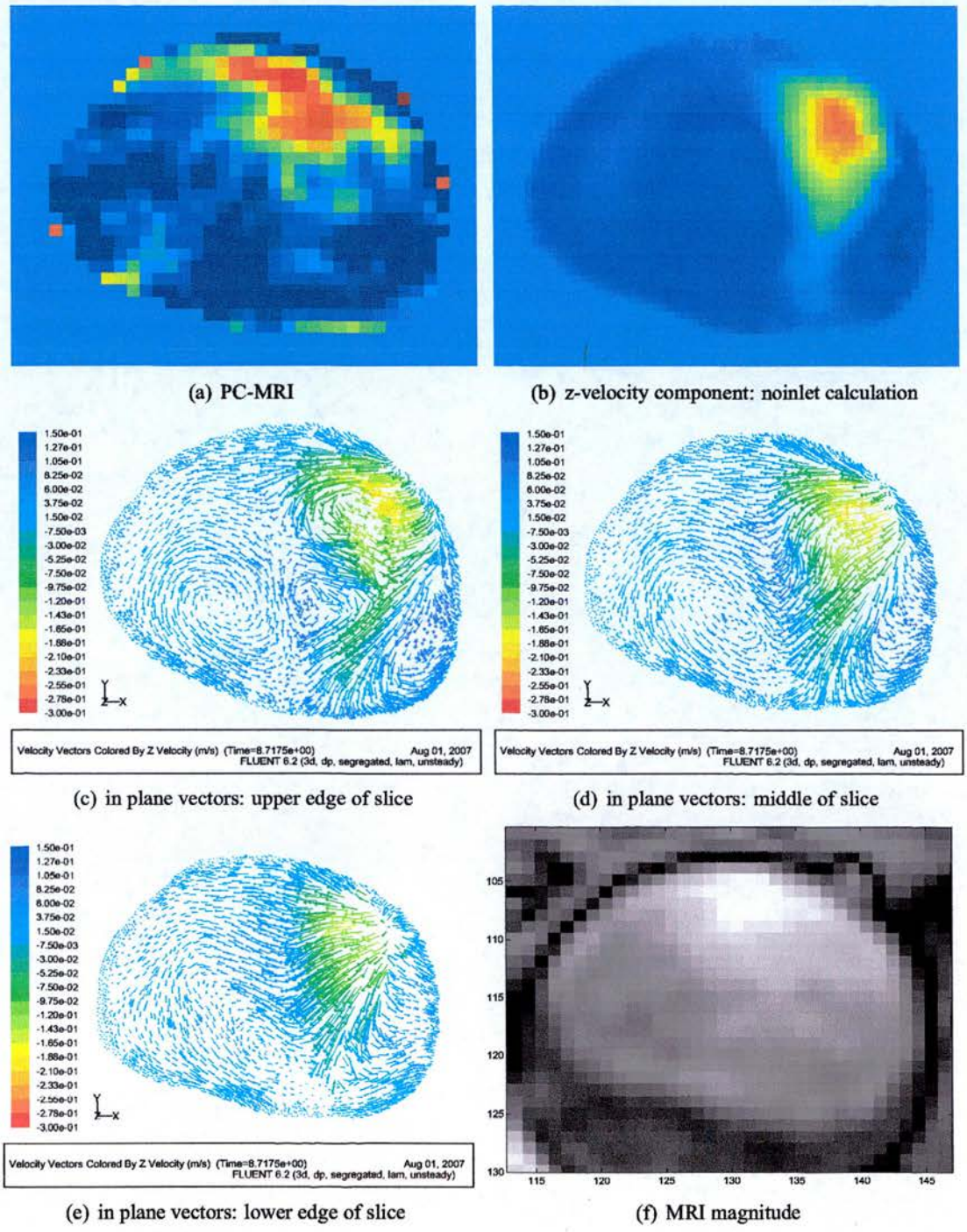

(a) PC-MRI

(b) z-velocity component: noinlet calculation

(c) in plane vectors: upper edge of slice

(d) in plane vectors: middle of slice

(e) in plane vectors: lower edge of slice

(f) MRI magnitude

Figure 4.31: *PC-MRI artefacts. Data for Pat002 at 483ms. In plane velocity vectors are coloured by through plane velocity.*

which results in dephasing of the spins and consequent signal loss. The effects are most significant in regions of low signal creating larger errors in these regions, particularly at the edges of the vessel [217].

Lee and Doorly [217] also showed that in regions were there was flow recirculation within the slice the MRI signal magnitude was reduced. This is partly because the through plane velocities are low resulting in reduced flow related signal enhancement from spins entering the slice. Also, intravoxel phase dispersion effects are potentially higher in recirculation regions because when the sequence is repeated to enable the whole of k-space to be sampled more particles contribute to the signal from a voxel. These effects can be seen in the data from Pat002. A circulating region is visible on the lower left side of the vector plots (figure 4.31c, d, and e) and this region corresponds to an area of low signal in the MRI magnitude image (figure 4.31f). Since aneurysms are full of recirculating regions these effects will have reduced the PC-MRI signal quality in all images.

4.4.3 Limitations

The most important limitations of the study appear to be the limited extent of the geometry of the aorta and the application of only the z component of the velocity on the inlet plane. Together these two factors were probably the main reasons for the differences between the numerical results and the PC-MRI results.

A sensible approach to only having the z-component of the velocity would have been to calculate the in plane components as being proportional to the z-component and resulting in flow at the same angle as the healthy aortic section measured from the planning MRI scans. Since the flow in the 'no-inlet' and 'inlet, specific' calculations was applied in different directions it would have been surprising if indeed they had resulted in the same flow patterns. This approach was not considered earlier but could be used in the future.

Flow to the renal arteries is high, Bax *et al.* [218] measured renal flow in 20 patients and found the mean total renal flow was 18 ml s^{-1}, but was up to 27 ml s^{-1} in some patients. This probably influenced the simulations of Pat001. Anatomical constraints make it difficult to locate a plane which is both distal to the renal arteries and proximal to the aneurysm bulge. Future studies could try scaling the inlet velocity profile by the iliac flow rate, or explicitly modelling the renal arteries.

Calculations were performed for 5 cardiac cycles and cyclic convergence was assessed by comparing the results from the 4th and 5th cycles. The mean percentage differences were mostly less than 12 % although two of the noinlet calculations had differences of about 35 % which suggests velocity gradients on the inlet may have made these take longer to become converged than the calculations with an inlet length. Mesh convergence was assessed by comparing results from coarse and fine meshes and percentage differences were about 20 - 30 %. Accuracy of the numerical simulations could have been improved by using finer meshes and calculating more cardiac cycles but this is unlikely to change the overall flow features and the comparison with PC-MRI results.

Wall motion was assessed as being less than 10 % and more like 2.5 % in the diseased region. This change in wall position with time will alter the blood velocities. From simulations of blood flow in the aortic arch, where wall motion was around 23 % of the diameter, it was apparent that the flow could only be realistically calculated by including the wall motion [148]. However, a study on the superior mesenteric artery, with dilation about 5 % and translation about 50 %, showed an average difference in WSS of just 2.1 % between simulations with moving and rigid walls [219]. The effects of wall motion on flow in aneurysms still needs to be determined.

Resolution of the MRI geometry data in the z direction was only 9.4 - 10 mm. Reconstruction of the artery from the slice contours was performed using splines. The reconstruction method was shown not to change the positions of the contours, but the accuracy of the geometry between the contours has not been assessed and could lead to errors in the simulated blood flow [204].

Manual segmentation is subjective and should ideally be performed by skilled radiologists with the intra and inter observer variation determined. In this work segmentation was performed by one physicist. In addition the images were displayed in colour for segmentation which may have resulted in the contours being positioned slightly outside the lumen boundary. Figure 4.32 shows four of the slices from Pat001 in both colour and greyscale. A region of lighter blue can be seen within the contours on some colour images, but on the greyscale images the same region looks black.

The SphygmoCor system calculates the aortic pressure wave in the ascending aorta rather than the abdominal aorta and which will give a different pressure wave due to propagation along the aorta. However, in a rigid walled model the pressure only has a small influence on the haemodynamics.

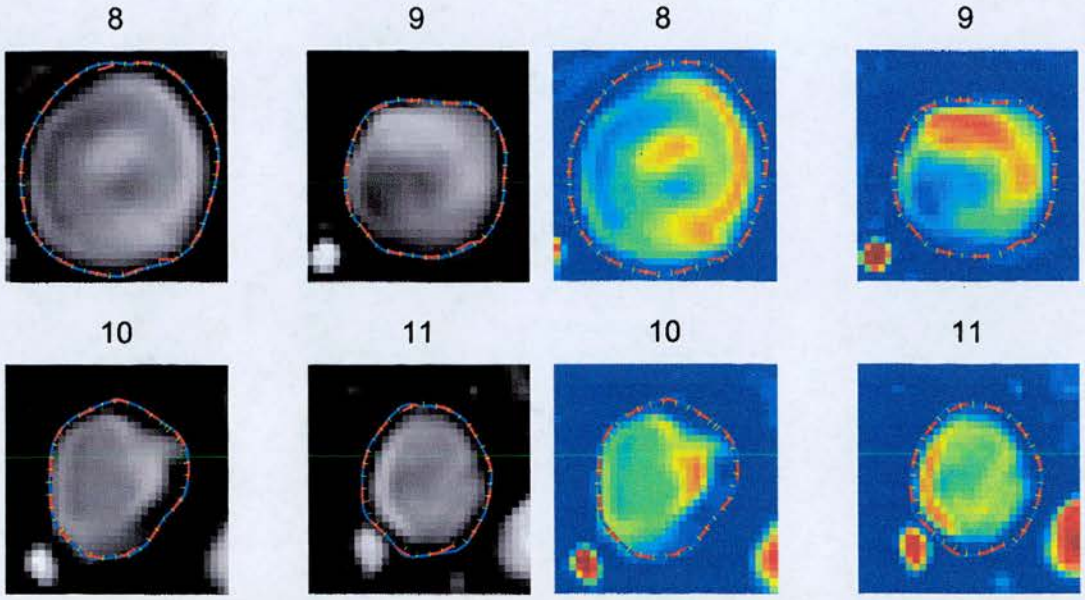

(a) greyscale images (b) colour images

Figure 4.32: *Viewing image data with different colour maps may lead to different interpretations. The time frames have been averaged to give images for four slices from Pat001.*

4.5 Conclusions

Numerical calculations of blood flow in abdominal aortic aneurysms have been compared with PC-MRI results. Calculation results were shown to be strongly dependent on the inlet flow conditions. Calculations of the flow in two patient geometries showed good agreement with the measurements but calculations in the third patient were completely different.

Application of the z-velocity at the aneurysm entrance does not, in general, produce the correct flow within the aneurysm, especially if the inlet plane is very close to the aneurysm bulge. However, application of the z-velocity when there is a short section of the correct aortic geometry before the aneurysm bulge appears to improve the flow predictions. More investigation would be required to confirm this. The renal arteries are another consideration as the flow should ideally be measured after these branches. It is difficult to calculate the flow in aneurysms since flow in the bulge is very sensitive to the flow in the inlet and small changes in the inlet flow can alter the flow in the bulge dramatically.

Chapter 5
Fluid Structure Interactions in Axially Symmetric Aneurysm Models

So far aneurysms have been modelled as having walls which are fixed in place. However, as the blood pressure pulse propagates along an artery the wall dilates under the pressure and then contracts behind the pulse. Thus in simulations the blood flow domain should dilate and contract, altering the flow patterns within. Also, the stress on the artery wall is a function of the blood pressure acting on it. Since the blood is flowing, the pressure on the wall is temporally and spatially inhomogeneous; the blood and the artery undergo a fluid-structure interaction. In this chapter fluid structure interaction in simple aneurysm models will be investigated to assess the effects of moving walls on the blood flow and the effects of the blood flow on the tissue stresses.

5.1 Introduction

In abdominal aortic aneurysms, the tissue stresses in the artery wall are considered to affect the rupture risk of the aneurysm [54, 57, 58] and are thought to be a more accurate indicator of rupture risk than diameter. So, accurate estimation of tissue stresses is desirable. There are many factors which are thought to influence the tissue stress: aneurysm size, shape [155, 156, 158], wall thickness [52] and the presence of an intraluminal thrombus. The haemodynamics may also affect the wall tissue stress via the fluid-structure interaction but the extent of their influence is unclear.

Fluid structure interactions (FSI) in abdominal aortic aneurysms have been used by several authors [56, 172, 173, 182, 220–222]. The influence of the FSI on the tissue stress in AAAs was studied by Scotti *et al.* [172] in simple geometries. They investigated the effects of a fluid structure interaction in models of AAA with varying asymmetry and wall thickness. With regard to the tissue stress, they conclude that in a symmetric model, with homogeneous wall thickness, neglecting the effect of the fluid structure interaction resulted in an underestimate of

the peak wall tissue stress of 9 %. This increased to 29 % with a heterogenous wall thickness, but increasing the asymmetry made little difference.

Leung *et al.* [173] examined the effects of incorporating the fluid structure interaction into patient specific models of AAA using patient geometries obtained by segmenting the lumen from CT scans. Since this only gave the blood flow domain they fabricated a wall by assuming a uniform thickness outside the lumen region. Their conclusions on tissue stress were in opposition to those of Scotti *et al.* [172]: they found less than 1 % difference between the peak stress in the static and fluid-structure interaction models. The reason for these differing conclusions is not obvious: both groups used similar boundary conditions, the same wall elasticity, and the same FSI interaction. One possibility is the aneurysm shapes used. Scotti *et al.* [172] used idealised shapes with a maximum diameter of 6 cm and an inlet diameter of 2 cm. Leung *et al.* [173] used lumen geometries obtained from patients and their diameters were in the range 3.2 to 4.2 cm. Since the diameter of the normal abdominal aorta is around 2.0 to 2.5 cm, the dilation of the geometries used by Leung *et al.* [173] is much smaller than that of the geometries used by Scotti *et al.* [172].

Papaharilaou *et al.* [185] modelled the wall tissue stress in a large, 10 cm, aneurysm without any significant thrombus using a decoupled fluid structure interaction. That is, they calculated the pressure on the wall from the fluid dynamics and applied that pressure to the solid model. They report that a static analysis gave a peak wall stress 12.5 % lower than their decoupled FSI analysis. None of the above papers included intraluminal thrombus in their calculations.

Although it is of less interest clinically, the blood flow in AAAs is very interesting from a biomechanical perspective. Briefly, the nature of the flow field affects the delivery of platelets and monocytes to the endothelium [40], or the thrombus layer, as well determining the shear stress which acts on the endothelial cells [34–36] and influences platelet activation and adhesion [2, 3].

Scotti *et al.* [172] found that the flow fields in their FSI models were very different from those in calculations using the same boundary conditions in rigid aneurysm models [153]. At the time of peak systolic pressure, which occurred during flow deceleration, the streamlines in all FSI models were laminar. However, in the rigid walled models vortices had formed in the proximal part of the aneurysm. The difference is due to contraction of the aneurysm during flow deceleration, which drives fluid out of the aneurysm and prevents the flow separation

driving the vortices. Further evidence that the wall motion significantly alters the flow is given by computational fluid dynamics (CFD) studies of healthy arteries with moving walls. For example Jin *et al.* [148] examined the affect of wall motion on flow in the ascending aorta, by comparing CFD with MRI measured velocities. They found that computed results agreed with the MRI measurements only when the full wall motion was accounted for. However, the aortic arch is a highly mobile section of the aorta. The abdominal aorta moves far less, which, combined with the increased stiffness of the aneurysmal aorta compared with the normal aorta, may mean that the wall motion has only a small affect on the flow.

In this work two commercial software packages were coupled together to model the FSI in simple aneurysm models. The complete FSI calculations were compared with simpler homogeneous pressure, rigid walled, and 1-way coupled simulations in order to assess the importance of incorporating the fluid structure interaction in aneurysms. The aims were: to investigate the effects of increasing the bulge diameter and altering the material stiffness on tissue stresses; to assess the effect of the thrombus on the peak tissue stress; and to assess the influence of the fluid structure interaction on blood flow patterns and wall shear stress (WSS) in aneurysms with increasing diameter, material stiffness and thrombus thickness.

5.2 Methods

5.2.1 Fluid Structure Interaction

Fluid structure interaction (FSI) problems can be solved using either a fully coupled approach or an iterative method [223]. In the fully coupled approach the fluid and solid equations are solved simultaneously [224]; the solution is likely to be stable, and efficient, but including all the complexities normally available for either fluid or solid calculations is difficult. In the iterative method the flow equations are solved first, assuming a rigid wall, then the deformation of the elastic wall is calculated by applying the pressure load. The iterative method is slower but state of the art codes for both fluid and solid domains can be included.

The iterative method used was developed by Li [223, 225] for investigating stenosed arteries. Similar methods have been used for studying, for example, the carotid bifurcation [226], and stented abdominal aortic aneurysms [220, 221].

The incompressible Navier-Stokes equations describe the three-dimensional time dependent

flow of a Newtonian fluid through the compliant tube. The distensible wall is incorporated using an Arbitrary Lagrangian Eulerian formulation. The fluid domain is an Eulerian reference frame while the solid is solved in a Lagrangian reference frame.

Two commercial packages were used: Fluent v. 6.2.16 (Fluent Inc., Lebanon, New Hampshire, USA) to calculate the flow domain; and Abaqus 6.54 (Abaqus Inc., Providence, RI) to calculate the solid domain. These were coupled using an in-house interface written in Matlab v. 6.5 r.13 (The Mathworks Inc., Natick, MA) code by Mingxiu Li [223, 225]. The code has been adapted here for use with aneurysms, in particular, the solid domain was modelled as 2D axisymmetric and deformations in the longitudinal direction were accounted for. Validation of FSI codes is important [227] and the code was validated by Li [223, 225] against the Moens-Korteweg equation for the wave speed in a thin walled elastic tube and the error was found to be within 10 %.

The flow was solved first and pressure from the fluid solution acted on the solid to deform it. The displacement of the solid was used to adjust the fluid domain and the flow was resolved. Hence the solution iterated between solid and fluid until convergence was achieved. A convergence parameter for pressure was defined,

$$P_n = \max\left(\frac{|p_i^n - p_i^{n-1}|}{|p_i^n|}\right) \tag{5.1}$$

where p_i^n was the pressure at node i at the nth iteration and max signifies that the maximum value for all the nodes is taken. A convergence parameter D_n was defined for the displacement in the same way. The solution was defined as being converged when,

$$P_n, D_n \leq 0.001 \tag{5.2}$$

that is, the difference in pressure and displacement between successive iterations was less than 0.1%. A small deformation in the flow domain causes a large change in the pressure [227] so it was necessary to use under-relaxation.

5.2.2 Simpler Methods

In addition to the complete FSI simulations (called FSI_2 below) simpler calculations were also performed in order to assess the importance of including the complete interaction. Complete

fluid-structure interaction calculations are computationally intense so if simpler calculations can be used they should be, and one of the aims of this work is to determine the conditions under which simpler simulations can be used.

Other simulations carried out in this work were:

SP - a homogeneous pressure analysis applying the time dependent outlet pressure wave along the whole length of the aneurysm.

RW - a fluid simulation with rigid walls. The wall was deformed to its position at diastolic pressure first using a SP calculation to ensure the diameter of the vessel was similar to that in the FSI calculations.

FSI_{1SP} - a one way coupled simulation with wall motion found from a SP calculation with the outlet pressure applied homogeneously and flow calculated in the moving domain.

FSI_{1RW} - a one way coupled simulation with wall motion obtained from applying pressure found from a RW calculation to the solid and then flow calculated in the moving domain.

FSI_2 - complete fluid structure interaction.

5.2.3 Models

5.2.3.1 Geometry

There have been many studies on abdominal aortic aneurysms based on simple models which have used various geometric shapes as the aneurysm bulge, for example: Gaussian curves [158], cosine curves [157] and ellipsoids [76]. Although real AAAs come in a wide range of shapes, from studying a number of AAAs, see figure 5.1, it appears that in many the change from a normal width aorta to the the bulged region is quite sudden and in general encompasses two regions of particularly high curvature over the length of the neck. From the work of Elger *et al.* [155], who examined tissue stresses in various aneurysm shapes analytically, these aneurysms with high curvature should experience higher stresses than more smoothly varying ones and so this type of shape was chosen for this study as a worst case scenario. The wall shape can be described mathematically as a parabola-exponential. That is, if the axis of symmetry is the x

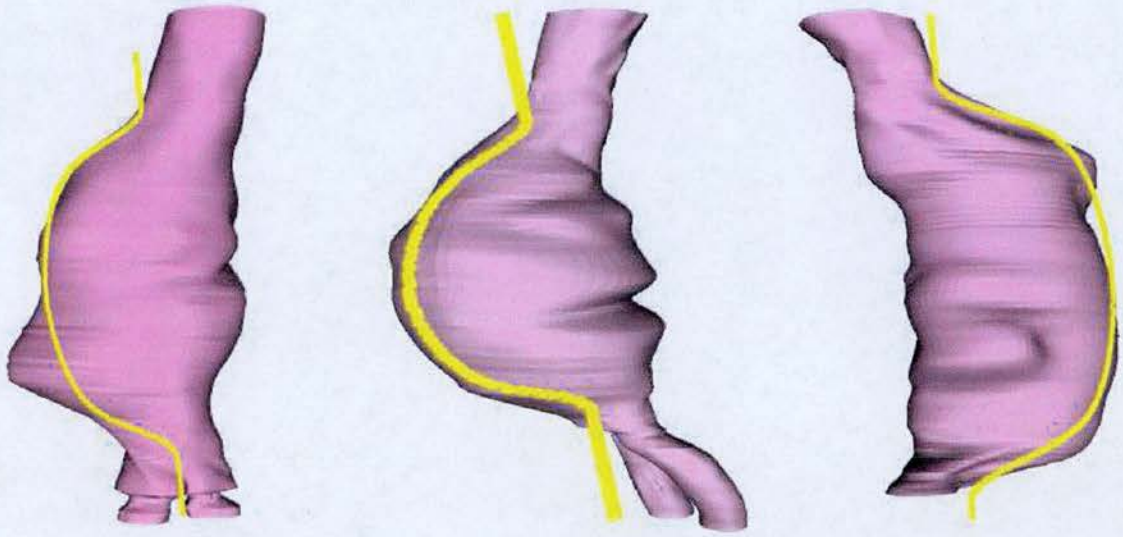

Figure 5.1: *Real AAAs and parabola-exponential curves*

axis and y describes the position of the wall then,

$$y = e^{-C_1|x/r_a|^{C_2}}\left[(r_b - r_a) - C_3\left(x^2/r_a\right)\right] + r_a \tag{5.3}$$

where r_a is the radius of the undilated section which was chosen to be 1 cm, as for the normal abdominal aorta, r_b is the maximum radius of the aneurysm and C_1, C_2 and C_3 are constants which were chosen to give an approximately realistic AAA curve: $C_1 = 10^{-3}$, $C_2 = 10$ and $C_3 = 0.2$. Aneurysm models were created with a range of r_b from 2 to 3.5 cm, see table 5.1.

5.2.3.2 Wall Properties

There have been many studies of the mechanical properties of both normal and aneurysmal abdominal aortic tissue. Vande Geest *et al.* [228] investigated the biaxial properties of the normal abdominal aorta and found that, although under equibiaxial tension there was no significant difference in the circumferential and longitudinal peak stretches, individual samples were anisotropic: stiffer in the circumferential direction than in the longitudinal direction.

He *et al.* [19] compared tissue from eight normal and eight aneurysmal aortas in uniaxial tests and found aneurysmal tissue to be significantly stiffer than normal tissue. They fitted the stress-

strain relationships to an exponential relationship:

$$\sigma = ae^{b\varepsilon} \tag{5.4}$$

were σ is the stress, ε is the strain, and a and b are fitting parameters. a was 319 ± 81 for aneurysmal tissue and was not significantly different for normal tissue, whereas there was a significant difference in the values of b: 25.0 ± 4.1 for normal tissue compared to 38.7 ± 6.6 for aneurysmal tissue. Raghavan *et al.* [60] also found AAA tissue to be significantly stiffer than normal tissue in uniaxial tests and their results suggested AAA tissue was essentially similar in circumferential and longitudinal directions. Thubrikar *et al.* [62] performed uniaxial texts on AAA tissue from different regions of aneurysms. In contrast to Raghavan *et al.* [60] they found that in all regions the wall stiffness was greater in the circumferential than the longitudinal direction, and in addition the lateral and anterior regions were stiffer in both directions than the posterior region. The most recent investigation of the *ex vivo* mechanical properties of AAA tissue was by Vande Geest *et al.* [149] who performed biaxial testing. As with their normal abdominal aortic specimens [228] there was no significant difference in the average values of circumferential and longitudinal peak stretches, but, the individual samples exhibited anisotropic behaviour which was stiffer circumferentially than longitudinally. They used the following strain energy function:

$$W = b_0 \left(e^{b_1 E_{\theta\theta}^2/2} + e^{b_2 E_{LL}^2/2} + e^{b_3 E_{\theta\theta} E_{LL}} - 3 \right) \tag{5.5}$$

where $E_{\theta\theta}$ and E_{LL} are the Green strain tensor components in the circumferential and longitudinal directions and b_0 - b_3 are the fitted parameters.

Although most authors have reported anisotropic stiffness, because the objective of this work was to evaluate the importance of FSI, it was felt that an isotropic model was sufficient. The model used was also homogeneous which is a further limitation.

The wall was modelled as an incompressible material with a hyperelastic stress-strain relationship given by Raghavan and Vorp [59] based on their earlier measurements [60]. The strain energy W, as a function of the first invariant, I_B, of the Left Cauchy-Green tensor, B, is given by,

$$W = \alpha(I_B - 3) + \beta(I_B - 3)^2 \tag{5.6}$$

Raghavan and Vorp [59] used the data from their earlier paper [60] to find mean and 95%

confidence intervals for the coefficients α and β. These values were used here to create three different materials to assess how variation in the material stiffness affects the tissue stress and blood flow. The stress strain relationship for the three models is shown graphically in figure 5.2.

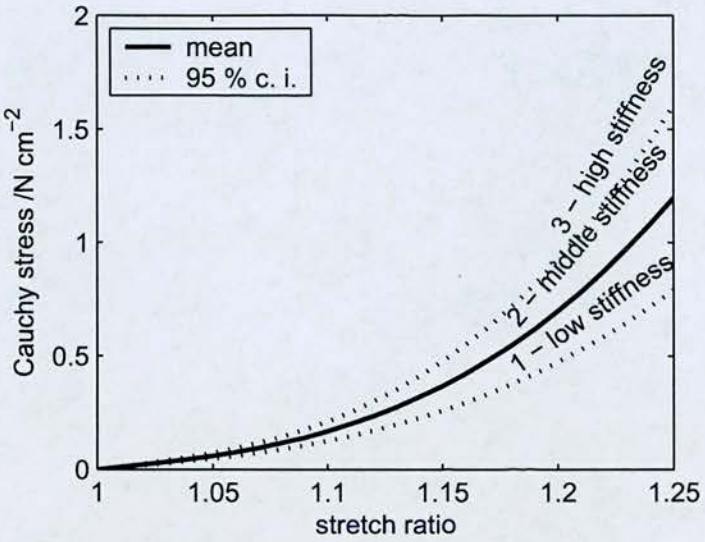

Figure 5.2: *Stress strain relationships for the three AAA wall material models used.*

Raghavan *et al.* [61] measured the wall thickness at 100 sites on 4 excised AAAs and found it was inhomogeneous, varying from 0.23 mm, near to a site of rupture, up to 4.26 mm, at a calcified site. In this work the wall had a homogeneous thickness of 1.48 mm, which is the median of the measurements by Raghavan *et al.* [61].

5.2.3.3 Thrombus Properties

There have been several studies of the mechanical properties of intraluminal thrombus. Di Martino *et al.* [161] performed uniaxial mechanical tests on thrombus samples and found a linear stress strain relationship with a Young's modulus, E_Y, of 0.13 ± 0.06 MPa. Wang *et al.* [43] fitted their data to a strain energy function:

$$W = c_1(\mathrm{II_B} - 3) + c_2(\mathrm{II_B} - 3)^2 \tag{5.7}$$

where $\mathrm{II_B}$ is the second invariant of the Left Cauchy-Green tensor, B, and c_1 and c_2 are the fitted parameters. They found no difference in c_1 and c_2 between circumferentially and longitudinally

oriented samples suggesting isotropic properties, but they were higher in the luminal than the medial layer, showing the thrombus is heterogeneous. With biaxial mechanical testing Vande Geest *et al.* [229] confirmed the thrombus is isotropic but their biaxial strain energy function was quite different to the uniaxial one [43].

In this work the linear model used by Mower *et al.* [163] was adopted for the thrombus with $E = 0.1$ MPa and Poisson's ratio 0.49 (as the thrombus is nearly incompressible [230]).

A further three models were created with varying thicknesses of thrombus. These three had the same wall as model 1 but with the addition of a thrombus layer which filled the space between the wall and a parabola-exponential, equation 5.3, with $r_a = 1.0$ cm, $r_b = 3\text{cm} - r_c$ where r_c is the maximum thickness of the layer and $C_1 = 10^{-3}$, $C_2 = 15$ and $C_3 = 0.2$.

model	maximum radius r_b/cm	maximum thrombus thickness r_c/cm	wall properties /MPa	
			α	β
1	3.0	0	0.174	1.881
2	3.0	0	0.144	1.152
3	3.0	0	0.204	2.610
4	3.5	0	0.174	1.881
5	3.0	0.5	0.174	1.881
6	3.0	1.0	0.174	1.881
7	3.0	1.5	0.174	1.881
8	2.0	0	0.174	1.881
9	2.5	0	0.174	1.881

Table 5.1: *Summary of model properties. Diameter is the diameter of the unstressed model.*

5.2.4 Meshes

The aneurysms were modelled as 2D axisymmetric and meshes were created in Gambit v. 2.2.30 (Fluent Inc., Lebanon, New Hampshire, USA).

5.2.4.1 Inlet and Outlet Lengths

The geometry of the 'standard' shape for the 6 cm diameter aneurysm is shown in figure 5.3. It was necessary to check that the inlet and outlet lengths were long enough; that is that the

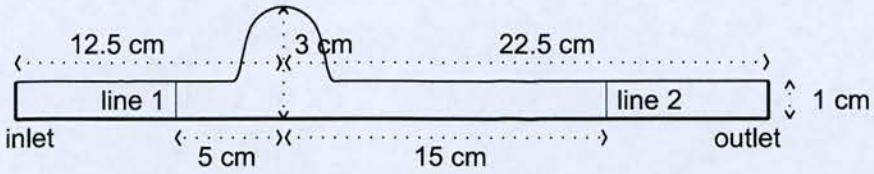

Figure 5.3: *Geometry of the 'standard' 6 cm diameter aneurysm*

solution was unaffected by making them longer.

The 'standard' 6 cm aneurysm has an inlet length of 12.5 cm, where the term 'inlet length' is defined as the distance from the inlet to the position of maximum diameter. Additional meshes were produced with inlet lengths of 11.5, 13.5 and 35.0 cm and the axial-velocity on line 1, throughout the cardiac cycle and after 3 cycles, was calculated for each mesh.

The 'standard' 6 cm aneurysm has an outlet length of 22.5 cm; the term 'outlet length' is defined as the distance from the position of maximum diameter to the outlet. Additional meshes were produced with outlet lengths of 21.5, 23.5 and 50.0 cm and the axial-velocity on line 2, was calculated for each mesh.

5.2.4.2 Lumen Mesh

The 6 cm aneurysm shape was meshed using structured quadrilaterals in the inlet and outlet zones as shown in figure 5.4. The central, bulged region was meshed using unstructured quadrilaterals.

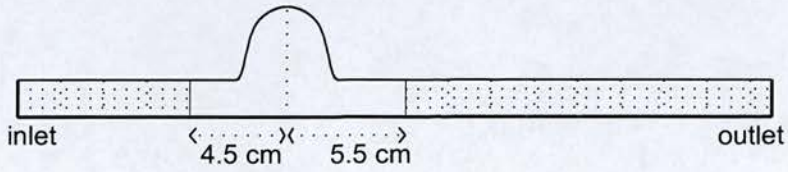

Figure 5.4: *Mesh for 6 cm aneurysm*

Three meshes were produced, each with a grid spacing half that of the coarser mesh; mesh parameters are given in table 5.2.

Flow was calculated using inlet flow and outlet pressure (described below) using the different meshes and with time steps as shown in table 5.2. Velocity magnitudes from the three meshes were compared to assess mesh convergence.

mesh	structured zones		unstructured zones	time step
	longitudinal spacing (mm)	radial spacing (mm)	spacing (mm)	(s)
8	1.6	0.8	0.8	0.012
4	0.8	0.4	0.4	0.006
2	0.4	0.2	0.2	0.003

Table 5.2: *Mesh parameters*

5.2.4.3 Wall Mesh

The wall of the 6 cm aneurysm was meshed using 3-node, axisymmetric shell elements. Three meshes were created with elements 0.4 mm, 0.8 mm and 1.6 mm long. The aneurysm was inflated to peak systolic pressure, 16.3 MPa (122 mmHg), and stresses and displacements with the three different meshes were compared.

5.2.4.4 Thrombus Mesh

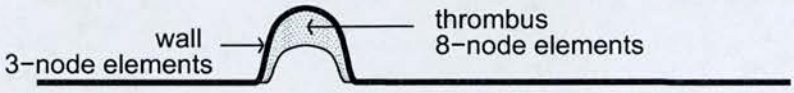

Figure 5.5: *Solid mesh for 6 cm aneurysm with 1 cm thrombus layer*

The geometry of the 6 cm aneurysm with a 1.5 cm thrombus layer is shown in figure 5.5. Three meshes were created with 0.4, 0.8 and 1.2 mm elements. The wall was meshed with 3-node, axisymmetric, shell elements and the thrombus was meshed with 8-node, axisymmetric elements. The aneurysm was inflated to peak systolic pressure, 16.3 MPa (122 mmHg), and stresses and displacements with the three different meshes were compared.

5.2.5 Boundary Conditions

A velocity condition was used at the inlet with the aortic bifurcation flow wave taken from the paper by Olufsen *et al.* [132] (figure 5.6) and the spatial velocity profile derived assuming fully developed, Womersley, flow [179]. The boundary condition used at the outlet was the aortic bifurcation pressure wave from the same paper [132]. Olufsen *et al.* measured the flow in the aorta of a healthy male using MRI and estimated the pressure by solving a 1D model of the arterial system with structured tree outflow conditions.

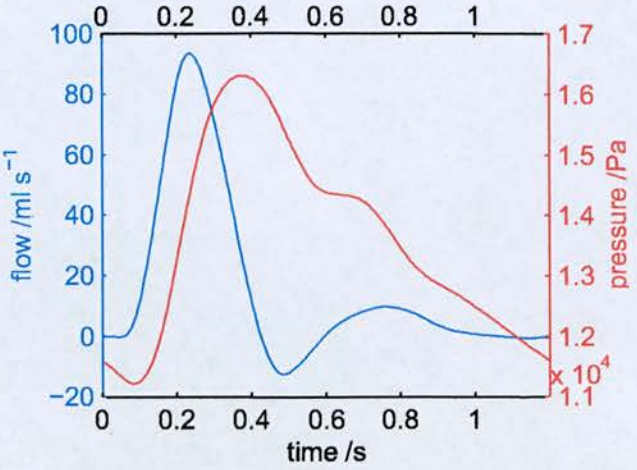

Figure 5.6: *Inlet flow and outlet pressure boundary conditions*

The aneurysm models were longitudinally tethered by constraining the nodes at both ends to only move radially.

5.3 Results

5.3.1 Meshes

5.3.1.1 Inlet and Outlet Lengths

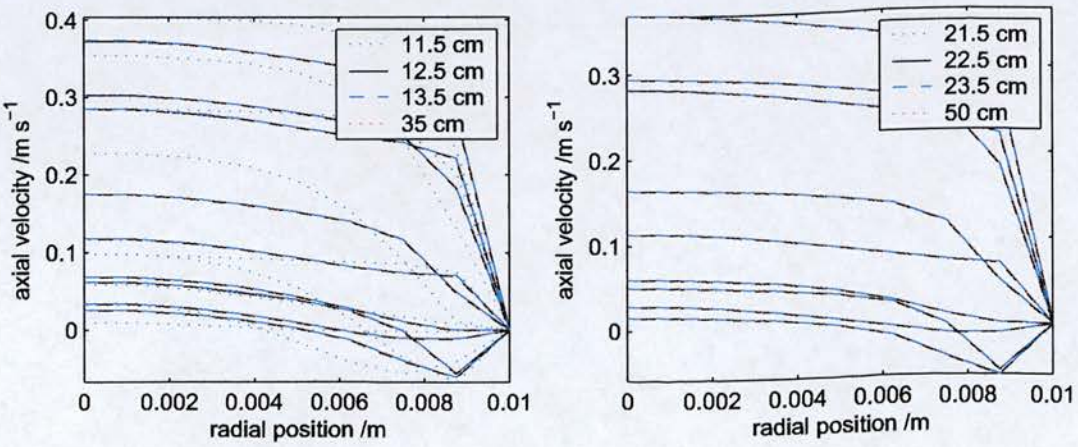

Figure 5.7: *Variation in axial velocity with length of inlet (left) or outlet (right)*

The variation in the axial velocity on line 1 with length of inlet is shown in figure 5.7. Extending the inlet length did not appear to make a difference to the axial velocity on line 1. The mean

percentage difference between the axial velocity on line 1 with the standard 12.5 cm inlet and with the 35 cm inlet was 0.9 %. The difference between the profiles at 11.5 and 12.5 cm is unlikely to be realistic and is probably a reflection of the coarseness of the mesh in these calculations.

The variation in axial velocity on line 2 with outlet length is also shown in figure 5.7. Small changes in the position of the outlet made no change to the velocity and neither did extending the outlet length. The mean percentage difference between the axial velocity on line 2 with the standard 22.5 cm outlet and with the 50 cm inlet was 0.8 %.

5.3.1.2 Lumen Mesh Convergence

The effect of mesh refinement was examined by comparing velocity magnitude at points on the three meshes. The order of mesh convergence, p, was calculated for each point using [194, 231]:

$$p = \ln\left(\frac{c_8 - c_4}{c_4 - c_2}\right) / \ln(r) \tag{5.8}$$

where c is the velocity magnitude and r is the mesh refinement ratio which was 2 here. p varied with position but the mean was found to be 2.1 so for most of the geometry the solution was 2nd order.

The following ordered error estimators [194] were used to calculate the mean percentage errors for each grid which are shown in figure 5.8:

$$E_{\text{fine}} = \frac{\varepsilon}{r^p - 1} \tag{5.9}$$

$$E_{\text{coarse}} = \frac{\varepsilon r^p}{r^p - 1} \tag{5.10}$$

where,

$$\varepsilon = \frac{c_2 - c_1}{c_2} \tag{5.11}$$

The solutions were in the asymptotic range [194]:

$$\frac{E_{48}}{r^p E_{24}} = 1.1 \tag{5.12}$$

The velocity magnitude on the radial line at the maximum bulge diameter with each mesh is

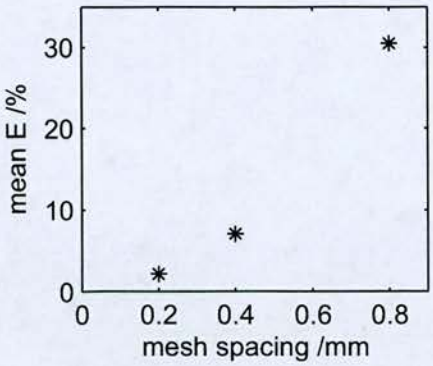

Figure 5.8: *mean error*

shown in figure 5.9. Also shown are the values for a '0 mm' mesh, the continuum values. These were calculated using Richardson extrapolation [194] with meshes 2 and 4:

$$c_0 \cong c_2 + \frac{c_2 - c_4}{r^p - 1} \tag{5.13}$$

5.3.1.3 Wall Mesh Convergence

The radial wall displacement and Mises stress on the inner edge of the wall are shown in figure 5.10. There is negligible difference in both stress and displacement over this range of mesh densities. The peak displacement was 1.75 mm for all three meshes and the peak Mises stress was 0.5569, 0.5551 and 0.5538 MPa for the 0.4, 0.8 and 1.6 mm meshes respectively. Errors in finite element analyses can be calculated based on Richardson extrapolation [232], in the same way as CFD errors. This gives an ordered error estimate of 0.1 % on the 0.4 mm wall mesh.

5.3.1.4 Thrombus Mesh Convergence

The radial wall displacement and Mises stress on the inner edge of the wall are shown in figure 5.11. As in the model without thrombus there is negligible difference in both stress and displacement over this range of mesh densities. The peak displacement was 1.53 mm with all three meshes and the peak Mises stress was 0.4322, 0.4318 and 0.4322 MPa with the 0.4, 0.8 and 1.2 mm meshes respectively. The ordered error estimate is 0.03 %.

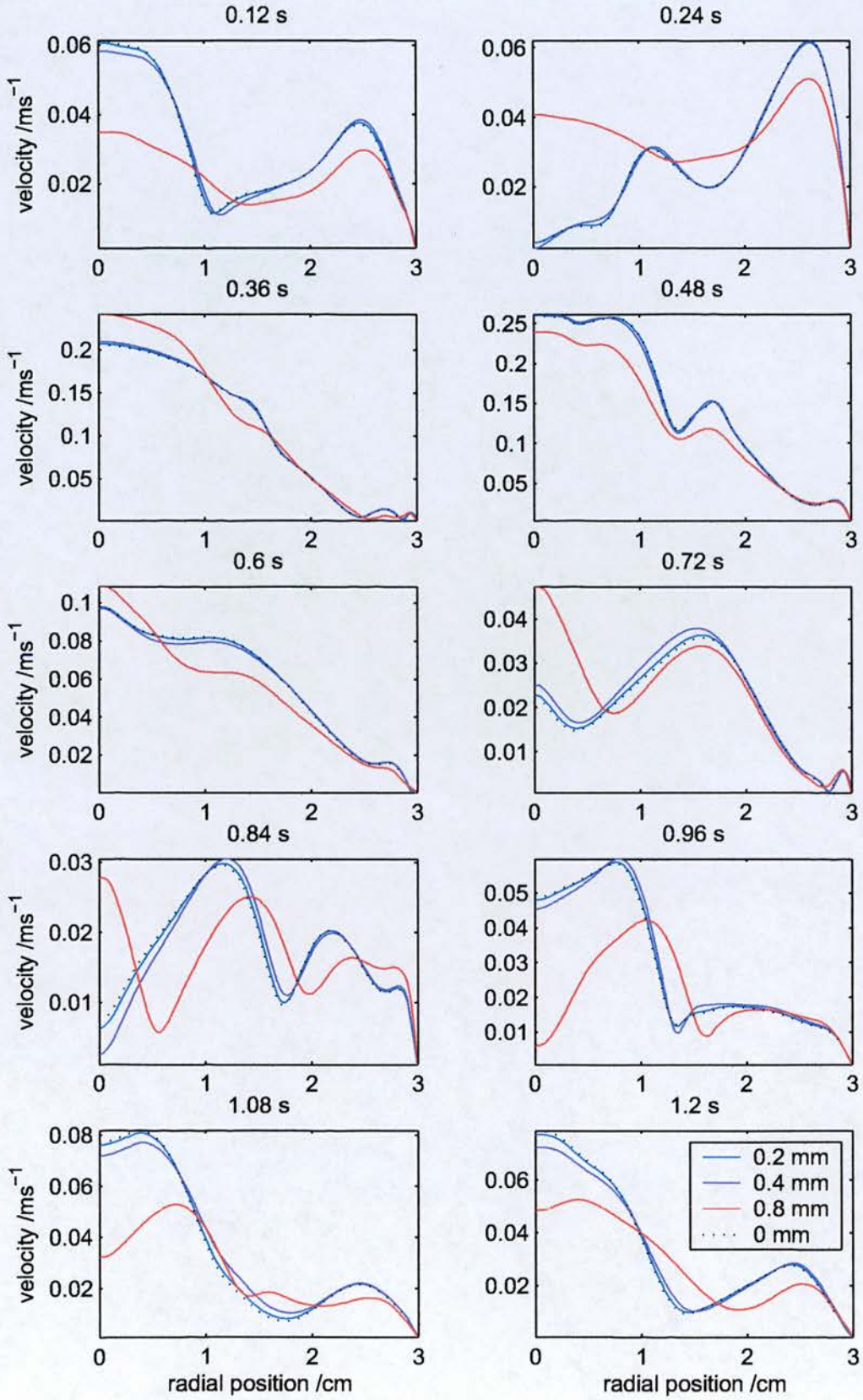

Figure 5.9: *velocity magnitude on centre line*

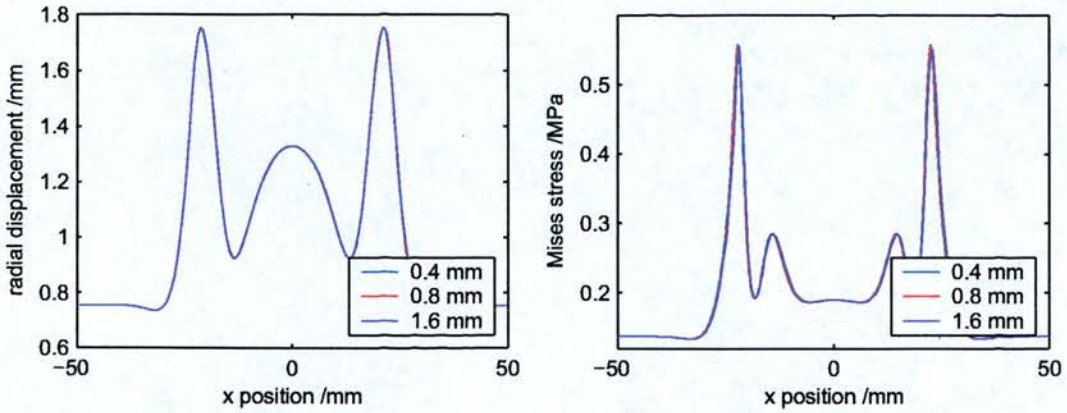

Figure 5.10: *Radial wall displacement and Mises stress on inner wall of aneurysm with varying mesh density*

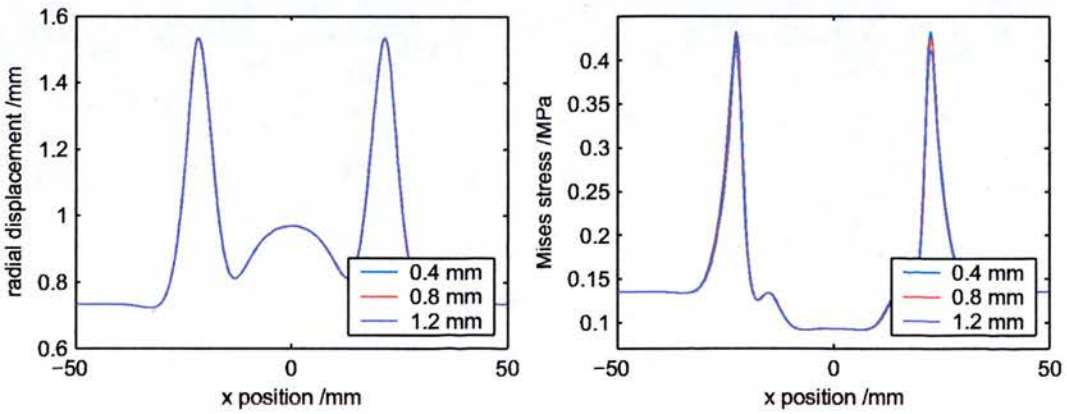

Figure 5.11: *Radial wall displacement and Mises stress on inner wall of aneurysm containing thrombus layer with varying mesh density*

5.3.1.5 Cyclic convergence

Cyclic convergence was assessed by comparing the velocity magnitude at 12 points within the aneurysm bulge at the same phase in successive cycles. The velocity magnitude and convergence at 4 of these points is shown in figure 5.12 along with velocity vector plots at selected time points. The difference in the velocity magnitudes between successive cycles, and the mean of the percentage differences, were calculated. The mean of the percentage differences, for all 200 phases and at 12 points, was found to be below 20% by the end of the fourth cycle and the difference between 4th and 5th cycles was just 3 %. These are percentage differences relative to the point velocity magnitudes which means that when the velocity is very small, such as in recirculation regions, even a very small difference in the velocity results in a large percentage error.

5.3.2 Tissue Stresses

The stress distribution in the 6 cm aneurysm is shown in figure 5.13 at diastole and systole. The stress shown is the von Mises stress, a scalar function giving the magnitude of the stress tensor.

The stress is concentrated in two regions at the 'necks' of the aneurysm. The stress varies across the thickness of the wall with the highest stress on the inner edge of the wall and the lowest stress in the middle of the wall. At systole there are also two local stress maxima on the 'corners' of the inner aneurysm wall. The magnitude of the stress distribution can be seen more clearly in figure 5.14 which shows the hoop, longitudinal and von Mises stress at the time of peak stress. The results for the three different FSI methods are shown. Values for the peak stresses are given in table 5.3.

FSI	von Mises		hoop		longitudinal	
method	stress /MPa	% difference from FSI_2	stress /MPa	% difference from FSI_2	stress /MPa	% difference from FSI_2
SP	0.5587	1.1	0.5433	1.1	0.3225	0.94
FSI_{1RW}	0.5435	1.7	0.5281	1.7	0.3150	1.4
FSI_2	0.5527	-	0.5373	-	0.3195	-

Table 5.3: *Peak stress at systolic pressure in 6 cm aneurysm*

The differences between the three different FSI methods are small, the maximum peak stress difference is only 1.7 %. These differences are bigger than the discretization error, which was estimated at 0.1 %, showing they are real differences, but they are far smaller than the variation

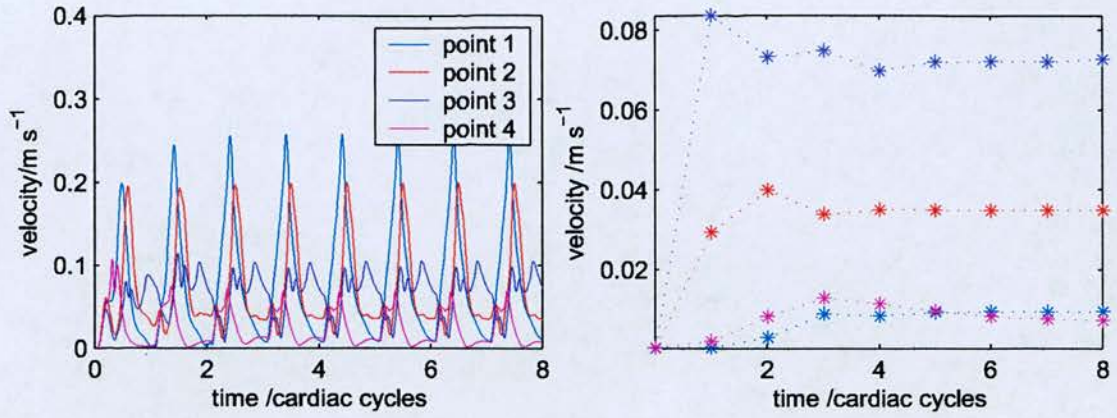

(a)

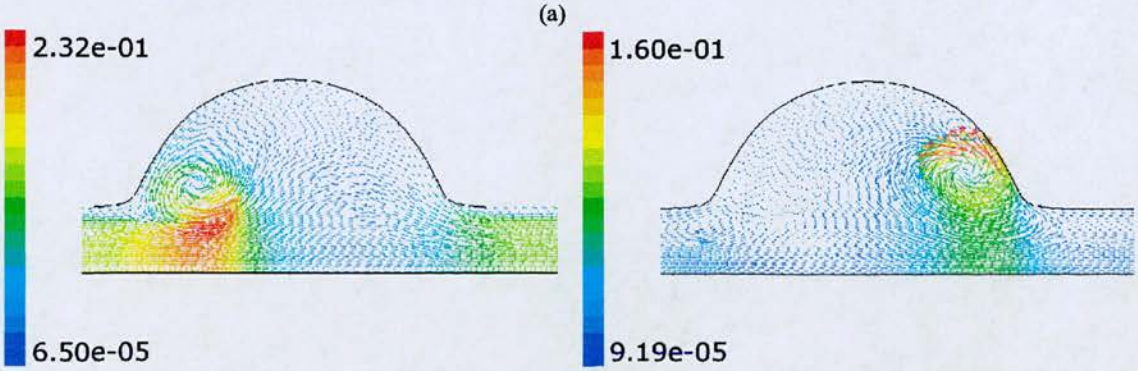

(b) 0.360 s - 0.3 cardiac cycles

(c) 0.960 s - 0.8 cardiac cycles

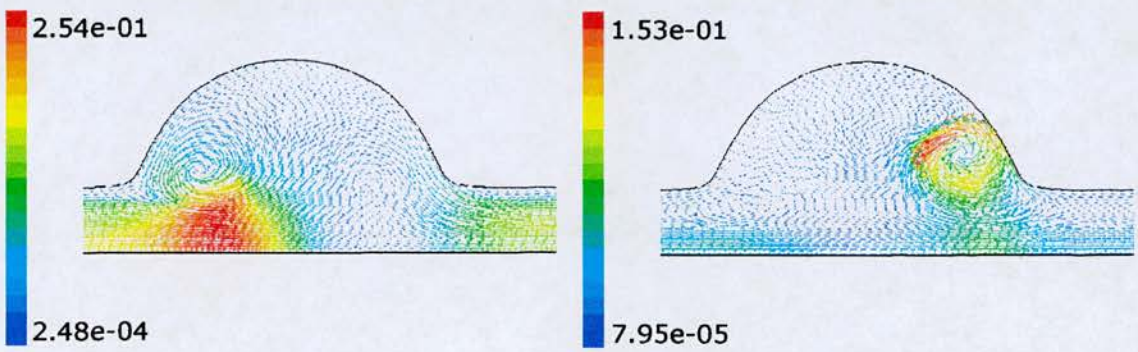

(d) 0.1560 s - 1.3 cardiac cycles

(e) 0.2160 s - 1.8 cardiac cycles

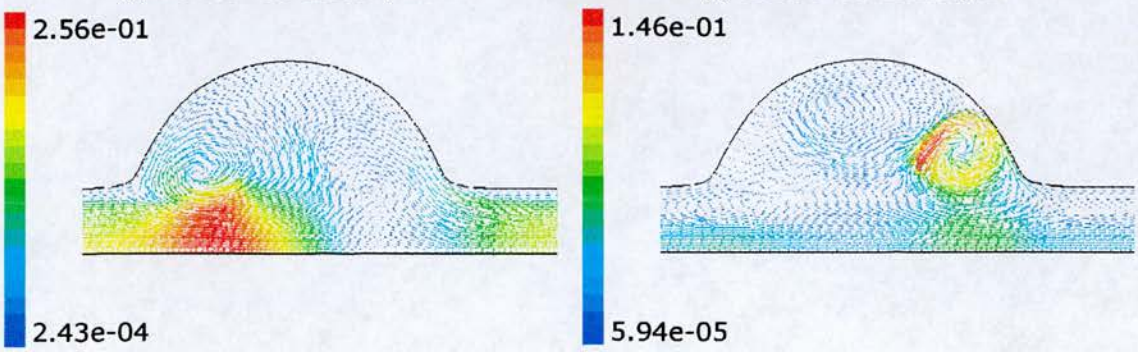

(f) 0.2760 s - 2.3 cardiac cycles

(g) 0.3360 s - 2.8 cardiac cycles

Figure 5.12: *Temporal, cyclic convergence*

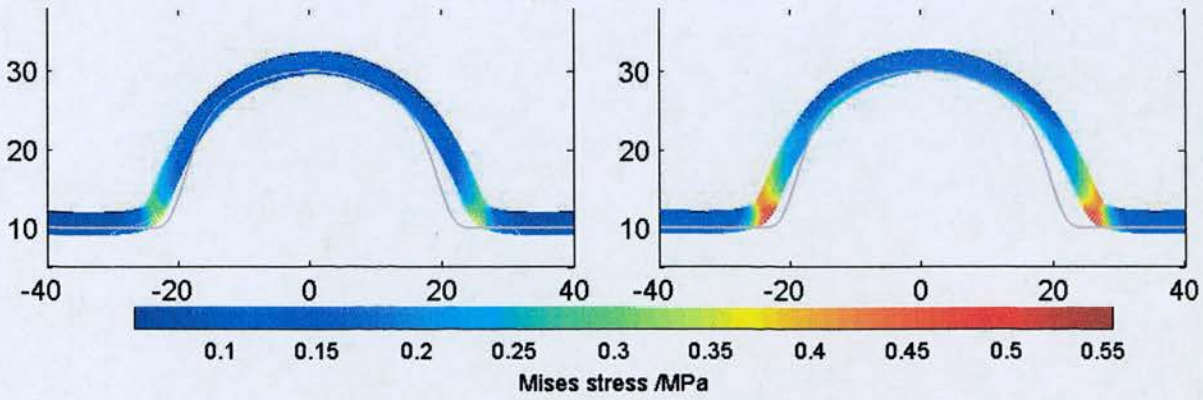

Figure 5.13: *Stress distribution at minimum pressure (left) and maximum pressure (right) with* FSI_2. *Wall thickness has been exaggerated for clarity. Grey line shows undeformed aneurysm shape.*

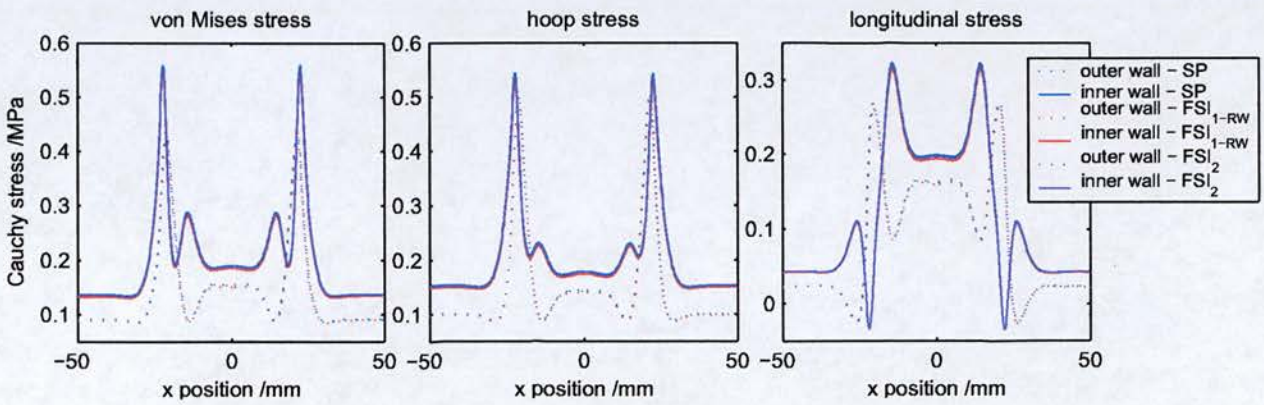

Figure 5.14: *Peak systolic stress in 6cm aneurysm with three different FSI methods*

in stress across the thickness of the artery wall. The differences in magnitude between the proximal and distal stress peaks were smaller than the errors.

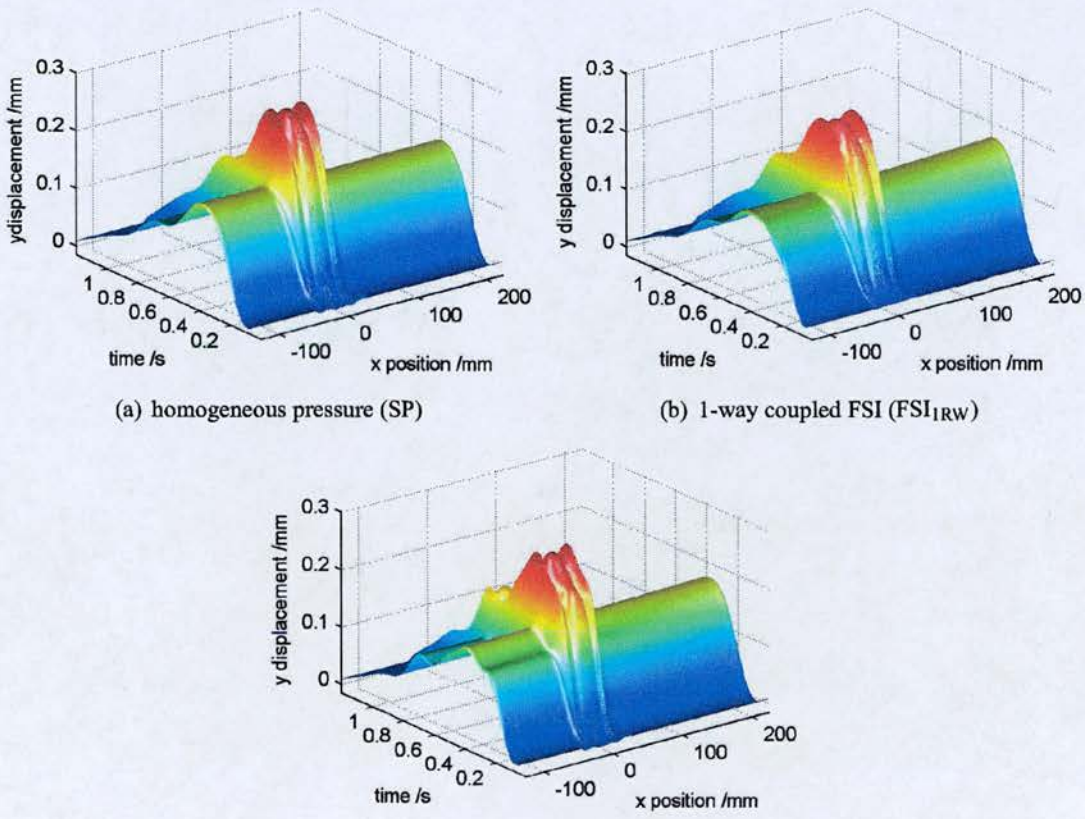

(a) homogeneous pressure (SP)

(b) 1-way coupled FSI (FSI_{1RW})

(c) 2-way coupled FSI (FSI_2)

Figure 5.15: *Wall motion in 6 cm aneurysm: distance moved between diastole and systole*

The wall motion perpendicular to the axis (y-direction), that is the difference between the positions at systole and diastole, along the length of the whole model and throughout the cardiac cycle is shown for each FSI method in figure 5.15. The maximum y displacement is 0.303, 0.287 and 0.297 mm for SP, FSI_{1RW} and FSI_2 respectively and occurs at the aneurysm 'necks'. If the total wall motion is considered, accounting for x as well as y motion the artery is seen to move most at the distal end of the aneurysm which corresponds to the middle of the artery model. This is clearly shown in figure 5.13 by the difference in the deformed and undeformed shapes. The reason is that the artery was constrained in the x direction at either end and so stretching of the wall results in more x motion in the middle. Reasons for the difference in the temporal variation in the y displacement are discussed later.

5.3.2.1 Effect of Diameter

Stresses along the inner and outer edges of the walls of the four different diameter aneurysms are shown in figure 5.16. The shapes of the stress plots for each diameter are very similar although there is a clear increase in the magnitudes with aneurysm diameter. Small differences include: absence of the third and fourth local hoop stress maxima in the 4 cm aneurysm; and negative, or compressive, longitudinal stresses for the two largest aneurysms (6 and 7 cm). The compressive stress is a result of bending which produces a compressive stress along one edge and a tensional stress on the other edge. There is no point along the wall where both edges were under compression, if this were the case the wall would buckle.

The peak systolic von Mises stress can be seen (in figure 5.17) to increase linearly with diameter as predicted by the Laplace equation but with an offset accounting for the straight tube parts. The error in the SP peak stress, compared to the FSI_2 peak stress, decreases with diameter from 2.2 % at 4 cm to 1.1 % at 7 cm whereas the error in the FSI_{1RW} peak stress increases with diameter from 0.61 % to 1.5 %.

5.3.2.2 Effect of Material Stiffness

Stresses in the models with different material stiffnesses are shown in figure 5.18. The 'middle stiffness' has the average parameters in the group of aneurysms investigated by Raghavan and Vorp [59] while 'low stiffness' and 'high stiffness' had the parameters of the lower and upper 95 % confidence intervals for the group. The stresses vary much less with stiffness than with diameter and there are only small changes.

Figure 5.19 shows that the peak von Mises stress decreases slightly with stiffness. The total change in stiffness over the full range of stiffnesses is only about 5 %. Since the change in stress is small the difference due to the FSI method becomes comparable. The error in the SP peak stress, compared to the FSI_2 peak stress, increases with stiffness from 0.97 to 1.2 % whereas the error in the FSI_{1RW} peak stress is fairly constant at around 1.6 %.

5.3.2.3 Effect of Thrombus

Figure 5.20 shows the effect of increasing the thickness of the thrombus layer on the stress distribution. Without a thrombus layer, the stress is concentrated in four regions, two being at

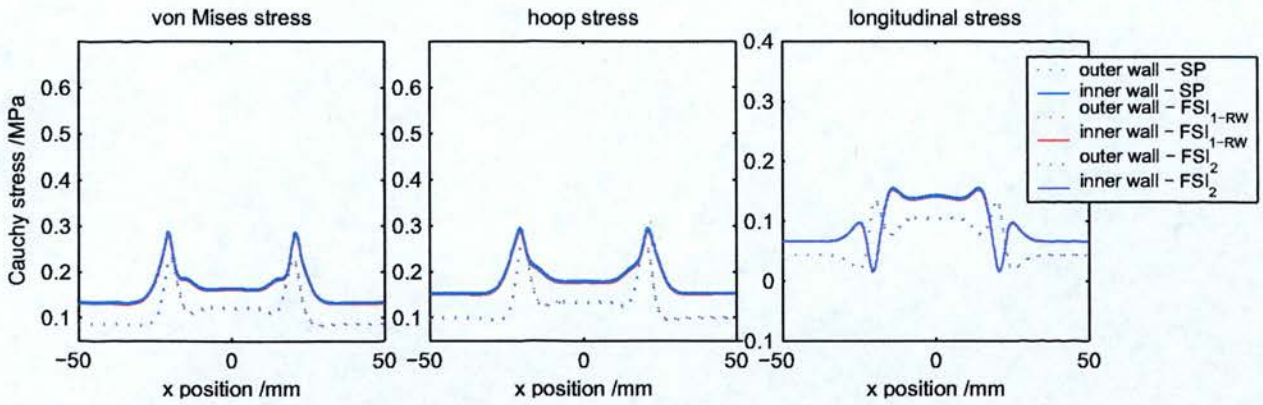

(a) 4 cm

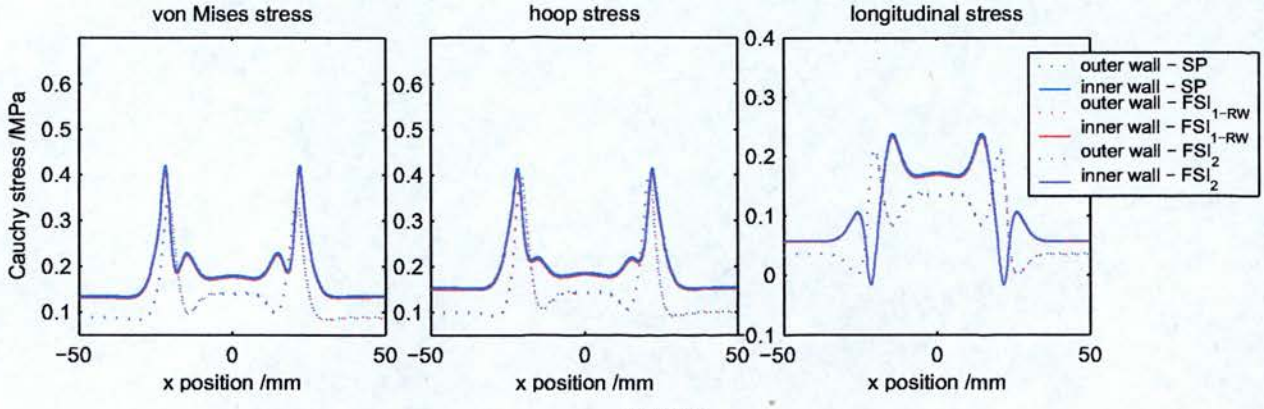

(b) 5 cm

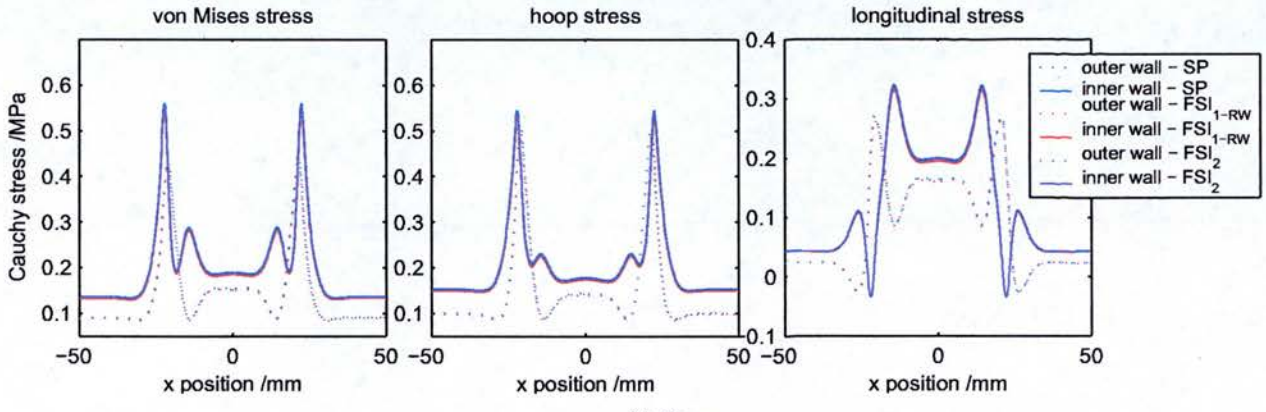

(c) 6 cm

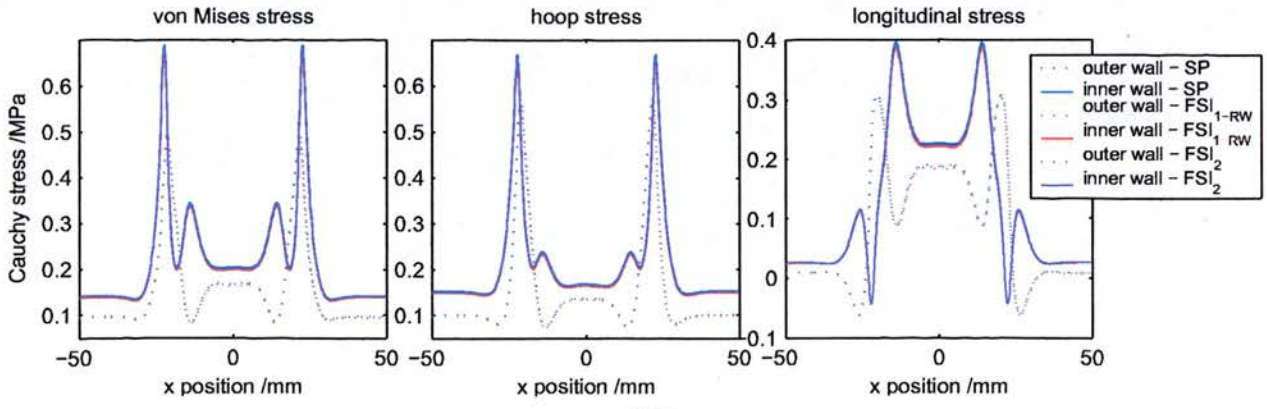

(d) 7 cm

Figure 5.16: *Peak systolic stress in aneurysms with increasing diameter*

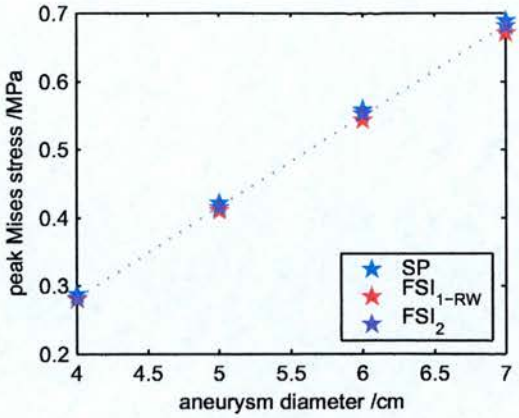

Figure 5.17: *Variation in peak von Mises stress with diameter. Linear fit for* FSI_2 *shown with dotted line.*

the necks of the aneurysm and the other two being on the inner edge of the 'corners' of the aneurysm. The presence of a thrombus layer reduces the stress magnitude over the whole wall. It also changes the stress distribution as with a thrombus layer there are no longer stress peaks at the aneurysm corners. Stress in the thrombus layer is much lower than that within the wall due to its much lower stiffness. In the models with 0.5 and 1.0 cm of thrombus the stress is concentrated at the inner 'corners' whereas in the model with a 1.5 cm layer the high stress region extends along the inner edge of the thrombus.

The tissue stresses within the walls of the models with different thrombus layers are shown in figure 5.21. Both peak hoop stress and peak longitudinal stress decrease with the thickness of the thrombus layer. As shown in pictures of stress distribution (figure 5.20) the local maxima at the aneurysm corners, visible at about ± 10 mm in the aneurysm without thrombus (figure 5.21a) are eliminated in the aneurysm with the thickest layer. The peak longitudinal stress shifts from the inner to the outer layer as the thrombus layer increases.

The decrease in the peak von Mises stress is shown more clearly in figure 5.22. The mean errors in the simpler methods as compared to FSI_2 are similar without thrombus and with a 0.5 or 1.0 cm layer: 1.5 % for SP and 1 % for FSI_{1RW}. There is a sudden increase at 1.5 cm of thrombus with mean errors of 3.4 and 3.2 % for SP and FSI_{1RW} respectively.

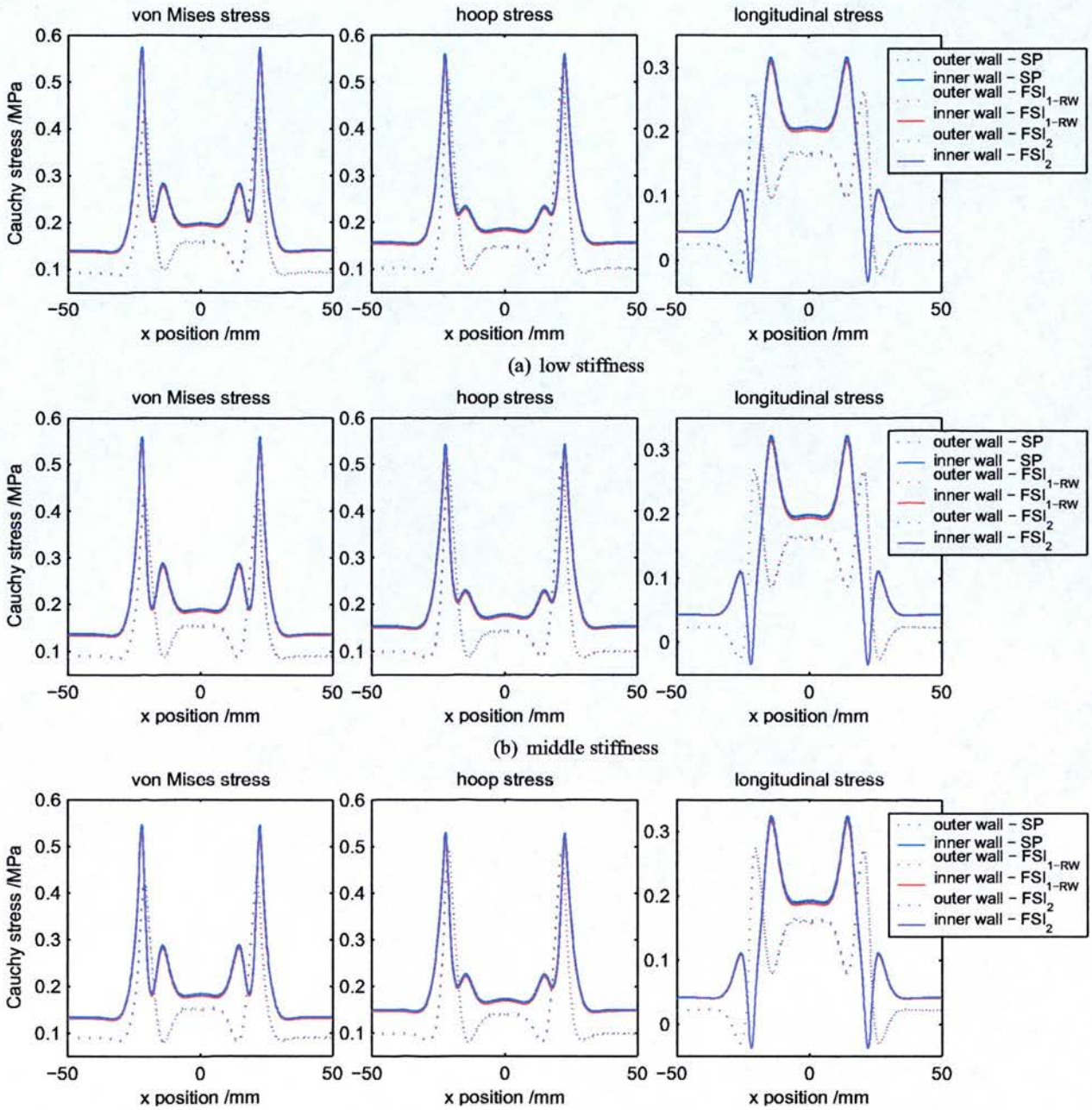

(a) low stiffness

(b) middle stiffness

Figure 5.18: *Peak systolic stress in aneurysms with increasing stiffness*

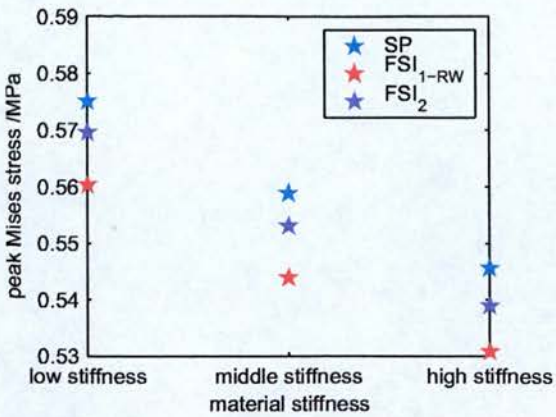

Figure 5.19: *Variation in peak von Mises stress with material stiffness*

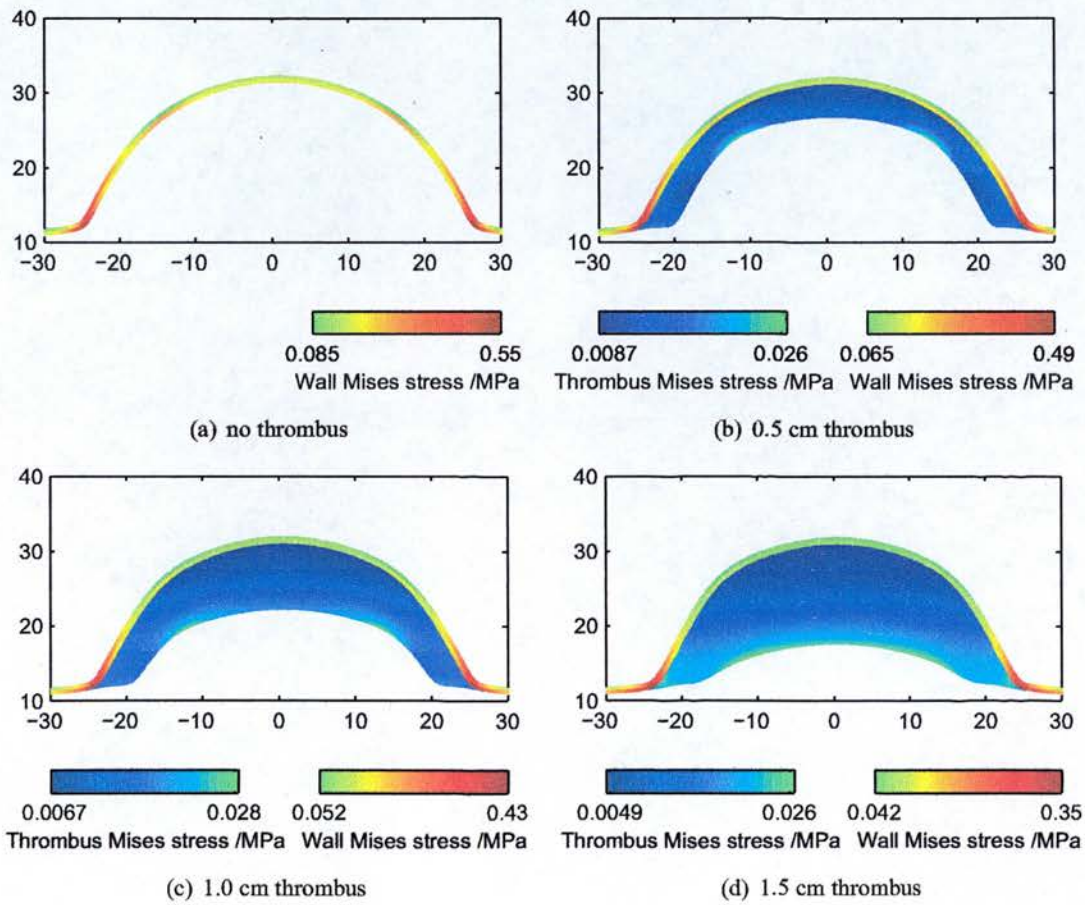

Figure 5.20: *Von Mises stress distribution in aneurysms with increasing thrombus thickness at peak systolic pressure*

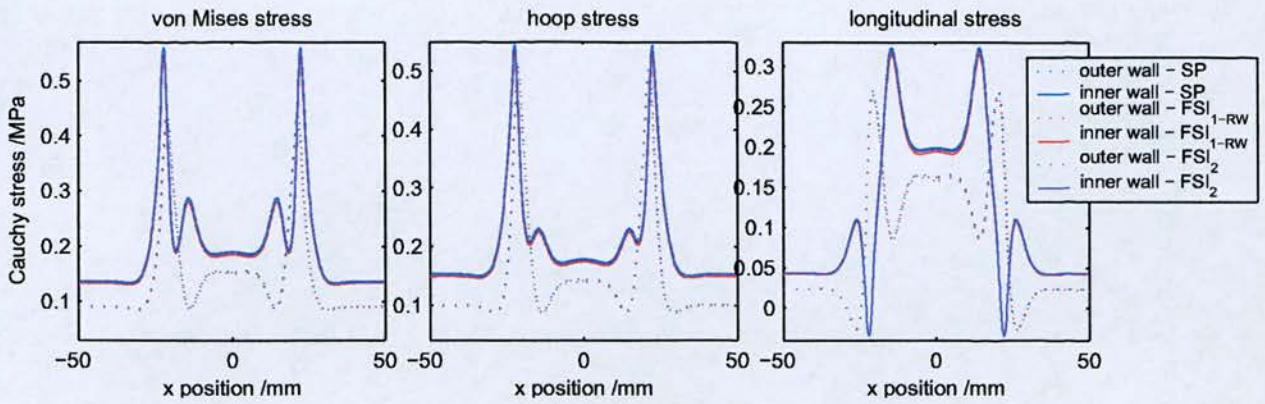

(a) 0.0 cm

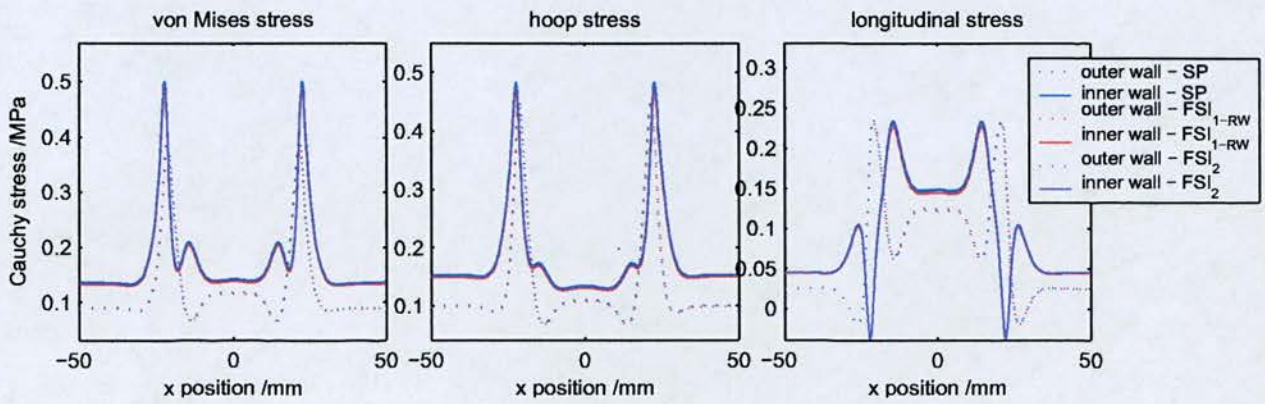

(b) 0.5 cm

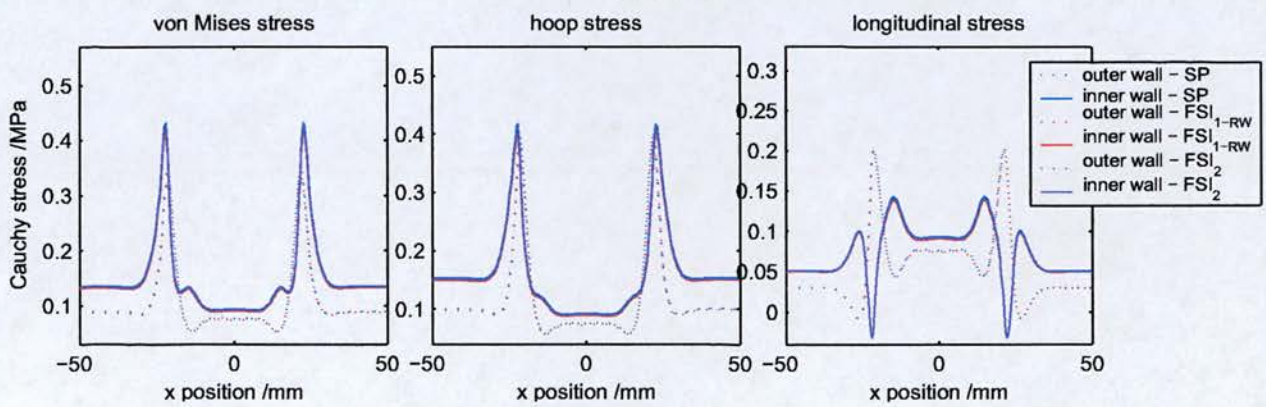

(c) 1.0 cm

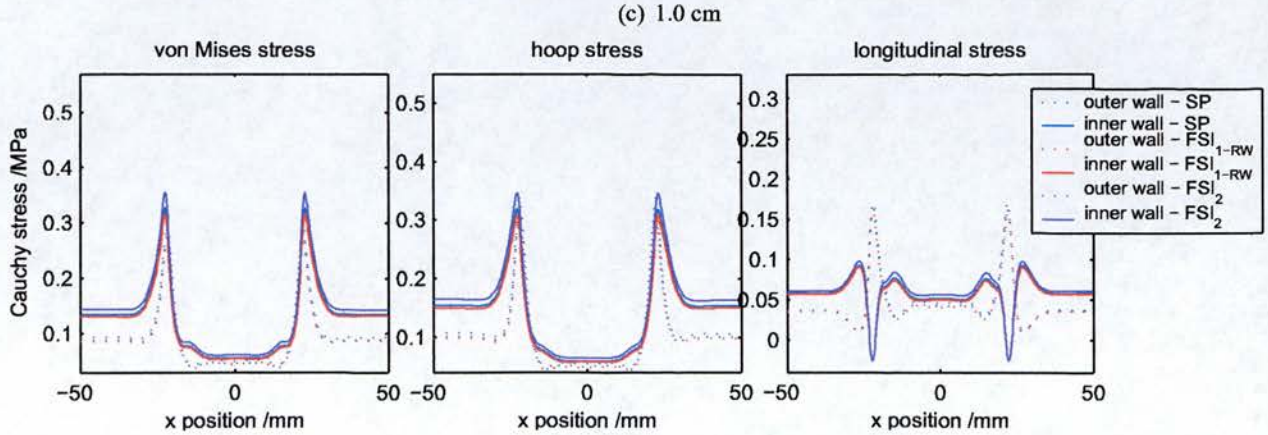

(d) 1.5 cm

Figure 5.21: *Peak systolic stress in aneurysms with increasing thickness of thrombus layer*

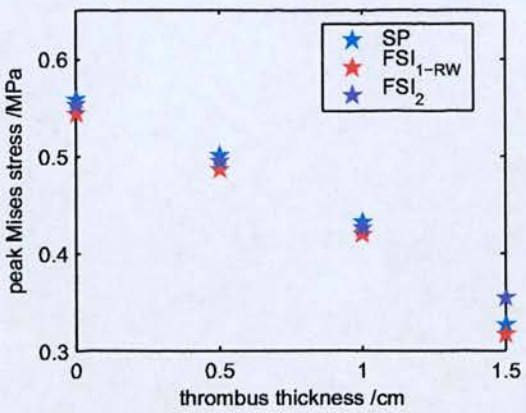

Figure 5.22: *Variation in peak von Mises stress with thrombus thickness*

5.3.3 Blood Flow

Flow patterns for the 6 cm aneurysm are shown in figure 5.23. At the start of the cardiac cycle a toroidal vortex sat at the distal end of the bulge. As the flow accelerated this vortex died away and a new one was formed at the proximal end of the bulge as the flow started to decelerate. This toroidal vortex moved down the aneurysm. The blood in the centre of the torus was squashed into a narrow passage and moved much faster than the surrounding blood. The vortex stopped moving distally when it reached the end of the aneurysm. As the flow slowed down the vortex lost strength so that at the start of the next cycle it no longer impinged on the blood in the core region and this moved slower than the blood in the vortex.

The vortex, and the fast flow in its core, moved across the aneurysm in a short pulse, also seen in the works by Deplano *et al.* [75] and Salsac *et al.* [79]. During the systolic acceleration phase the flow remained attached at the wall because the adverse pressure gradient created by the diverging walls was counteracted, and exceeded, by the positive pressure gradient due to temporal acceleration. As the flow rate peaked the adverse pressure gradient became greater than the positive pressure gradient, the flow in the aneurysm cavity slowed down, the boundary layer thickened and the wall shear stress went to zero so the flow detached from the wall and vortices formed. In the rapidly decelerating flow the adverse pressure gradient dominated, pushing the flow backwards, except in the central core which had more momentum. In the decelerating flow the vortex moved along the aneurysm cavity (average speed 7.8 cm s^{-1}, peak speed in the middle 11 cm s^{-1}) crossing the 4.5 cm in 0.2 s and reached the distal end at peak reverse flow. The vortex moved slower than the blood in the core which had a speed of

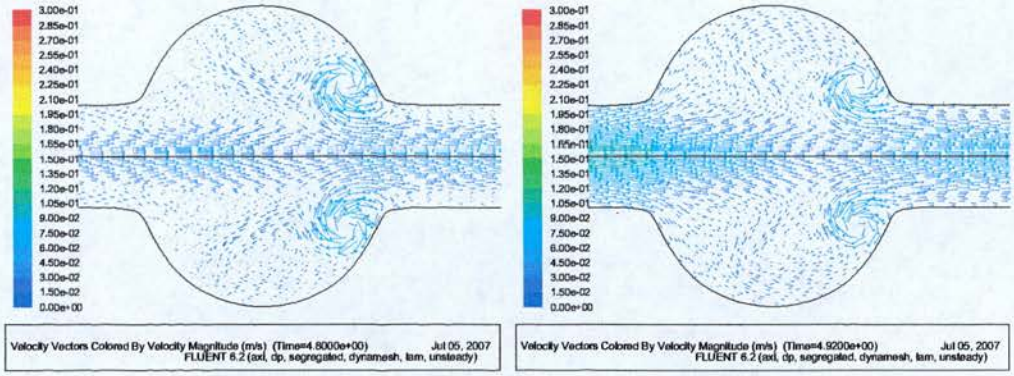

(a) 0.0 cardiac cycles (b) 0.1 cardiac cycles

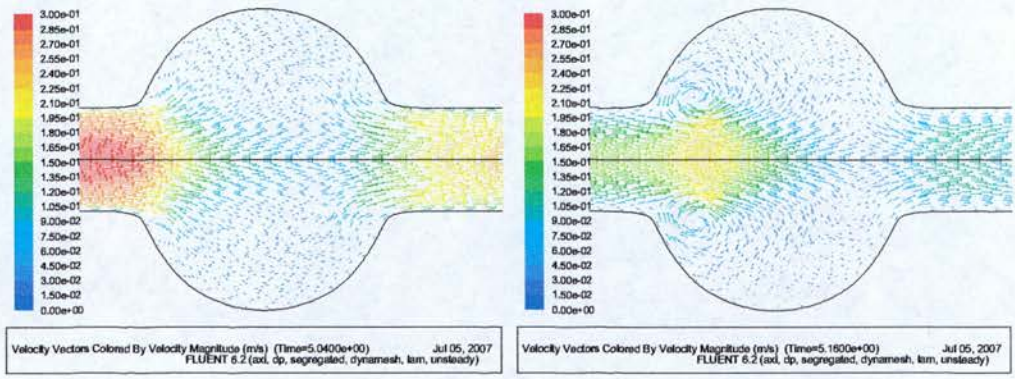

(c) 0.2 cardiac cycles (d) 0.3 cardiac cycles

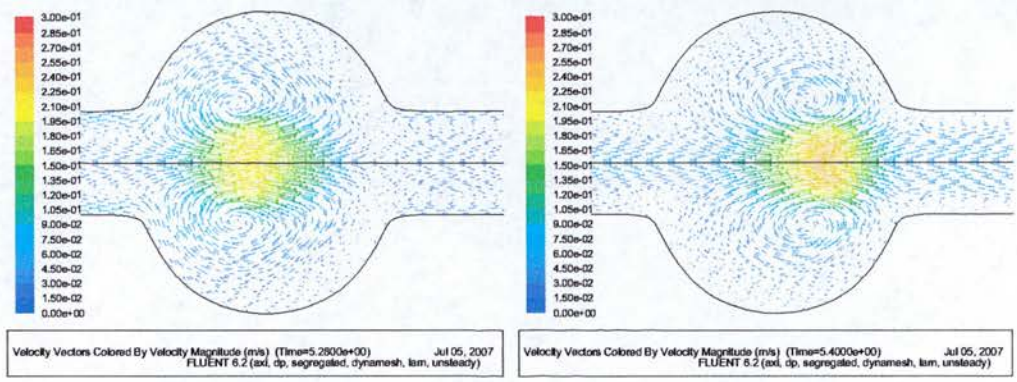

(e) 0.4 cardiac cycles (f) 0.5 cardiac cycles

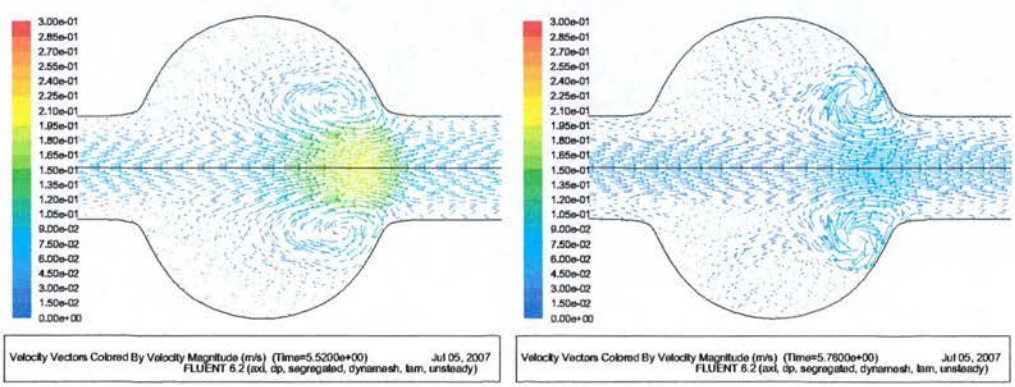

(g) 0.6 cardiac cycles (h) 0.8 cardiac cycles

Figure 5.23: *Flow patterns throughout cardiac cycle in 6 cm aneurysm*

22 cm s^{-1}. As the flow then started to accelerate again the pressure gradient reduced (became less adverse) and the strength of the vortex diminished.

In comparison the blood flow pattens in the rigid walled calculation were similar. However, the axial velocity inside the vortex ring in the RW calculations was higher and the vorticity magnitude was larger. The vortex position was slightly ahead of that in the FSI_2 calculation and reached the distal end slightly earlier.

The axial velocity along the axis, and the wall shear stress, throughout the cardiac cycle and for each FSI method, are shown in figure 5.24. The general characteristics of the plots are the same for each method. The region of fast flowing blood in the centre of the toroidal vortex is clearly visible as a diagonal ridge in the plots of axial velocity. The velocities at peak systolic flow in the rigid walled (RW) model are faster than in the three flexible models due to the expansion in these models. In RW the lowest velocities occur in two areas: in the aneurysm bulge at the very end of the cycle and the start of the next one; and at the time of peak reverse flow in the distal part of the aneurysm ahead of the toroidal vortex. In the flexible models the lowest velocities occur around the same times but they are never as low, the velocity along the axis is never reversed. The maximum velocity on the axis of RW is the same before and after the aneurysm, while the compliant models store up some of the blood during systole, releasing it later so the peak velocity distal to the bulge is smaller than that proximal, but the velocity during the diastolic peak is higher than that in RW.

The WSS is very low within the aneurysm cavity throughout the cycle. It peaks at around 0.15 Pa during peak systolic flow and has a minimum of around -0.15 Pa during peak reverse flow. For the rest of the cycle the WSS in the aneurysm is almost zero. In RW there is a large spike in the WSS at the distal end of the bulge which corresponds to the bottle neck region where the blood is accelerated into a narrower region. The peak in the flexible models is similar but smaller. The lowest WSS values occur at the distal end of the aneurysm during the diastolic flow peak (0.8 s) which is when the vortex impacts on the wall.

A feature which is more apparent in the smaller aneurysms, but is there in all of them, is a trough in the WSS which follows the ridge in the axial velocity in space-time with a slight shift. This is also due to the distally moving vortex which has fast forward flow through its core, but reverse flow on its outer edge. Figure 5.25 shows velocity on the axis, WSS and velocity vectors at 0.6 s to illustrate this.

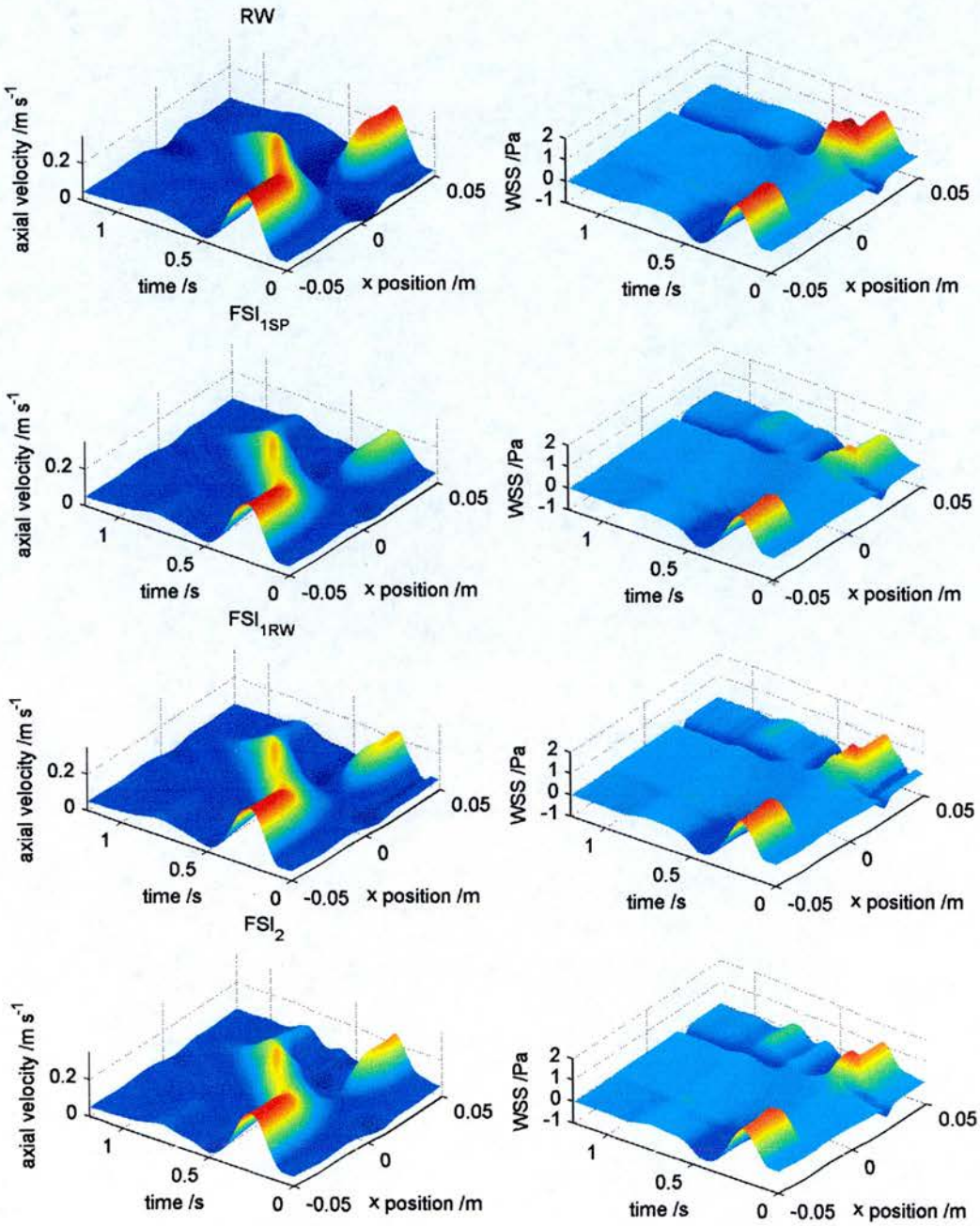

Figure 5.24: *Axial velocity and WSS in 6 cm aneurysm with four different FSI methods*

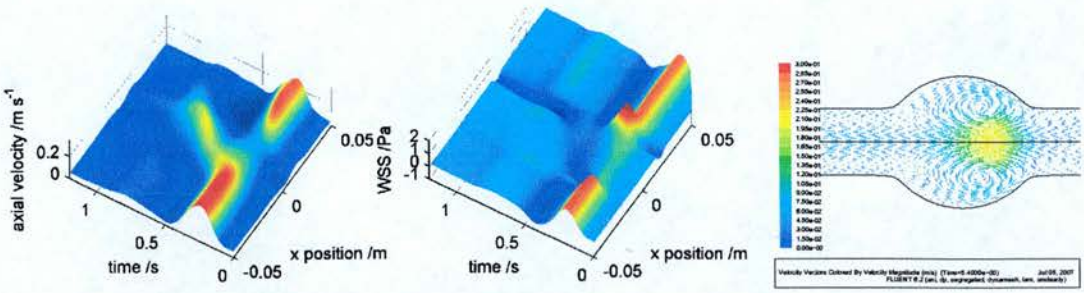

(a) Axial velocity and WSS (b) Blood flow pattern

Figure 5.25: *Axial velocity and WSS and flow pattern in 4 cm aneurysm with* FSI_2

5.3.3.1 Effect of Diameter

Mean, maximum and minimum WSS for the aneurysms of increasing diameter are shown in figure 5.26. Note that the maximum and minimum plots are taken over the whole cycle and not plots from a single time step. The mean WSS within the aneurysm bulge decreases from around 0.022 in the 4 cm aneurysm to around 0.0025 Pa in the 7 cm aneurysm. The oscillation in the WSS in the bulge also decreases from −0.25 - 0.27 Pa at 4 cm to −0.05 - 0.05 Pa at 7 cm.

The mean error in the WSS, as compared with the WSS in FSI_2, varied with diameter with an increasing trend, see figure 5.27. The largest errors occurred in RW while both the one way FSI methods performed similarly, FSI_{1SP} being slightly better than FSI_{1RW} for small aneurysm volumes and vice versa for the 7 cm aneurysm. The reason for the WSS large errors in RW are clear, the wall deformation is not included and so the flow and hence the WSS are quite different. However, the reason for the relative errors in FSI_{1SP} and FSI_{1RW} is less apparent. The largest contribution to the mean WSS error is from errors in the outlet section of the aneurysm model. Errors in the volume of the aneurysm model, due to incorrect prediction of the wall position, account for the error in the mean WSS. If the volume change over time is incorrect flow in the outlet length will also be incorrect as blood must be either sucked in or pushed out to fill the model. Errors in the outlet flow rate will create errors in the WSS in the outlet region. Figure 5.28 shows the temporal volume derivative (dV/dt) in the 6 cm aneurysm as an example along side the variation in the error in dV/dt with diameter.

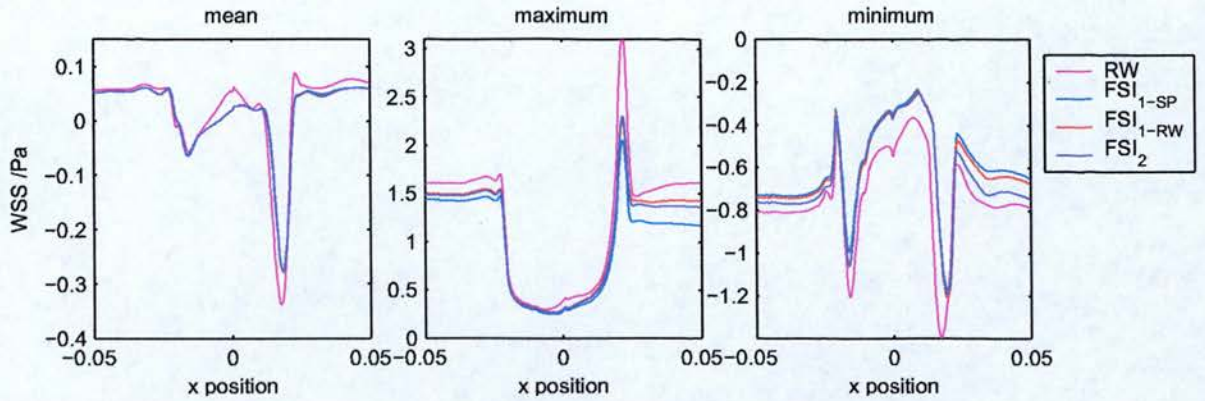

(a) 4 cm

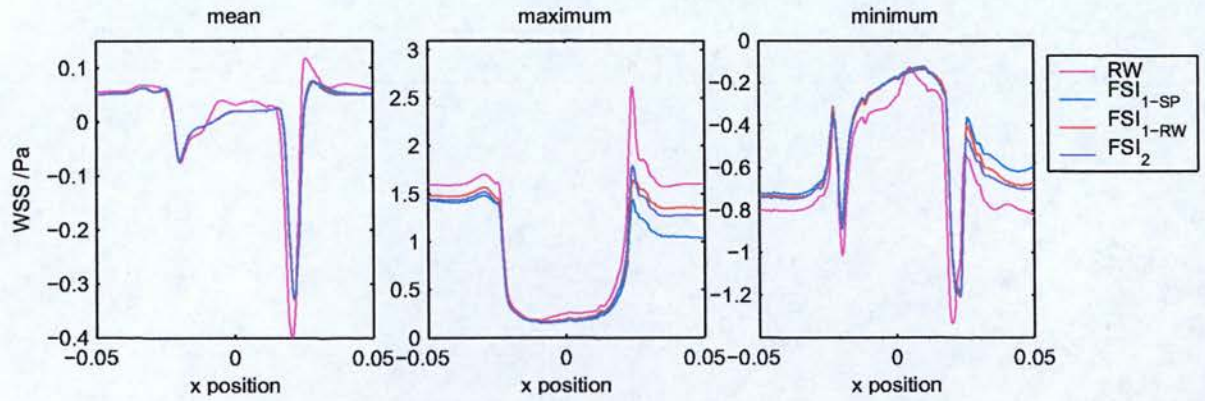

(b) 5 cm

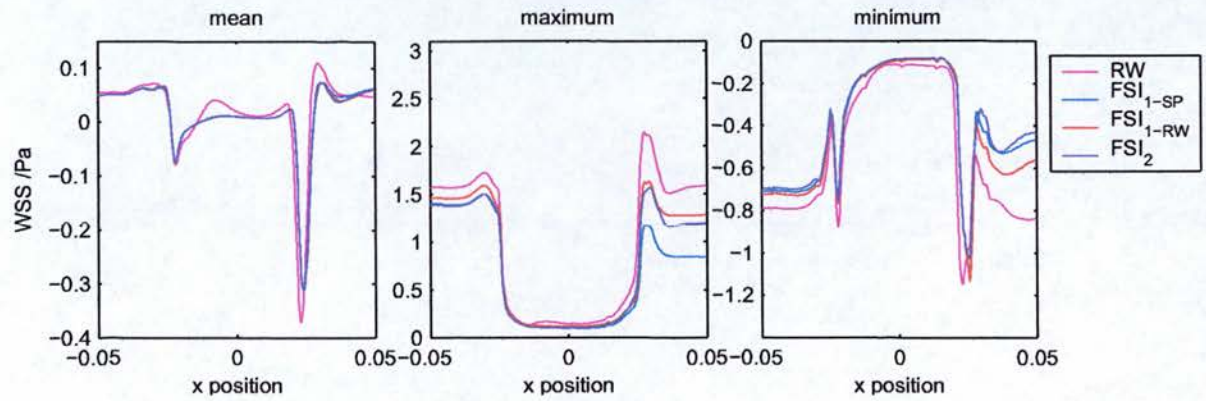

(c) 6 cm

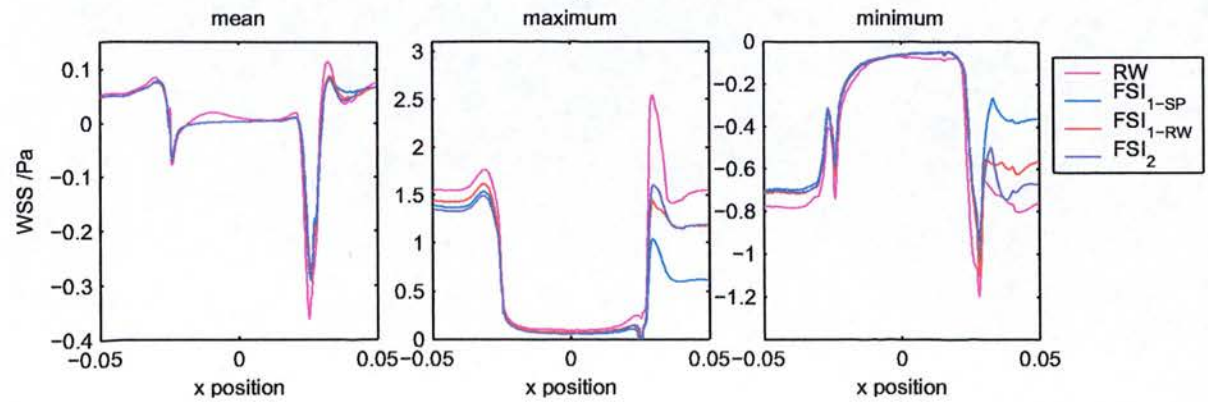

(d) 7 cm

Figure 5.26: *WSS in aneurysms with increasing diameter*

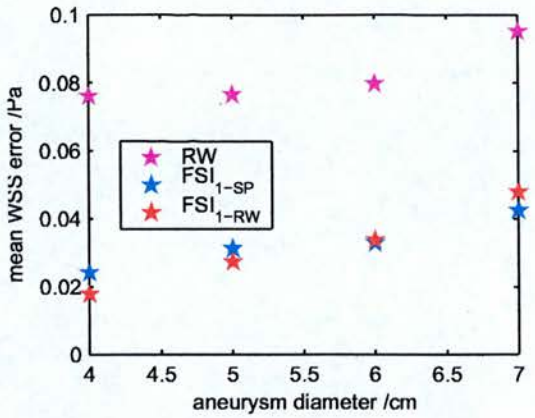

Figure 5.27: *Variation in mean WSS error (as compared with* FSI_2 *results) with diameter. Calculated over the region -0.05 to 0.05 m.*

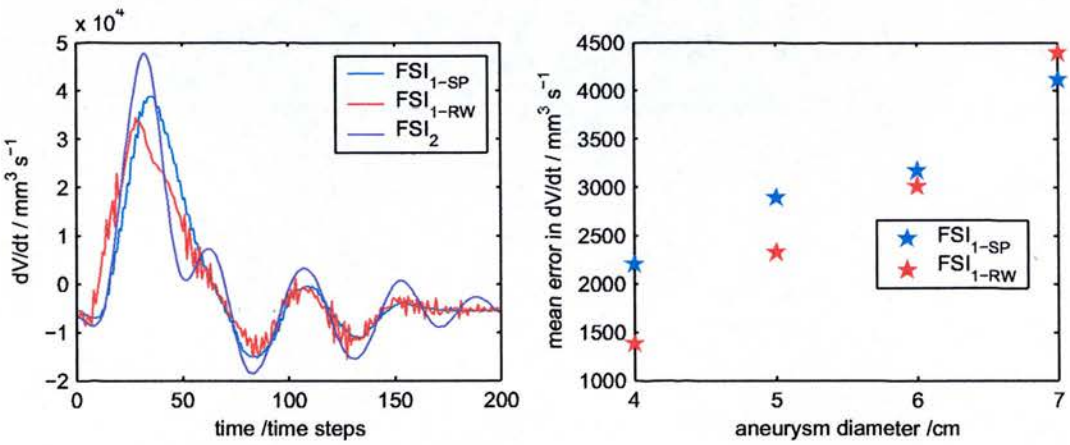

(a) temporal volume derivative

(b) volume error

Figure 5.28: *Temporal volume derivative (dV/dt) in 6 cm aneurysm and variation in mean error of (dV/dt) (as compared with* FSI_2 *results) with diameter.*

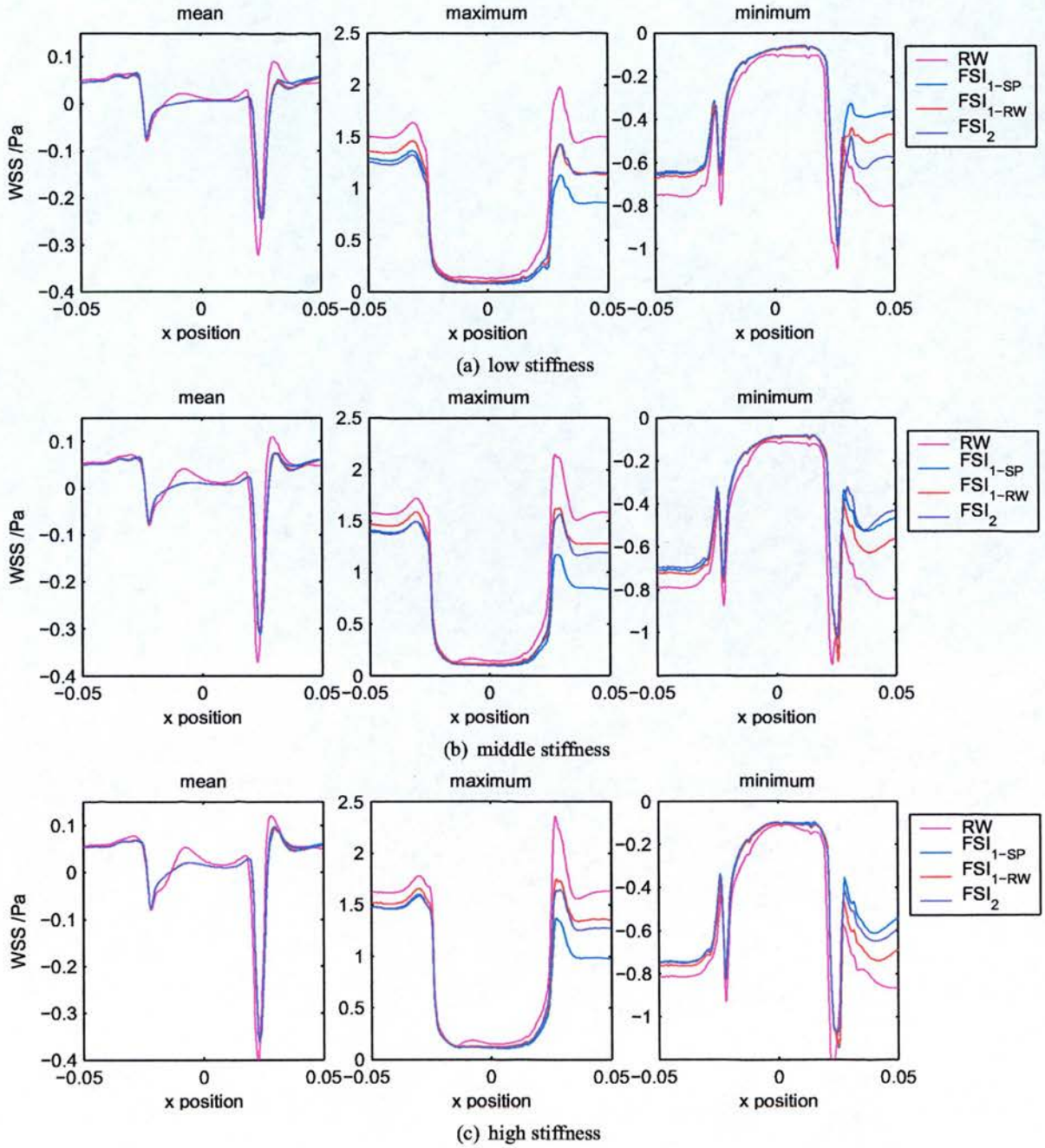

(a) low stiffness

(b) middle stiffness

(c) high stiffness

Figure 5.29: *WSS in aneurysms with increasing stiffness*

5.3.3.2 Effect of Material Stiffness

Mean, maximum and minimum WSS, taken over the cardiac cycle, for the aneurysms of increasing stiffness are shown in figure 5.29. The mean WSS within the aneurysm bulge increases from around 6.5×10^{-3} Pa in the aneurysm with the lowest stiffness to around 0.014 Pa in the high stiffness aneurysm. The oscillation in the WSS in the bulge also increases from -0.062 - 0.0062 Pa at low stiffness to -0.10 - 0.014 Pa at high stiffness.

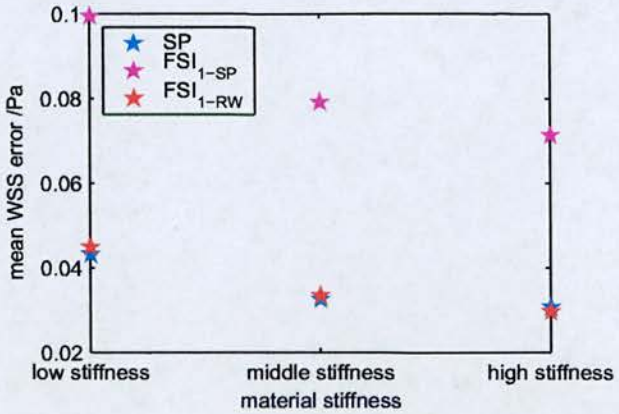

Figure 5.30: *Variation in mean WSS error (as compared with* FSI_2 *results) with material stiffness. Calculated over the region -0.05 to 0.05 m.*

The variation in the mean WSS error, as compared with FSI_2, with stiffness is shown in figure 5.30. As the material stiffness increases the aneurysm dilates less and wall motion has less of an effect so the errors in all three simplified methods are reduced.

5.3.3.3 Effect of Thrombus

Figure 5.31 shows blood flow patterns in the aneurysm with the thickest layer of thrombus (1.5 cm) in a rigid wall and FSI_2 calculation. The flexible walls effect the blood flow dramatically, for example, at 0.2 cardiac cycles the inlet flow is much faster than the outlet flow since the aneurysm is expanding so some of the blood gets stored up and then released later in the cycle (figure 5.31f).

Figure 5.32 shows the mean, maximum and minimum WSS, taken over the cardiac cycle, for the aneurysms with increasing thrombus thickness. Without the thrombus layer there are just two negative peaks in the mean WSS whereas when the thrombus is included there are several negative peaks. This is due to the change in lumen diameter going from the region where the

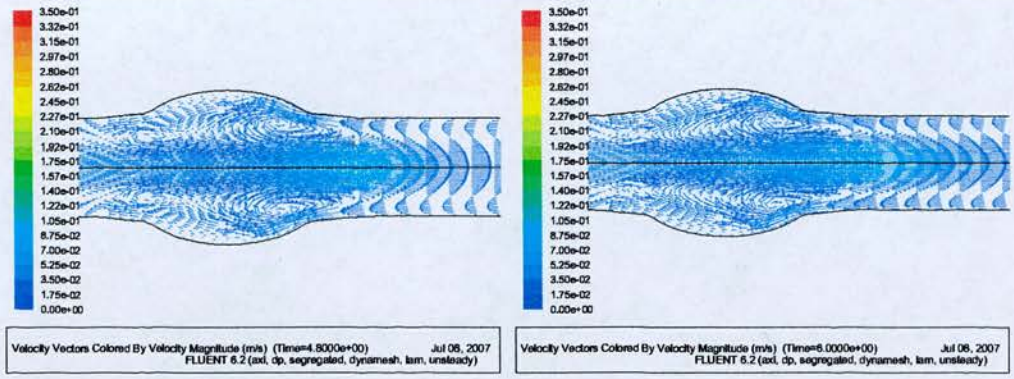

(a) rigid wall: 0.0 cardiac cycles (b) flexible wall: 0.0 cardiac cycles

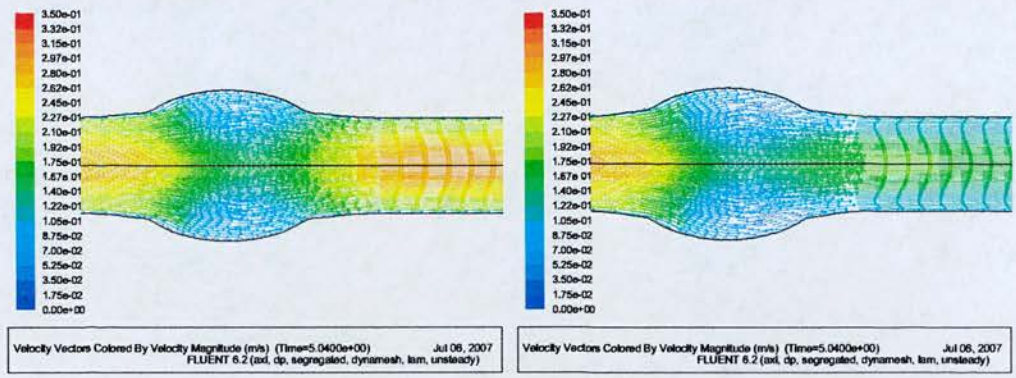

(c) rigid wall: 0.2 cardiac cycles (d) flexible wall: 0.2 cardiac cycles

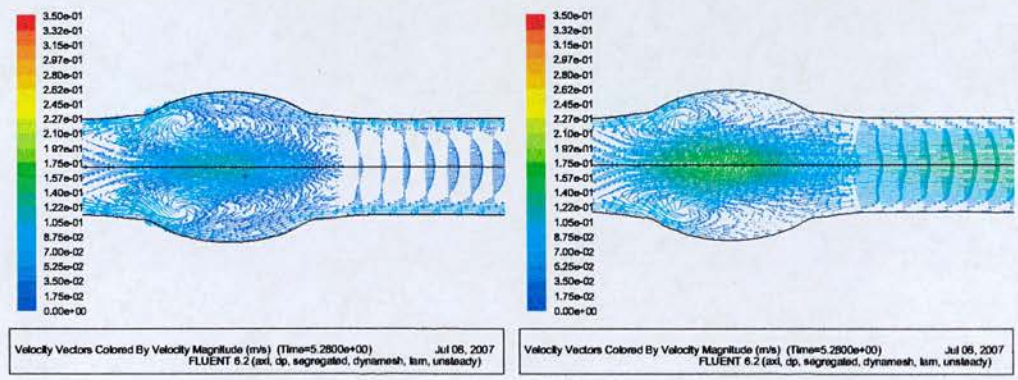

(e) rigid wall: 0.4 cardiac cycles (f) flexible wall: 0.4 cardiac cycles

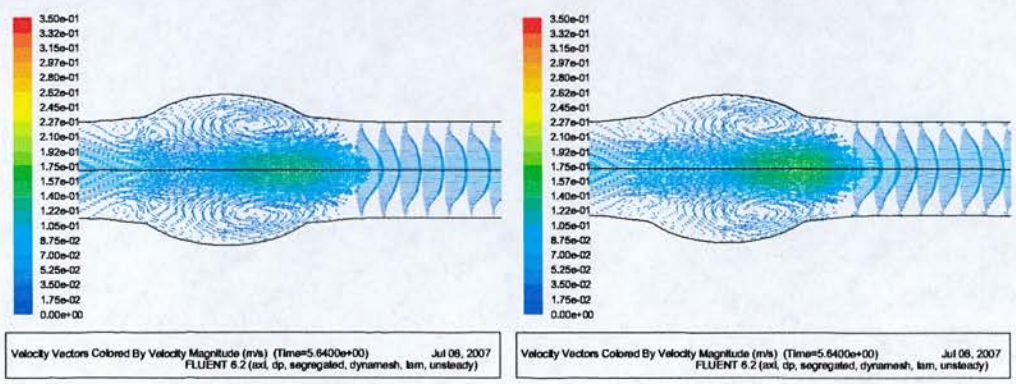

(g) rigid wall: 0.7 cardiac cycles (h) flexible wall: 0.7 cardiac cycles

Figure 5.31: *Flow fields in rigid and flexible* (FSI_2) *walled aneurysms with 1.5 cm thrombus layer*

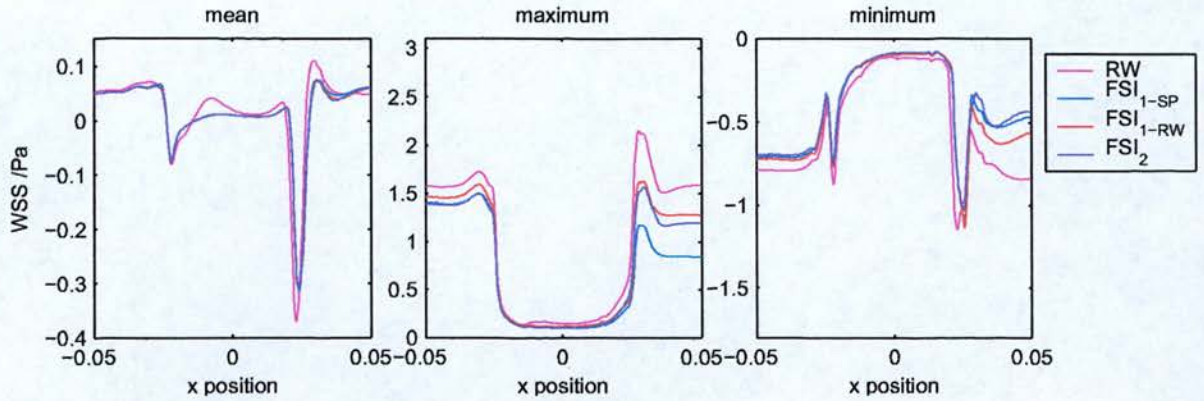

(a) 0.0 cm

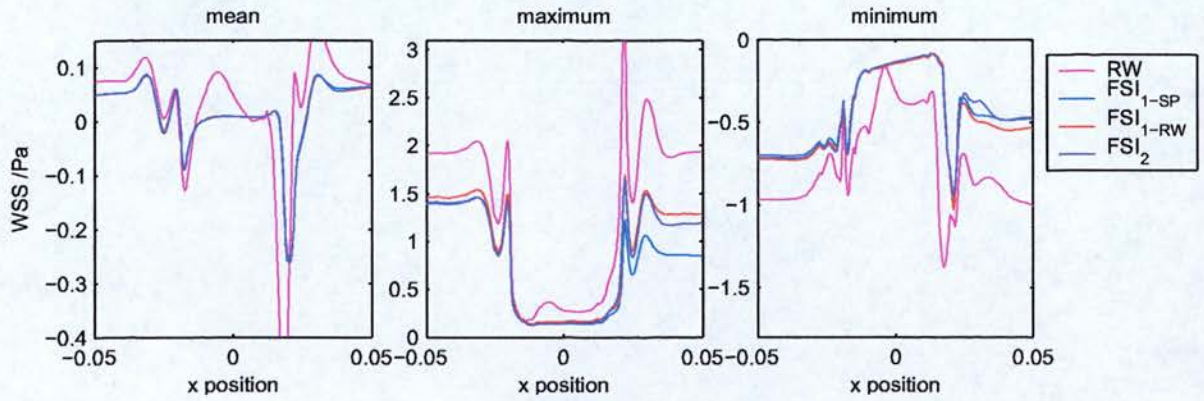

(b) 0.5 cm

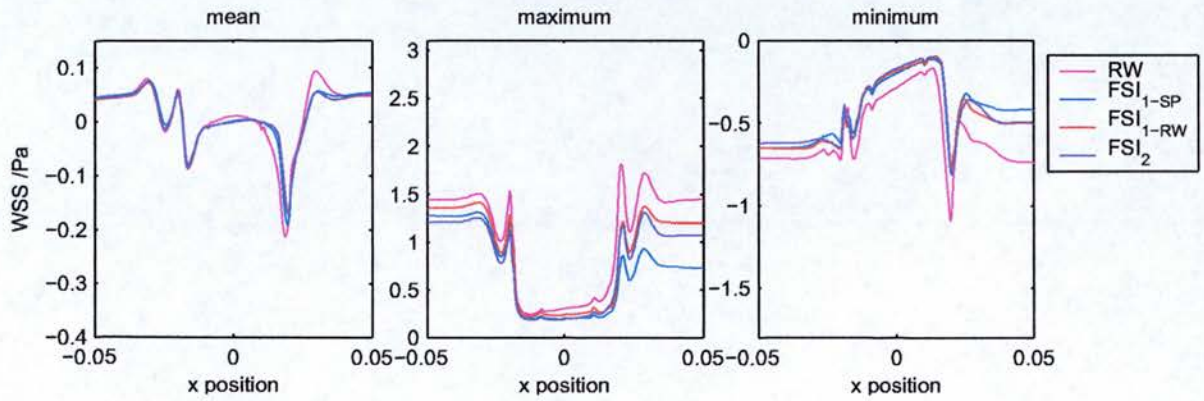

(c) 1.0 cm

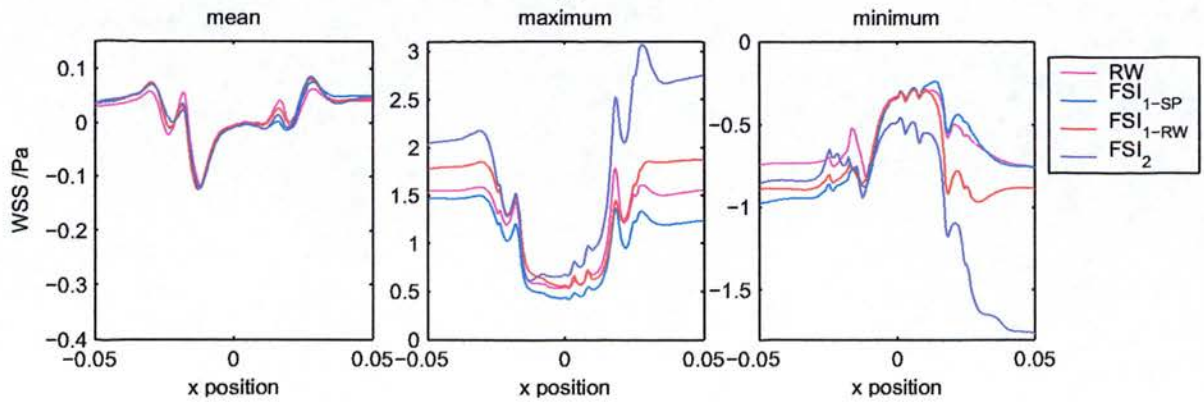

(d) 1.5 cm

Figure 5.32: *WSS in aneurysms with increasing thrombus thickness*

blood is in contact with the wall to the region where the blood contacts the thrombus and then back again at the distal end. This change in geometry can be seen in figure 5.20. Figure 5.31g shows small vortices are established in this region at the proximal end of the aneurysm which complicates the flow pattern compared to the models without thrombus. With 1.5 cm thrombus there is no negative spike in the WSS at the distal end. The maximum WSS and minimum WSS in the aneurysm bulge increase and decrease respectively with the amount of thrombus as the velocities in the bulge are bigger when the lumen diameter is smaller.

Comparing the different FSI methods the errors in FSI_{1SP} and FSI_{1RW} were similar, around 0.04 Pa with 0, 0.5 and 1.0 cm thrombus. With 1.5 cm the error increased to 0.2 Pa for both FSI_{1SP} and FSI_{1RW}.

5.4 Discussion

In this work a thorough comparison of tissue stresses and blood flow in axially symmetric aneurysms with and without fluid-structure interactions has been performed.

The effect of incorporating the FSI (FSI_2) on the tissue stress is minimal with errors between 2.2 and 1.1 % with varying diameter from 4 to 7 cm when a homogeneous pressure (SP) calculation is used. Variation in the error due to omitting the FSI was similar to that due to changing the material stiffness over the range found within the AAA population. Incorporating a thrombus layer reduced the tissue stresses in the aneurysm but errors due to FSI omission were the same as those without the thrombus layer except with the thickest layer when they increased to 3.4 %. Hence the use of a homogeneous pressure calculation of the tissue stresses is most probably accurate enough for the majority of purposes. Use of a 1-way coupled simulation based on the pressure obtained from a fluid simulation in a rigid walled model FSI_{1RW} does not always reduce the error in the peak stress below that of the SP error.

These results are similar to those of Leung *et al.* [173] who found the difference in peak stress between SP and FSI_2 to be less than 1 %. They used patient-specific lumen geometries with a wall fabricated at the lumen-thrombus boundary. Scotti *et al.* [172] found much larger differences between SP and FSI_2 estimated stresses of 9 % for their model with homogeneous wall thickness.

There is no evidence that aneurysm rupture risk correlates with systolic pressure whereas rup-

ture is strongly correlated with diastolic pressure [64, 199]. This suggests that modelling the stresses throughout the cardiac cycle may be important in assessing rupture risk. Errors in the mean tissue stress found here were very similar to those of the peak tissue stress.

The tissue stress is not expected to vary with material stiffness when the applied force is the same since stress is defined as a ratio of force to the applied area. However, due to the aneurysm shape, and the decrease in deformation with increasing stiffness, which results in a lower area for the pressure to act on, a small, but significant, reduction in the peak stress was found with increasing material stiffness. The analysis was geometrically (as well as materially) nonlinear. This is in agreement with the results of Raghavan and Vorp [59]. Wilson *et al.* [123] found that ruptured aneurysms were significantly more compliant than unruptured ones and Lindholt *et al.* [233] found that aneurysm walls which were more calcified, which would tend to make them stiffer [168, 234], had lower expansion rates and reduced need for surgery. It is likely that the compliance of aneurysms, being dependent on their biological formulation, is a symptom of the strength or thickness of the material and that highly compliant aneurysms which have failed to remodel and produce extra collagen are weaker. However, it appears that reduced stiffness may also increase tissue stress by up to 5 % which would enhance the correlation between rupture and compliance.

Including flexible walls in the models with either FSI_{1SP}, FSI_{1RW} or FSI_2 changed the blood flow patterns compared to rigid walled (RW) models with slower flow in the outlet during systolic dilation and faster flow during diastolic contraction. The velocity on the axis of the flexible models is never reversed as it is in the RW model. WSS in the bulge oscillates slightly more in RW compared to the flexible models with a slightly higher maximum WSS and slightly lower minimum WSS. Errors in the mean WSS in RW varied between 0.075 and 0.095 Pa which is between 30 and 60 % of the mean WSS in the bulge. The inclusion of flexible walls therefore has a much larger effect on the WSS than on the tissue stress. However, the wall motion can be predicted using FSI_{1SP} or FSI_{1RW} methods which are considerably faster than FSI_2. Errors in the mean WSS in FSI_{1SP} or FSI_{1RW} were similar, varying between 0.02 and 0.05 Pa or 10 to 30 % of mean WSS in the bulge.

Scotti *et al.* [172] describe more dramatic differences in their blood flow patterns with FSI compared to RW models. However, their use of a linear material produced larger wall displacements (peak displacement was 2 mm or 6.66 % of the aneurysm radius) than in this work, which would make more of a difference to the blood flow patterns. In this work the peak displacement

in the 6 cm aneurysm was just 0.65 mm or 2.2 % of the aneurysm radius. In the aneurysms with thrombus the percentage displacement of the lumen boundary was higher, up to 0.84 mm or 5.6 % of the maximum lumen radius. These displacements are smaller than the often quoted value of 10 % for normal arteries, but they are in line with the values found in the MRI scans of AAA patients in Chapter 4. These patients had lumen area changes of about 5 % in the diseased region which is a radius dilation of about 2.5 %.

5.4.1 Pulse Wave Propagation

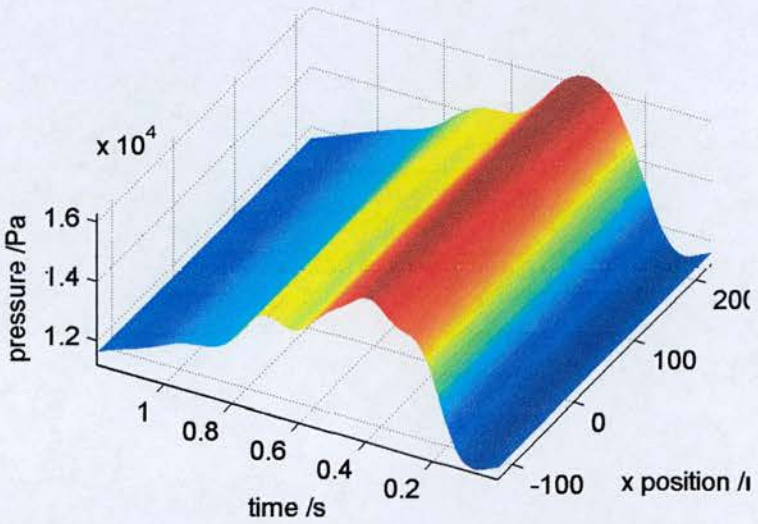

Figure 5.33: *Spatial and temporal pressure distribution in 6 cm aneurysm with* FSI_2

It has been suggested that the variation in the spatial pressure distribution due to fluid dynamics may influence the tissue stress distribution and for this reason several groups have developed FSI models of both simple and patient specific aneurysms [56, 173, 182, 185, 222]. Deplano *et al.* [75] studied the flow in rigid and compliant idealized aneurysm models and suggested that vortices impacting on the distal wall would result in localized regions of high pressure.

Figure 5.33 shows the variation in pressure in the 6 cm aneurysm throughout space and time. The spatial variation is less than 10 % of the temporal variation and occurs over the whole length of the vessel, rather than locally. The cause of the differences between the FSI_2 results and the other simulations is the propagation of the pressure wave along the vessel, which produces pressure variations which are not included in the other models.

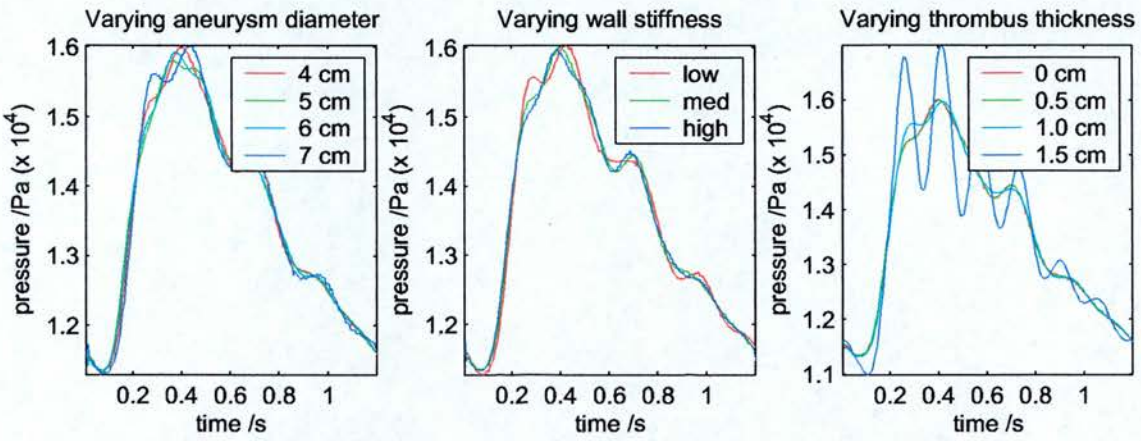

(a) Inlet Pressure

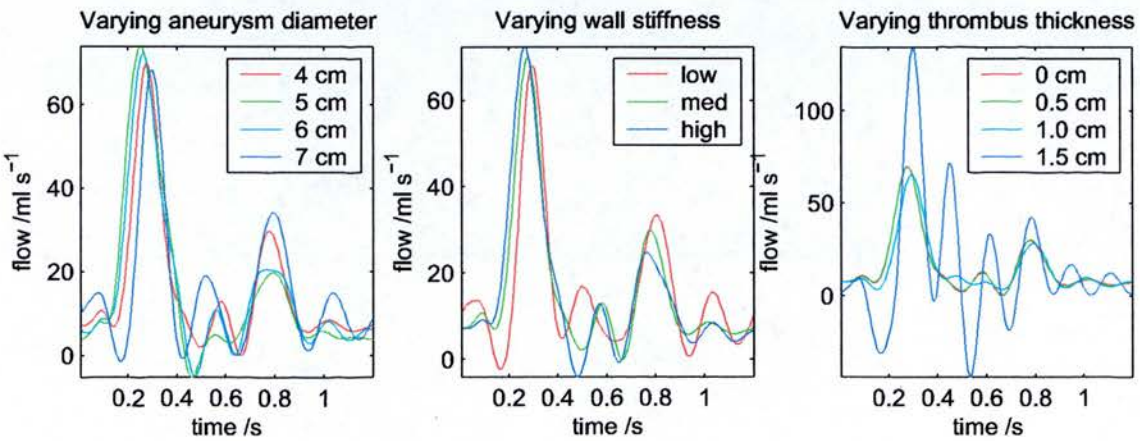

(b) Outlet Flow

Figure 5.34: *Wiggles in the inlet pressure and outlet flow due to unmatched boundary conditions*

The pressure wave at the inlet to the 6 cm aneurysm model can be seen to be a different shape to that at the outlet. This is shown more clearly in figure 5.34 along with the outlet flow rate. Although the 'wobbles' in the inlet pressure are fairly small the resulting wobbles in the outlet flow are considerable. Similar wobbles can be seen in the paper by Scotti *et al.* [172] where they manifest as oscillations in the volume of the models. These wobbles are thought to be due to the fact that the boundary conditions were not matched to the aneurysm models and are therefore inconsistent with each other. In a rigid walled model the pressure has no affect on the flow which is governed entirely by the inlet flow. However, in a flexible model the pressure causes the vessel to dilate, but if the vessel dilates there must be flow into the model in order to fill the extra volume. Hence the inlet flow and outlet pressure must be consistent with each other and with the geometry and material properties of the model. This is a limitation of the work in this chapter but using matched boundary conditions is expected to result in smaller errors rather than larger ones and would therefore not change the overall conclusions.

5.4.2 Transient Vortices

In reality, transient conditions occur for much of the time *in vivo*; for example when someone wakes and stands up a sudden pressure difference is introduced between the upper and lower body. Figure 5.35 shows the effect of a sudden reduction in the inlet pressure. In this case it was caused by sudden expansion of the aneurysmal tube from its zero pressure configuration to its configuration at diastolic pressure. The sudden pressure drop caused blood to be sucked up from downstream at flow rates of over 4000 $cm^3\ s^{-1}$. This immediately established vortices in the bulge and as the blood in the outlet length decelerated down towards more normal values a series of counter rotating vortices was created. By 0.120 s (0.1 cardiac cycles) velocities in the outlet tube had diminished but a fast vortex remained inside the aneurysm containing velocities up to 4 $m\ s^{-1}$. Another two vortices were also present but with smaller velocities.

Figure 5.35h shows how these vortices evolved over subsequent cardiac cycles. The patterns changed and blood gradually slowed down. At the end of the third cardiac cycle three vortices were still present and the solution had not yet reached the steady state. By examining the velocities at specific points and at the same phase in successive cardiac cycles it could be seen that it takes about 7 cardiac cycles in order to reach a steady state solution. The difference in the velocity magnitude for successive cycles was calculated and the mean percentage difference was calculated. The mean of the percentage differences, for all 200 phases and at 12 points,

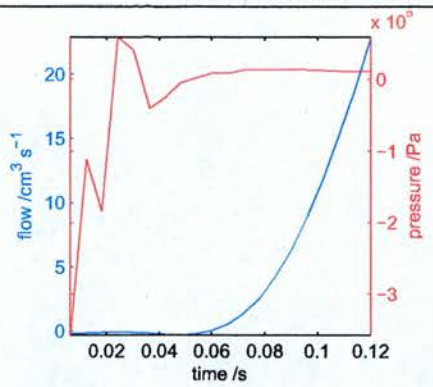

(a) inlet conditions

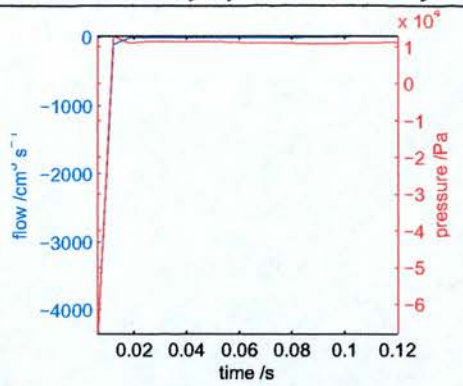

(b) outlet conditions

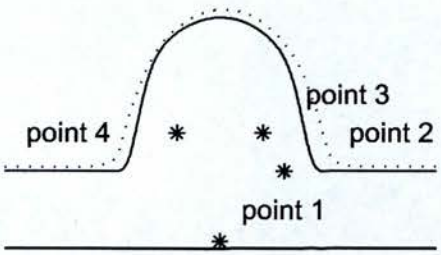

(c) point positions: wall position is shown both undeformed (solid) and deformed to diastolic pressure

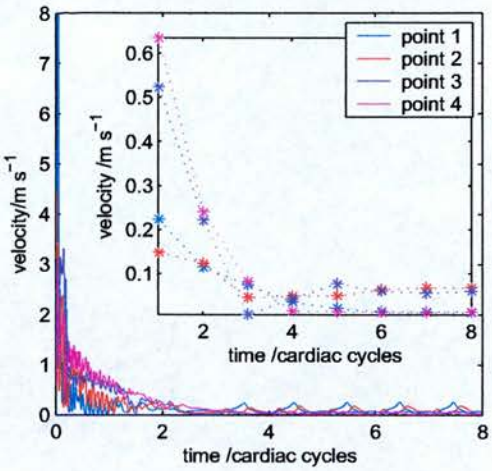

(d) velocity magnitude at specific points: note that the time scale on the inset graph starts at 1 cardiac cycle

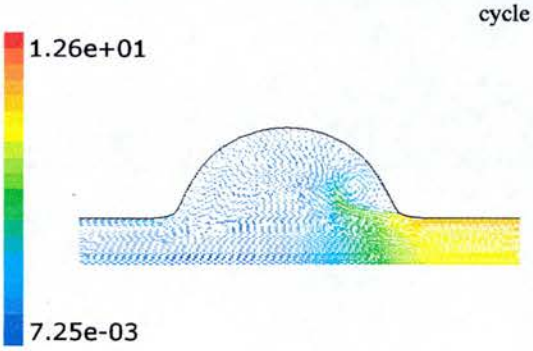

(e) 0.006 s, 0.005 cardiac cycles

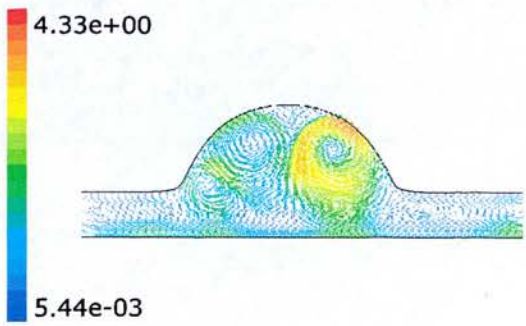

(f) 0.120 s, 0.1 cardiac cycles

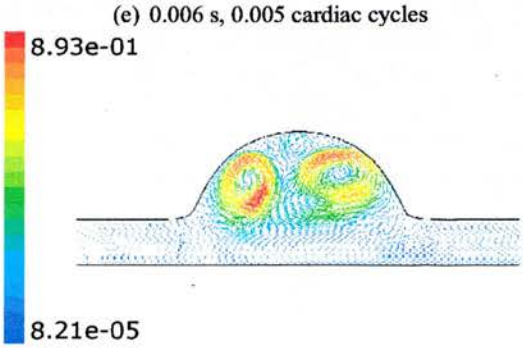

(g) 0.960 s, 0.8 cardiac cycles

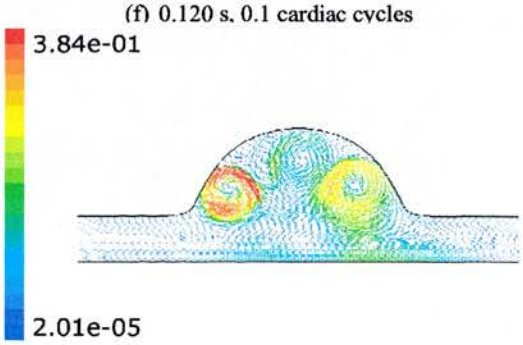

(h) 0.2160 s - 1.8 cardiac cycles

Figure 5.35: *Initialization and evolution of transient vortices*

was found to be below 20% by the end of the seventh cycle.

Turbulence has not been included in any of these simulations so in reality the vortices would die away faster. These results are an example of how changing the boundary conditions temporarily results in changes in the blood flow patterns, which must be happening frequently *in vivo* throughout a normal day. The results are an example of how the Navier-Stokes equations depend on the initial conditions and not just the conditions at the edges, and that even with the same conditions at the edges there are different solutions if the initial conditions are different.

5.4.3 Limitations

The residual stress has not been included in this work. Residual stress is the stress in the artery wall which remains when there is no pressure in the artery [17]. Residual stress causes an artery to open out if it is sliced longitudinally; the opening angle is a measure of the residual stress. The residual stress is highest on the outer edge of the artery wall and it is this variation across the wall thickness which causes the artery to open out. In the calculations here, the tissue stress is highest on the inner wall. It is expected that including the residual stress in the calculations would cancel out some of the variation in stress across the wall thickness and result in the stress distribution evening out.

The wall was modelled as a hyperelastic material so the stress at any given time is a function only of the internal pressure at that time and so all the techniques will give similar stresses at any time. However, if visco-elasticity were incorporated into the material model there would be a phase shift between the pressure and distension which would make the FSI more complicated and incorporating the complete FSI may make more of a difference.

The use of an isotropic, homogeneous wall is a further limitation which would alter the stress values and the wall motion but is not expected to alter the conclusions regarding the influence of FSI. The assumption of blood as a Newtonian fluid is justified since non-Newtonian effects are only significant in small arteries.

The geometry of the aneurysm models is a huge simplification of the geometry of real aneurysms. These are asymmetric, come in an infinite variety of shapes and have the iliac bifurcation at the distal end. However, the purpose of this work was to establish the differences in tissue stress and blood flow when different fluid structure interaction models were used which is easier in a simplified model. *In vivo* the blood flow patterns and tissue stresses would be modified by

the geometry of the aneurysm but the differences in the results due to different model techniques are expected to be similar. The use of a symmetrical model prevents any asymmetric phenomena from being studied. For example vortex shedding from a stenosis is asymmetric [47, 224, 235].

Steady flow studies on simple aneurysms found that turbulence was encouraged by the geometry, with turbulent flow for Re greater than about 1750 - 2000 [109, 110]. The maximum Re here was comparable with this range, $Re = 1730$ based on the inlet conditions and calculated as $Re = dV_{mean}/\nu$ for consistency with [109, 110] and where V_{mean} was the mean velocity across the inlet at peak flow and d was the diameter of the inlet. A limitation of this work was the omission of a turbulence model, which would allow for more realistic energy dissipation in the vortices.

5.5 Conclusions

A thorough analysis of the blood flow and tissue stress in axially symmetric, flexible aneurysms has been conducted. Peak tissue stress was found to increase linearly with aneurysm diameter over the range 4 to 7 cm. Peak tissue stress decreased by 5 % over the range of increasing material stiffnesses found in aneurysm patients. A thrombus layer also reduced the peak tissue stress, when the thrombus layer was 50 % of the aneurysm radius the peak stress was reduced by 36 %. Omission of the fluid-structure interaction made little difference to the calculation of peak tissue stress with a 1.1 % error in a 6 cm aneurysm with average stiffness and without thrombus.

Blood flow patterns consisted of toroidal vortices which formed during systolic deceleration and moved down the aneurysm in agreement with other similar studies. WSS in the aneurysm bulge decreased with aneurysm diameter and increased slightly with material stiffness. The blood flow patterns were altered by the flexible walls compared to models with rigid walls. Flow in the rigid walled models was faster in the core of the vortex ring and the flow was reversed during diastole. WSS errors in the rigid walled model were between 30 and 60 % of the mean WSS. Wall motion could be predicted using simpler 1-way coupled fluid-structure interactions which had errors of 10 to 30 % of the mean WSS compared with the complete fluid-structure interaction.

In conclusion, the decision as to what modelling technique to use depends on whether it is tissue

stresses or blood flow that is interesting. Incorporation of the complete FSI is unnecessary for prediction of tissue stresses within the aneurysm wall. Predictions of blood flow patterns and WSS are altered by including flexible walls and it may be necessary to simulate the fluid-structure interaction for calculating these.

Chapter 6
A Lumped Parameter Model of an Aneurysm to find the Outlet Pressure

Stresses in the arterial wall are determined by the blood pressure in the vessel and wall shear stress on the lumen surface is determined by the flow rate. However, interaction of the blood and the artery wall, which causes a time varying lumen geometry, was shown in Chapter 5 to influence calculations of both tissue stress and wall shear stress albeit in a fairly small way. Propagation of the pressure and flow waves through the artery is the cause of these effects. Modelling the pulse wave propagation requires inlet and outlet boundary conditions which are compatible with each other and with the arterial geometry between them. This chapter investigates the use of a lumped parameter model of the aneurysmal artery for finding the outlet pressure boundary, with the aim of removing the unphysiological 'wobbles' in the inlet pressure and outlet flow seen in Chapter 5.

6.1 Introduction

Three dimensional CFD models of arteries are ideal for calculating local wall shear stress (WSS) and tissue stress distributions in patient specific arterial geometries, and with patient specific boundary conditions when these are available. However, in order to study pulse wave propagation in three dimensional geometries, complete fluid-structure interaction models are required. These are computationally expensive, and therefore unsuitable for modelling larger sections of the arterial network. For many purposes, for example estimating the central pressure wave from the radial wave as in pressure tonometry using a Sphygmocor type system, they are also excessively complicated. Several different types of lower dimensional models have been developed for studying various aspects of the cardiovascular system.

Lumped parameter models take the properties of the whole vascular system and 'lump' them together into a few parameters. A single tube with properties of the whole system is used to represent the whole of the network structure [124]. These models exploit an analogy between fluid

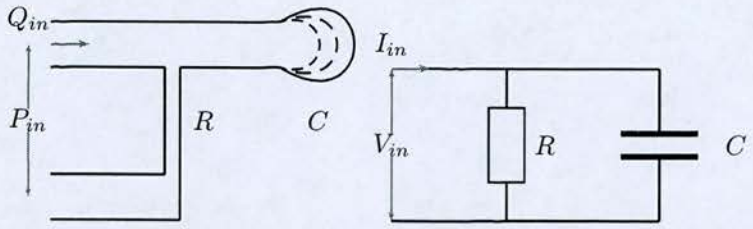

(a) mechanical model (b) electrical model

Figure 6.1: *Windkessel*

flow in a system with compliant walls, and electrical circuits consisting of resistors, capacitors and inductors [125]. Viscosity is treated as resistance, compliance is accounted for by capacitors and fluid inertia is inductance. Flow is then analogous to electrical current, while pressure is analogous to voltage. The simplest lumped parameter model is the Windkessel: a resistor and a capacitor in parallel, see figure 6.1 for a comparison of the mechanical and electrical models [32, 124]. There is no inductance, so the fluid in the mechanical system is massless.

Lumped parameter models provide no information about the spatial variation in pressure or flow waves, which is where distributed models can be useful. Models such as the ones by Avolio [128], or Stroev *et al.* [129, 130], consider each arterial segment as a transmission line, with resistance, capacitance and inductance, and all the segments connected to form the arterial tree.

Other types of lower dimensional models of blood flow in the arterial system solve the Navier-Stokes equations in one dimension with an equation of state for the arterial wall [131, 132, 236].

Connecting sections of artery modelled in full 3D to sections, either proximal or distal, which are approximated using a reduced model, is nontrivial since the 3D section requires the boundary conditions to be specified on the whole cross section, while the reduced models only provide averaged data. Methods have been developed for dealing with these issues by incorporating all the models into one set of equations [30, 224, 237]. Alternatively the reduced model and 3D models can be solved sequentially [238]. In this case the 3D model is represented as a section of the reduced model of the whole vascular system. If flow in the 3D section is calculated using approximate boundary conditions, a reduced model of this section can be created by fitting its parameters to the 3D results. The reduced model can then be used to find correct boundary conditions for the 3D section. One of the advantages of this method is that multiple diseased sites can be incorporated [238]. This is useful as patients with AAA often also have associ-

ated aneurysms in the iliacs or other arteries [160], and many have atherosclerotic plaques too [15, 199].

A lumped parameter model of the aneurysm and downstream impedance will be used to investigate the possibility of producing boundary conditions, based on the ones for the healthy abdominal aorta found by Olufsen *et al.* [132], but adjusted to match the geometry and material properties of the models in this study, thereby improving on the outlet pressure boundary condition used in Chapter 5.

6.2 Methods

Axially symmetric aneurysm models with flexible walls were created and the full 3D flow within was calculated using a fully coupled fluid-structure interaction (FSI) as described in Chapter 5. The boundary conditions used were the flow and pressure found by Olufsen *et al.* [132] in the abdominal aorta, with the flow applied at the inlet of the model and the pressure at the outlet. Pressure at the inlet and flow at the outlet were obtained from the 3D simulation.

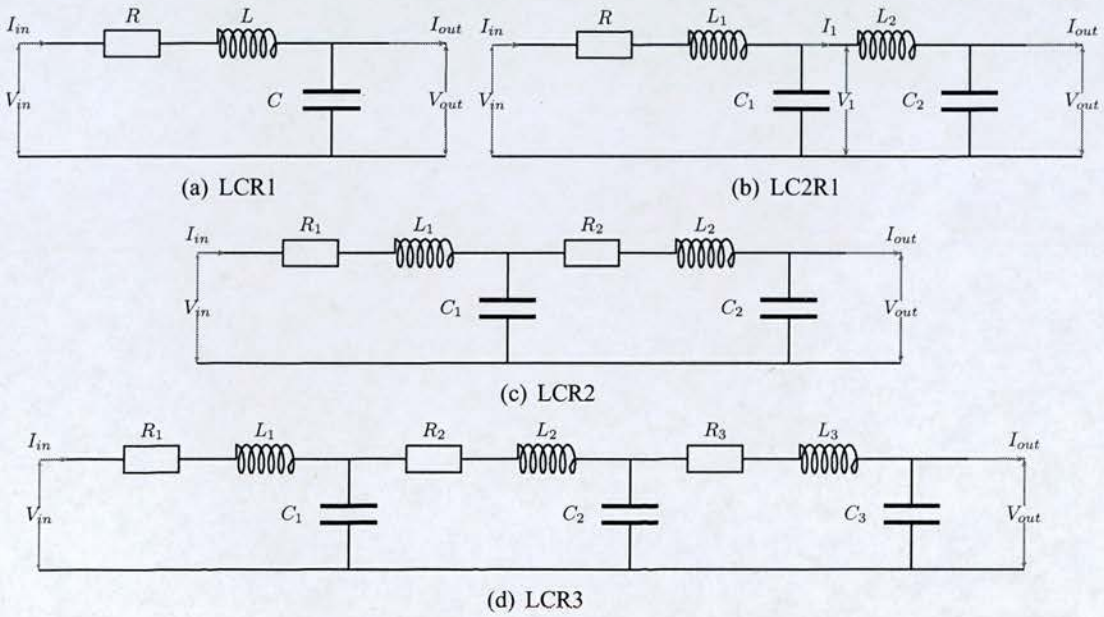

(a) LCR1

(b) LC2R1

(c) LCR2

(d) LCR3

Figure 6.2: *Lumped parameter models of an aneurysm*

A series of four lumped parameter models of the aneurysmal artery were created (figure 6.2), based on the electrical circuit analogy, and with increasing numbers of inductors (L), capacitors (C) and resistors (R). Using circuit theory, equations could be found for the outlet flow (I_{out}) and

pressure (V_{out}) in terms of the inlet flow (I_{in}) and pressure (V_{in}) and the L, C, and R parameters. As an example the equations for LC2R1 are derived below, it is straightforward to alter these for LCR1, LCR2 and LCR3.

From Kirchhoff's laws:

$$V_1 = V_{in} - RI_{in} - L_1 \frac{dI_{in}}{dt} \tag{6.1}$$

$$I_1 = I_{out} + \frac{dQ_2}{dt} \tag{6.2}$$

$$V_{out} = V_{in} - RI_{in} - L_1 \frac{dI_{in}}{dt} - L_2 \frac{dI_1}{dt} \tag{6.3}$$

$$I_{out} = I_{in} - \frac{dQ_1}{dt} - \frac{dQ_2}{dt} \tag{6.4}$$

where Q_1 and Q_2 are the charges on C_1 and C_2, and since the charge on a capacitor is $Q = CV$, 6.2 and 6.4 become,

$$I_1 = I_{out} + C_2 \frac{dV_{out}}{dt} \tag{6.5}$$

$$I_{out} = I_{in} - C_1 \frac{dV_1}{dt} - C_2 \frac{dV_{out}}{dt} \tag{6.6}$$

Then substituting $I' = Ie^{i\omega t}$ and $V' = Ve^{i\omega t}$ to get flow and pressure in terms of frequency gives:

$$V_1' = V_{in}' - RI_{in}' - i\omega L_1 I_{in}' \tag{6.7}$$

$$I_1' = I_{out}' + i\omega C_2 V_{out}' \tag{6.8}$$

$$V_{out}' = V_{in}' - RI_{in}' - i\omega LI_{in}' - i\omega L_2 I_1' \tag{6.9}$$

$$I_{out}' = I_{in}' - i\omega C_1 V_1' - i\omega C_2 V_{out}' \tag{6.10}$$

The individual frequency components for I_{in}', I_{out}', V_{in}' and V_{out}' were found using a Fourier transform. The high frequency components were set to zero to avoid fitting to noise. An equation for the difference between the values of I_{out}' and V_{out}' calculated as above, and the values from the simulation, was then formulated:

$$\chi^2 = \sum |I_{out}' - I_{in}' + i\omega C_1 V_1' + i\omega C_2 V_{out}'|^2 + \sum |V_{out}' - V_{in}' + RI_{in}' + i\omega LI_{in}' + i\omega L_2 I_1'|^2 \tag{6.11}$$

where the summation is over all the frequency components.

χ^2 was then minimised using Matlab 6.5 r.13 (MathWorks Inc., Natick, MA, USA) to find values for all the L, C and R parameters. In this way lumped parameter models of each of the 3D aneurysms were produced.

The fitted results from the lumped parameter models were compared with the results of the 3D simulations, and of the four lumped parameter models LC2R1 was found to give the best fit with the fewest parameters.

To produce the new boundary conditions it was necessary to embed the lumped parameter aneurysm within a model of the whole arterial system. A transmission line model of the arterial tree [128, 129] could have been used, with the abdominal section replaced with the lumped parameter aneurysm. However, for simplicity, and as a first approximation, it was decided that the inlet boundary condition could remain the same, that is the healthy abdominal aortic flow rate from Olufsen *et al.* [132], and the outlet would be terminated with some downstream impedance representing all of the arteries below the aortic bifurcation. Using just a resistor would mean the flow and pressure where in phase at the outlet which is physiologically unrealistic. Instead a Windkessel was used (figure 6.1). Then, using the flow wave for the initial 3D simulation, the outlet pressure wave could be calculated.

The value of R_{out} was chosen such that the inlet and outlet pressures were in the physiological range and C_{out} was chosen so that the inlet and outlet flows maintained the same basic shape. With such a simple downstream impedance it was not possible to get a very realistic outlet flow wave or pressure waves but if the Windkessel worked it should be possible to extend the idea by using a complete transmission line model of the arterial system.

Having found the new outlet pressure the full 3D calculations were performed in the same way as the original ones, described in Chapter 5, but with the new boundary conditions.

6.3 Results and Discussion

6.3.1 Lumped parameter aneurysm

Of the four different lumped parameter models LC2R1, LCR2 and LCR3 were all found to fit the 3D results well (figure 6.3). LC2R1 was then chosen as it has the fewest parameters. The fits for LC2R1 are shown for a straight tube and the aneurysms with different diameters in figure 6.4. The fits are slightly worse for the larger aneurysms, most noticeably during the

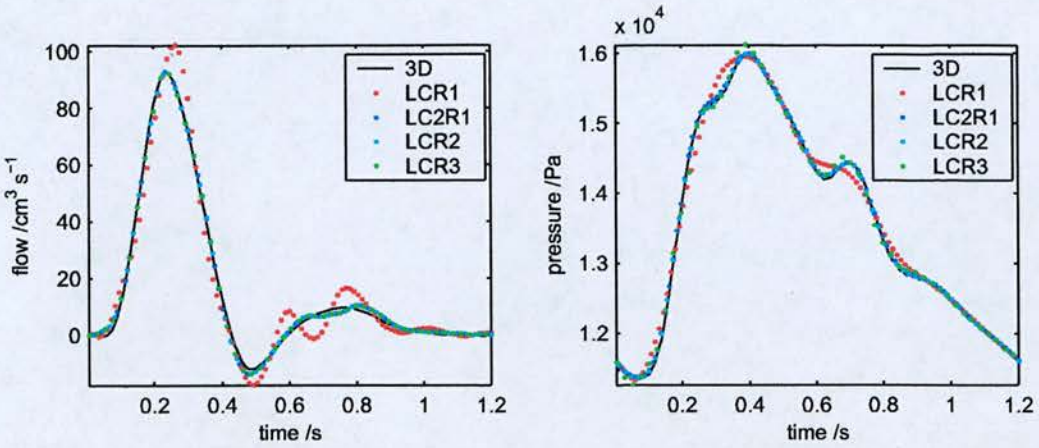

(a) Inlet flow

(b) Inlet pressure

Figure 6.3: *Inlet flow and pressure in the 6 cm aneurysm fitted with the 4 different lumped parameter models.*

reverse flow phase.

The individual R, L and C parameters and the total resistance, inductance and capacitance are shown in figures 6.5 and 6.6. The resistance increases with aneurysm diameter, the total inductance decreases and the total capacitance increases.

Changes in the capacitance with aneurysm diameter and stiffness are the largest changes. These changes are intuitive, however, the smaller changes in resistance and inductance are less so. Since they are less intuitive the reasons for the resistance and inductance trends will be derived from fluid dynamic principles in the next two sections.

6.3.1.1 Resistance

The resistance due to steady flow in a straight tube is predicted by Poiseuille's law to decrease with tube diameter according to:

$$R = \frac{8\mu L}{\pi r^4} \tag{6.12}$$

where L is the length of the tube and r is its radius. That is, the resistance decreases with tube radius, apparently contradictory to what has been found in the aneurysm models. However, the situation in tubes with diameters which vary along their length is more complicated. Changes in diameter are a source of 'minor losses' in pipe lines; when the flow is disturbed there is flow separation and energy is lost due to increased viscous effects [112].

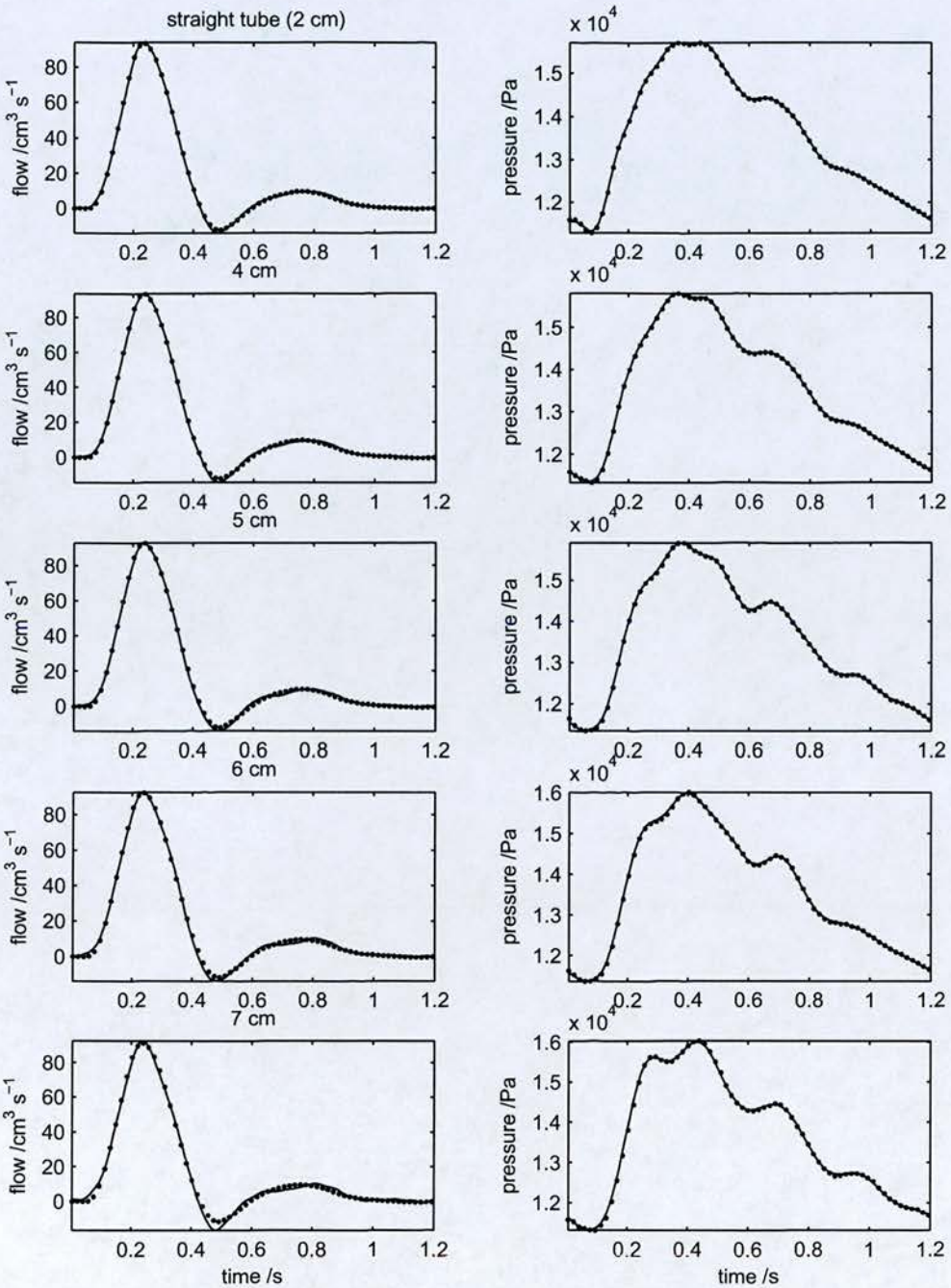

Figure 6.4: *Inlet flow and pressure fitted with the LC2R1 lumped parameter model in the straight tube and the aneurysm models with different diameters. Dots are the 3D simulation results and the line is the fit from LC2R1.*

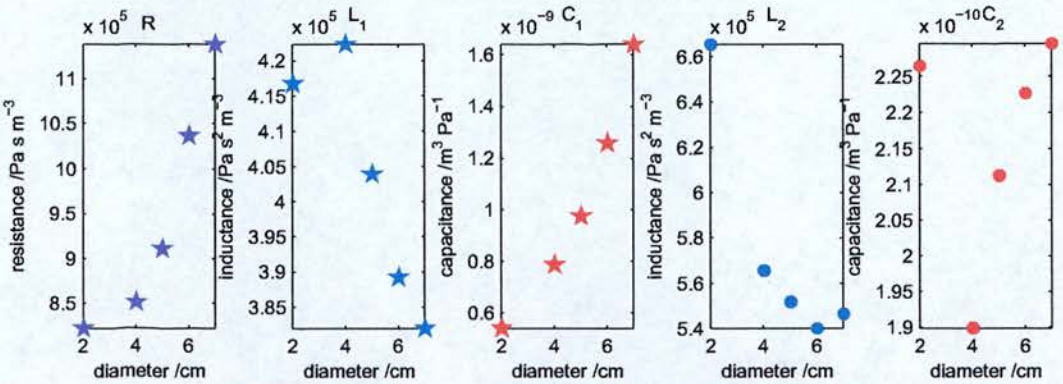

(a) Variation in individual R, L and C parameters with aneurysm diameter

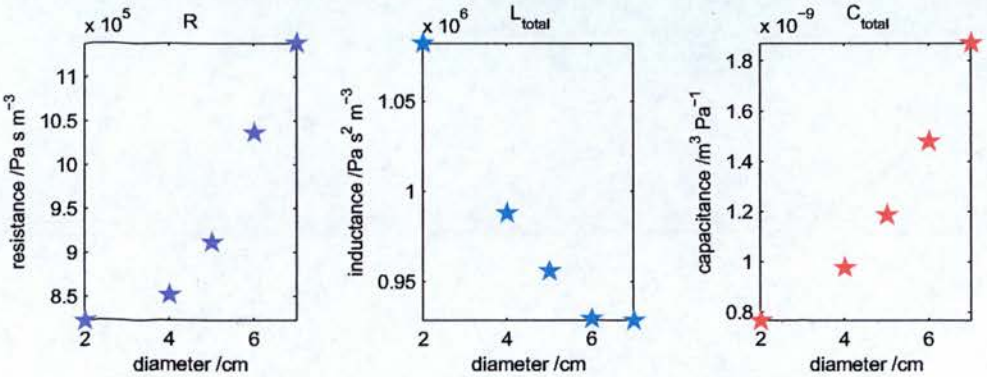

(b) Variation in total resistance, inductance and capacitance with aneurysm diameter

Figure 6.5: *Variation in model parameters with aneurysm diameter*

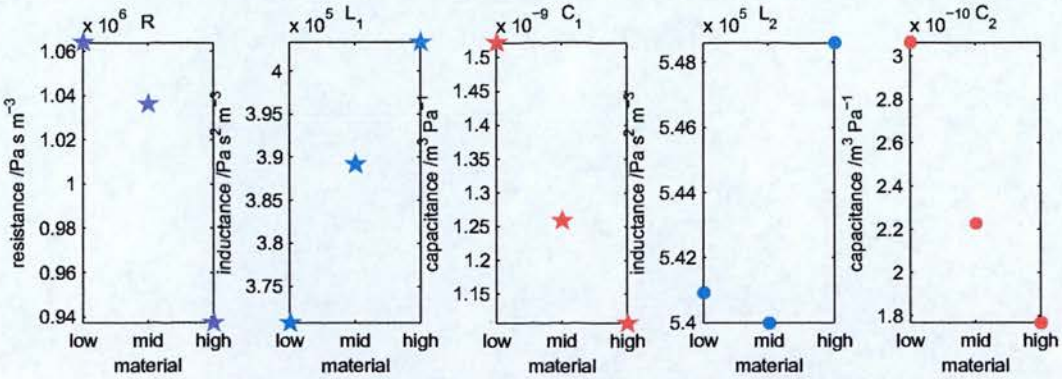

(a) Variation in individual R, L and C parameters with aneurysm wall stiffness

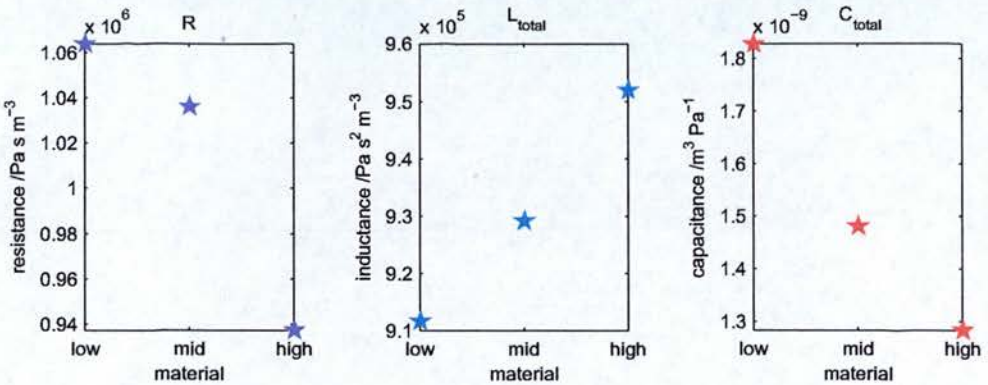

(b) Variation in total resistance, inductance and capacitance with aneurysm wall stiffness

Figure 6.6: *Variation in model parameters with aneurysm wall stiffness*

Consider two planes through a sudden expansion shown in figure 6.7. The velocity on a plane S_1, with area A_1, is v_1 and the area of S_2 is A_2 and velocity is v_2. v_1 and v_2 vary with position on the plane but have the mean velocities $\overline{v_1}$ and $\overline{v_2}$.

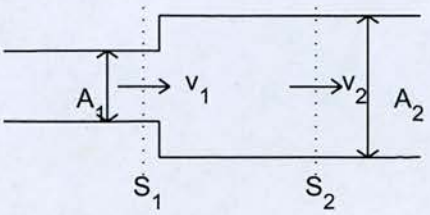

Figure 6.7: *a sudden expansion*

The equation for continuity of mass is:

$$A_1\overline{v_1} = A_2\overline{v_2} \tag{6.13}$$

and equating impulse and momentum change gives:

$$(p_1 - p_2)A_2 = \rho A_1\overline{v_1}(\overline{v_2} - \overline{v_1}) \tag{6.14}$$

and then the energy loss is given by the work done on the fluid minus the change in kinetic energy:

$$E_{lost} = \frac{p_1 - p_2}{\rho} - \frac{\overline{v_2}^2 - \overline{v_1}^2}{2} \tag{6.15}$$

Substituting 6.13 and 6.14 into 6.15 gives:

$$E_{lost} = \frac{\overline{v_1}^2}{2}\left(1 - \frac{A_1}{A_2}\right)^2 \tag{6.16}$$

And so, the energy loss increases with the difference in areas. In the aneurysm model the expansion is not sudden and so the loss is lower than this prediction. The energy is dissipated by the vortex in the aneurysm, the size of which increases with aneurysm diameter. Sudden constrictions also produce losses [112] and so there is a further energy loss due to the diameter constriction at the distal end of the aneurysm. A sudden constriction produces a submerged jet following the contraction after which the flow must expand to refill the tube. It is this expansion which produces the majority of the loss due to a sudden constriction.

The loss of energy due to the aneurysm bulge also results in a loss of momentum. Since blood

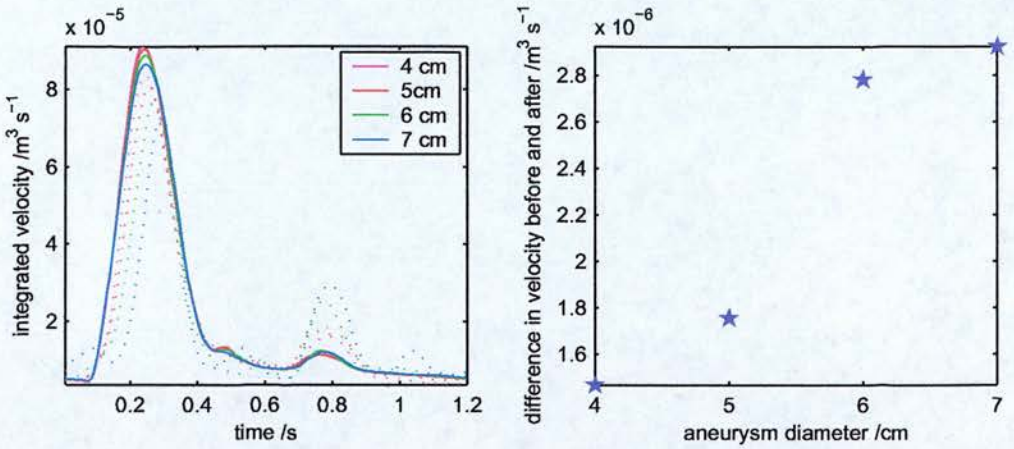

(a) axial-velocity integrated over planes before (solid lines) and after aneurysm (dashed lines)

(b) difference in mean integrated velocity before and after aneurysm

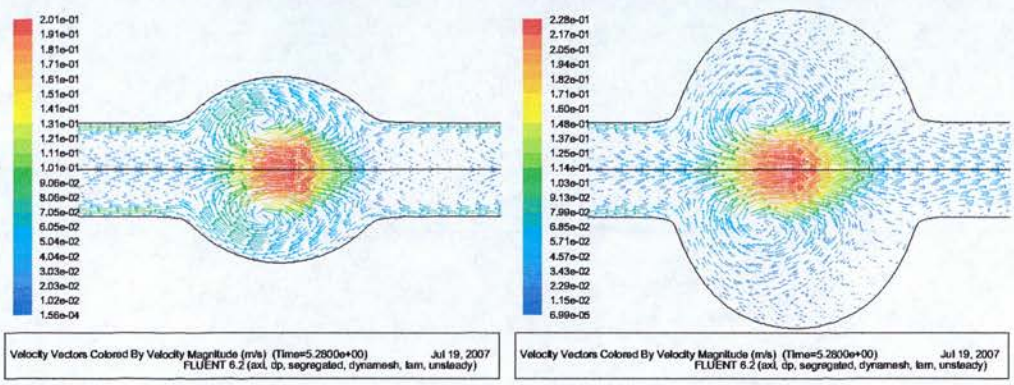

(c) Vortex in 4 cm aneurysm

(d) Vortex in 7 cm aneurysm

Figure 6.8: *Energy losses increase with the aneurysm size as shown by the decrease in momentum. Energy is transferred into the vortex which increases in size as the aneurysm diameter increases.*

is an incompressible fluid, the density is constant, and the momentum is proportional to the velocity. Figure 6.8a shows the integral of the velocity, over planes at the x locations -0.05 and 0.05 m for each of the aneurysms of different sizes. Figure 6.8b shows how the difference in the average momentum before and after the aneurysm increases with the aneurysm diameter.

Resistance decreases very slightly with material stiffness which is simply due to the slight differences in the diameter of the aneurysms of different stiffness because they expand differently under the same pressure.

6.3.1.2 Inductance

In the mechanical analogy the inductance of the system is attributable to the fluid inertia, or momentum. In a straight tube the inductance would be expected to increase with diameter as the mass of the fluid increases. The decrease in the inductance with aneurysm diameter can be explained as follows.

Consider two planes through the simple aneurysm shown in figure 6.9. The velocity on a plane S_1, with area A_1, is v_1 and the area of S_2 is A_2 and velocity is v_2. v_1 and v_2 vary with position on the plane but have the mean velocities $\overline{v_1}$ and $\overline{v_2}$.

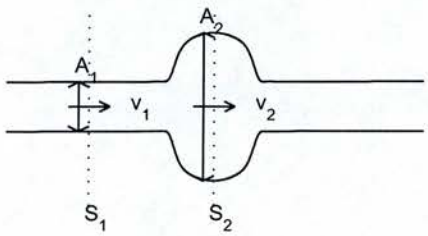

Figure 6.9: *a simple aneurysm*

By continuity of mass:

$$A_1\overline{v_1} = A_2\overline{v_2} \tag{6.17}$$

Considering the momentum in the direction of the axis leads to a relationship between the momentum within the bulge and the bulge diameter. The momentum on S_2 is:

$$u_2 = \rho\overline{v_2}^2 A_2 = \rho\overline{v_1}^2 A_1 \left(\frac{A_1}{A_2}\right) \tag{6.18}$$

So as the diameter increases the momentum in the bulge decreases and the overall inductance of the aneurysm decreases. In figure 6.10a the variation in the volume integral of the axial component of the velocity, proportional to the momentum, with time for each of the aneurysms with different diameters is shown. The peak integrated velocity is clearly smaller in the larger aneurysms, however, this is not the case during the diastolic phase. Figure 6.10b shows the mean of the integrated velocity over time and the graph clearly has a very similar shape to that of the change in total inductance with diameter (see figure 6.5). Figures 6.10c and 6.10d show the spatial distribution of axial velocity in the smallest and largest aneurysms at the times of peak axial-velocity.

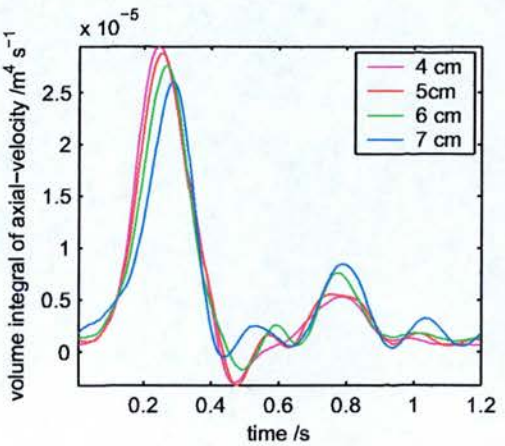

(a) axial-velocity integrated over volume

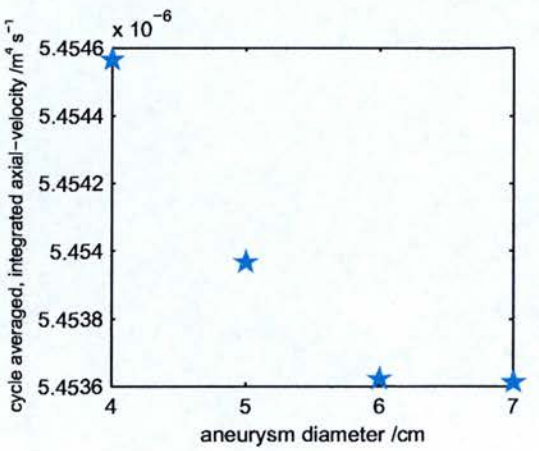

(b) variation in cycle averaged volume integral of axial velocity

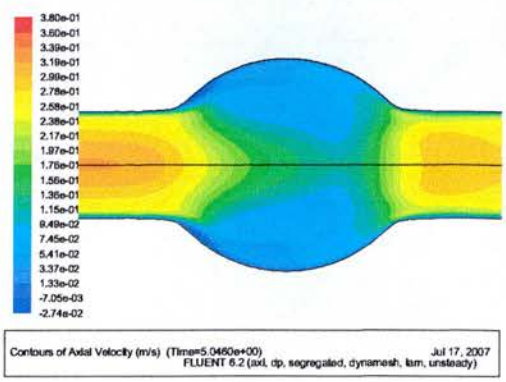

(c) distribution of axial velocity in 4 cm aneurysm at time of peak

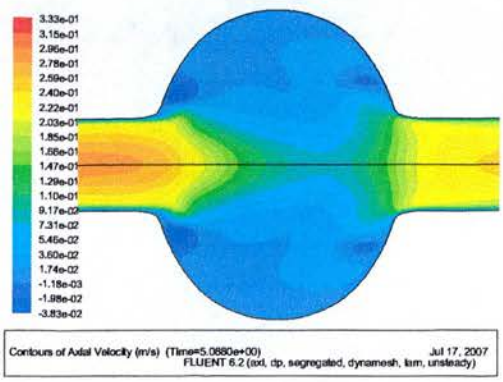

(d) distribution of axial velocity in 7 cm aneurysm at time of peak

Figure 6.10: *Axial-velocity integrated over the cardiac cycle decreases with aneurysm size.*

Like resistance, the change in inductance with material stiffness is due to the slightly different expansions.

6.3.2 Downstream Impedance

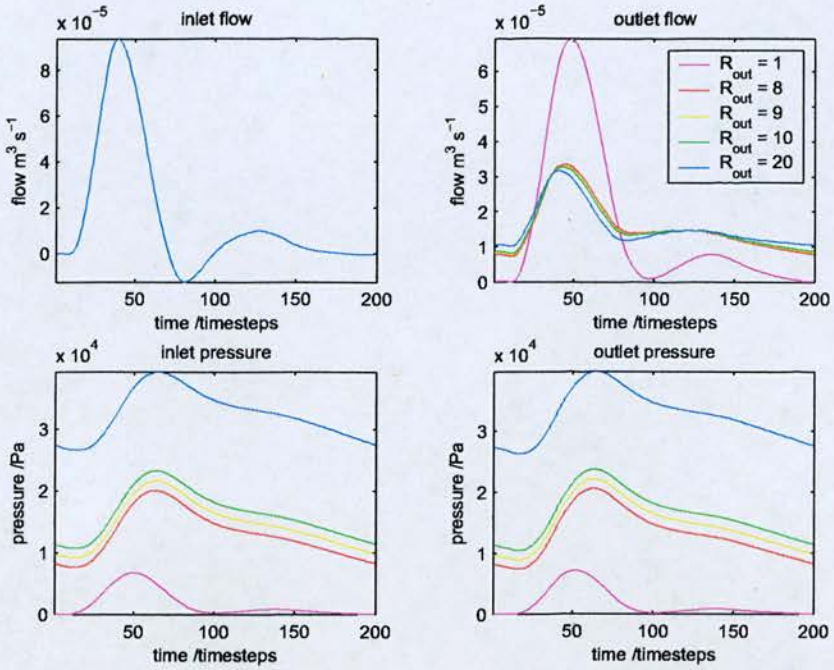

Figure 6.11: *Influence of downstream impedance parameters R_{out} and C_{out} on aneurysm boundary conditions. Effect of varying R_{out} (R_{out} in* Pa s m^3*) with C_{out} =* 0.02 m^3 Pa^{-1}

The downstream impedance model was a Windkessel with resistance R_{out} and capacitance C_{out}. Figures 6.11 and 6.12 show the effect of varying the values of R_{out} and C_{out} on the boundary conditions of the lumped parameter straight tube if the inlet flow is kept constant.

At low values of R_{out} the outlet flow compares well with the inlet flow in both shape and magnitude, however, the shape of the pressure wave is incorrect. Increasing R_{out} produces a more realistic pressure wave but produces an outlet flow wave without reverse flow. Low values of C_{out} produce reasonable pressure waves but give outlet flow waves the same shape as the pressure waves. Increasing C_{out} changes the shape of the outlet flow wave so that it is more similar to the inlet flow wave than the pressure waves but also introduces a high frequency oscillation.

Values of R_{out} and C_{out} (9 Pa s m^3 and 0.02 m^3 Pa^{-1} respectively) were chosen as a compromise between producing realistically shaped boundary conditions, having realistic magnitudes and minimizing the high frequency oscillation. Figure 6.13 shows the outlet pressure boundary condition for each of the aneurysms with different diameters.

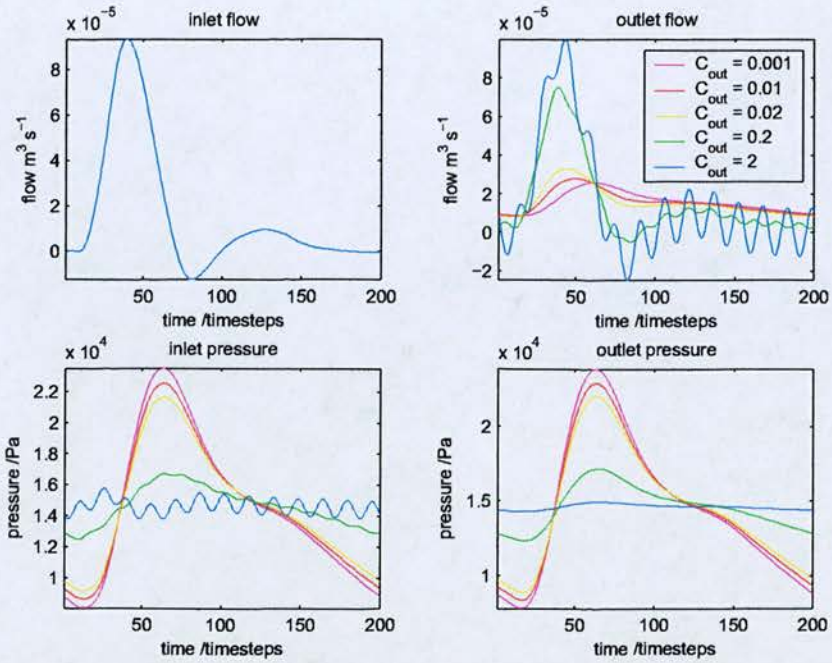

Figure 6.12: *Influence of downstream impedance parameters R_{out} and C_{out} on aneurysm boundary conditions. Effect of varying C_{out} (C_{out} in $\mathrm{m^3Pa^{-1}}$) with R_{out} =* $9\ \mathrm{Pa\ s\ m^3}$

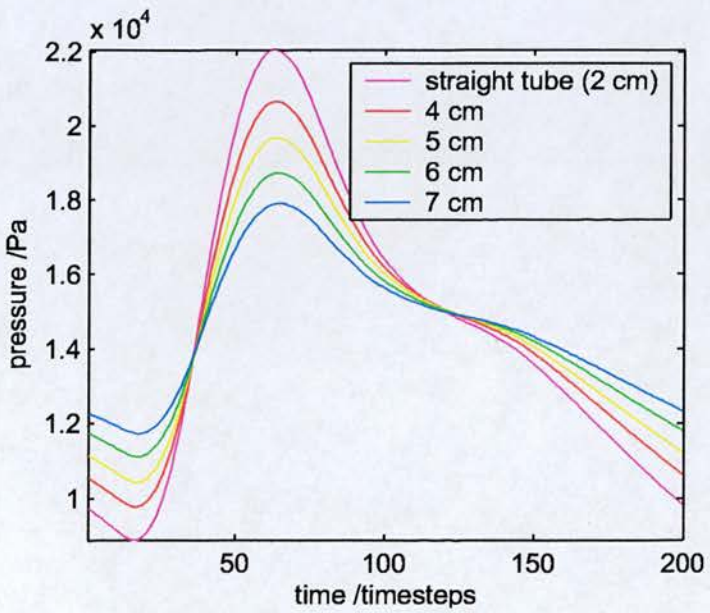

Figure 6.13: *Outlet pressure boundary conditions for aneurysms with varying diameters and downstream impedance boundary conditions R_{out} =* $9\mathrm{Pa\ s\ m^3}$ *and C_{out} =* $0.02\mathrm{m^3Pa^{-1}}$

6.3.3 3D calculations

The complete FSI calculations for a straight tube and the four different diameters of aneurysm were repeated using the boundary conditions derived with the lumped parameter model. The outlet flow and inlet pressure for the the third cardiac cycle are shown in figure 6.14. Although the inlet pressure results fit the prediction from the 1D model fairly well, the outlet flow shows less agreement and as the aneurysm diameter increases the quality of the fit is reduced.

The lumped parameter model fitted the original 3D model results well, that is, it was an accurate model of the 3D model with the original boundary conditions. However, the results from the new 3D calculations do not fit the lumped parameter predictions so well, which shows that the lumped parameter model must depend not only on the geometry of the 3D model but also, to some extent, on the boundary conditions. The reasonable agreement in the straight tube and smaller aneurysm results shows that these lumped parameter models are more transferable than the larger aneurysm models.

The total resistance, inductance and capacitance for the new lumped parameter models follow the same trends as the original ones. With the new boundary conditions R is larger than with the original ones, increasing from 1.1×10^6 to $1.8 \times 10^6 \text{Pasm}^{-3}$ with increasing aneurysm diameter from 4 to 7 cm. This is due to the new pressure boundary condition being larger and hence the aneurysms have dilated more and the energy loss from the expansion is greater. The new values for L_{total} are lower than the original ones, decreasing from 8×10^5 to $5.5 \times 10^5 \text{Pas}^2\text{m}^{-3}$, for the same reason. In contrast C_{total} is similar increasing from 0.9×10^{-9} to $1.8 \times 10^{-9} \text{m}^3\text{Pa}^{-1}$ over the range of aneurysm diameters.

The 3D models are nonlinear: the Navier-Stokes equations are nonlinear and the constitutive relationship for the artery wall was also nonlinear. This accounts for the why the lumped parameter model is not completely transferable. To obtain complete agreement between the lumped parameter and 3D results it would be necessary to iterate between the models. Alternatively a nonlinear lumped parameter model could be introduced, although this would prevent the use of Fourier space methods.

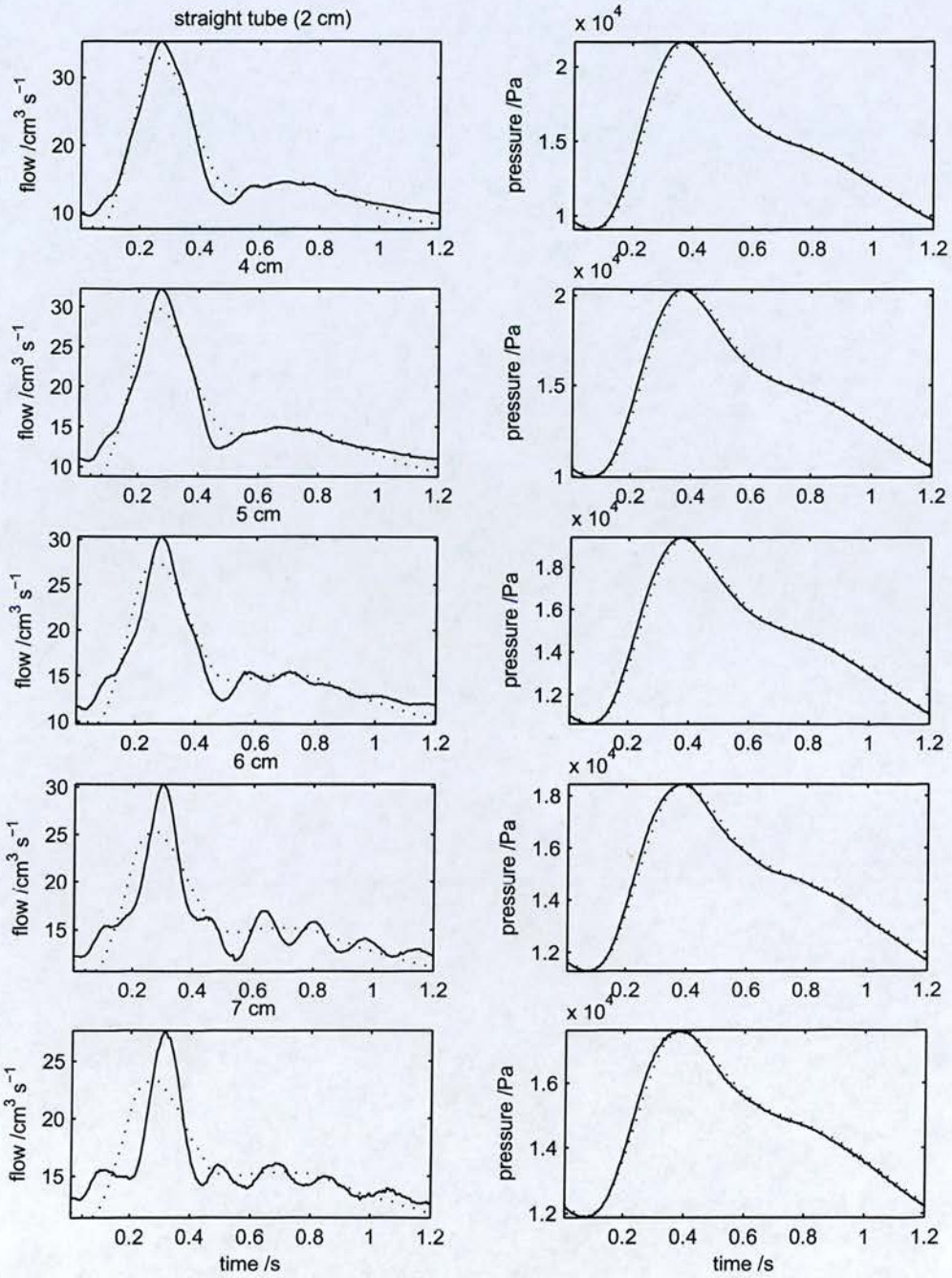

Figure 6.14: *Comparison of the 1D model prediction and the 3D results. Dotted line shows 1D model prediction and solid line shows the 3D model results.*

6.4 Conclusions

A lumped parameter model of an abdominal aortic aneurysm was created using an electrical circuit analogy. The model consisted of a resistor, two capacitors and two inductors and was shown to reproduce the flow and pressure in the 3D model accurately. Variations of the total resistance and inductance with aneurysm diameter were explained in terms of energy losses and reduction in total momentum respectively. The lumped parameter model was found to be transferable for small aneurysms but not for larger aneurysms. The 'wobbles' in the inlet pressure from Chapter 5 were removed.

Chapter 7
Conclusions and Future Work

Abdominal aortic aneurysm is a potentially fatal disease of the aorta affecting approximately 5 % of the elderly population, and yet the progression of the disease is still not fully understood. The extent to which biomechanical processes influence the disease is unknown but it has been shown that peak tissue stress can predict aneurysm rupture, and more recently that tissue stresses also correlate with aneurysm growth. The latter is an example of arterial remodelling; the growth of the arterial wall in response to the stresses experienced. The role of fluid mechanical factors in aneurysm disease has been studied less, but work in animal models has shown that macrophage density gradients are influenced by haemodynamic conditions, and that inhibition of platelet aggregation limits aneurysm expansion. The shear force exerted by blood flow is considerably smaller than the tissue stresses felt by the arterial wall, but these small forces could still play an important part in AAA, possibly in the initiation or early development of the disease. With this in mind, the aim of this thesis was to investigate blood flow and tissue stresses in models of abdominal aortic aneurysm.

In chapter 2 a method was developed for calculating the blood flow in patient specific aneurysms. CT scans were segmented using a semi automatic, threshold based algorithm and the slice contours were reconstructed to form the arterial geometries. Fluent's mesh adaption was used to refine the mesh along the wall and in areas of high velocity gradients to create a mesh which was both fine enough and fast enough. Blood flow was calculated in three patients using the same inlet velocity and outlet pressure, and flow patterns were found to be highly dependent on the specific geometry of the aneurysm, with crescent shaped vortices and helical flow. Mean WSS magnitude was lower in the aneurysm bulge than in the inlet length, OSI was more variable in the bulge and spatial WSSG was highest in the aneurysm neck and at the distal end.

In chapter 3 an archetypal velocity wave in the aorta of patients with AAA was found which would be suitable for the inlet boundary condition to *in vitro* or *in silico* studies of blood flow in AAA. The diastolic maximum velocity was found to be significantly different in AAA patients to that in young healthy normals, although there were no significant differences between the

waveforms of AAA patients and older healthy subjects. Womersley's solution for fully developed flow was used to calculate a typical flow wave in AAA patients and the errors in assuming fully developed flow were discussed. The archetypal velocity wave, and intersubject variation in the characteristic points, found here could be used to investigate the effects of variation amongst the population on flow parameters such as vortices, wall shear stress and oscillatory shear index.

The blood flow patterns found in the aneurysms in chapter 2 were interesting, but without validation of the method there is no way to know if they are accurate. Chapter 4 compared CFD estimations of blood flow with phase-contrast (PC) MRI measurements in three patients. Generally, applying the correct velocity profile at the inlet, produced velocities in the aneurysm bulge in better agreement with the PC-MRI results than simply applying the correct flow rate, at the entrance to an inlet length. However, this was not always the case. The length of healthy aorta from the inlet section to the aneurysm bulge is likely to be an important factor in calculating the velocities within the bulge correctly, since flow in the bulge is sensitive to the inlet conditions. The velocity profile at the inlet should be measured after the renal arteries, which does not leave much space. A possible solution may be to obtain a long portion of the healthy section of the aorta and apply the flow measured just above the aneurysm bulge to the entrance of the longer section of anatomically correct geometry. This would allow the flow profile to develop correctly and enter the aneurysm bulge with a more correct inlet condition. Flow leaving the aorta to the renal arteries directly before the aneurysm could still influence the velocity profiles within the bulge. These two effects, that is the length of the healthy aorta proximal to the aneurysm, and the flow to the renal arteries, should be investigated. This could be done with *in vivo* studies using MRI, as in chapter 4 but with more of the aortic geometry scanned, or by registering the MRI measured flow to CT scans as in the work by Kose *et al.* [208] but with a longer aortic section. Alternatively, a more accurate approach may be to investigate these effects by comparing flow in an anatomically realistic phantom, measured using optical techniques, with CFD results.

Chapter 5 investigated the effects of the fluid-structure interaction (FSI) on the blood flow and tissue stresses in axially symmetric aneurysm models by comparison with rigid walled and homogeneous pressure techniques. Omission of the fluid-structure interaction made little difference to the calculation of peak tissue stress with a 1.1 % error in a 6 cm aneurysm with average stiffness and without thrombus. However, the blood flow was influenced more by the

interaction with the moving wall. WSS errors in the rigid walled model were between 30 and 60 % of the mean WSS. Wall motion could be predicted using simpler 1-way coupled fluid-structure interactions which had errors of 10 to 30 % of the mean WSS compared with the complete fluid-structure interaction. Although blood patterns were fairly similar in rigid and flexible aneurysm models there were significant differences in the WSS, which implies differences in the other haemodynamic wall properties. If clinical, or animal, studies of the effects of flow on aneurysm development revealed that the underlying processes were dependent on haemodynamic wall properties, rather than bulk flow characteristics, it would be important to include wall motion in aneurysm modelling. Aneurysm geometries have been found by other authors to promote turbulence, so future work could investigate turbulence modelling in flexible aneurysm models.

The boundary conditions are much more important in a FSI model, than in a rigid walled simulation of blood flow, as revealed in the wobbles contained in the inlet pressure and outlet flow in the results from Chapter 5. The boundary conditions need to be matched to each other and to the geometry and material properties of the aneurysm model. Even *in vivo* measurements of the boundary conditions applied to a geometrically accurate aneurysm model may not match exactly, unless the inhomogeneous material properties were reproduced completely. Chapter 6 showed how a lumped parameter model of the aneurysm could be formed by fitting its parameters to the inlet and outlet pressure and flow from the 3D simulation. The lumped parameter model was then used to find new boundary conditions for the 3D simulation. The lumped parameter model was shown to be accurate and to have some transferability. More iterations between the 3D and lumped parameter models could resolve the transferability issue. This method of finding the boundary conditions could be used in future FSI models of aneurysms, but realistically, faster FSI methods would be required if more complicated, for example asymmetric or patient-specific, aneurysms were to be simulated. The lumped parameter models of aneurysms of varying diameter and material properties could be used to investigate how aneurysms affect flow and pressure elsewhere in the circulation. The relationship between the flow waves before and after the aneurysm was shown to depend on both aneurysm size and material stiffness. Material properties are difficult to assess *in vivo* and investigation of this relationship in the blood flow before and after the aneurysm could lead to a novel assessment of aneurysm global wall properties.

The aim of this thesis was to investigate blood flow and tissue stresses in abdominal aortic

aneurysms, and this aim was accomplished via several objectives. Methods were developed for modelling the blood flow in patient specific aneurysms. The blood flow in realistic aneurysms was found to be far more complicated than studies on simple models suggested. The method was validated against *in vivo* measurements with some success. The main finding from this study was that aneurysmal flow is highly sensitive to the inlet flow conditions, without accurate knowledge of these flow inside the aneurysm cannot be predicted. The blood flow was found to have little effect on the tissue stresses. However, the effect of the wall motion on the blood flow was larger, with significant differences in the wall shear stresses in flexible and rigid walled models.

In summary, the results from the patient specific studies are promising but further validation studies are required before the method could be used to look at correlating disease progression and blood flow parameters. More studies with rigid walled aneurysms could be conducted to begin with, before progressing to the smaller effects of the wall motion.

Appendix A
Publications

A.1 Papers

- K. H. Fraser, T. L. Poepping, A. McNeilly, I. L. Megson and P. R. Hoskins *Acoustic Speed and Attenuation Coefficient in Sheep Aorta Measured at 5-9 MHz* Ultrasound in Medicine and Biology, 32:971-980, 2006

- K. H. Fraser, S. Meagher, J. R. Blake, W. J. Easson and P. R. Hoskins *Characterization of an Abdominal Aortic Velocity Wave in Patients with Abdominal Aortic Aneurysm* Ultrasound in Medicine and Biology, available online: doi:10.1016/j.ultrasmedbio.2007.06.015

- W. T. Lee, K. H. Fraser, M. Li, P. Stroev, W. J. Easson and P. R. Hoskins *Integrating Three Dimensional and One Dimensional Simulations of Hæmodynamic Flow: Modified Windkessel Model of a Diseased Artery* Medical and Biological Engineering and Computing, submitted

- J. R. Blake, S. Meagher, K. H. Fraser, W. J. Easson and P. R. Hoskins *A method to estimate wall shear rate with a clinical ultrasound scanner* Ultrasound in Medicine and Biology, submitted.

A.2 Conference Proceedings

- K. H. Fraser, M. Li, W. J. Easson and P. R. Hoskins *Fluid-structure Interactions In Abdominal Aortic Aneurysms* Journal of Biomechanics, 39:S1:S605-S606, 2006

References

[1] D. P. Giddens, C. K. Zarins, and S. Glagov, "The role of fluid mechanics in the localization and detection of atherosclerosis," *J Biomech Eng-T ASME*, vol. 115, no. 0, pp. 588–594, 1993.

[2] D. N. Ku, "Blood flow in arteries," *Annu Rev Fluid Mech*, vol. 29, pp. 399–434, 1997.

[3] H. J. Weiss, "Flow-related platelet deposition on subendothelium," *Thromb Haemostasis*, vol. 74, no. 1, pp. 117–122, 1995.

[4] A. V. Stanton, "Haemodynamics, wall mechanics and atheroma: a clinician's perspective," *P I Mech Eng*, vol. 213, no. 5, pp. 385–390, 1999.

[5] M. G. St. John Sutton and J. D. Rutherford, *Clinical Cardiovascular Imaging*. Philadelphia: Elsevier Inc., 2004.

[6] R. Uflacker and J. Robinson, "Endovascular treatment of abdominal aortic aneurysm: a review," *Eur J Radiol*, vol. 11, pp. 739–753, 2001.

[7] R. B. Galland and T. R. Magee, "Acute (non-ruptured) abdominal aortic aneurysms," *Eur J Vasc Endovasc*, vol. 14, pp. 421–422, 1997.

[8] T. U. S. A. T. Participants, "Mortality results for randomised controlled trial of early elective surgery or ultrasonographic surveillance for small abdominal aortic aneurysms," *The Lancet*, vol. 352, pp. 1649–55, 1998.

[9] F. A. Lederle, S. E. Wilson, G. R. Johnson, and D. B. R. *et al.*, "Immediate repair compared with surveillance of small abdominal aortic aneurysms," *N Engl J Med*, vol. 346, no. 19, pp. 1437–1444, 2002.

[10] F. A. Lederle, G. R. Johnson, S. E. Wilson, D. J. Ballard, J. Blebea, F. Littooy, J. A. Freischlag, D. Bandyk, J. H. Rapp, and A. A. Salam, "Rupture rate of large abdominal aortic aneurysm in patients refusing or unfit for elective repair," *J Amer Med Assoc*, vol. 287, no. 22, pp. 2968–2972, 2002.

[11] S. C. Nicholls, J. B. Gardner, M. H. Meissner, and K. H. Johansen, "Rupture in small abdominal aortic aneurysms," *J Vasc Surg*, vol. 28, pp. 884–888, 1998.

[12] G. M. Baxter, "The abdominal vasculature," in *Clinical Diagnostic Ultrasound* (G. M. Baxter, P. L. P. Allan, and P. Morley, eds.), ch. 20, pp. 293–294, Oxford: Blackwell Science Ltd, 1999.

[13] T. Wilmink, M. W. C. Claridge, A. Fries, O. Will, C. S. Hubbard, D. J. Adam, C. R. G. Quick, and A. W. Bradbury, "A comparison between the short term and long term benefits of screening for abdominal aortic aneurysms from the Huntingdon aneurysm screening programme," *Eur J Vasc Endovasc Surg*, vol. 32, pp. 16–20, 2006.

[14] R. M. Sandford, M. J. Brown, N. J. London, and R. D. Sayers, "The genetic basis of abdominal aortic aeurysm: A review," *Eur J Vasc Endovasc Surg*, 2007.

[15] A. Wanhainen, D. Bergqvist, K. Boman, T. K. Nilsson, J. Rutegård, and M. Björck, "Risk factors associated with abdominal aortic aneurysm: A population-based study with historical and current data," *J Vasc Surg*, vol. 41, no. 3, pp. 390–396, 2005.

[16] J. M. Millis, S. L. Brown, and R. W. Busuttil, "Thoracic and abdominal aneurysms," in *Surgical Management of Vascular Disease* (P. R. F. Bell, C. W. Jamieson, and C. V. Ruckley, eds.), ch. 56, pp. 797–825, London: W. B. Saunders, 1992.

[17] J. D. Humphrey, *Cardiovascular Solid Mechanics: Cells, Tissues and Organs*. New York: Springer-Verlag, 2002.

[18] V. L. Rowe, S. L. Stevens, T. T. Reddick, M. B. Freeman, R. Donnell, R. C. Carroll, and M. H. Goldman, "Vascular smooth muscle cell apoptosis in aneurysmal, occlusive and normal human aortas," *J Vasc Surg*, vol. 31, pp. 567–576, 2000.

[19] C. M. He and M. R. Roach, "The composition and mechanical properties of abdominal aortic aneurysms," *J Vasc Surg*, vol. 20, no. 1, pp. 6–13, 1994.

[20] R. W. Thompson and W. C. Parks, "Role of matrix metalloproteins in abdominal aortic aneurysms," *Ann NY Acad Sci*, vol. 800, pp. 157–174, 1996.

[21] J. M. Reilly, "Plasminogen activators in abdominal aortic aneurysmal disease," *Ann NY Acad Sci*, vol. 800, pp. 151–156, 1996.

[22] A. Ghorpade and B. T. Baxter, "Biochemistry and molecular regulation of matrix macromolecules in abdominal aortic aneurysms," *Ann NY Acad Sci*, vol. 800, pp. 138–150, 1996.

[23] G. M. Longo, W. Xiong, T. C. Greiner, Y. Zhao, N. Fiotti, and B. T. Baxter, "Matrix metalloproteinases 2 and 9 work in concert to produce aortic aneurysms," *The Journal of Clinical Investigation*, vol. 110, no. 5, pp. 625–632, 2002.

[24] M. J. Davies, "Abdominal aortic aneurysm formation: Lessons from human studies and experimental models," *Circulation*, vol. 98, pp. 193–195, 1998.

[25] J. C. Lasheras, "The biomechanics of arterial aneurysms," *Annu. Rev. Fluid Mech.*, vol. 39, pp. 293–319, 2007.

[26] B. L. Y. Cheuk, S. S. F. Lau, and S. W. K. Cheng, "Carotid intima-media thickness in patients with abdominal aortic aneurysms," *Eur J Vasc Endovasc Surg*, vol. 33, pp. 149–153, 2007.

[27] B. G. Halloran, V. A. Davis, B. M. McManus, T. G. Lynch, and B. T. Baxter, "Localization of aortic disease is associated with intrinsic differences in aortic structure," *Journal of Surgical Research*, vol. 59, pp. 17–22, 1995.

[28] H. Kobayashi, M. Matsushita, K. Oda, N. Nishikimi, T. Sakurai, and K. Komori, "Effects of atherosclerotic plaque on the enlargement of an experimental model of abdominal aortic aneurysm in rabbits," *Eur J Vasc Endovasc Surg*, vol. 28, pp. 71–78, 2004.

[29] R. C. Lallemand, K. G. E. Brown, and P. S. Boulter, "Vessel dimensions in premature atheromatous disease of aortic bifurcation," *British Medical Journal*, vol. 2, no. 5808, pp. 255–257, 1972.

[30] I. E. Vignon and C. A. Taylor, "Outflow boundary conditions for one-dimensional finite-element modeling of blood flow and pressure waves in arteries," *Wave motion*, vol. 39, pp. 361–374, 2004.

[31] S. E. Greenwald, A. C. Carter, and C. L. Berry, "Effect of age on the in vitro reflection coefficient of the aortoiliac bifurcation in humans," *Circulation*, vol. 82, pp. 114–123, 1990.

[32] W. W. Nichols and M. F. O'Rourke, *McDonald's Blood Flow in Arteries*. Kent, U.K.: Edward Arnold, 1990.

[33] R. P. Brandes, I. Fleming, and R. Busse, "Endothelial aging," *Cardiovascular Research*, vol. 66, pp. 286–294, 2005.

[34] R. S. Reneman, T. Arts, and A. P. G. Hoeks, "Wall shear stress - an important determinant of endothelial cell function and structure - in the arterial system in vivo," *Journal of Vascular Research*, vol. 43, pp. 251–269, 2006.

[35] K. Hoshina, E. Sho, M. Sho, T. K. Nakahashi, P. S. Tsao, and R. L. Dalman, "Wall shear stress and strain modulate experimental aneurysm cellularity," *J Vasc Surg*, vol. 37, pp. 1067–1074, 2003.

[36] T. K. Nakahashi, K. Hoshina, P. S. Tsao, E. Sho, M. Sho, J. K. Karwowski, C. Yeh, R.-B. Yang, J. N. Topper, and R. L. Dalman, "Flow loading induces macrophage antioxidative gene expression in experimental aneurysms," *Arterioscler Thromb Vasc Biol*, vol. 22, pp. 2017–2022, 2002.

[37] J. M. Cook-Mills and T. L. Deem, "Active participation of endothelial celss in inflammation," *J Leukoc Biol*, vol. 77, pp. 487–495, 2005.

[38] P. F. Davies and S. C. Tripathi, "Mechanical stress mechanisms and the cell. an endothelial paradigm.," *Circ Res*, vol. 72, pp. 239–245, 1993.

[39] J.-J. Chiu, C.-N. Chen, P.-L. Lee, C. T. Yang, H. S. Chuang, S. Chien, and S. Usami, "Analysis of the effect of disturbed flow on monocytic adhesion to endothelial cells," *J Biomech*, vol. 36, pp. 1883–1895, 2003.

[40] E. Sho, M. Sho, K. Hoshina, H. Kimura, T. K. Nakahashi, and R. L. Dalman, "Hemodynamic forces regulate mural macrophage infiltration in experimental aortic aneurysms," *Exp Mol Pathol*, vol. 76, pp. 108–116, 2004.

[41] X. Bao, C. Lu, and J. A. Frangos, "Temporal gradient in shear but not steady shear stress induces PDGF-A and MCP-1 expression in endothelial cells: Role of NO, NFκB and egr-1," *Arterioscler Thromb Vasc Biol*, vol. 19, pp. 996–1003, 1999.

[42] Z. Touat, V. Ollivier, J. Dai, M.-G. Huisse, A. Bezeaud, U. Sebbag, T. Palombi, P. Rossignol, O. Meilhac, M.-C. Guillin, and J.-B. Michel, "Renewal of mural thrombus releases plasma markers and is involved in aortic abdominal aneurysm evolution," *American Journal of Pathology*, vol. 168, no. 3, pp. 1022–1030, 2006.

[43] D. H. Wang, M. Makaroun, M. W. Webster, and D. A. Vorp, "Mechanical properties and microstructure of intraluminal thrombus from abdominal aortic aneurysm," *J Biomech Eng-T ASME*, vol. 123, pp. 536–539, 2001.

[44] L. Sarda-Mantel, M. Coutard, F. Rouzet, O. Raguin, J.-M. Vrigneaud, F. Hervatin, G. Martet, Z. Touat, P. Merlet, D. L. Guludec, and J.-B. Michel, "99mTc-annexin-V functional imaging of luminal thrombus activity in abdominal aortic aneurysms," *Arteriosclerosis, Thrombosis and Vascular Biology*, vol. 26, pp. 2153–2159, 2006.

[45] D. Bluestein, L. Niu, R. T. Schoephoerster, and M. K. Dewanjee, "Steady flow in an aneurysm model: Correlation between fluid dynamics and blood platelet deposition," *J Biomech Eng-T ASME*, vol. 118, no. 3, pp. 280–286, 1996.

[46] T. David, S. Thomas, and P. G. Walker, "Platelet deposition in stagnation point flow: an analytical and computational simulation," *Med Eng Phys*, vol. 23, pp. 299–312, 2001.

[47] J. Bernsdorf, S. E. Harrison, S. M. Smith, P. V. Lawford, and D. R. Hose, "Numerical simulation of clotting processes: A lattice Boltzmann application in medical physics," *Mathematics and computers in simulation*, vol. 72, pp. 89–92, 2006.

[48] J. H. Leung, A. Wright, N. Cheshire, S. A. Thom, A. D. Hughes, J. Crane, and X. Y. Xu, "Relationship between growth rate and maximum wall stress in abdominal aortic aneurysms," *J Biomech*, vol. 39, no. Suppl. 1, p. S274, 2006.

[49] S. Baek, C. A. Figuero, C. A. Taylor, and J. D. Humphrey, "Towards patient-specific modelling - ii. biomechanics of a growing aneurysm," in *Progress in Biomedical Optics and Imaging. Medical Imaging 2006: Physiology, Function and Structure from Medical Images*, vol. 7, pp. 61432C1–6, 2006.

[50] P. N. Watton, N. A. Hill, and M. Heil, "A mathematical model for the growth of the abdominal aortic aneurysm," *Biomech Model Mechanbiol*, vol. 3, p. 98, 2004.

[51] D. A. Vorp, D. W. Chew, N. Sakamoto, M. Sakamoto, and M. S. Makaroun, "Association of biophysical forces with impaired remodelling mechanisms of the abdominal aortic aneurysm wall," *J Biomech*, vol. 39, no. Suppl. 1, p. S289, 2006.

[52] M. J. Thubrikar, J. Al-Soudi, and F. Robicsek, "Wall stress studies of abdominal aortic aneurysm in a clinical model," *Ann Vasc Surg*, vol. 15, pp. 355–366, 2001.

[53] M. L. Raghavan, D. A. Vorp, M. P. Federle, M. S. Makaroun, and M. W. Webster, "Wall stress distribution on three-dimensionally reconstructed models of human aortic aneurysm," *J Vasc Surg*, vol. 31, pp. 760–769, 2000.

[54] A. K. Venkatasubramaniam, M. J. Fagan, T. Mehta, K. J. Mylankal, B. Ray, G. Kuhan, I. C. Chetter, and P. T. McCollum, "A comparative study of aortic wall stress using finite element analysis for ruptured and non-ruptured abdominal aortic aneurysms," *Eur J Vasc Endovasc*, vol. 28, pp. 168–176, 2004.

[55] M. Truijers, J. A. Pol, L. J. SchultzeKool, S. M. van Sterkenburg, M. F. Fillinger, and J. D. Blankensteijn, "Wall stress analysis in small asymptomatic, symptomatic and ruptured abdominal aortic aneurysms," *Eur J Vasc Endovasc Surg*, vol. 33, no. 4, pp. 401–407, 2007.

[56] M. Breeuwera, U. Götte, K. Visser, R. Hoogeveen, F. Laffargue, J.-M. Rouet, B. Wolters, and S. de Putter, "Assessment of the rupture risk of abdominal aortic aneurysms by patient specific hemodynamic modeling - initial results," in *Proceedings of the International Society of Magnetic Resonance Medicine*, vol. 11, p. 1868, International Society of Magnetic Resonance Medicine, 2004.

[57] M. F. Fillinger, S. P. Marra, M. L. Raghavan, and F. E. Kennedy, "Prediction of rupture risk in abdominal aortic aneurysm during observation: Wall stress versus diameter," *J Vasc Surg*, vol. 37, no. 4, pp. 724–732, 2003.

[58] M. F. Fillinger, M. L. Raghavan, S. P. Marra, J. L. Cronenwett, and F. E. Kennedy, "In vivo analysis of mechanical wall stress and abdominal aortic aneurysm rupture risk," *J Vasc Surg*, vol. 36, pp. 589–597, 2002.

[59] M. L. Raghavan and D. A. Vorp, "Toward a biomechanical tool to evaluate rupture potential of abdominal aortic aneurysm: identification of a finite strain constitutive model and evaluation of its applicability," *J Biomech*, vol. 33, pp. 475–482, 2000.

[60] M. L. Raghavan, M. W. Webster, and D. A. Vorp, "Ex vivo biomechanical behaviour of abdominal aortic aneurysm: Assessment using a new mathematical model," *Ann Biomed Eng*, vol. 24, pp. 573–582, 1996.

[61] M. L. Raghavan, J. Kratzberg, E. M. C. de Tolosa, M. M. Hanoka, P. Walker, and E. S. da Silva, "Regional distribution of wall thickness and failure properties of human abdominal aortic aneurysm," *J Biomech*, vol. 39, pp. 3010–3016, 2006.

[62] M.J.Thubrikar, M.Labrosse, F.Robicsek, J.Al-Soudi, and B.Fowler, "Mechanical properties of abdominal aortic aneurysm wall," *J Med Eng Technol*, vol. 25, no. 4, pp. 133–142, 2001.

[63] D. A. Vorp and J. P. Vande Geest, "Biomechanical determinants of abdominal aortic aneurysm rupture," *Arterioscler Thromb Vasc Biol*, vol. 25, pp. 1558–1566, 2005.

[64] C. Kleinstreuer and Z. Li, "Analysis and computer program for rupture-risk prediction of abdominal aortic aneurysms," *Biomedical Engineering Online*, vol. 5, no. 19, 2006.

[65] J. P. Vande Geest, D. H. J. Wang, S. R. Wisniewski, M. S. Makaroun, and D. A. Vorp, "Towards a noninvasive method for determination of patient-specific wall strength in abdominal aortic aneurysms," *Annals of Biomedical Engineering*, vol. 34, no. 7, pp. 1098–1106, 2006.

[66] S. S. Kantha, "An appraisal of Albert Einstein's chronic illness," *Medical Hypotheses*, vol. 42, pp. 340–346, 1994.

[67] A. Balducci, M. Grigioni, G. Querzoli, G. P. Romano, C. Daniele, G. D'Avenio, and V. Barbaro, "Investigation of the flow field downstream of an artificial heart valve by means of PIV and PTV," *Exp Fluids*, vol. 36, no. 1, pp. 204–213, 2004.

[68] D. E. M. Palmen, F. N. Van De Vosse, J. D. Janssen, and M. E. H. Vandongen, "Analysis of the flow in stenosed carotid-artery bifurcation models - hydrogen-bubble visualisation," *J Biomech*, vol. 27, no. 5, pp. 581–590, 1994.

[69] M. Ojha and B. L. Langille, "Evidence that turbulence is not the cause of poststenotic dilation in rabbit carotid arteries," *Arteriosclerosis, Thrombosis and Vascular Biology*, vol. 13, no. 7, pp. 977–984, 1993.

[70] A. Kirpalani, H. Park, J. Butany, K. W. Johnston, and M. Ojha, "Velocity and wall shear stress patterns in the human right coronary artery," *J Biomech Eng - T ASME*, vol. 121, no. 4, pp. 370–375, 1999.

[71] Q. M. Ramadan, O. Hamid, and K. O. Lim, "Steady flow visualization in a rigid model of the aortic-renal junction: application to atherosclerosis," *Physica Medica*, vol. 19, no. 4, pp. 295–303, 2003.

[72] S. Sivanesan, T. V. How, R. A. Black, and A. Bakran, "Flow patterns in the radiocephalic arteriovenous fistula: an in vitro study," *J Biomech*, vol. 32, pp. 915–925, 1999.

[73] E. M. Pedersen, H.-W. Sung, A. C. Burlson, and A. P. Yoganathan, "Two-dimensional velocity measurements in a pulsatile flow model of the normal abdominal aorta simulating different hemodynamic conditions," *J Biomech*, vol. 26, no. 10, pp. 1237–1247, 1993.

[74] C. J. Egelhoff, R. S. Budwig, D. F. Elger, T. A. Khraishi, and K. H. Johansen, "Model studies of the flow in abdominal aortic aneurysms during resting and exercise conditions," *J Biomech*, vol. 32, no. 0, pp. 1319–1329, 1999.

[75] V. Deplano, Y. Knapp, E. Bertrand, and E. Gaillard, "Flow behaviour in an asymmetric compliant experimental model for abdominal aortic aneurysm," *J Biomech*, in press.

[76] S. C. M. Yu, "Steady and pulsatile flow studies in abdominal aortic aneurysm models using particle image velocimetry," *Heat Fluid Flow*, vol. 21, pp. 74–83, 2000.

[77] S. C. M. Yu and J. B. Zhao, "A particle image velocimetry study on the pulsatile flow characteristics in straight tubes with an asymmetric bulge," *P I Mech Eng*, vol. 214, pp. 655–671, 2000.

[78] S. C. M. Yu and J. B. Zhao, "A steady flow analysis on the stented and non-stented sidewall aneurysm models," *Med Eng Phys*, vol. 21, pp. 133–141, 1999.

[79] A.-V. Salsac, S. R. Sparks, J.-M. Chomaz, and J. C. Lasheras, "Evolution of the wall shear stresses during the progressive enlargement of symmetric abdominal aortic aneurysms," *J Fluid Mech*, vol. 560, pp. 19–51, 2006.

[80] C. J. P. M. Teirlinck, R. A. Bezemer, C. Kollman, J. Lubbers, P. R. Hoskins, P. Fish, K.-E. Fredfeldt, and U. G. Schaarschmidt, "Development of an example flow test object and comparison of five of these objects, constructed in various laboratories," *Ultrasonics*, vol. 36, pp. 653–660, 1998.

[81] K. V. Ramnarine, T. Anderson, and P. R. Hoskins, "Construction and geometric stability of physiological flow rate wall-less stenosis phantoms," *Ultrasound Med Biol*, vol. 27, no. 2, pp. 245–250, 2001.

[82] T. L. Poepping, H. N. Nikolov, M. L. Thorne, and D. W. Holdsworth, "A thin-walled carotid vessel phantom for Doppler ultrasound flow studies," *Ultrasound Med Biol*, vol. 30, no. 8, pp. 1067–1078, 2004.

[83] T. L. Poepping, H. N. Nikolov, R. N. Rankin, M. Lee, and D. W. Holdsworth, "An *in vitro* system for doppler ultrasound flow studies in the stenosed carotid artery bifurcation," *Ultrasound in Medicine and Biology*, vol. 28, no. 4, pp. 495–506, 2002.

[84] S. Tateshima, J. Grinstead, S. Sinha, Y.-L. Nien, Y. Murayama, P. Villablanca, K. Tanichita, and F. V. nuela, "Intraaneurysmal flow visualization by using phase-contrast magnetic resonance imaging: feasibility study based on a geometrically realistic in vitro aneurysm model," *J Neurosurg*, vol. 100, pp. 1041–1048, 2004.

[85] E. M. Pedersen, A. P. Yoganathan, and X. P. Lefebvre, "Pulsatile flow visualization in a model of the human abdominal aorta and aortic bifurcation," *J Biomech*, vol. 25, no. 8, pp. 935–944, 1992.

[86] J. E. Moore Jr, C. Xu, S. Glagov, C. K. Zarins, and D. N. Ku, "Fluid wall shear stress meaurements in a model of the human abdominal aorta: oscillatory behaviour and relationship to atherosclerosis," *Atherosclerosis*, vol. 110, pp. 225–240, 1994.

[87] S. A. Berger and L. Talbot, "Flow in curved pipes," *Ann Rev Fluid Mech*, vol. 15, pp. 461–512, 1983.

[88] P. Vennemann, K. T. Kiger, R. Lindken, B. C. W. Groenendijk, S. S. de Vos, T. L. M. ten Hagen, N. T. C. Ursem, R. E. Poelmann, J. Westerweel, and B. P. Hierck, "In vivo micro particle image velocimetry measurements of blood-plasma in the embryomic avian heart," *Journal of Biomechanics*, vol. 39, pp. 1191–1200, 2006.

[89] C. J. Mills, "A catheter tip electromagnetic velocity probe," *Phys Med Biol*, vol. 11, no. 2, pp. 323–324, 1966.

[90] C. J. Mills, I. T. Gabe, J. H. Gault, D. T. Mason, J. J. Ross, E. Braunwald, and J. P. Shillingford, "Pressure-flow relationships and vascular impedance in man," *Cardiovasc Res*, vol. 4, pp. 405–417, 1970.

[91] P. Suetens, *Fundamentals of Medical Imaging*. Cambridge University Press, 2002.

[92] R. A. Close, G. R. Duckwiler, and F. Viñuela, "Fluid equation applied to blood flow measurement using digital videodensitometry," *Investigative Radiology*, vol. 27, no. 7, pp. 504–509, 1992.

[93] C. R. Hill, J. C. Bamber, and G. R. ter Haar, *Physical Principles of Medical Ultrasonics*. John Wiley and Sons Ltd, 2004.

[94] M. J. Bennett, S. McLaughlin, T. Andersen, and W. N. McDicken, "Error analysis of ultrasonic tissue Doppler velocity estimation techniques for quantification of velocity and strain," *Ultrasound Med Biol*, vol. 33, pp. 74–81, 2007.

[95] A. Vieli, U. Moser, S. Maier, D. Meier, and P. Boesiger, "Velocity profiles in the normal human abdominal aorta: A comparison between ultrasound and magnetic resonance data," *Ultrasound Med Biol*, vol. 15, no. 2, pp. 113–119, 1989.

[96] M. T. Vlaardingerbroek and J. A. den Boer, *Magnetic Resonance Imaging Theory and Practice*. Berlin: Springer-Verlag, 2003.

[97] J. Lotz, C. Meier, A. Leppert, and M. Galanski, "Cardiovascular flow measurement with phase-contrast MR imaging: Basic facts and implementation," *Radiographics*, vol. 22, pp. 651–671, 2002.

[98] S. Oyre, E. M. Pedersen, S. Ringgaard, P. Boesiger, and W.P.Paaske, "*In vivo* wall shear stress measured by magnetic resonance velocity mapping of the normal human adominal aorta," *Eur J Vasc Endovasc Surg*, vol. 13, pp. 263–271, 1997.

[99] C. A. Taylor, C. P. Cheng, L. A. Espinosa, B. T. Tang, D. Parker, and R. J. Herfkens, "In vivo quantification of blood flow and wall shear stress in the human abdominal aorta during lower limb exercise," *Ann Biomed Eng*, vol. 30, pp. 402–408, 2002.

[100] C. P. Cheng, R. J. Herfkens, and C. A. Taylor, "Abdominal aortic hemodynamic conditions in healthy subjects aged 50-70 at rest and during lower limb exercise: in vivo quantification using MRI," *Atherosclerosis*, vol. 168, pp. 323–331, 2003.

[101] W. N. McDicken, G. R. Sutherland, C. M. Moran, and L. N. Gordon, "Colour Doppler velocity imaging of the myocardium," *Ultrasound Med Biol*, vol. 18, pp. 651–654, 1992.

[102] S. Urheim, T. Edvardsen, H. Torp, B. Angelsen, and O. A. Smiseth, "Myocardial strain by Doppler echocardiography," *Circulation*, vol. 102, pp. 1158–1164, 2000.

[103] J. A. Schaar, C. L. de Korte, F. Mastik, C. Strijder, G. Pasterkamp, E. Boersma, P. W. Serruys, and A. F. W. van der Steen, "Characterizing vulnerable plaque features with intravascular elastography," *Circulation*, vol. 108, pp. 2636–2641, 2003.

[104] J. Dineley, S. Meagher, T. L. Poepping, W. N. McDicken, and P. R. Hoskins, "Design and characterisation of a wall motion phantom," *Ultrasound Med Biol*, vol. 32, no. 9, pp. 1349–1357, 2006.

[105] P. R. Hoskins, P. J. Fish, W. N. McDicken, and C. Moran, "Developments in cardiovascular ultrasound. part 2: Arterial applications," *Med Biol Eng Comput*, vol. 36, pp. 259–269, 1998.

[106] K. L. Wedding, M. T. Draney, R. J. Herfkens, C. K. Zarins, C. A. Taylor, and N. J. Pelc, "Measurement of vessel wall strain using cine phase contrast MRI," *J Magn Reson Imaging*, vol. 15, pp. 418–428, 2002.

[107] R. Krug, J. M. Boese, and L. R. Schad, "Determination of aortic compliance from magnetic resonance images using an automatic active contour model," *Phys Med Biol*, vol. 48, pp. 2391–2404, 2003.

[108] J. M. Boese, M. Bock, S. O. Schoenberg, and L. R. Schad, "Estimation of aortic compliance using magnetic resonance pulse wave velocity measurement," *Phys. Med. Biol.*, vol. 45, pp. 1703–1713, 2000.

[109] R. Budwig, D. Elger, H. Hooper, and J. Slippy, "Steady flow in abdominal aortic aneurysm models," *J Biomech Eng - T ASME*, vol. 115, pp. 418–423, 1993.

[110] R. A. Peattie, C. L. Asbury, E. I. Bluth, and J. W. Ruberti, "Steady flow in models of abdominal aortic aneurysms part i: Investigation of the velocity patterns," *J Ultrasound Med*, vol. 15, pp. 679–688, 1996.

[111] R. A. Peattie, C. L. Asbury, E. I. Bluth, and J. W. Ruberti, "Steady flow in models of abdominal aortic aneurysms part ii: Wall stresses and their implication for in vivo thrombosis and rupture," *J Ultrasound Med*, vol. 15, pp. 689–696, 1996.

[112] R. H. F. Pao, *Fluid Mechanics*. New York: John Wiley and Sons, 1966.

[113] S. C. M. Yu, W. K. Chan, and L. P. C. B. T. H. Ng, "A numerical investigation on the steady and pulsatile flow characteristics in axi-symmetric abdominal aortic aneurysm models with some experimental evaluation," *J Med Eng Technol*, vol. 23, no. 6, pp. 228–239, 1999.

[114] R. A. Peattie, T. J. Riehle, and E. I. Bluth, "Pulsatile flow in fusiform models of abdominal aortic aneurysms: Flow fields, velocity patterns and flow-induced wall stresses," *J Biomech Eng - T ASME*, vol. 126, pp. 438–446, 2004.

[115] E. I. Bluth, S. M. Murphey, L. H. Hollier, and M. A. Sullivan, "Color flow doppler in the evaluation of aortic aneurysms," *Int Angiol*, vol. 9, no. 1, pp. 8–10, 1990.

[116] C. L. Asbury, J. W. Ruberti, E. I. Bluth, and R. A. Peattie, "Experimental investigation of steady flow in rigid models of abdominal aortic aneurysms," *Annals of Biomedical Engineering*, vol. 23, pp. 29–39, 1995.

[117] R. Brekken, J. Bang, A. O/dega.rd, T. A. N. Hernes, and H. O. Myhre, "Strain estimation in abdominal aortic aneurysms from 2d ultrasound," *Ultrasound Med Biol*, vol. 32, no. 1, pp. 33–42, 2006.

[118] S. MacSweeney, G.Young, R.M.Greenhalgh, and J.T.Powell, "Mechanical properties of the aneurysmal aorta," *Brit J Surg*, vol. 79, pp. 1281–1284, 1992.

[119] G. Koullias, R. Modal, M. Tranquilli, D. P. Korkolis, P. Barash, and J. A. Elefteriades, "Mechanical deterioration underlies malignant behaviour of aneurysmal human ascending aorta," *J Thorac Cardiovasc Surg*, vol. 130, pp. 677–683, 2005.

[120] A. Long, L. Rouet, A. Bissery, P. Rossignol, D. Mouradian, and M. Sapoval, "Compliance of abdominal aortic aneurysms: evaluation of tissue Doppler imaging," *Ultrasound Med Biol*, vol. 30, no. 9, pp. 1099–1108, 2004.

[121] K. A. Wilson, P. R. Hoskins, A. J. Lee, F. G. R. Fowkes, C. V. Ruckley, and A. W. Bradbury, "Ultrasonic measurement of abdominal aortic aneurysm wall compliance: A reproducibility study," *J Vasc Surg*, vol. 31, no. 3, pp. 507–513, 2000.

[122] K. Wilson, M. Whyman, P. Hoskins, A. J. Lee, A. W. Bradbury, F. G. R. Fowkes, and C. V. Ruckley, "The relationship between abdominal aortic aneurysm wall compliance, maximum diameter and growth rate," *Cardiovasc surg*, vol. 7, no. 2, pp. 208–213, 1999.

[123] K. Wilson, A. W. Bradbury, M. Whyman, P. Hoskins, A. J. Lee, F. G. R. Fowkes, P. McCollum, and C. V. Ruckley, "Relationship between abdominal aortic aneurysm wall compliance and clinical outcome: a preliminary analysis," *Eur J Vasc Endovasc*, vol. 15, pp. 472–477, 1998.

[124] M. Zamir, *The Physics of Coronary Blood Flow*. New York: Springer, 2005.

[125] E. B. Shim, J. Y. Sah, and C. H. Youn, "Mathematical modeling of cardiovascular system dynamics using lumped parameter method," *Japanese Journal of Physiology*, vol. 54, pp. 545–553, 2004.

[126] P. Segers, N. Stergiopulos, N. Westerhof, P. Wouters, P. Kolh, and P. Verdonck, "Systemic and pulmonary hemodynamics assessed with a lumped-parameter heart-arterial interaction model," *Journal of Engineering Mathematics*, vol. 47, pp. 185–199, 2003.

[127] B. J. B. M. Wolters, M. Emmer, M. C. M. Rutten, G. W. H. Schurink, and F. N. van der Vosse, "Assessment of endoleak significance after endovascular repair of abdominal aortic aneurysms: A lumped parameter model," *Med Eng Phys*, vol. in press.

[128] A. P. Avolio, "Multi-branched model of the human arterial system," *Med Biol Eng Comput*, vol. 18, pp. 709–718, 1980.

[129] P. Stroev, *A subject-specific mathematical model of the human systemic circulation for estimating hemodynamic parameters*. PhD thesis, The University of Edinburgh, 2006.

[130] P. V. Stroev, P. R. Hoskins, and W. J. Easson, "Distribution of wall shear rate throughout the arterial tree: A case study," *Atherosclerosis*, vol. 191, pp. 276–280, 2007.

[131] L. Formaggia and A. Veneziani, "Geometrical multiscale models for the cardiovascular system," in *Blood flow modelling and diagnostics, ABIOMED lecture notes, Vol. 6* (T. A. Kowalewski, ed.), pp. 309–359, Warsaw: ABIOMED IFTR PAS, 2005.

[132] M. S. Olufsen, C. S. Peskin, W. Y. Kim, E. M. Pedersen, A. Nadim, and J. Larsen, "Numerical simulation and experimental validation of blood flow in arteries with structured-tree outflow conditions," *Ann Biomed Eng*, vol. 28, pp. 1281–1299, 2000.

[133] H. K. Versteeg and W. Malalasekera, *An Introduction to Computational Fluid Dynamics: The Finite Volume Method*. Essex: Pearson Education Limited, 2007.

[134] C. A. Taylor and M. T. Draney, "Experimental and computational methods in cardiovascular fluid mechanics," *Annu Rev Fluid Mech*, vol. 36, pp. 197–231, 2004.

[135] X. He and D. N. Ku, "Pulsatile flow in the human left coronary artery bifurcation: Average conditions," *J Biomech Eng - T ASME*, vol. 118, pp. 74–82, 1996.

[136] A. D. Augst, D. C. Barratt, A. D. Hughes, S. A. M. Thom, and X. Y. Xu, "Various issues relating to computational fluid dynamics simulations of carotid bifurcation flow based on models reconstructed from three-dimensional ultrasound images," *P I Mech Eng H*, vol. 217, pp. 393–403, 2003.

[137] K. R. Moyle, L. Antiga, and D. A. Steinman, "Inlet conditions for image-based CFD models of the carotid bifurcation: Is it reasonable to assume fully developed flow?," *J Biomech Eng - T ASME*, vol. 128, no. 371, pp. 371–379, 2006.

[138] L. Morris, P. Delassus, A. Callanan, M. Walsh, F. Wallis, P. Grace, and T. McGloughlin, "3-d numerical simulation of blood flow through models of the human aorta," *J Biomech Eng-T ASME*, vol. 127, pp. 767–775, 2005.

[139] N. Shahcheraghi, H. A. Dwyer, A. Y. Cheer, A. I. Barakat, and T. Rutaganira, "Unsteady and three-dimensional simulation of blood flow in the human aortic arch," *J Biomech Eng-T ASME*, vol. 124, pp. 378–387, 2002.

[140] X. Y. Xu, Q. Long, M. W. Collins, M. Bourne, and T. M. Griffith, "Reconstruction of blood flow patterns in human arteries," *Proc Instn Mech Engrs*, vol. 213, pp. 411–421, 1999.

[141] C. A. Taylor, T. J. R. Hughes, and C. K. Zarins, "Finite element modeling of three-dimensional pulsatile flow in the abdominal aorta: Relevance to atherosclerosis," *Annals of Biomedical Engineering*, vol. 26, pp. 975–987, 1998.

[142] M. J. Kunov, D. A. Steinman, and C. R. Ethier, "Particle volumetric residence time calculations in arterial geometries," *J Biomech Eng-T ASME*, vol. 118, pp. 158–164, 1996.

[143] S. Hyun, C. Kleinstreuer, and J. P. Archie Jr, "Hemodynamics analyses of arterial expansions with implications to thrombosis and restenosis," *Medical Engineering and Physics*, vol. 22, pp. 13–27, 2002.

[144] D. A. Steinman, D. A. Vorp, and C. R. Ethier, "Computational modeling of arterial biomechanics: Insights into pathogenesis and treatment of vascular disease," *J Vasc Surg*, vol. 37, no. 5, pp. 1118–1128, 2003.

[145] F. P. Glor, J. J. M. Westenberg, J. Vierendeels, M. Danilouchkine, and P. Verdonck, "Validation of the coupling of magnetic resonance imaging velocity measurements with computational fluid dynamics in a U bend," *Artificial Organs*, vol. 26, no. 7, pp. 622–635, 2002.

[146] C. A. Taylor, T. J. R. Hughes, and C. K. Zarins, "Finite element modeling of blood flow in arteries," *Comp Meth Appl Mech Eng*, vol. 158, pp. 155–196, 1998.

[147] Q. Long, X. Y. Xu, M. Bourne, and T. M. Griffith, "Numerical study of blood flow in an anatomically realistic aorto-iliac bifurcation generated from MRI data," *Magnet Reson Med*, vol. 43, pp. 565–576, 2000.

[148] S. Jin, J. Oshinski, and D. P. Giddens, "Effects of wall motion and compliance on flow patterns in the ascending aorta," *J Biomech Eng - T ASME*, vol. 125, pp. 347–354, 2003.

[149] J. P. Vande Geest, M. S. Sacks, and D. A. Vorp, "The effects of aneurysm on the biaxial mechanical behavior of human abdominal aorta," *J Biomech*, vol. 39, pp. 1324–1334, 2006.

[150] O. C. Zienkiezicz and R. L. Taylor, *The Finite Element Method.* Oxford: Butterworth-Heinemann, 2002.

[151] R. A. Baldewsing, C. L. de Korte, J. A. Schaar, F. Mastik, and A. F. W. van Der Steen, "A finite element model for performing intravascular ultrasound elastography of human atherosclerotic coronary arteries," *Ultrasound Med Biol*, vol. 30, no. 6, pp. 803–813, 2004.

[152] R. P. Vito and S. A. Dixon, "Blood vessel constitutive models 1995-2002," *Annu Rev Biomed Eng*, vol. 5, pp. 413–439, 2003.

[153] E. A. Finol, K. Keyhani, and C. H. Amon, "The effect of asymmetry in abdominal aortic aneurysms under physiologically realistic flow condiitons," *J Biomech Eng - T ASME*, vol. 125, pp. 207–217, 2003.

[154] J. J. Yeung, H. J. Kim, T. A. Abbruzzese, I. E. Vignon-Clementel, M. T. Draney-Blomme, K. K. Yeung, I. Perkash, R. J. Herfkens, C. A. Taylor, and R. L. Dalman, "Aortoiliac hemodynamic and morphologic adaptation to chronic spinal cord injury," *J Vasc Surg*, vol. 44, pp. 1254–1265, 2006.

[155] D. F. Elger, D. M. Blackketter, R. S. Budwig, and K. H. Johansen, "The influence of shape on the stresses in model abdominal aortic aneurysms," *J Biomech Eng-T ASME*, vol. 118, pp. 326–331, 1996.

[156] W. R. Mower, L. J. Baraff, and J. Sneyd, "Stress distributions in vascular aneurysms: Factors affecting risk of aneurysm rupture," *J Surg Res*, vol. 55, no. 2, pp. 155–161, 1993.

[157] B. Johnson Hua and P. William R. Mower, MD, "Simple geomteric characteristics fail to reliably predict abdominal aortic aneurysm wall stress," *J Vasc Surg*, vol. 34, no. 2, pp. 308–315, 2001.

[158] D. A. Vorp, M. L. Raghavan, and M. W.Webster, "Mechanical wall stress in abdominal aortic aneurysm: Influence of diameter and asymmetry," *J Vasc Surg*, vol. 27, pp. 632–639, 1998.

[159] M. L. Raghavan, M. F. Fillinger, S. P. Marra, B. P. Naegelein, and F. E. Kennedy, "Automated methodology for determination of stress distribution in human abdominal aortic aneurysm," *J Biomech Eng-T ASME*, vol. 127, pp. 868–871, 2005.

[160] E. S. da Silva, A. J. Rodrigues, E. M. C. de Tolosa, C. J. Rodrigues, G. V. B. do Prado, and J. C. Nakamoto, "Morphology and diameter of intrarenal aortic aneurysms: a prospective study," *Cardiovasc surg*, vol. 8, no. 7, pp. 526–532, 2000.

[161] E. Di Martino, S. Mantero, F. Inzoli, G. Melissano, D. Astore, R. Chiesa, and R. Fumero, "Biomechanics of abdominal aortic aneurysm in the presence of endoluminal thrombus: experimental characterisation and structural static computational analysis," *Eur J Vasc Endovasc*, vol. 15, pp. 290–299, 1998.

[162] D. H. J. Wang, M. S. Makaroun, M. W. Webster, and D. A. Vorp, "Effect of intraluminal thrombus on wall stress in patient-specific models of abdominal aortic aneurysm," *J Vasc Surg*, vol. 36, pp. 598–604, 2002.

[163] W. R. Mower, W. J. Quinones, and S. S. Gambhir, "Effect of intraluminal thrombus on abdominal aortic aneurysm wall stress," *J Vasc Surg*, vol. 26, pp. 602–608, 1997.

[164] E. S. D. Martino and D. A. Vorp, "Effect of variation in intraluminal thrombus constitutive properties on abdominal aortic aneurysm wall stress," *Ann Biomed Eng*, vol. 31, pp. 804–809, 2003.

[165] M. J. Thubrikar, F. Robicsek, M. Labrosse, V. Chervenkoff, and B. L. Fowler, "Effect of thrombus on abdominal aortic aneurysm wall dilation and stress," *J Cardiovasc Surg*, vol. 44, no. 1, pp. 67–77, 2003.

[166] K. H. Fraser, T. L. Poepping, A. M. Neilly, I. L. Megson, and P. R. Hoskins, "Acoustic speed and attenuation coefficient in sheep aorta measured at 5-9 MHz," *Ultrasound Med Biol*, vol. 32, no. 6, pp. 971–980, 2006.

[167] S. de Putter, F. N. van de Vosse, M. Breeuwer, and F. A. Gerritsen, "Local influence of calcifications on the wall mechanics of abdominal aortic aneurysms," in *Progress in Biomedical Optics and Imaging. Medical Imaging 2006: Physiology, Function and Structure from Medical Images*, vol. 7, pp. 61432C1–6, 2006.

[168] L. Speelman, A. Bohra, E. M. H. Bosboom, G. W. H. Schurink, F. N. van de Vosse, M. S. Makaroun, and D. A. Vorp, "Effects of wall calcifications in patient-specific wall stress analyses of abdominal aortic aneurysms," *J Biomech Eng - T ASME*, vol. 129, pp. 105–109, 2007.

[169] M. L. Raghavan, B. Ma, and M. F. Fillinger, "Non-invasive determination of zero-pressure geometry of arterial aneurysms," *Annals Biomed Eng*, vol. 34, no. 9, pp. 1414–1419, 2006.

[170] J. Lu, X. Zhou, and M. L. Raghavan, "Inverse elastostatic stress analysis in pre-deformed biological structures: Demonstration using abdominal aortic aneurysms," *J Biomech*, vol. 40, pp. 693–696, 2007.

[171] S. de Putter, B. J. B. M. Wolters, M. C. M. Rutten, M. Breeuwer, F. A. Gerritsen, and F. N. van de Vosse, "Patient-specific initial wall stress in abdominal aortic aneurysms with a backward incremental method," *J Biomech*, vol. 40, pp. 1081–1090, 2007.

[172] C. M. Scotti, A. D. Shkolnik, S. C. Muluk, and E. A. Finol, "Fluid-strucure interaction in abdominal aortic aneurysms: effects of asymmetry and wall thickness," *BioMedical Engineering OnLine*, vol. 4, p. 64, 2005.

[173] J. H. Leung, A. R. Wright, N. Cheshire, J. Crane, S. A. Thom, A. D. Hughes, and Y. Xu, "Fluid-structure interaction of patient specific abdominal aortic aneurysms: a comparison with solid stress models," *BioMedical Engineering OnLine*, vol. 5, p. 33, 2006.

[174] D. A. Steinman, "Image-based computational fluid dynamics modeling in realistic arterial geometries," *Annals of Biomedical Engineering*, vol. 30, pp. 483–497, 2002.

[175] J. J. Wentzel, R. Krams, J. C. H. Schuurbiers, J. A. Oomen, J. Kloet, W. J. van der Giessen, P. W. Serruys, and C. J. Slager, "Relationship between neointimal thickness and shear stress after wallstent implantation in human coronary arteries," *Circulation*, vol. 103, pp. 1740–1745, 2001.

[176] D. A. Steinman, J. B. Thomas, H. M. Ladak, J. S. Milner, B. K. Rutt, and J. D. Spence, "Reconstruction of carotid bifurcation hemodynamics and wall thickness using computational fluid dynamics and MRI," *Magnetic Resonance in Medicine*, vol. 47, pp. 149–159, 2002.

[177] J. Leung, A. Wright, N. Cheshire, S. A. Thom, A. D. Hughes, and X. Y. Xu, "Flow patterns and wall shear stresses in patient-specific models of the abdominal aortic aneurysm," *Studies in Health Technology and Informatics*, vol. 103, pp. 235–242, 2004.

[178] J.-D. Boissonnat and B. Geiger, "Three-dimensional reconstruction of complex shapes based on the Delaunay triangulation," Rapport de recherche 1697, INRIA, 1992.

[179] J. R. Womersley, "Method for the calculation of velocity, rate of flow and viscous drag in arteries when the pressure gradient is known," *Journal of Physiology*, vol. 127, pp. 553–563, 1955.

[180] Fluent Inc., *Fluent 6.2 Users Guide*. Lebanon, New Hampshire, USA, 2005.

[181] G. W. De Keulenaer, D. C. Chappell, N. Ishizaka, M. Nerem, Robert, R. W. Alexander, and K. K. Griendling, "Oscillatory and steady laminar shear stress differentially affect human endothelial redox state," *Circulation Research*, vol. 82, pp. 1094–1101, 1998.

[182] E. S. Di Martino, G. Guadagni, A. Fumero, G. Ballerini, R. Spirito, P. Biglioli, and A. Redaelli, "Fluid-structure interaction within realistic three-dimensional models of the aneurysmatic aorta as a guidance to assess the risk of rupture of the aneurysm," *Med Eng Phys*, vol. 23, pp. 647–655, 2001.

[183] B. M. Johnston, P. R. Johnston, S. Corney, and D. Kilpatrick, "Non-newtonian blood flow in human right coronary arteries: Transient simulations," *J Biomech*, vol. 39, pp. 1116–1128, 2006.

[184] E. A. Finol and C. H. Amon, "Blood flow in abdominal aortic aneurysms: Pulsatile flow haemodynamics," *J Biomech Eng-T ASME*, vol. 123, pp. 474–484, 2001.

[185] Y. Papaharilaou, J. A. Ekaterinaris, E. Manousaki, and A. N. Katsamouris, "A decoupled fluid structure approach for estimating wall stress in abdominal aortic aneurysms," *J Biomech*, vol. 40, no. 2, pp. 367–377, 2007.

[186] R. J. Daigle, A. T. Stravros, and R. M. Lees, "Overestimation of velocity and frequency values by multi-element linear array Dopplers," *J Vasc Technol*, vol. 14, pp. 206–213, 1990.

[187] P. R. Hoskins, S. F. Li, and W. N. McDicken, "Velocity estimation using duplex scanners," *Ultrasound Med Biol*, vol. 17, pp. 195–199, 1991.

[188] P. R. Hoskins, "A review of the measurement of blood velocity and related quantities using Doppler ultrasound," *P I Mech Eng H*, vol. 213, no. 3, pp. 391–404, 1999.

[189] P. R. Hoskins, P. J. Fish, S. D. Pye, and T. Anderson, "Finite beam-width ray model for geometric spectral broadening," *Ulrasound Med Biol*, vol. 25, no. 5, pp. 391–400, 1999.

[190] P. R. Hoskins, "Accuracy of maximum velocity estimates made using Doppler ultrasound systems," *Brit J Radiol*, vol. 69, pp. 172–177, 1996.

[191] D. W. Holdsworth, C. J. D. Norley, R. Frayne, D. A. Steinman, and B. K. Rutt, "Characterization of common carotid artery blood-flow waveforms in normal human subjects," *Physiol Meas*, vol. 20, pp. 219–240, 1999.

[192] J. Peacock, T. Jones, C. Tock, and R. Lutz, "The onset of turbulence in physiological pulsatile flow in a straight tube," *Exp Fluids*, vol. 24, pp. 1–9, 1998.

[193] M. F. O'Rourke, R. Kelly, and A. Avolio, *The Arterial Pulse*. Pennsylvania, U.S.A.: Lea and Febiger, 1992.

[194] P. J. Roache, "Perspective: A method for uniform reporting of grid refinement studies," *J Fluid Eng*, vol. 116, pp. 405–413, 1994.

[195] T. H. Dawson, *Engineering Design of the Cardiovascular System of Mammals*, ch. 4, p. 83. New Jersey: Prentice Hall, 1991.

[196] K. K. Shung, R. A. Sigelmann, and J. M. Reid, "Scattering of ultrasound by blood," *IEEE T Biomed Eng*, vol. 23, pp. 460–467, 1976.

[197] A. Thrush, "Spectral Doppler ultrasound," in *Diagnostic Ultrasound* (P. R. Hoskins, A. Thrush, K. Martin, and T. A. Whittingham, eds.), ch. 9, pp. 113–127, London: Greenwich Medical Media Limited, 2003.

[198] P. D. Stein, H. N. Sabbah, D. T. Anbe, and F. J. Walburn, "Blood velocity in the abdominal aorta and common iliac artery of man," *Biorheology*, vol. 16, pp. 249–255, 1979.

[199] T. Hatakeyama, H. Shigematsu, and T. Muto, "Risk factors for rupture of abdominal aortic aneurysm based on three-dimensional study," *J Vasc Surg*, vol. 33, pp. 453–461, 2001.

[200] T. Shipkowitz, V. G. J. Rodgers, L. J. Frazin, and K. B. Chandran, "Numerical study on the effect of secondary flow in the human aorta on local shear stresses in abdominal aortic branches," *J Biomech*, vol. 33, pp. 717–728, 2000.

[201] C. J. Freitas, "Perspective: Selected benchmarks from commercial CFD codes," *J Fluids Eng*, vol. 117, pp. 208–218, 1995.

[202] U. Köhler, I. Marshall, M. Robertson, Q. Long, X. Y. Xu, and P. R. Hoskins, "MRI measurement of wall shear stress vectors in bifurcation models and comparison with CFD predictions," *Journal of Magnetic Resonance Imaging*, vol. 14, pp. 563–573, 2001.

[203] J. P. Ku, C. J. Elkins, and C. A. Taylor, "Comparison of CFD and MRI flow and velocities in an *In Vitro* large artery bypass graft model," *Annals of Biomedical Engineering*, vol. 33, no. 3, pp. 257–269, 2005.

[204] J. A. Moore, D. A. Steinman, D. W. Holdsworth, and C. R. Ethier, "Accuracy of computational hemodynamics in complex arterial geometries reconstructed from magnetic resonance imaging," *Annals of Biomedical Engineering*, vol. 27, pp. 32–41, 1999.

[205] K. Perktold, M. Hofer, G. Rappitsch, M. Loew, B. D. Kuban, and M. H. Friedman, "Validated computation of physiologic flow in a realistic coronary artery branch," *J Biomech*, vol. 31, pp. 217–228, 1998.

[206] J. G. Myers, J. A. Moore, M. Ojha, K. W. Johnston, and C. R. Ethier, "Factors influencing blood flow patterns in the human right coronary artery," *Annals of Biomedical Engineering*, vol. 29, pp. 109–120, 2001.

[207] T. Frauenfelder, M. Lotfey, T. Boehm, and S. Wildermuth, "Computational fluid dynamics: Hemodynamic changes in abdominal aortic aneurysm after stent-graft implantation," *Cardiovasc Intervent Radiol*, vol. 29, pp. 613–623, 2006.

[208] U. Kose, S. de Putter, R. Hoogeveen, and M. Breeuwer, "Computational fluid dynamics of abdominal aortic aneuryms with patient-specific inflow boundary conditions," in *Progress in Biomedical Optics and Imaging. Medical Imaging 2006: Physiology, Function and Structure from Medical Images*, vol. 7, pp. 61432D1–11, 2006.

[209] T. McInerney and D. Terzopoulos, "Deformable models in medical image analysis: a survey," *Medical Image Analysis*, vol. 1, no. 2, pp. 91–108, 1996.

[210] D. L. Pharm, C. Xu, and J. L. Prince, "Current methods in medical image segmentation," *Annu Rev Biomed Eng*, vol. 2, pp. 315–337, 2000.

[211] M. Subašić, S. Lončarić, and E. Sorantin, "Model-based quantitative AAA image analysis using a priori knowledge," *Comput Meth Prog Bio*, vol. 80, pp. 103–114, 2005.

[212] M. de Bruine, B. van Ginneken, M. A. Viergever, and W. J. Niessen, "Interactive segmentation of abdominal aortic aneurysms in CTA images," *Medical Image Analysis*, vol. 8, no. 2, pp. 127–138, 2004.

[213] S. D. Olabarriaga, J.-M. Rouet, M. Fradkin, M. Breeuwer, and W. J. Niessen, "Segmentation of thrombus in abdominal aortic aneurysms from CTA with nonparametric statistical grey level appearance modeling," *IEEE T Med Imaging*, vol. 24, no. 4, pp. 477–485, 2005.

[214] S. de Putter, M. Breeuwer, U. Kose, F. Laffargue, J.-M. Rouet, R. Hoogeveen, H. van den Bosch, J. Buth, F. van de Vosse, and F. Gerritsen, "Automatic determination of the dynamic geometry of abdominal aortic aneurysm from MR with application to wall stress simulation," *International Congress Series*, vol. 1281, pp. 339–344, 2005.

[215] B. S. Gow and M. G. Taylor, "Measurement of viscoelastic properties of arteries in the living dog," *Circ Res*, vol. 23, pp. 111–122, 1968.

[216] R. C. Gonzalez and R. E. Woods, *Digital Image Processing*. New Jersey: Prentice-Hall Inc., 2002.

[217] K. L. Lee and D. J. Doorly, "Numerical simulations of phase contrast velocity mapping of complex flows in an anatmically realistic bypass graft geometry," *Med Phys*, vol. 33, pp. 2621–2631, 2006.

[218] L. Bax, C. J. G. Bakker, W. M. Klein, N. Blanken, J. J. Beutler, and W. P. R. M. Mali, "Renal blood flow measurements with the use of phase-contrast magnetic resonance imaging: normal values and reproducibility," *J Vasc Interv Radiol*, vol. 16, pp. 807–814, 2005.

[219] A. D. Jeays, P. V. Lawford, R. Gillott, P. Spencer, D. C. Barber, K. D. Bardhan, and D. R. Hose, "Characterisation of the haemodynamics of the superior mesenteric artery," *Journal of Biomechanics*, vol. 40, pp. 1916–1926, 2007.

[220] Z. Li and C. Kleinstreuer, "Blood flow and structure interactions in a stented abdominal aortic aneurysm model," *Med Eng Phys*, vol. 27, pp. 369–382, 2005.

[221] Z. Li and C. Kleinstreuer, "Fluid structure interaction effects on sac-blood pressure and wall stress in a stented aneurysm," *J Biomech Eng-T ASME*, vol. 127, pp. 662–671, 2005.

[222] B. J. B. M. Wolters, M. C. M. Rutten, G. W. H. Schurink, U. Kose, J. de Hart, and F. N. van de Vosse, "A patient-specific computational model of fluid-structure interaction in abdominal aortic aneurysms," *Med Eng Phys*, vol. 27, no. 10, pp. 871–883, 2005.

[223] M. Li, *Numerical Simulation of Blood Flow and Vessel Wall Stresses in Stenosed Arteries*. PhD thesis, The University of Edinburgh, 2006.

[224] C. A. Figueroa, I. E. Vignon-Clementel, K. E. Jansen, T. J. R. Hughes, and C. A. Taylor, "A coupled momentum method for modeling blood flow in three-dimensional deformable arteries," *Comput Methods Appl Mech Engrg*, vol. 195, pp. 5685–5706, 2006.

[225] M. Li, J. J. Beech-Brandt, W. J. Easson, and P. R. Hoskins, "Numerical simulation of pulsatile flow through a compliant stenotic tube," in *Biomechanics, BioMech 2005, 9/7/2005 - 9/26/2005, Benidorm, Spain* (M. H. Hamza, ed.), 2005.

[226] K. Perktold and G. Rappitsch, "Computer simulation of local blood flow and vessel mechanics in a compliant carotid artery bifurcation model," *J Biomech*, vol. 28, no. 7, pp. 845–856, 1995.

[227] D. R. Hose, P. V. Lawford, A. J. Narracott, J. M. T. Penrose, and I. P. Jones, "Fluid - solid interaction: benchmarking of an external coupling of ANSYS with CFX for cardiovascular applications," *J Med Eng Tech*, vol. 27, no. 1, pp. 23–31, 2003.

[228] J. P. Vande Geest, M. S. Sacks, and D. A. Vorp, "Age dependency of the biaxial biomechanical behavior of human abdominal aorta," *J Biomech Eng - T ASME*, vol. 126, pp. 815–822, 2004.

[229] J. P. V. Geest, M. S. Sacks, and D. A. Vorp, "A planar biaxial constitutive relation for the lumnial layer of intra-lumnial thrombus in abdominal aortic aneurysms," *J Biomech*, vol. 39, no. 13, pp. 2347–2354, 2006.

[230] D. A. Vorp, W. A. Mandarino, M. W. Webster, and J. Gorcsan III, "Potential influence of intraluminal thrombus on abdominal aortic aneurysm as assessed by a new non-invasive method," *Cardiovasc Surg*, vol. 4, no. 6, pp. 732 – 739, 1996.

[231] P. J. Roache, "Quantification of uncertainty in computational fluid dynamics," *Annu. Rev. Fluid. Mech*, vol. 29, pp. 123–60, 1997.

[232] O. C. Zienkiewicz and R. L. Taylor, *The Finite Element Method: Volume 1*. Oxford: Butterworth-Heinemann, 2002.

[233] J. S. Lindholt, "Aneurysmal wall calcification predicts natural history of small abdominal aortic anuerysms," *Atherosclerosis*, vol. in press.

[234] G. A. Holzapfel, G. Sommer, and P. Regitnig, "Anisotropic mechanical properties of tissue components in human atherosclerotic plaques," *J Biomech Eng - T ASME*, vol. 126, pp. 657–665, 2004.

[235] D. Bluestein, C. Gutierrez, M. Londono, and R. T. Schoephoerster, "Vortex shedding in steady flow through a model of an arterial stenosis and its relevance to mural platelet deposition," *Ann Biomed Eng*, vol. 27, pp. 763–773, 1999.

[236] L. Formaggia, J. F. Gerbeau, F. Nobile, and A. Quarterioni, "On the coupling of 3d and 1d Navier-Stokes equations for flow problems in compliant vessels," *Comput Methods Appl Mech Engrg*, vol. 191, pp. 561–582, 2001.

[237] I. E. Vignon-Clementel, C. A. Figueroa, K. E. Jansen, and C. A. Taylor, "Outflow boundary conditions for three-dimensional finite element modeling of blood flow and pressure in arteries," *Comput methods in appl mech and engrg*, vol. 195, pp. 3776–3796, 2006.

[238] W. T. Lee, K. H. Fraser, M. Li, P. Stroev, W. J. Easson, and P. R. Hoskins, "Integrating three dimensional and one dimensional simulations of hæmodynamic flow: modified windkessel model of a diseased artery," *Medical and biological engineering and computing*, vol. in press.